Modélisation atmospherique régionale du cycle des isotopes stables de l'eau

Kristof Sturm

LABORATOIRE DE GLACIOLOGIE
ET GEOPHYSIQUE DE L'ENVIRONNEMENT
UMR5183
Centre National de la Recherche Scientifique
Université Joseph Fourier
54, rue Molière - Domaine Universitaire
BP 96 - 38402 - Saint Martin d'Hères Cedex (France)

Regional atmospheric modelling of the stable water isotope cycle.

Modélisation atmosphérique régionale du cycle des isotopes stables de l'eau.

Kristof Sturm

Thèse de doctorat de l'Université Joseph Fourier (Grenoble 1)
(Arrêtés ministériels du 5 juillet 1984 et 30 mars 1992)

Spécialité : Sciences de la Terre et de l'Univers

Date de Soutenance :
13 Juin 2005

Composition du jury :

Pr. Hans von Storch	*Directeur du jury*
Pr. Hartmut Grassl	*Rapporteur*
Pr. Pierre Ribstein	*Rapporteur*
Pr. Hans Graf	*Directeur de thèse*
Dr. Gerhard Krinner	*Directeur de thèse*
Dr. Georg Hoffmann	*Examinateur*
Dr. Patrick Ginot	*Examinateur*

Abstract

Climate change has recently become a major concerning among scientists and the general public. A better knowledge of past climates helps forecasting the future evolution of climate. Stable water isotopes stand as an outstanding paleo-climate proxy. Physical properties of heavy stable water isotopes ($H_2^{18}O, HDO$) cause fractionation processes related to temperature and degree of distillation. If the isotopic signal is correctly inverted, past climate change can be inferred from isotopic archives.

Andean ice-cores offer a unique records of tropical climate and its variability through time. However, the interpretation of the isotopic signal is difficult because of complex atmospheric dynamic over South America. For this purpose, we developed a module handling the stable water isotope fractionation processes within the regional circulation model REMO and applied it to South America.

The manuscript outlines the major milestones of the present PhD. We first introduce the research topic in the wider scope of climate change; the description of the stable water isotope enabled regional circulation model REMOiso; an initial validation of REMOiso over Europe; an investigation of the seasonal variations of precipitation, atmospheric circulation and isotopic signal over South America; and at last the recording of the south American monsoon system (SAMS) by stable water isotope diagnostics.

$\star \ ^{\star} \ \star$

Dans un contexte de changement climatique, la connaissance des climats passés permet de mieux cerner l'évolution future du climat. Les isotopes stables de l'eau constituent un excellent proxy paléo-climatique. Les propriétés physiques des isotopes lourds de l'eau ($H_2^{18}O, HDO$) induisent des fractionnements isotopiques, qui dépendent de la température et du taux de distillation. Sous réserve d'une inversion bien conditionnée du signal isotopique, on peut reconstruire les variations passées du climat à partir d'archives isotopiques. Les carottes de glace andines constituent un enregistrement unique de la variabilité du climat tropical. En revanche, la complexité de la circulation atmosphérique rend plus ardue l'interprétation de leur signal isotopique.

En conséquence, nous avons développé au cours de cette thèse un module traitant du fractionnement des isotopes stables de l'eau au sein du modèle de circulation régionale REMO pour application au cas de l'Amérique du Sud. Le manuscrit retrace les principales étapes de la thèse. Il s'agit de la mise en perspective du travail de thèse dans la problématique du changement climatique ; la description du modèle de circulation régionale REMO_{iso} et de son module traitant des isotopes de l'eau ; la validation initiale de REMO_{iso} sur l'Europe ; l'étude des variations saisonnières des précipitations, de la circulation atmosphérique régionale et du signal isotopique en Amérique du Sud ; de l'enregistrement par les isotopes stables de l'eau de la mousson sud-américaine.

$\star \ ^{\star} \ \star$

Klimawandel regt steigendes Interesse unter Wissenschaftlern und in der öffentlichen Meinung an. In diesem Zusammenhang kann eine bessere Kenntnis des vergangenen Klimas dazu verhelfen, die zukünftige

Entwicklung des Klimas genauer vorherzusagen. Die stabilen Wasserisotopen machen einen vorbildlichen paleoklimatischen Proxy aus. Die physischen Eigenschaften der schweren Wasserisotopen ($H_2^{18}O, HDO$) bewirken isotopische Fraktionierungen, die von der Temperatur und dem Ausregnensgrad abhängen. Wenn das isotopische Signal richtig invertiert wird, können klimatischen Schwankungen aus isotopischen Archiven nachgebildet werden. Die Andinischen Eisbohrkerne liefern eine einmalige Aufzeichnung der klimatischen Variabilität in den Tropen. Wegen der komplexen atmosphärischen Zirkulation kann deren Isotopensignal aber nicht direkt gedeutet werden.

Von daher haben wir im Laufe dieser Doktorarbeit einen Modul entwickelt, der den Kreislauf der stabilen Wasserisotope im regionalen Zirkulationsmodell REMO nachbildet. Im Manuskript werden die wesentlichen Etappen der Doktorarbeit beschrieben. Die wissenschaftliche Fragestellung der Doktorarbeit wird in der Perspektive der Klimawandelforschung eingeleitet; die technische Beschreibung des regionalen Zirkulationsmodell REMO und dessen Wasserisotopenmodul folgt; die ursprüngliche Validation von REMO$_{iso}$ über Europa wird dargestellt; die säzonalen Variationen des Niederschlags, der atmosphärischen Zirkulation und des isotopischen Signals über Südamerika werden untersucht; zuletzt wird die Aufzeichnung des südamerikanischen Monsuns in dem isotopischen Signals hervorgehoben.

$\star \ ^{\star} \ \star$

Acknowledgements

Voici donc le résultat de trois années de travail, qui n'auraient jamais abouti sans la participation et le soutien de nombreuses personnes. C'est à vous que je souhaite aujourd'hui dire un grand merci.

Naturellement, c'est à Georg Hoffmann que je pense en premier, son enthousiasme contagieux, son contact chaleureux, son incitation à l'autonomie. Je suis très reconnaissant également à Gerhard Krinner d'avoir encadré cette thèse, et de prodiguer conseils scientifiques et encouragements amicaux dans les moments cruciaux.

De Grenoble je garde de bons souvenirs, ses montagnes enneigées, ses terrasses de café, son laboratoire de glaciologie... Merci pour toutes les rencontres effectuées en ces murs depuis un matin de décembre 2000 qui vit mes premiers pas dans la recherche. Ici l'émulation scientifique va de pair avec une atmosphère cordiale, avec l'illustration quotidienne de la recherche comme métier-passion. Une mention spéciale à la joyeuse bande des thésards pour avoir consacré notre bureau comme antre du café et de la convivialité.

Au-delà de ce premier cercle, je tiens à remercier tous ceux qui m'ont accompagné au cours de cette aventure. A l'origine de ce projet se trouve la découverte de l'unité Great Ice/IRD, sous la conduite de Bernard Francou et Pierre Ribstein. Je tiens à les remercier chaleureusement pour m'avoir initié aux joies du terrain et de la curiosité scientifique. Par la suite, j'ai toujours trouvé dans cette équipe un accueil chaleureux autant qu'une invitation au voyage, des Andes jusqu'en Himalaya. Merci également à Françoise Vimeux pour sa pédagogie et sa bonne humeur, ainsi qu'à l'équipe de Valérie Masson au LSCE pour les visites enrichissantes que j'y ai effectuées.

Ainsi se termine cette première étape. Je vous suis tous sincèrement reconnaissant de m'avoir donné l'envie de poursuivre dans cette voie...

♣ ♢ ♠ ♡

Wie reich und vielfältig die Zeit der Promotion gewesen ist... Ich bin dafür dankbar, daß mir die Möglichkeit angeboten worden ist, eine weitere deutsch-französische Erfahrung zu erleben. Trotz den praktischen Umständlichkeiten war es angesichts aller Begegnungen und Lebenserfahrungen eindeutig der Mühe wert.

Die stärkste Erinnerung meines Aufenthalts am Max-Planck-Institut ist mit der netten Stimmung der Schlump-WG verbunden. An ersten Stelle möchte ich mich bei Bärbel Langamnn dafür bedanken, dass sie meine ersten Schritte als MPI-Doktorand geleitet und dabei mich an dem Gebrauch von $REMO_{iso}$ eingeführt hat. Ich behalte die lebhafte Diskussionen mit Hans Graf in Erinnerung, samt seiner ermunternden Anregungen und enthusiastische Perspektiven. Ralf Podzuns Bereitschaft unter der ganzen Doktorarbeit, um verschlüsselte Geheimnisse des REMO-Codes zu entziffern, war von höchst wertvoller Hilfe. Schließlich möchte ich mich bei Guy Brasseur und Hartmut Grassl bedanken, mich in der wissenschaftlich stimulierenden Gemeinschaft des Max-Planck-Institutes aufgenommen zu haben.

Georg und Gerhard gehören selbstverständlich auch in dieser Kategorie der Danksagungen, denn mit ihr konnte das transnational Abenteuer nach meiner Rückkehr weitegeführt werden.

♣ ♢ ♠ ♡

English has not only imposed itself as major working language, but often ends up as the smallest common denominator among uprooted students. Life in the Hansestadt would never have been as enjoyable without the IMPRS gang, like a live

Woody Allen comedy in italoportuñol with Bollywood flavours. "Man is nomad, because life is a journey" as an old proverb says, I am glad we had some good time on the way.

Finally, I bear in minds all the people encountered in Vienna, Sapporo or Huaraz and the exciting feeling of entering the large science family.

♣ ♢ ♠ ♡

Table of Contents

List of Figures

List of Tables

LABORATOIRE DE GLACIOLOGIE ET
GÉOPHYSIQUE DE L'ENVIRONNEMENT
54, rue Molière - Domaine Universitaire
BP 96 - 38402 - Saint Martin d'Hères Cedex (France)

MAX PLANCK INTITUT FÜR METEOROLOGIE
Zentrum für Marine und Atmosphärische Wissenschaften
Bundesstraße 53
20146 Hamburg (Deutschland)

Regional atmospheric modelling of the stable water isotope cycle.

Modélisation atmosphérique régionale du cycle des isotopes stables de l'eau.
Regionale Modellierung des atmosphärischen Kreislaufs stabiler Wasserisotope.

'Bud of spring', by Noriko Nakazato

Joint supervision PhD thesis by / Thèse de doctorat en co-tutelle de /
Dissertation in Kobetreuung von

Kristof STURM – May 2005
Université Joseph Fourier-Grenoble I – Universität Hamburg

Till Maya, tack för allting och mer...

Chapter 1

Introduction: regional modelling of the stable isotope cycle for the interpretation of observations

Résumé

L'introduction ci-après présente le cadre général du travail de thèse. Elle s'est déroulée en co-tutelle franco-allemande entre le Laboratoire de Glaciologie et Géophysique de l'Environnement (LGGE – rattaché à l'Université Joseph Fourier-Grenoble I) et le Max Planck Institut für Meteorologie (MPIfM – rattaché à l'Université de Hambourg). Dans un contexte de changement climatique, la connaissance des climats passés permet de mieux cerner l'évolution future du climat. Or il n'existe pas de mesure directe pour décrire les climats antérieurs. Il faut donc se baser sur des mesures indirectes, pour reconstruire par modélisation inverse les températures et cycles hydrologiques du passé.

Les isotopes stables de l'eau constituent un excellent proxy paléo-climatique. Les propriétés physiques des isotopomères lourds de l'eau ($H_2^{18}O$, HDO) induisent des fractionnements isotopiques, qui dépendent de la température et du taux de distillation. Sous réserve d'une inversion bien conditionnée du signal isotopique, on peut reconstruire les variations passées du climat à partir d'archives isotopiques.

Les carottes de glace andines constituent un enregistrement unique de la variabilité du climat tropical. En revanche, la complexité de la circulation atmosphérique rend plus ardue l'interprétation de leur signal isotopique. L'application de modèles de circulation générale incluant les isotopes de l'eau donnent lieu à des interprétations divergentes quant aux contrôles dominants du signal isotopique. La prolongation logique de ces recherches réside dans une modélisation à plus haute résolution. C'est la raison pour laquelle une version isotopique du modèle de circulation régionale REMO_{iso} a été développée au cours de cette thèse, pour application au cas de l'Amérique du Sud.

Zusammenfassung

Die nachfolgende Einführung stellt den allgemeinen Rahmen der Doktorarbeit. Diese verlief in deutsch-französischer Kobetreuung zwischen dem Laboratoire de Glaciologie et Géophysique de l'Environnement (LGGE – in Verbindung mit der Universität Grenoble I-Joseph Fourier) und dem Max Planck Institut für Meteorologie (MPIfM – in Verbindung mit der Universität Hamburg). Gegenüber der heutigen Klimaveränderung ermöglicht die Grundkenntnis der vergangenen Klimavariationen, die künftige Evolution des Klimas besser zu erfassen. Da es keine direkte Messungen für die Vergangenheit verfügbar sind, müssen Temperatur- und Wasserzyklusvariationen aus Inversmodellierung von Paleoklimaproxy rekonstruiert werden.

Die atmomphysiche Eigenschaften der stabilen Wasserisotopomeren ($H_2^{18}O$, HDO), etwas schwerer als gewöhnliche Wassermolekülen, verleiten zu isotopischen Fraktionierungen, die von Temperatur und Destillationsgrad abhängen. Unter Vorbehalt einer gut konditionierten Inversion des Isotopensignal können vergangenen Klimaveränderungen aus Isotopenarchiven wiederhergestellt werden.

Andinische Eisbohrkerne bilden angesichts dessen ein einmaliges Archiv der tropischen Klimavariabilität. Nichtsdestotrotz erschwert die komplexe Regionalzirkulation die Interpretation deren Isotopensignal. Trotz Anwendung von Generalzirkulationsmodellen mit Wasserisotopenmodulen, bestehen divergierenden Deutungen über vorherrschenden Klimakontrollen des Wasserisotopensignals. Logische Fortsetzung zu diesen Erforschungen war eine feiner aufgelöste Modellierung. Aus dieser Begründung richtet sich die jetzige Doktorarbeit auf die Entwicklung einer isotopischen Version des Regionalzirkulationsmodelles REMO_{iso}, hinsichtlich einer Anwendung über Südamerika.

Climate change has recently become a major concern for scientists, officials and public opinion. The intergovernmental panel on climate change (IPCC) underlines in its latest report [IPCC, 2001] the evidence of observed climate change since 1765. Its most striking manifestation concerns temperature. However, less obvious consequences should not be overseen, affecting atmospheric circulation patterns and hydrological regimes with large regional disparities.

1.1 From climate change to paleo-climatology

Figure 1.1 displays in its upper row the past evolution of mean global temperatures and the foreseeable evolution of global temperatures in its lower row. Figure 1.1B reflects the global warming as evidenced from direct measurements, reaching +0.75°C over the last 140 years. Based on different scenarios of green gas emissions for the XXIst century, global circulation models (GCM) predict a global warming by 2°to 4.5°C. The consensus among the scientific community on global warming * does not obscure highly controversial issues concerning other aspects of climate change. IPCC [2001] underlines the regional disparities which are masked by the rise of mean global temperature. In particular, the evolution of the regional hydrological regimes in a globally warming climate is still a matter of debate. Hence, GCM predictions should be completed by high resolution, limited area modelling tools such as the regional circulation models (RCM).

The discussion about the confidence level of GCM predictions raises the question about GCM validation. An obvious constraint for GCM validation is to reproduce accurately present-day climate. Because of highly un-linear responses in the climate system, this validation is not sufficient to assert reliable predictions of the future climate. This requirement underlies the recent infatuation for past evolution of climate variations, or paleo-climatology. If the same physical parameterisations allow GCMs to reproduce a large spectrum of past and present climates, they ought to be reliable for future climate predictions. Prior to 1850 A.D., experimental records are rare and lack a global coverage for climate parameters such as temperature, circulation patterns and precipitation amounts. Instead of direct measurements, climate variations need to be inferred by indirect methods. Climate parameters, most commonly temperature, are reconstructed on the basis of quantities (or *proxies*) that can be measured in climate archives.

1.2 Stable water isotopes: a major climate proxy

The 'isotopic signal' in climate archives usually refers to the composition in stable water isotopes (SWI) $^1H_2^{18}O$ and $^1H^2H^{16}O$. Strictly speaking, the water molecules incorporating a heavier isotope of oxygen (^{18}O)† or hydrogen (^2H or deuterium D) should be referred to as stable water isotopomers (or isotopologues), but the term 'water isotopes' has gained common practice for the sake of simplicity.

The isotope abundance is defined as the molar ratio of the rare isotope concentration and the and the dominant isotope concentration, as defined in Equation 1.1.

$$\begin{aligned} {}^{18}R(H_2O) &= \frac{[^1H_2^{18}O]}{[^1H_2^{16}O]} \\ {}^{2}R(H_2O) &= \frac{[^1H^2H^{16}O]}{[^1H_2^{16}O]} \end{aligned} \tag{1.1}$$

The natural abundance of stable oxygen and hydrogen isotopes is given in Table 1.1. Since the values of isotope abundance are very small, it is more convenient to describe the isotopic composition of a given water sample as the deviation from a standard value instead of its absolute abundance. The deviation, noted δ, is taken according to Equation

*By its constituting rules, the IPCC brings together recognised scientists from all nations and climate disciplines. It is thus representative of the community of climate scientists. Because of the serious implications for the economy and life-style of industrialised countries, several among the most prominent industrial and political leaders are reluctant to admit the conclusions of the research studies. This might explain why the reality of climate change is still controversial in the public opinion, although this fundamental debate has expired among mainstream scientists themselves.

†^{17}O is another naturally occurring oxygen isotope. In the tropospheric water cycle, it behaves identically to ^{18}O. Since it is rarer than ^{18}O, difficult to measure, and does not bring any further information than ^{18}O, ^{17}O is generally not considered by environmental scientists. In recent years, a mechanism involving stratospheric ozone photochemistry revealed mass-independent fractionation between $^1H_2^{18}O$ and $^1H_2^{17}O$. The $^1H_2^{17}O$ signal can hence be used to trace stratospheric inclusions in polar ice-cores [Savarino, personal communication].

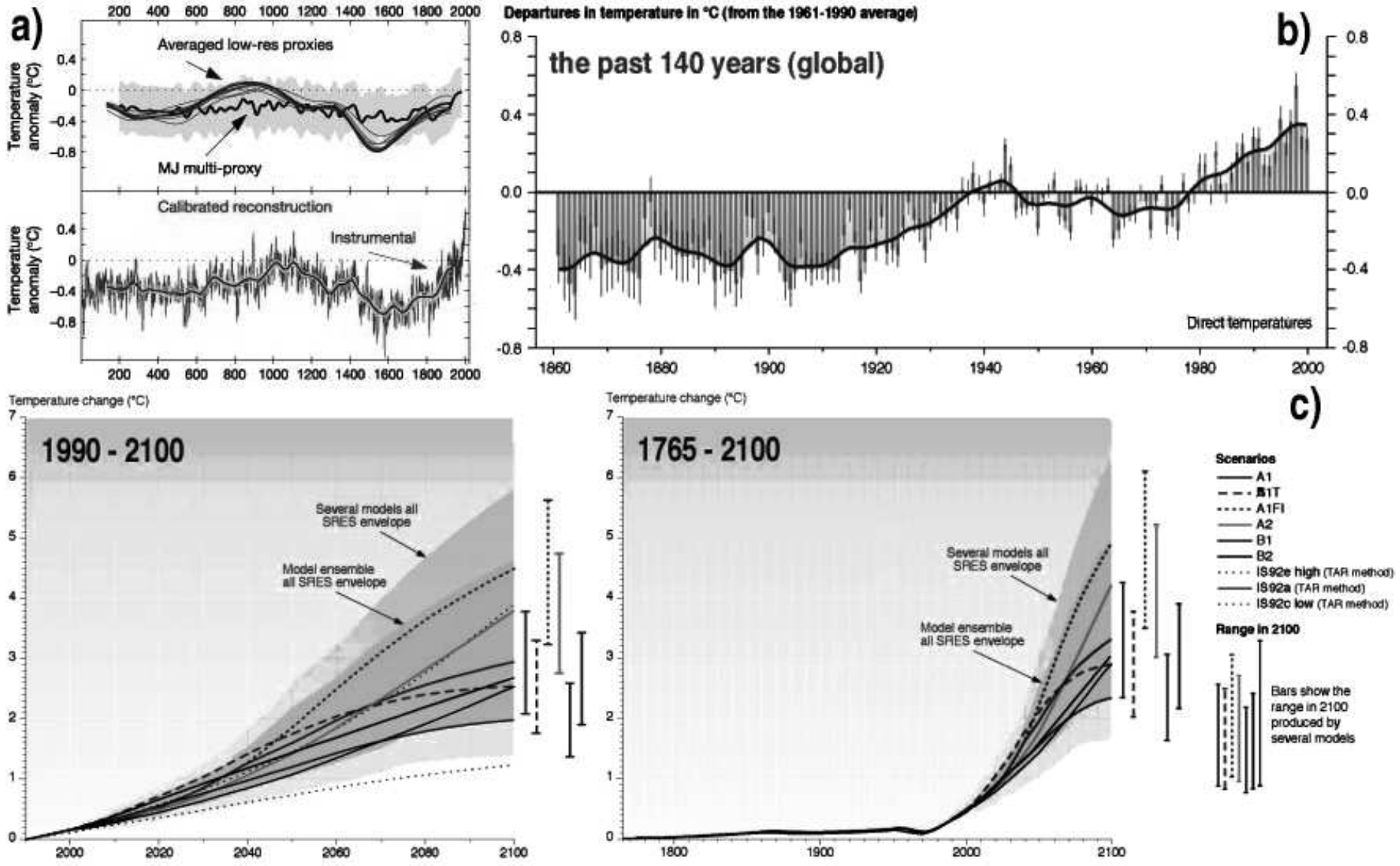

Figure 1.1: Past and future evolution of mean global temperatures, a state-of-the-art synthesis by the IPCC. Sub-figure (a) displays the inferred Northern Hemisphere temperature variations over the last 2000 years. The reconstruction is based on a compilation of all available proxy data. Sub-figure (b) displays the measured mean global temperature evolution over the last 140 years. Sub-figure (c) shows the global warming estimations predicted by various global circulation models, under optimistic and pessimist scenarios of future green-house gas emissions for the XXIst century. Graph (a) is quoted from Moberg et al. [2005], graphs (b-c) are quoted from IPCC [2001].

Isotope	^{16}O	^{17}O	^{18}O	^{1}H	$^{2}H\,(D)$
Natural abundance	0.9976	0.00038	0.00205	0.99985	0.00015
R_{V-SMOW}	1	-	0.0020052	1	0.00015575

Table 1.1: Naturally occurring stable water oxygen and hydrogen isotopes. R_{V-SMOW} represents the Vienna standard mean ocean water molar ratio.

1.2 from the largest reservoir of water molecules: the Earth oceans. The standard commonly used is the Vienna standard mean ocean water, whose values are reported in Table 1.1.

$$\begin{aligned} \delta^{18}\mathrm{O}\,(H_2O) = & \left(\frac{^{18}R(H_2O)_{sample}}{^{18}R_{V-SMOW}} - 1\right)\,[‰] \\ (1.1) \Rightarrow & \\ \delta^{18}\mathrm{O}\,(H_2O) = & \left(\frac{([^1H^2H^{16}O]/[^1H_2^{16}O])_{sample}}{^{18}R_{V-SMOW}} - 1\right)\,[‰] \end{aligned} \tag{1.2}$$

An analogue formulation to Equation 1.2 defines the deviation of deuterium abundance in a water sample $\delta\mathrm{D}\,(H_2O)$.

What determines the variations of $\delta^{18}\mathrm{O}$, and how to relate them to climate parameters ? The analysis of mass-dependent fractionation processes answers that question. The ^{18}O (D) isotope possesses 2 (1) neutrons more than the standard O (H) isotope, hence the mass of the water isotopomer will be heavier by $2\,(1) \times 1.67492728 \cdot 10^{-27}$ kg the standard water molecule, that is 11.1% (5.56%) of the molecular mass. Boltzmann demonstrated that the molecular kinetic energy $kT = 1/2 \cdot mv^2$ depends on temperature only. At the same temperature, heavier isotopomers will have a slightly smaller velocity. As a consequence, the heavier isotopomers have a diffusion velocity quadratically inverse to their mass. Since heavier molecules have a higher binding energy, the energy threshold to break the inter-molecular bonds (evaporation heat) will be higher. As a practical consequence, $H_2^{18}O$ and HDO will have a lower saturation vapour pressure than $H_2^{16}O$: they will evaporate less easily and condensate the first.

The physical properties described above are responsible for the fractionation processes which alter the isotopic composition of a moisture sample along the hydrological cycle. Thermodynamical fractionation takes place during phase changes under equilibrium conditions. Heavy isotopomers are more likely to be found in an aggregate phase (typically, liquid water) than a volatile phase (typically, water vapour). If evaporation occurs from an initial reservoir (δ_0), the vapour will be depleted in heavy isotopes ($\delta_{vap} < \delta_0$) and the remaining liquid will be enriched in heavy isotopes ($\delta_{liq} > \delta_0$).

$$\begin{aligned} \alpha = & \frac{R_{liq}}{R_{vap}} \\ (1.2) \Rightarrow \alpha = & \frac{\delta_{liq}+1}{\delta_{vap}+1} \\ \varepsilon = & \alpha - 1 \\ = & \frac{\delta_{liq}-\delta_{vap}}{\delta_{vap}+1} \\ \delta \ll 1 \Rightarrow \varepsilon \simeq & \delta_{liq} - \delta_{vap} \end{aligned} \tag{1.3}$$

Quantatively, thermodynamical fractionation is characterised by the *fractionation factor* α, defined in Equation 1.3. Majoube [1971] exhibited empirical relations of the fractionation factor $\alpha(T)$ with temperature $T \in [273.15K; 373.15K]$, given in Equation 1.4.

$$\begin{aligned} H_2^{18}O \quad \ln\left(^{18}\alpha(T)\right) = & \frac{1.137\,10^3}{T^2} - \frac{0.4156}{T} - 2.0667\,10^{-3} \\ HDO \quad \ln\left(^{2}\alpha(T)\right) = & \frac{24.844\,10^3}{T^2} - \frac{76.248}{T} - 52.612\,10^{-3} \end{aligned} \tag{1.4}$$

The physical parameterisation of in-situ equilibrium fractionation can be extended to the evolution of cloud vapour $\delta^{18}O$ along its trajectory. The Rayleigh distillation model accounts for the progressive depletion of heavy isotopes in the cloud vapour as a function of the rain-out rate. The Rayleigh distillation is characterised by an open system (e.g. a cloud), where a prescribed amount of condensation occurs under equilibrium conditions and is immediately removed from the system (e.g. as precipitation). The Rayleigh distillation law, and derived equations of the cloud vapour (δ_{vap}) and rain (δ_{liq}) isotopic composition are given in Equation 1.5 as a function of the rain-out rate f, the previously defined fractionation factor $\alpha(T)$ and the reservoir initial composition δ_0.

$$\begin{aligned} \frac{R_{vap}}{R_0} &= f^{\alpha(T)-1} = f^{\varepsilon(T)} \\ \Rightarrow \delta_{vap} &= \left[(\delta_0+1)\cdot f^{\alpha(T)-1}\right]-1 \\ \Rightarrow \delta_{liq} &= \alpha(T)\cdot\left[(\delta_0+1)\cdot f^{\alpha(T)-1}\right]-1 \end{aligned} \tag{1.5}$$

The gradual rainout of air masses during their travel poleward, combined with dependence of the isotopic composition on temperature (Equation 1.4) explains that the isotopic signal in ice-cores is used as a paleo-thermometer. *If* the hydrological cycle is assumed not to have changed significantly (i.e. parameters R_0, f have not varied) and cloud condensation to occur at equilibrium, *then* the $\delta^{18}O_{liq}$ recorded in the ice-core can be related to the mean in-cloud temperature of condensation. Independent observations indicate that neither of the model parameters are constant in time and space (varying accumulation rates affect f, foraminifer $\delta^{18}O$ records from ocean cores reveal varying δ_0, convective motion and ice-crystal condensation are out of equilibrium processes...).

Despite (or because) of its extreme simplicity, the Rayleigh distillation model offers a good conceptual comprehension of the classical 'isotope effects' [Dansgaard, 1964].

Latitude (or annual temperature) effect accounts for the progressive depletion of precipitation $\delta^{18}O$ at high latitudes. In compliance with Equation 1.4, the fractionation factor increases with decreasing temperatures ($\partial\alpha(T)/\partial T < 0$). Hence the depletion of cloud vapour is more pronounced under colder climates, at high latitudes.

Continental effect accounts for progressive depletion of precipitation $\delta^{18}O$ with increasing distance from the evaporation site (usually, distance from the nearest upstream water body). As air masses penetrate further inland, the rain-out rate increases and causes the remaining $\delta^{18}O$ to decrease. The identification of the continental effect requires to know the mean air mass trajectories (moisture advection by the regional circulation). This effect can partially be balanced during summer over vegetated areas. Transpiration by the vegetation releases soil moisture (i.e. previous precipitation) into the atmosphere without performing any isotopic fractionation.

Amount effect accounts for the anti-correlation of $\delta^{18}O$ and precipitation amounts in tropical regions. As for the continental effect, intense convective storms raise the rain-out rate, resulting in a more pronounced depletion of heavy isotopes.

Altitude effect accounts for the decrease of $\delta^{18}O$ with height. A combination of temperature and rain-out effect is here at hand. Upon a steep relief, increased orographic precipitation causes the rain-out rate to increase. At the same time, the tropospheric lapse rate causes air masses to cool as they are lifted. Both processes combine to produce a significant depletion over high topography.

Seasonal (temperature) effect in regions with temperate climates, winter $\delta^{18}O$ are lower than summer $\delta^{18}O$ because of the temperature dependence of the fractionation factor α.

Apart from thermodynamical fractionation processes, the lower diffusivity of heavy isotopomers gives rise to kinetic fractionation processes whenever a sudden, out of equilibrium phase change occurs. E.g. evaporation over the ocean under strong wind shear [Merlivat and Jouzel, 1979], ice-crystal condensation below -40°C [Jouzel and Merlivat, 1984], partial isotopic re-equilibration of rain drop in the sub-cloud undersaturated atmosphere [Hoffmann et al., 1998] witness kinetic fractionation processes. Kinetic fractionation is particularly interesting, since it affects $H_2^{18}O$ stronger than HDO

isotopomers, whereas thermodynamical fractionation processes maintain a constant ratio between them. The leads to the definition of a second-order isotopic signal, referred to as deuterium excess *d* (Equation 1.6).

$$d = \delta D - 8 \times \delta^{18}O \, [‰] \tag{1.6}$$

Due to the characteristics of isotope fractionation, stable water isotopes represent a major climate proxy. The pioneering work by Dansgaard [1964] reveals experimental and theoretical evidence about the stable water isotope 'effects', as discribed above. A detailed description of the isotope effects is given in Sturm et al. [2005b, cf. following chapters]. For a comprehensive description of stable water isotopes in the climate system, the reader is conferred to Mook et al. [2001, cf.http://www.iaea.org/programmes/ripc/ ih/volumes/volumes.htm].

Thereafter, we focus on the stable water isotope signal in ice-core archives. The longest ice-core records were recorded from the Antarctic ice-shield. The Vostok ice-core [Petit et al., 1999, Jouzel et al., 1987] uncovered the climate history of the past 420 000 years, later extended by the Dome C ice-core [EPICA, 2004] to 740 000 years. Several ice-cores were recovered from the Greenland ice-core [NorthGRIP, 2004, Johnsen et al., 1995, Johnsen et al., 2001], reaching down to 123 000 years B.P. In the case of polar climate, the isotopic composition of precipitation is predominantly controlled by temperature. Hence past temperature variations can be estimated from the isotopic signal in polar ice-cores. Yet the precision and accuracy of temperature estimations from ice-core isotopic signal is still investigated [Jouzel et al., 1997, Krinner and Werner, 2003, Krinner et al., 1997, Werner and Heimann, 2002]. While the major stages of the 100 000 year glacial cycle are recorded in both Arctic and Antarctic ice-cores, the isotopic signal is not rigorously synchronous at both poles. So, if past climate change witnessed phase differences between both hemispheres, the question remains: which climate conditions prevailed at mid- and low latitudes ?

1.3 Stable water isotopes in tropical South American ice-cores

Numerous ice-cores were recovered from mid-latitude glaciers, e.g. as reported by Schotterer et al. [1997]. Tropical ice-cores detain a highly valuable information, since they record the climate variability of the inter-tropical belt. The latter is proved to be particularly sensitive to global climate variations. Nevertheless, only high altitude sites can offer no-melting conditions in spite of intense zenith radiation at tropical latitudes. The requirements are met at tropical latitudes in the South American Andes only, where summits commonly exceed 6000 m. Table 1.2 summarises the locations of 6 tropical and 1 sub-tropical ice-core drilling sites in the Andes. Several ice-cores records extend back to 20 000 years B.P., i.e. they comprise the transition from the last glacial maximum (LGM) to the present Holocene inter-glacial stage [Pierrehumbert, 1999, Thompson et al., 1995, 1998, 2000, Ginot, personal communication]. The no-melting condition is essential for preserving the isotopic signal in the ice-core archive. The energy balance on high altitude / low latitude glaciers show that significant sublimation of ice occurs. However, Stichler et al. [2001] reports that bulk sublimation is a non-fractionating process, hence it does not affect the isotopic signal.

Summit	λ ° W	φ ° S	*z* masl	*Reference*
Quelccaya	70.83°	13.93°	5670	Thompson et al., 1985
Huascarán	77.62°	9.117°	6048	Thompson et al., 1995
Sajama	68.88°	18.°1	6548	Thompson et al., 1998
Illimani	67.77°	16.62°	6438	Ramirez et al., 2003
Chimborazo	78.83°	1.5°	6268	Ginot et al., 2002
Tapado	69.83°	30.18°	5550	Ginot et al., 2001
Coropuna	72.62°	15.52°	6450	Ginot, *pers. comm.*

Table 1.2: Location of the Andean ice-core drilling sites. λ stands for western longitude, φ for southern latitude [both in °– degrees] and *z* for altitude [in masl – meters above sea-level. Apart from the sub-tropical Tapado, all sites are located within the inter-tropical belt.

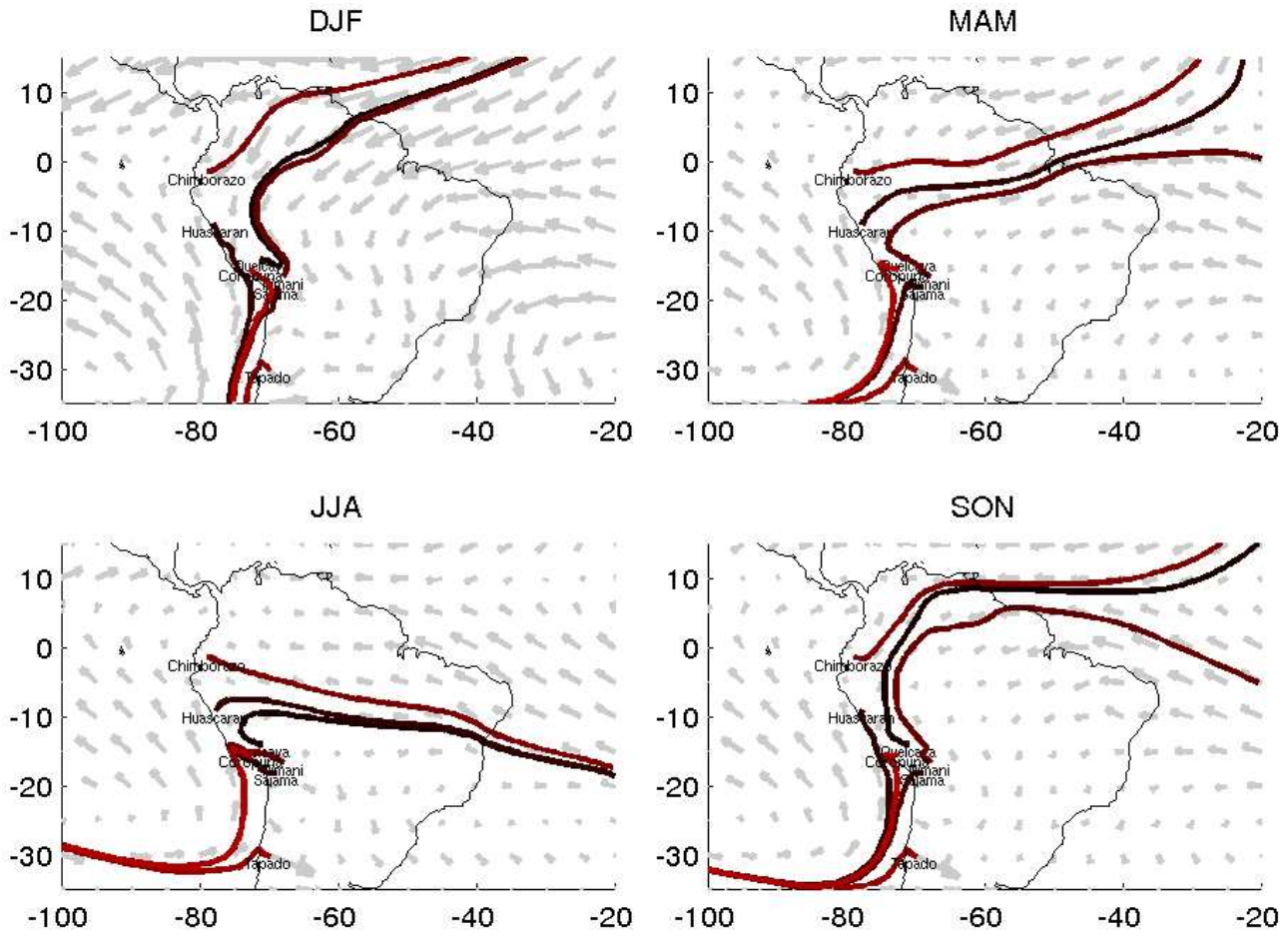

Figure 1.2: Location of the Andean ice-core drilling sites. Each four sub-figures display the seasonal mean advection respectively for December to February, March to May, June to August and September to November. The mean moisture advection represent a climatology from a 5-year REMO$_{iso}$ simulation. For each location, the thick line represents the climatological streamline of vapour advection to the drilling site, according to the method described in Sturm et al. [2005a].

The interpretation of the SWI as a climate proxy is even more complex for tropical ice-core than polar ones: unlike the latter, the site of precipitation evaporation is highly variable, which later undergoes recycling (transpiration) by the vegetation and condensates dominantly in convective instead of stratiform clouds. Figure 1.2 illustrates the location of ice-core drilling sites. The origin of precipitation at the drilling site is inferred from streamlines based on the mean seasonal moisture advection. An extensive description of the applied method is given in Sturm et al. [2005a, cf. following chapters]. Although being very close to the Pacific ocean, most of the Andean precipitation during the rainy season (austral summer, from December to February) originally evaporate over the Atlantic ocean, and are later recycled over the Amazon basin. In order to calibrate the SWI signal in the tropical Andes in term of climate proxy [Edwards et al., 2002], a network of precipitation sampling stations was established across Bolivia by Françoise Vimeux [Vimeux et al., -]. This calibration reveals that local temperature has hardly any control on the isotopic composition of precipitation. Yet the proximity of Andean ice-cores to the tropical Pacific is reflected in the SWI signal. Bradley et al. [2003] reports a good correlation between the SWI signal and sea-surface temperature (SST) anomalies in the tropical Pacific, home of the El Niño Southern Oscillation (ENSO) phenomenon. How can these contradicting observations be explained ?

1.4 Atmospheric modelling of the stable water isotope cycle

Rayleigh-based SWI distillation models [Dansgaard, 1964] are unable to account for observed variations of the isotopic signal in tropical ice-cores. One the other hand, SWI enabled general circulation models shed a new light on the climate controls of the regional isotopic signal. Vuille et al. [1998, 2003b,a] reports that inter-annual variability is dominated by ENSO mode. The authors argue that the regional SWI patterns, ultimately recorded in the Andean ice-cores, are remotely controlled by SST anomalies in the tropical Pacific. Yet this statistical evidence is not consistent with the regional circulation patterns over South America. Hoffmann [2003], Hoffmann et al. [2003] underline the similarity of the SWI signal in all tropical ice-core records. Accordingly, the authors define an Andean Isotope Index (AII) that reinforces the importance of circulation patterns east of the Andes, including soil-atmosphere interactions across the Amazon basin. The actual control of the SWI signal in the tropical ice-cores is still a controversial issue. The poor representation of orography notably restricts the representativeness of GCM simulations for the particular case of high altitude records. At a horizontal resolution commonly used in GCMs (3.75 $^\circ$, i.e. $\sim$ 420 km), the smoothed Andean cordillera culminates at 1500 masl. How well are meso-scale features then represented, when the actual relief exceeds 6000 m above the Altiplano at 4000 masl ?

Facing this limitation, the need of SWI simulations at a finer resolution was patent. This gave rise to the present PhD project: incorporating stable water isotope diagnostics in a regional circulation model, in order to account both for synoptic and meso-scale controls of the SWI signal over South America and eventually in the tropical ice-cores. The present thesis illustrates the successive steps required to address this initial question, each of which constitute one chapter.

Implementation of SWI diagnostics. The technical implementation of SWI diagnostics in the regional circulation model REMO constitutes a significant part of the present work, despite the similarity between the physical parameterisation scheme of REMO and the SWI enabled GCM ECHAM$_{iso}$. Technical details are presented in chapter 2 *Presentation of REMO$_{iso}$* on page 15. Bärbel Langmann (Max Planck Institute for Meteorology – MPIfMet), Georg Hoffmann (Laboratoire des Sciences du Climat et de l'Environnement) and Ralf Podzun (MPIfMet) contributed to this work.

Initial validation of REMO$_{iso}$ over Europe. Following the different steps of SWI implementation in REMO, we conducted an initial validation of the isotope module over Europe. REMO has been extensively applied over this domain. The characteristics of the European climate are well reproduced by REMO. Furthermore, Europe features a dense coverage of reliable SWI measurements. These results are presented in chapter 3 *Validation over Europe* on page 29. They are published in a special issue of the publication Hydrological Processes, consecutive to the IAEA Symposium on isotope hydrology [Sturm, Hoffmann, Langmann, and Stichler, 2005b].

Mean annual cycle over South America. In accordance with the general objectives of the present PhD, REMO$_{iso}$'s study domain was shifted from Europe to South America. No thorough evaluation of the model skills is available in the South American climatic context. Hence a pre-requisite consists evaluating to which extend REMO is able to reproduce typical characteristics of the South American climate. The representation of the annual SWI cycle is then assessed on the basis of monthly SWI measurements. This study further provides the opportunity to test the sensitivity of the simulated SWI signal to horizontal resolution. REMO$_{iso}$ is compared to ECHAM$_{iso}$ at T30 and T106 resolution. These results constitute chapter 4 *South America isotope climatology* on page 61. They are currently submitted for publication in the Journal of Climate [Sturm, Hoffmann, and Langmann, 2005a].

The South American monsoon system recorded by SWI. Once the validity of REMO$_{iso}$ over South America is established, we focus on the dominant intra-seasonal mode during the rainy season (austral summer – December to February). Precipitation features a dipole pattern between the Paraná and Nordeste regions. This bimodal behaviour is also captured in the SWI, which further reveals the meteorological mechanisms responsible for the latter. The South American monsoon system offers a comprehensive framework for the explanation of the precipitation dipole. This process-based analysis provides new elements for the interpretation of the SWI signal in Andean ice-core records. These results are presented in chapter 5 *South American monsoon system* on page 95, to be submitted for publication in the Journal of Geophysical Research [Sturm, Vimeux, and Krinner, 2005c].

Conclusion and outlooks. The logical links between the successive research stages listed above are highlighted in chapter 6 on page 127. Furthermore, we suggest scientific questions, which the application of REMO$_{iso}$ would be suitable for. These include the recent implementation of nudging techniques to address specific case studies with REMO$_{iso}$. Further improvements of parameterisation of fractionation processes are also proposed.

The appendixes briefly present sideline projects conducted with REMO$_{iso}$. Appendix A on page 135 is a technical memorandum on the computation of mean sea-level pressure (SLP) for regional climate models. Appendix B on page 143 shows preliminary results by REMO$_{iso}$ at sub-polar and polar latitudes: the study domain comprises Canada and Greenland. This work was performed in collaboration with Jean Birks (Uni. of Waterloo, Canada). Appendix C on page 153 introduces the international project IPILPS (Isotopes in the Project for Inter-comparison of Land-surface Parameterisation Schemes). REMO$_{iso}$ provided forcing conditions at three locations (Manaus – Brazil, Neuherberg – Germany, Tumbarumba – Australia) for various SWI enabled land-surface schemes. The validation was conducted with Matthew Fischer (Australian Nuclear Science and Technology Organisation – ANSTO) and Kendal McGuffie (Uni. of Technology, Sydney), under supervision of Ann Henderson-Sellers (ANSTO).

Bibliography

R. S. Bradley, M. Vuille, D. Hardy, and L. G. Thompson. Low latitude ice cores record Pacific sea surface temperatures. *Geophysical Research Letters*, 30:23–1, February 2003. 8

W. Dansgaard. Stable isotopes in precipitation. *Tellus*, XVI:436 – 468, 1964. 6, 7, 9

T.W.D. Edwards, S.J. Birks, and J.J. Gibson. Isotope tracers in global water and climate studies of the past and present. In *International Conference on the Study of Environmental Change Using Isotope Techniques*, volume 66. International Atomic Energy Agency, Vienna, 2002. 8

EPICA. Eight glacial cycles from an Antarctic ice core. *Nature*, 429:623 – 238, 2004. EPICA team: L. Augustin, C. Barbante, P.R.F. Barnes, J.M. Barnola, M. Bigler, E. Castellano, O. Cattani, J. Chappellaz, D. Dahl-Jensen, B. Delmonte, G. Dreyfus, G. Durand, S. Falourd, H. Fischer, J. Flückiger, M.E. Hansson, P. Huybrechts, G. Jugie, S.J. Johnsen, J. Jouzel, P. Kaufmann, J. Kipfstuhl, F. Lambert, VY. Lipenkov, G.C. Littot, A. Longinelli, R. Lorrain, V. Maggi, V. Masson-Delmotte, H. Miller, R. Mulvaney, J. Oerlemans, H. Oerter, G. Orombelli, F. Parrenin, DA. Peel, J.R. Petit, D. Raynaud, C. Ritz, U. Ruth , J. Schwander, U. Siegenthaler, R. Souchez , B. Stauffer, J.P. Steffensen, B. Stenni , T.F. Stocker, I.E. Tabacco, R. Udisti, R.S.W. van de Wal, M. van den Broeke, J. Weiss , F. Wilhelms, J.G. Winther, E.W. Wolff, M. Zucchelli. 7

P. Ginot, C. Kull, M. Schwikowski, U. Schotterer, and H. W. Gäggeler. Effects of postdepositional processes on snow composition of a subtropical glacier (Cerro Tapado, Chilean Andes). *Journal of Geophysical Research*, 106(15):32375–32386, December 2001. 7

P. Ginot, M. Schwikowski, U. Schotterer, W. Stichler, H. W. Gäggeler, B. Francou, R. Gallaire, and B. Pouyaud. Potential for climate variability reconstruction from Andean glaciochemical records. *Annals of Glaciology, vol.35, pp.443-450*, 35:443–450, 2002. 7

G. Hoffmann. Taking the Pulse of the Tropical Water Cycle. *Science*, 301:776 – 777, Aug 2003. 9

G. Hoffmann, E. Ramirez, J.D. Taupin, B. Francou, P. Ribstein, R. Delmas, H. Dürr, R. Gallaire, J. Simões, U. Schotterer, M. Stievenard, and M. Werner. Coherent isotope history of Andean ice cores over the last century. *Geophysical Research Letters*, 30:28–1, February 2003. 9

G. Hoffmann, M. Werner, and M. Heimann. Water isotope module of the ECHAM atmospheric general circulation model: A study on timescales from days to several years. *Journal of Geophysical Research*, 103(14):16 871 – 16 896, 1998. 6

Intergovernmental Panel on Climate Change IPCC. Climate Change 2001: The Scientific Basis – Contribution of Working Group I to the Third Assessment Report of IPCC. *UNEP/WMO Publications*, 2001. 3, 4

S. Johnsen, D. Dahl-Jensen, W. Dansgaard, and N. Gundestrup. Greenland paleotemperatures derived from GRIP bore hole temperature and ice core isotopic profiles. *Tellus*, 47B:624–629, 1995. 7

S. J. Johnsen, D. Dahl-Jensen, N. Gundestrup, J. P. Steffensen, H. B. Clausen, H. Miller, V. Masson-Delmotte, A. E. Sveinbjörnsdottir, and J. White. Oxygen isotope and palaeotemperature records from six Greenland ice-core stations: Camp Century, Dye-3, GRIP, GISP2, Renland and NorthGRIP. *Journal of Quaternary Science*, 16:299–307, May 2001. 7

J. Jouzel, R.B. Alley, K.M. Cuffey, W. Dansgaard, P. Grootes, G. Hoffmann, S.J. Jonsen, R.D. Koster, D. Peel, C.A. Shuman, M. Stievenard, M. Stuiver, and J.W.C. White. Validity of the temperature reconstruction from water isotopes in ice cores. *Journal of Geophysical Research*, 102:26471 – 26487, 1997. 7

J. Jouzel, C. Lorius, J.-R. Petit, C. Genthon, N.I. Barkov, V.M. Kotlyakov, and V.M. Petrov. Vostok ice core: a continuous isotope temperature record over the last climatic cycle (160000 years). *Nature*, 329:402–408, 1987. 7

J. Jouzel and L. Merlivat. Deuterium and oxygen 18 in precipitation: modeling of the isotopic effects during snow formation. *Journal of Geophysical Research*, 89:11 749 – 11 757, 1984. 6

G. Krinner, C. Genthon, and J. Jouzel. GCM analysis of local influences on ice core δ signals. *Geophysical Research Letters*, 24:2825–2828, 1997. 7

G. Krinner and M. Werner. Impact of precipitation seasonality changes on isotopic signals in polar ice cores: A multi-model analysis. *Earth Planetary Science Letters*, 216:525–538, 2003. 7

M. Majoube. Fractionnement en oxygène 18 et en deutérium entre l'eau et sa vapeur. *Journal of Chemical Physics*, 10: 1423 – 1436, 1971. 5

L. Merlivat and J. Jouzel. Global climatic interpretation of the deuterium-oxygen 18 relationship for precipitation. *Journal of Geophysical Research*, 84:5029 – 5033, 1979. 6

A. Moberg, D. M. Sonechkin, K. Holmgren, N. M. Datsenko, and W. Karlén. Highly variable Northern Hemisphere temperatures reconstructed from low- and high-resolution proxy data. *Nature*, 433:613 – 617, Feb 2005. 4

W.G. Mook, J. Gat, K. Rozanski, W. Stichler, M. Geyh, K.P. Seiler, and Y. Yurtsever. Environmental isotopes in the hydrological cycle, principles and applications. *Vol. I & II, UNESCO/IAEA Series*, 2001. http://www.iaea.org/programmes/ripc/ih/volumes/volumes.htm. 7

NorthGRIP. High-resolution record of northern hemisphere climate extending into the last interglacial period. *Nature*, 431:147 – 151, Sep 2004. North Greenland Ice Coring Project participants: K. K. Andersen, N. Azuma, J.-M. Barnola, M. Bigler, P. Biscaye, N. Caillon, J. Chappellaz, H. B. Clausen, D. Dahl-Jensen, H. Fischer, J. Flückiger, D. Fritzsche, Y. Fujii, K. Goto-Azuma, K. Grønvold, N. S. Gundestrup, M. Hansson, C. Huber, C. S. Hvidberg, S. J. Johnsen, U. Jonsell, J. Jouzel, S. Kipfstuhl, A. Landais, M. Leuenberger, R. Lorrain, V. Masson-Delmotte, H. Miller, H. Motoyama, H. Narita, T. Popp, S. O. Rasmussen, D. Raynaud, R. Rothlisberger, U. Ruth, D. Samyn, J. Schwander, H. Shoji, M.-L. Siggard-Andersen, J. P. Steffensen, T. Stocker, A. E. Sveinbjörnsdóttir, A. Svensson, M. Takata, J.-L. Tison, Th. Thorsteinsson, O. Watanabe, F. Wilhelms and J. W. C. White. 7

J.-R. Petit, J. Jouzel, D. Raynaud, J.-M. Barnola, I. Basile, M. Bender, J. Chappellaz, M. Davis, G. Delaygue, M. Delmotte, V.M. Kotlyakov, M. Legrand, V.Y. Lipenkov, C. Lorius, L. Pépin, C. Ritz, E. Saltzman, and M. Stievenard. Climate and atmospheric history of the past 420000 years from the Vostok ice core, Antarctica. *Nature*, 399:429–436, 1999. 7

R. T. Pierrehumbert. Huascaran $\delta^{18}O$ as an indicator of tropical climate during the Last Glacial Maximum. *Geophysical Research Letters*, 26:1345–1348, May 1999. 7

E. Ramirez, G. Hoffmann, J. D. Taupin, B. Francou, P. Ribstein, N. Caillon, F. A. Ferron, A. Landais, J. R. Petit, B. Pouyaud, U. Schotterer, J. C. Simoes, and M. Stievenard. A new Andean deep ice core from Nevado Illimani (6350 m), Bolivia. *Earth and Planetary Science Letters*, 212:337–350, July 2003. 7

U. Schotterer, K. Fröhlich, H. W. Gäggeler, S. Sandjordj, and W. Stichler. Isotope records from Mongolian and Alpine ice cores as climate indicators. *Climatic Change*, 36(3):519 – 530, 1997. 7

W. Stichler, U. Schotterer, K. Fröhlich, P. Ginot, C. Kull, H. Gäggeler, and B. Pouyaud. Influence of sublimation on stable isotope records recovered from high-altitude glaciers in the tropical Andes. *Journal of Geophysical Research*, 106(15): 22613–22620, 2001. 7

K. Sturm, G. Hoffmann, and B. Langmann. Climatology of stable water isotopes in South America: comparing general to regional circulation models. *Journal of Climate – submitted*, 2005a. 8, 9

K. Sturm, G. Hoffmann, B. Langmann, and W. Stichler. Simulation of $\delta^{18}O$ in precipitation by the regional circulation model $REMO_{iso}$. *Hydrological Processes – in press*, 2005b. 7, 9

K. Sturm, F. Vimeux, and G. Krinner. The South American Monsoon recorded in Stable Water Isotopes. *Journal of Geophysical Research – submitted*, 2005c. 9

L. G. Thompson, M. E. Davis, E. Mosley-Thompson, T. A. Sowers, K. A. Henderson, V. S. Zagorodnov, P.-N. Lin, V. N. Mikhalenko, R. K. Campen, J. F. Bolzan, J. Cole-Dai, and B. Francou. A 25,000-Year Tropical Climate History from Bolivian Ice Cores. *Science*, 282:1858–+, December 1998. 7

L. G. Thompson, E. Mosley-Thompson, J. F. Bolzan, and B. R. Koci. A 1500-Year Record of Tropical Precipitation in Ice Cores from the Quelccaya Ice Cap, Peru. *Science*, 229:971–973, September 1985. 7

L. G. Thompson, E. Mosley-Thompson, M. E. Davis, P.-N. Lin, K. A. Henderson, J. Cole-Dai, J. F. Bolzan, and K.-B. Liu. Late Glacial Stage and Holocene Tropical Ice Core Records from Huascaran, Peru. *Science*, 269:46–50, July 1995. 7

L. G. Thompson, E. Mosley-Thompson, and K. A. Henderson. Ice-core palaeoclimate records in tropical South America since the Last Glacial Maximum. *Journal of Quaternary Science*, 15:377–394, May 2000. 7

F. Vimeux, R. Gallaire, S. Bony, G. Hoffmann, and J.C. Chiang. What are the controls on δD in precipitation in the Zongo Valley (Bolivia) ? Implications for the Illimani ice core interpretation. *Earth and Planetary Science Letters*, -. submitted. 8

M. Vuille, R. S. Bradley, R. Healy, M. Werner, D. R. Hardy, L. G. Thompson, and F. Keimig. Modeling $\delta^{18}O$ in precipitation over the tropical Americas: 2. Simulation of the stable isotope signal in Andean ice cores. *Journal of Geophysical Research*, 108(6):2–1, March 2003a. 9

M. Vuille, R. S. Bradley, M. Werner, R. Healy, and F. Keimig. Modeling $\delta^{18}O$ in precipitation over the tropical Americas: 1. Interannual variability and climatic controls. *Journal of Geophysical Research*, 108(6):1–1, March 2003b. 9

M. Vuille, D. R. Hardy, C. Braun, F. Keimig, and R. S. Bradley. Atmospheric circulation anomalies associated with 1996/1997 summer precipitation events on Sajama Ice Cap, Bolivia. *Journal of Geophysical Research*, 103(12):11191 – 11204, 1998. 9

M. Werner and M. Heimann. Modeling interannual variability of water isotopes in Greenland and Antarctica. *Journal of Geophysical Research (Atmospheres)*, 107(1):1–+, January 2002. 7

Chapter 2

Presentation of the regional circulation model REMO, enabled with stable water isotope diagnostics

Résumé

Ce chapitre présente le modèle de circulation régional $REMO_{iso}$, auquel est intégré un module traitant des isotopes stables de l'eau. Le développement et la mise au point du module isotopique a constitué une tâche déterminante de ce travail de thèse.

En premier lieu sont décrites caractéristiques techniques du modèle de circulation régional REMO. Cela concerne en particulier la discrétisation horizontale sur une grille en rotation, la discrétisation verticale en coordonnées mixtes σ-pression, ainsi que l'organisation sommaire des sub-routines du programme.

En deuxième lieu sont développées les paramétrisations des processus sous-maille, tant pour la physique du cycle hydrologique que pour les fractionnements isotopiques inhérents. En particulier, la diffusion verticale à travers la couche limite atmosphérique, la micro-physique des nuages et les interactions entre surface et atmosphère sont expliquées.

En dernier lieu est explicitée la procédure des pré-traitement des conditions aux limites pour une simulation méso-échelle. Cela comprend d'abord les paramètres de surface invariants (p. ex. topographie, propriétés de végétation, rugosité), ainsi que les conditions aux limites latérales, fournies toutes les 6 heures par le modèle hôte.

Zusammenfassung

Dieser Kapitel stellt das Regionalzirkulationsmodell REMOiso mit eingebautem Wasserisotopenmodul vor. Die Entwicklung und Einstellung des Wasserisotopenmoduls hat einen Großteil dieser Doktorarbeit ausgemacht. Erstens werden technische Eigenschaften des Regionalzirkulationsmodell REMO beschrieben. Dies betrifft die horizontale Diskretisierung auf einem rotierten Gitter, die vertikale Diskretisierung in gemischter σ-Druck Koordinaten und die kurzgefasste Organisierung der Programmroutinen.

Zweitens werden die Parametrisierung von unaufgelöste, subskalige Prozessen erläutert, sowohl für die Wasserzyklusphysik wie inhärente isotopische Fraktionierungen. Insbesondere werden die Vertikaldiffusion durch die atmosphärische Grenzschicht, die Wolkenmicrophysik und Wechselwirkungen zwischen Landoberfläche in Atmosphäre erklärt.

Leztens wird die Vorverarbeitung von Grenzbedingungen angesichts einer mezzoskaligen Simulation dargestellt. Dies umfasst invariante Landoberflächenparameter (z.B. Topographie, Vegetations- und Rautiefeneigenschaften), und die 6-stündigen vom Hostmodell gelieferten lateralen Grenzbedingungen.

The present chapter introduces the REgional circulation MOdel REMO. It is based on the former numerical weather prediction model Europa-Modell by the German Weather Service (Deutscher Wetterdienst - DWD, [Majewski, 1991, Majewski and Schrodin, 1995]). A central task of the BALTEX (Baltic Sea Experiment) project was to develop a circulation model suitable for climate studies. Several prominent German institutes contributed to the development of REMO. The German Weather Service (DWD) and the GKSS research centre focussed on the application of REMO in forecast mode. According to this procedure, REMO is re-initialised from its host model (ECMWF analyses) on a daily basis. The Max-Planck Institute for Meteorology (MPIfM) and the German High Performance Computing Centre for Climate and Earth System Research (Deutsches Klimarechenzentrum - DKRZ) developped a REMO version to be used on climate mode (without re-initialization). Furthermore, the physical parameterisation scheme of the general circulation model ECHAM 4 [Roekner et al., 1996] was implemented in REMO. REMO took part in an RCM intercomparison study (Pilot study of Intense Data Collection and Analyses of Precipitation (PIDCAD), and proved to be among the currently best performing RCMs [Jacob, 2001, Jacob et al., 2001]. Further documentation about REMO can be found in Podzun et al. [1995], Jacob and Podzun [1997], Hagemann et al. [2002], Semmler [2002].

2.1 Structure of the regional circulation model REMO

REMO is a numerical three-dimensional regional circulation model (RCM). Primitive equations are simplified by assuming hydrostatical equilibrium. Horizontal discretisation is performed onto a rotated Arakawa-C grid. The rotated North Pole is chosen such that the rotated Equator runs through the middle of the study domain. Hence, grid cells in °have a nearly equal area all over the study domain.

2.1.1 Rotated horizontal grid

The rotated North Pole (EN) has the geographical coordinates $[\lambda_{EN}, \varphi_{EN}]$ and the geographic North Pole GN has the rotated coordinate $[\lambda'_{GN}, \varphi'_{GN}]$. This immediately implies that $\lambda_{EN} = \lambda'_{GN}$ and $\varphi_{EN} = \varphi'_{GN}$. The coordinate transformation from the geographical longitude/latitude ($[\lambda, \varphi]$) to the rotated longitude/latitude ($[\lambda', \varphi']$) is given in Equation 2.1.

$$\begin{cases} \varphi' = & \sin^{-1}\left(\sin\ \varphi\ \sin\ \varphi_{EN} + \cos\ \varphi\ \cos\ \varphi_{EN} \cos(\lambda_{EN} - \lambda)\right) \\ \lambda' = & \lambda'_{EN} + \tan^{-1}\left(\dfrac{cos\ \varphi\ \sin(\lambda_{EN} - \lambda)}{\sin\ \varphi\ \cos\ \varphi_{EN} - \cos\ \varphi\ \sin\ \varphi_{EN} \cos(\lambda_{EN} - \lambda)}\right) \end{cases} \tag{2.1}$$

The reversed transformation, from rotated coordinates ($[\lambda', \varphi']$) back to geographical longitude/latitude ($[\lambda, \varphi]$) is in given in Equation 2.2.

$$\begin{cases} \varphi = & \sin^{-1}\left(\sin\ \varphi'\ \sin\ \varphi'_{GN} + \cos\ \varphi'\ \cos\ \varphi'_{GN} \cos(\lambda'_{GN} - \lambda')\right) \\ \lambda = & \lambda_{EN} + \tan^{-1}\left(\dfrac{cos\ \varphi'\ \sin(\lambda'_{GN} - \lambda')}{\sin\ \varphi'\ \cos\ \varphi'_{GN} - \cos\ \varphi'\ \sin\ \varphi'_{GN} \cos(\lambda'_{GN} - \lambda')}\right) \end{cases} \tag{2.2}$$

Figure 2.1 shows the four study domains on which REMO was integrated during the present PhD. The specifications of each domain are given in Table 2.1.

Domain	λ_{EN}	φ_{EN}	λ'_{LL}	φ'_{LL}	X	Y
Europe	-170°	32.5°	-19.5°	-25	81	91
South Am.	0°	90°	-100°	-35°	161	101
Australia	-50°	117.5°	-25°	-23°	101	91
Canada	90°	27.5°	-24°	-25°	101	97

Table 2.1: Details of the rotated grid for each study domain. [λ_{EN}, φ_{EN}] represent the geographical longitude/latitude of the rotated North Pole.[λ'_{LL}, φ'_{LL}] represent the rotated longitude/latitude of the lower-left corner of the study domain. (X,Y) represent the number of grid points in the longitude/latitude direction.

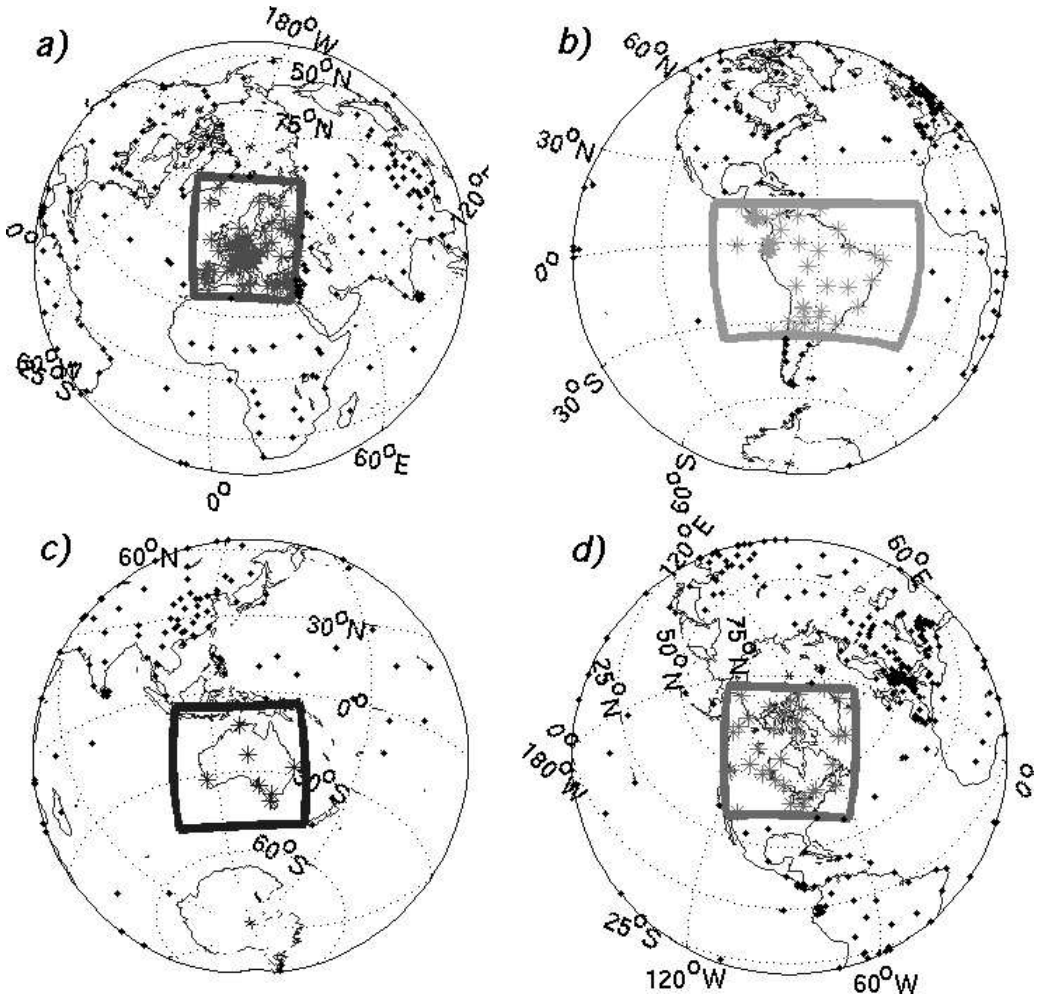

Figure 2.1: Azimuthal equal-area projection of the study domains over which REMO$_{iso}$ was integrated. Horizontal resolution in 0.5°in each case. Europe domain (a) covers 81×91, South American domain (b) covers 161×101, the Australian domain (c) 101×91 and the Canadian domain covers 101×97 grid points.

2.1.2 Vertical discretisation

The vertical discretisation scheme adopts an hybrid σ-pressure coordinate system. Near the surface, the model layers follow the orography, which then gradually tend towards levels of uniform pressure at higher levels. An illustration of the vertical coordinate system is given in Figure 2.2: the cross section of pressure levels at $\varphi = 27°S$ reveal how REMO takes on the steep orography of the Andean Cordillera.

Simulations were performed with 19 vertical levels, in order to be consistent with lateral boundary conditions by ECHAM. Table 2.2 indicates the pressure ($A_{k+1/2}$) and σ ($B_{k+1/2}$) coefficients for the calculus of mid-level pressure. The corresponding pressure and geopotential heights represent the median values of a 5 year integration of REMO over South America. For further details, the reader is conferred to Roeckner et al. [1992].

2.1.3 Partial REMO flow diagram

To give an idea of the complexity of REMO$_{iso}$, the code is organised in 273 routines, summing up to 29682 lines. Core of REMO is coded in FORTRAN 77 programming language, but recent add-ons integrate vectorised procedure from FORTRAN 90. Only major routines, especially dealing with the water cycle are represented in the simplified flow diagram, in Figure 2.3.

REMO dynamical core considers following prognostic variables: surface pressure, temperature, horizontal wind com-

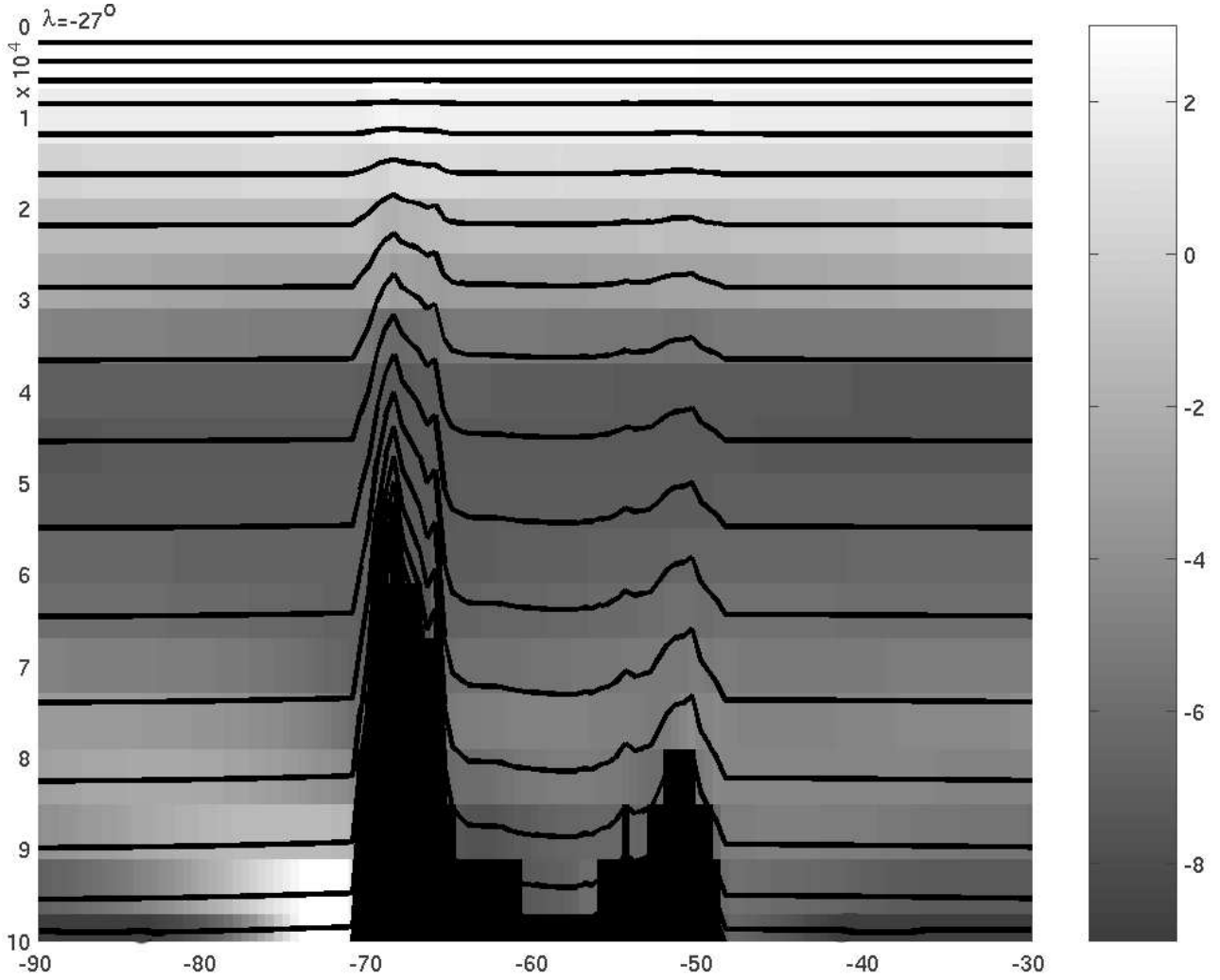

Figure 2.2: Example of vertical discretisation: vertical cross section of pressure levels (thick lines) and mean annual tropospheric gradient (shaded) across latitude $\varphi = 27°S$, South American domain. The steep Andean topography ($z_{max} = 5019$ *masl*) affects up to the 15^{th} σ-level.

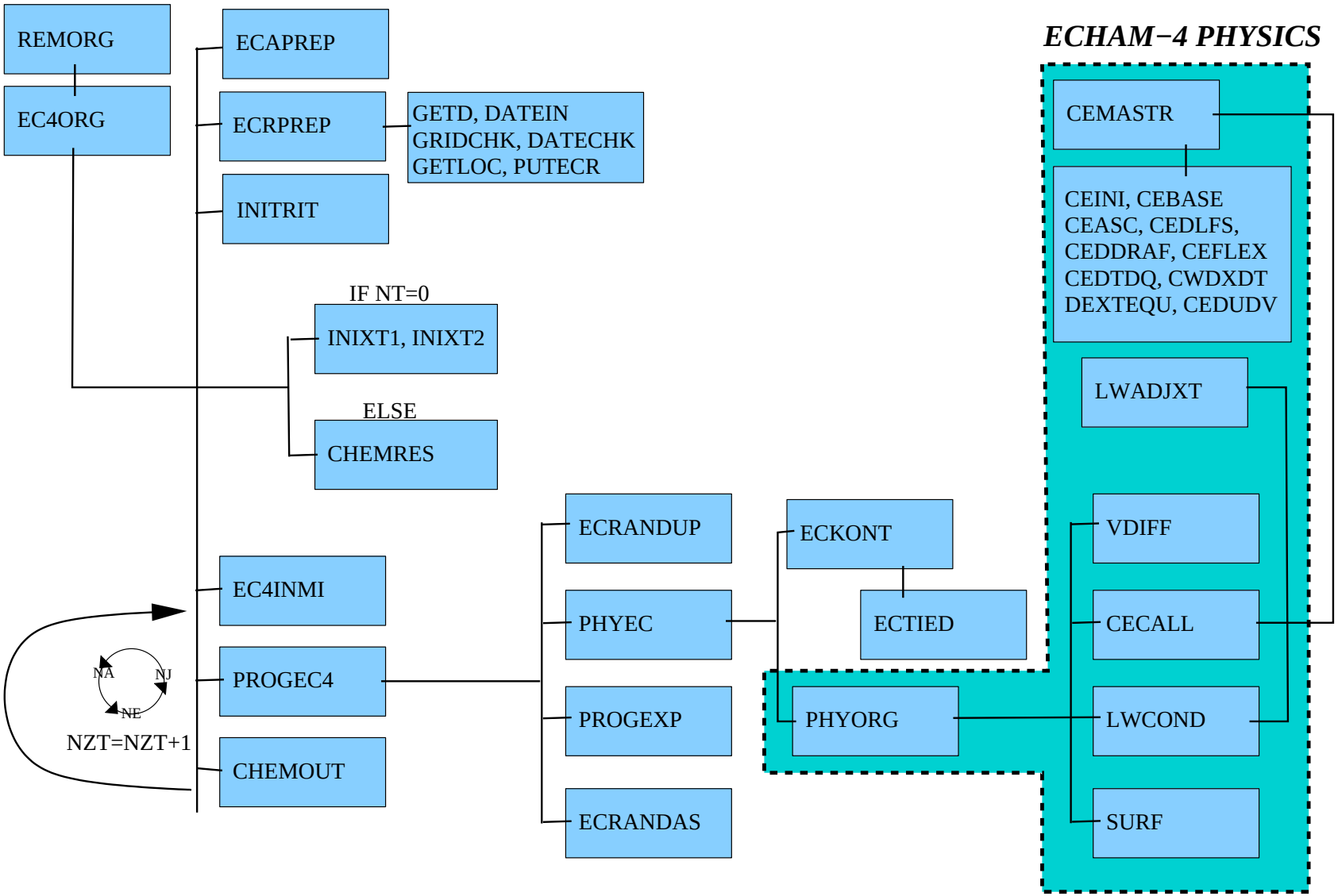

Figure 2.3: Partial flow diagram of REMO$_{iso}$. Selected routines are described in the text.

k	$A_{k+1/2}$ [Pa]	$B_{k+1/2}$ [Pa]	P_k [Pa]	z_k [m]
19	0	1	100771.3951	67.29763729
18	0	0.9922814815	99404.96135	237.5811796
17	0	0.9729851852	96582.92312	567.2468155
16	783.19503	0.9287469142	91962.82364	1083.340498
15	2549.969411	0.8564375573	85583.16944	1797.352149
14	5125.141747	0.7596983769	77733.09538	2709.868154
13	8127.144155	0.6461079479	68846.62162	3814.979716
12	11101.56199	0.5249322235	59419.01984	5101.190912
11	13621.46043	0.4054091989	49942.80586	6552.746185
10	15356.92411	0.2955196487	40860.8762	8147.297671
9	16116.23661	0.2011954093	32534.30567	9854.484174
8	15861.12518	0.1259166826	25222.32333	11636.22061
7	14698.49809	0.0706498323	19071.98423	13457.19727
6	12851.10017	0.0340771467	14115.05412	15299.80834
5	10609.51323	0.0130700434	10269.62451	17189.0951
4	8267.92756	0.0033571866	7343.975192	19244.20649
3	6046.110595	0.0003389933	5040.201885	21806.9117
2	4000	0	3000	26351.2685
1	2000	0	1000	31669

Table 2.2: Vertical discretisation in REMO. k indicates the hybrid $\sigma - P$ level. Mid-level pressure is defined as $P_k = (P_{k+1/2} + P_{k-1/2})/2$, with $P_{k+1/2} = A_{k+1/2} + P_0 \times B_{k+1/2}$. $z_{k+1/2}$ represents the corresponding mean geopotential height.

ponents, water vapour content, cloud water content. The stable water isotope enabled REMO version furthermore includes the isotopic composition of liquid and gaseous atmospheric moisture. A linear fourth-order horizontal diffusion scheme is applied to momentum, temperature and water content. For solving the differential primitive equations, a leap-frog time stepping with semi-implicit correction and Asselin-filter is used. The stable water isotope enabled version of REMO correspond to the REMO 5.0 version [Semmler, 2002].
General remarks about routines in Figure 2.3 are given hereafter.

REMORG Master routine of REMO. This routine switches between the original DWD [Majewski, 1991] and the ECHAM4 [Roekner et al., 1996] physical schemes. Thereafter, EC4 refers to the ECHAM-4 physics.

EC4ORG Master routine of REMO with EC4 physics

ECAPREP reads at start-up, checks and allocates to REMO variables the initial conditions from pre-processed isotopic (c*) and meteorological (e*) files, [ce]`EXP`x`a`DDMMYYHH. `[DD,MM,YY,HH]` stand for 2-digit day, month year and hour of the simulation start.

ECRPREP reads, checks and allocates to REMO variables the boundary conditions from pre-processed isotopic (c*) and meteorologic (e*) files [ce]`EXP`x`a`DDMMYYHH. The read-in frequency depends on the host model (usually 6 hour).

INITRIT initialises at start-up the isotopic constant for all tracers. In the present layout, tracers #1-2 represent the vapour/liquid $H_2^{18}O$, tracers #3-4 stand for $HD^{16}O$ and tracers #5-6 for $H_2^{16}O$. The latter tracer, which does not undergo any fractionation, is controlled to be equal to the bulk vapour/liquid water content in the non-isotopic REMO code.

Start procedure depends whether a new simulation of REMO is started, or whether a previous run is continued.

- Initial start. Meteorological fields are initialised with the implicit normal mode initialisation (INMI) in **EC4INMI**. Atmospheric moisture is set to (δ^{18}O=-80$^\circ/_{\circ\circ}$,δD=-630$^\circ/_{\circ\circ}$), soil reservoirs to δ^{18}O=δD=0$^\circ/_{\circ\circ}$.

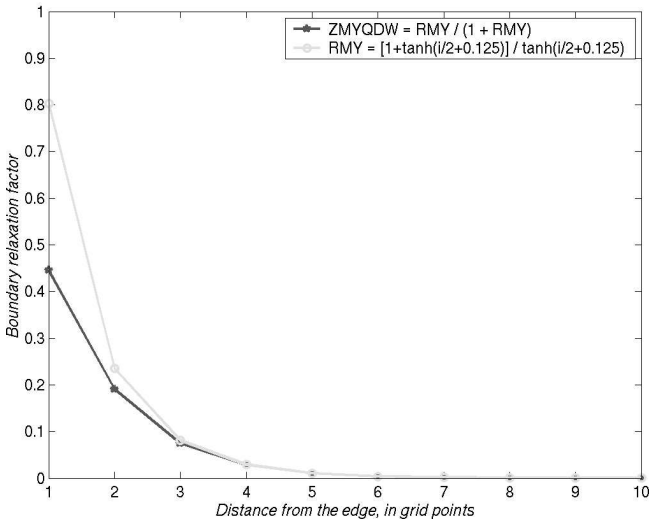

Figure 2.4: Assimilation of prognostic variables to lateral boundary conditions. The light grey curve shows the weighing function (or boundary relaxation factor) across the 8 grid-cell buffer zone.

- Restart procedure. Meteorological fields are read from the restart file e`EXP`x[fg]`DDMMYYHH` in **ECAPREP**. Isotopic soil and atmospheric reservoirs are read-in from the restart file c`EXP`xf`DDMMYYHH` by **CHEMRES**.

PROGEC4 controls at each model time step (typically 300 seconds) the physical parameterisation and dynamical prognosis.

CHEMOUT prints out all cumulated isotopic-related fields at a pre-defined frequency (typically, 6 hours). Similarly to the standard REMO output, isotopic output files c`EXP`xe`DDMMYYHH` are in IEEE format.

ECRANDUP initialises the NE time-level to be prognosed in the present model time-step. The near-surface humidity QDB is set diagnostically to the saturation vapour pressure, for all time-levels NA/NJ/NE.

PHYEC prepares the execution of the EC4 physical parameterisation scheme.

ECKONT and **ECTIED** perform a preliminary prognosis (similar to PROGEXP), which is needed for the execution of the Tiedke convection scheme in PHYORG.

PHYORG Master routine of the EC4 physical parameterisation, which accounts for all sub-grid processes. Specific aspects relevant for the water cycle and related fractionation processes are addressed in the next section.

PROGEXP computes the actual dynamical prognosis, i.e. resolves the primitive equations. Basis of circulation models, these partial differential equations formalise the conservation of mass, energy, and momentum, constrained by the equation of state.

ECRANDAS performs the assimilation of lateral boundary conditions within a 8 grid-cell buffer zone after Davies [1976]. The weighing function applied to adjust prognostic variables in the buffer zone is shown in Figure 2.4. Asselin filter is applied to the leap-frog time stepping.

2.2 Physical parameterisation and isotopic fractionation

Diagnostics of stable water isotope fractionation were first integrated in the ECHAM3 general circulation model by Hoffmann and Heimann [1993], Hoffmann [1995], Hoffmann et al. [1998]. It was later ported to ECHAM4 with further

enhancements [Werner et al., 2000, Werner, 2000]. In the present section, we introduce the parameterisation of fractionation processes inbedded in the EC4 physics scheme. In particular, the necessary modifications of the original ECHAM code to match the REMO structure are underlined hereafter.

The core of the ECHAM-4 physical parameterisation is enclosed in a dashed polygon in Figure 2.3. Routines in Figure 2.3 are related to paragraphs thereafter as follows. VDIFF treats the vertical diffusion, especially in the planetary boundary layer. CECALL and subsequent routines control the parameterisation of convection precipitation. LWCOND handles large-scale (stratiform) precipitation. SURF stand for the default low-complexity land-surface scheme.

2.2.1 Vertical diffusivity

Citing Hagemann et al. [2002], 'vertical diffusion and turbulent fluxes are calculated from the Monin-Obukhov similarity theory with a higher order closer scheme for the transfer coefficients of momentum, heat, moisture, cloud water within and above the planetary boundary layer. The eddy coefficient parameters are calculated as functions of the turbulent kinetic energy.'

Unlike ECHAM, the semi-implicit prognosis in REMO requires a 'near-surface humidity' variable (QDB) to compute water vapour in the lowest layer, i.e. an analog to 2-m temperature for specific humidity. QDB is prognostic over land, and records evaporation/dew fluxes from the surface and vapour advection/diffusion. Over the ocean (in the absence of sea-ice), QDB is first diagnostically set to saturation vapour pressure (in the ECRANDUP routine), before being modified in VDIFF.

The implementation of the water isotope tracers and related fractionation processes in the vertical diffusion scheme was a major challenge when porting the ECHAM stable water isotope to REMO. After several attempts, following solution was adopted. Instead of computing explicitly the specific near-surface humidity of isotopic species, we define the relative depletion (δ^{iso}_{SMOW}). Absolute are obtained by multiplying the relative depletion with the bulk moisture. Relative depletion is defined in Equation 2.3.

$$\delta^{iso}_{SMOW} = \left(\frac{[H_2O]_{iso}/[H_2O]_{bulk}|_{sample}}{[H_2O]_{iso}/[H_2O]_{bulk}|_{SMOW}} - 1 \right) [‰] \tag{2.3}$$

In Equation 2.3, *SMOW* represents the standard mean ocean water, $[H_2O]_{iso}$ stands for the mass concentration of either $HD^{16}O$ or $H_2^{18}O$ and $[H_2O]_{bulk}$ for the mass of the water sample.

Vertical diffusion over sea At the time step NZT-1, the relative isotopic signature of near-surface humidity is stored. At the time-step NZT, near-surface humidity is initialised to the saturation vapour pressure. The isotopic tracer are defined as saturation vapour pressure multiplied by its isotopic signature at time step NZT-1 $P_{iso} = P_{sat} \times (1 + \delta^{iso}_{SMOW}/1000)$. Furthermore, kinetic fractionation processes dependent on the surface wind drag in parameterised following Merlivat and Jouzel [1979]. The final implementation of stable water isotopes in the vertical diffusion scheme correctly reproduces the initial deuterium excess during evaporation.

Vertical diffusion over land Near-surface humidity is a prognostic variable over land, which interacts with prognostic soil reservoirs (soil moisture, rain interception by the canopy, snow layer). The δ^{iso}_{SMOW} near-surface humidity is determined as a weighted mean between evaporation fluxes and low-level atmospheric moisture. At present, moisture fluxes from the surface are considered non-fractionating (cf. below). The specific near-surface humidity is then computed as the multiplication of the interpolated δ^{iso}_{SMOW} with bulk near-surface humidity.

2.2.2 Cloud microphysics

Precipitation in the ECHAM4 [Roekner et al., 1996] physics is divided in convective and stratiform convection. Stratiform clouds water content is calculated from budget equation including sources and sinks due to phase changes and precipitation formation by coalescence of cloud droplets and gravitational settling of ice crystals. The convective cloud water detrained at the top of cumulus clouds is used as a source term in stratiform cloud water equation. Convection is parameterised

as a mass flux scheme following Tiedtke [1989], adapted by Nordeng [1994]. Three types of convection are prescribed: shallow, middle and deep convection, of which a single type occurs in each grid cell at a given time step. Aldrian [2003] investigates the sensitivity of selected parameters in the convection scheme. To account for typical convection over Indonesia, the minimum cloud thickness over land was raised from 75 hPa to 300 hPa, the relative humidity threshold to launch condensation was raised from 80% to 90% and the rain condensation efficiency was lowered from .02 to .0006.

The in- and sub-cloud fractionation processes described in Hoffmann [1995] are taken over in REMO. All aggregate states of in-cloud water (vapour, liquid, ice) are primarily considered in isotopic equilibrium, which is temperature dependent [Majoube, 1971]. Below -20°C, isotope diffusion through the oversaturated zone around the forming ice-crystals induces an additional kinetic fractionation [Jouzel and Merlivat, 1984]. A similar formulation for kinetic fractionation is adopted for the partial evaporation of raindrops in the sub-cloud undersaturated atmosphere. Convective precipitation usually produces larger, faster falling drops than large-scale (stratiform) precipitation. Hence partial re-equilibration occurs to 45% for the former and 95% for the latter.

2.2.3 Land-surface scheme

The land-surface scheme is extensively described in Semmler [2002]. Soil temperatures are computed from diffusion equations at 5 levels between 10 m depth and the surface, with an additional diffusion through the snow layer (if present). Only bulk soil moisture is computed (bucket-type). Soil hydrology is computed by a budget equation including precipitation fluxes, snow-melt and evapo-transpiration. According to the soil water capacity and terrain pitch, superfluous water is diagnosed as runoff, but no runoff collection scheme is implemented in REMO v5.0. Apart from soil moisture, two other prognostic reservoirs are considered: interception of precipitation by the canopy (also referred to as skin layer) and snow layer depth.

Stable water isotopes are treated as passive tracers in soil moisture and snow layer. During evaporation, isotopic equilibrium is assumed at the snow and skin layer interface with the atmosphere. The vertical description scheme does not differentiate between evaporation from bare soils and transpiration by vegetation. Furthermore, the bucket-type soil moisture reservoir does not permit to trace the isotopic signature of root-zone versus surface and ground water. Hence all vapour fluxes from the surface are considered non-fractionating, as it is observed for transpiration by the vegetation [Bariac et al., 1994b,a]. As a consequence of the latter, recycling of water over the continent induces a positive bias. Sturm et al. [2005a] discusses this issue assessing the dry-season continental gradient of δ^{18}O across the Amazon basin.

2.3 Pre-processing of REMO boundary files

As an atmospheric regional circulation model, REMO requires a priori information about characteristics of the study domain at the requested horizontal resolution. Furthermore, initial and boundary conditions must be provided. This section covers the processing steps that precede a simulation with REMO$_{iso}$.

2.3.1 Invariant soil libraries

Hagemann [2002] introduces a detailed description of land surface parameter data-set used in pre-processing of REMO. The BODLIB package [Podzun, personal communication] interpolates global data sets to the rotated horizontal grid for a given experiment. Resulting fields are presented in Table 2.3.

Orography is derived from the GTOPO30 data set [Gesh and Greenlee, 1996]. GTOPO30 is a global digital elevation model (DEM) with a horizontal grid spacing of 30 arc-seconds (approximately 1 kilometre). Completed in late 1996, it was developed over a three year period through a collaborative effort led by staff at the U.S. Geological Survey's EROS Data Center (EDC). Orographic variance is used in surface runoff computation. It is defined in equation 2.4.

$$var(\lambda', \varphi') = \frac{1}{n} \sum_{i=1}^{n} \left(h_i - \overline{h(\lambda', \varphi')} \right)^2 \tag{2.4}$$

CODE	Description
Required surface libraries	
129	orography [m]
172	land-sea mask
173	roughness length [m]
174	albedo
198	fraction of vegetation (mean)
199	orography variance
200	leaf area index (mean)
212	forest ratio
226	FAO-dataset
229	max. soil field capacity
Additional surface information	
1721	fraction of land
1981	frac. vegetation (dormancy season)
1982	frac. vegetation (growing season)
198	frac. vegetation (mean)
2001	leaf area index (dormancy season)
2002	leaf area index (growing season)
2291	plant avail. soil water holding capacity
1731	roughness length (vegetation)
199	variance of the orography
614	latitude (φ) of the rotated grid
615	longitude (λ) of the rotated grid

Table 2.3: Required surface libraries and additional information computed by the BODLIB package.

In Equation 2.4, *n* stands for the number of grid points from the GTOPO30 data-set located within the rotated grid cell (λ', φ'). Other parameters are based on the upscaling of the 1 km global distribution of major ecosystem types, released by the U.S. Geological Survey's (USGS) Earth Resources Observation System (EROS) Data Center [Brown et al., 2002].

2.3.2 Time-dependant boundary conditions

As a limited area model, lateral boundary conditions for the prognostic variables (surface pressure, horizontal wind speed, vapour and liquid water content) must be specified in order to account for atmospheric motion *outside* the study domain. Typically, the frequency of lateral forcing is taken every 6 hours (0:00 / 6:00 / 12:00 / 18:00 UTC), in order to account for the diurnal cycle. At every time-step, the ECRPREP routines performs a linear interpolation of the prognostic variables.

Pre-processing packages were developed at the Max Planck Intitute for Meteorology to nest REMO in either ECMWF (re-)analyses or ECHAM output [Majewski and Schrodin, 1995, Podzun, personal communication]. Prognostic variables from the host model are interpolated onto the finer rotated REMO grid, taking into account the interpolated GTOPO30 orography and resulting surface pressure. The a bi-cubic interpolation is performed on in $5^\circ \times 5^\circ$ running average window, constrained by steadiness of first and second order derivatives. In a first set-up, REMO$_{iso}$ was nested into ECMWF analyses. The isotopic composition of air masses entering the study domain was then parameterised with regard to temperature. As discussed in Sturm et al. [2005b], the ECMWF-nested REMO$_{iso}$ simulation leads to an underestimation of δ^{18}O in precipitation by -5 $‰$, with an increasing bias in winter.

Alternatively, isotopic composition can be assimilated at the lateral boundaries in a similar way to other prognostic variables. This requires that isotopic information be included in the host model, e.g. a simulation by ECHAM$_{iso}$. The pre-processing program was enhanced to perform the interpolation of vapour and liquid water content for isotopic tracers. The isotopic ratio δ^{iso}_{SMOW} is computed for atmospheric vapour. The δ^{iso}_{SMOW} is then interpolated like other prognostic variables. Once bulk atmospheric vapour is computed, the specific humidity of isotopic species is obtained by multiplying bulk vapour with the interpolated δ^{iso}_{SMOW}. If present, cloud water is considered to be in isotopic equilibrium with the vapour.

Isotopic boundary conditions are stored in a separate file, using the c`EXP`xa`DDMMYYHH` naming convention.
In accordance with the modification of the boundary conditions, the routines ECRPREP, ECRANDUP and ECRANDAS were modified. Furthermore, the name-list controlling the execution of REMO was modified to include a switch ('LXTR'), to chose between both isotopic boundary options.

Being an *atmospheric* regional circulation model, REMO considers the ocean as an external component. Hence, sea-surface temperatures (SST) need to be prescribed as boundary conditions. The current procedure downscales SST used in the host model (ECMWF/ECHAM) and include them in the 6 hour lateral boundary conditions. Typically, SST data sets used in ECHAM are temporal interpolation of monthly satellite derived SSTs (e.g. HadSST).

2.4 Practical considerations

As indicated in Table 2.1, the number of nodes ($N_{lon} \times N_{lat} \times N_{vert}$) in REMO is in the order of 2.10^5. This is 2 times larger than the standard T30 resolution ($\Delta\varphi = 2.5^\circ$) for the global spectral grid ($96 \times 48 \times 19 \sim 10^5$) commonly used in ECHAM.

Furthermore, the Courant-Friedrichs-Lewy (CFL) stability criterion defined in Equation 2.5 imposes a drastic reduction of the computing time-step. In Equation 2.5, Δx represents the horizontal resolution, Δt the computing time step and U the velocity of the fastest propagating simulated wave.

$$\begin{aligned} CFL = &\quad \frac{\Delta x \cdot U}{\Delta t} > 1 \\ U_{REMO} = &\quad U_{ECHAM} \\ \Rightarrow \Delta t_{REMO} = &\quad \frac{\Delta x_{ECHAM}}{\Delta x_{REMO}} \cdot \Delta t_{ECHAM} \end{aligned} \tag{2.5}$$

In fact, ECHAM T30 runs on a 30' time-step, whereas REMO 0.5°runs on a 5' time step. Accordingly, a climate simulation with the regional model REMO will demand about 10 times more resources, that is CPU computing time than with the global circulation model ECHAM T30.

Integrations of REMO analysed in the following chapters were performed at the High Performance Computer Centre for Climate and Earth System Research (Deutsches Klimarechenzentrum - DKRZ). The available supercomputer is a NEC SX6 based on 24 PVP-nodes with 8 CPUs each. Further hardware resources include a 3.5 Pb (i.e. 10^15 bytes) tape storage system, and several IA64-nodes for cross-compiling and post-processing purposes.
The REMO$_{iso}$ FORTRAN code is currently not optimised for parallel compilation. As a practical example, a five years integration of REMO over the European domain require 200 CPUh. Including the monitoring of execution and post-processing, it correspond to an approximate 1 month duration.

After execution, the model output requires post-processing prior to manipulation by its end-user. A package [Podzun, personal communication] is readily available to convert output files from the big endian to little endian encoding and extract the desired model variables into an internal service (SV) format. The climate data operators (CDO) package [Schulzweida, 2005] the converts it to either portable (NetCDF) or native (GrADS) binary format. In the course of the PhD, a comprehensive IO package was developped to read/write GrADS binary files into/from the MATLAB® workspace. All consecutive data analysis, including graphics plotting, was performed under MATLAB®.

Bibliography

E. Aldrian. *Simulations of Indonesian Rainfall with a Hierarchy of Climate Models*. Mpi report 92, Max Planck Institut für Meteorologie, July 2003. 23

T. Bariac, J. Gonzalez-Dunia, N. Katerji, O. Béthenod, J.M. Bertolini, and D. Mariotti. Spatial variation of the isotopic composition of water (^{18}O, ^{2}H) in organs of aerophytic plants: 2. Assessment under field conditions. *Chemical Geology*, 115(3-4):317 – 333, Aug 1994a. 23

T. Bariac, J. Gonzalez-Dunia, F. Tardieu, T. Tessier, and D. Mariotti. Spatial variation of the isotopic composition of water (^{18}O, ^{2}H) in organs of aerophytic plants: 1. Assessment under laboratory conditions. *Chemical Geology*, 115(3-4):307 – 315, Aug 1994b. 23

J.F. Brown, T.R. Loveland, D.O. Ohlen, and Z. Zhu. Global Land Cover Characteristics Database (GLCCD), version 2.0. Technical report, U.S. Geological Survey, 2002. http://edcdaac.usgs.gov/glcc/globe_int.asp. 24

H.C. Davies. A lateral boundary formulation for multi-level prediction models. *Quarterly Journal of the Royal Meteorological Society*, 102:405–418, 1976. 21

D. Gesh and S. Greenlee. Global 30-arc seconds digital elevation model - GTOPO30. Technical report, U.S. Geological Survey, 1996. http://edcdaac.usgs.gov/gtopo30/gtopo30.html. 23

S. Hagemann. An Improved Land Surface Parameter Dataset for Global and Regional Climate Models. Technical Report 336, Max-Planck-Institute for Meteorology, 2002. 23

S. Hagemann, B. Machenhauer, O.B. Christensen, M. Déqué, D. Jacob, R. Jones, and P.L. Vidale. Intercomparison of water and energy budgets simulated by regional climate models applied over Europe. Technical Report 338, Max-Planck-Institute for Meteorology, 2002. 16, 22

G. Hoffmann. *Stabile Wasserisotope im allgemeinen Zirkulationsmodell ECHAM*. PhD thesis, Max Planck Institut für Meteorologie, 1995. 21, 23

G. Hoffmann and M. Heimann. Water tracers in the General Circulation Model ECHAM. Technical Report 110, Max Planck Institut für Meteorologie, 1993. 21

G. Hoffmann, M. Werner, and M. Heimann. Water isotope module of the ECHAM atmospheric general circulation model: A study on timescales from days to several years. *Journal of Geophysical Research*, 103(14):16 871 – 16 896, 1998. 21

D. Jacob. A note to the simulation of the annual and inter-annual variability of the water budget over the Baltic Sea drainage basin. *Meteorology and Atmospheric Physics*, 77:61 – 73, 2001. 16

D. Jacob, U. Andrae, G. Elgered, C. Fortelius, L.P. Graham, S.D. Jackson, U. Karstens, C. Koepken, R. Lindau, R. Podzun, B. Rockel, F. Rubel, H.B. Sass, R.N.D. Smith, B.J.J.M. Van den Hurk, and X. Yang. Comprehensive Model Intercomparison Study Investigating the Water Budget during the BALTEX-PIDCAP Period. *Meteorology and Atmospheric Physics*, 77:19 – 43, 2001. 16

D. Jacob and R. Podzun. Sensituvity studies with the regional climate model REMO. *Meteorology and Atmospheric Physics*, 63:119 – 129, 1997. 16

J. Jouzel and L. Merlivat. Deuterium and oxygen 18 in precipitation: modeling of the isotopic effects during snow formation. *Journal of Geophysical Research*, 89:11 749 – 11 757, 1984. 23

D. Majewski. The Europa-Modell of the Deutscher Wetterdienst. *ECMWF Seminar on numerical methods in atmospheric models*, 2:147 – 191, 1991. 16, 20

D. Majewski and R. Schrodin. Documentation of the EM/DM System. Technical report, Deutscher Wetterdienst - DWD, Jun 1995. 16, 24

M. Majoube. Fractionnement en oxygène 18 et en deutérium entre l'eau et sa vapeur. *Journal of Chemical Physics*, 10: 1423 – 1436, 1971. 23

L. Merlivat and J. Jouzel. Global climatic interpretation of the deuterium-oxygen 18 relationship for precipitation. *Journal of Geophysical Research*, 84:5029 – 5033, 1979. 22

T.E. Nordeng. Extended versions of the convective parametrization scheme at ECMWF and their impact on the mean and transient activity of the model in the tropics. *ECMWF Research Department, Technical Memorandum No. 206*, 1994. 23

R. Podzun, A. Cress, D. Majewski, and V. Renner. Simulation of European climate with a limited area model. PartII: AGCM boundary conditions. *Beiträge zur Physik der Atmopshäre*, 68(3):205 – 225, Aug 1995. 16

E. Roeckner, K. Arpe, L. Bengtsson, S. Brinkop, L. Dümenil, M. Esch, E. Kirk, F. Lunkeit, M. Ponater, B. Rockel, R. Sausen, S. Schlese, U. andSchubert, and M. Windelband. The ECHAM3 atmospheric general circulation model. Technical Report 6, Deutsches Klimarechenzentrum - DKRZ, 1992. 17

E. Roekner, E.K. Arpe, L. Bengtsson, M. Christoph, M. Claussen, L. Dümenil, M. Esch, M. Giorgetta, U. Schlese, and U. Schulzweida. The atmospheric circulation model ECHAM-4: model description and simulation of the present day climate. *Max-Planck-Institute für Meteorologie Report*, 218, 1996. 16, 20, 22

U. Schulzweida. *Climate Data Operators (CDO) User's Guide*. Max Planck Institut für Meteorologie, version 0.9.6 edition, Apr 2005. http://www.mpimet.mpg.de/ cdo/cdo.pdf. 25

T. Semmler. *Der Wasser- und Energiehaushalt der arktischen Atmosphäre*. PhD thesis, Max-Planck-Institut für Meteorologie, Apr 2002. 16, 20, 23

K. Sturm, G. Hoffmann, and B. Langmann. Climatology of stable water isotopes in South America: comparing general to regional circulation models. *Journal of Climate – submitted*, 2005a. 23

K. Sturm, G. Hoffmann, B. Langmann, and W. Stichler. Simulation of $\delta^{18}O$ in precipitation by the regional circulation model $REMO_{iso}$. *Hydrological Processes – in press*, 2005b. 24

M. Tiedtke. A comprehensive mass flux scheme for cumulus parametrizations in large-scale models. *Monthly Weather Review*, 117:1779 – 1800, 1989. 23

M. Werner. *Spatial and Temporal Variability of Water Isotopes in Polar Precipitation*. PhD thesis, Max Planck Institut für Meteorologie, 2000. 22

M. Werner, U. Mikolajewicz, M. Heimann, and G. Hoffmann. Borehole versus isotope temperatures on Greenland : seasonality does matter. *Geophysical Research Letters*, 27:723 – 726, 2000. 22

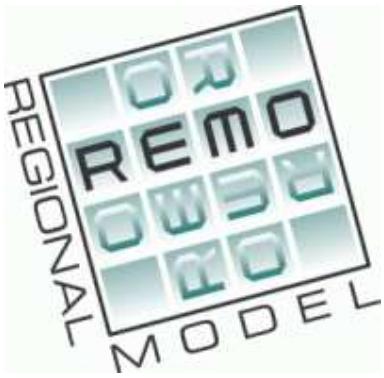

Figure 2.5: Community logo of the REMO suite.

Chapter 3

Simulation of the $\delta^{18}O$ in precipitation by the regional circulation model $REMO_{iso}$ †

Résumé

Les premiers résultats du modèle de circulation régional $REMO_{iso}$, intégrant le cycle des isotopes stables de l'eau, sont présentés dans ce chapitre. Ils concluent ainsi un an et demi de travail consacrés au développement et à la mise au point du module isotopique de $REMO_{iso}$. Pour sa première performance, $REMO_{iso}$ est appliqué au continent européen sur une période de 2 ans. Il était logique pour une première validation d'appliquer la version isotopique de REMO sur la zone géographique où ce modèle régional a le plus été étudié. Le continent européen comprend également la plus haute densité surfacique de mesures isotopiques fiables au sein du réseau mondial de collecte des isotopes dans les précipitations (global network of isotopes in precipitation – GNIP).

Deux formulations de la composition isotopique sont testées aux limites latérales du domaine. En première alternative, les conditions aux limites sont fixées par les analyses du centre européen pour la prévision météorologique à moyen terme (European Centre for Medium-Range Weather Forecasts – ECMWF). Comme elles ne disposent d'aucune information sur la composition en isotopes stables de l'eau, le $\delta^{18}O$ aux frontières de REMO est prescrit linéairement en fonction de la température, d'après une relation empirique établie par W. Dansgaard. Il faut néanmoins souligner que les hypothèses sous-jacentes à la relation empirique ne sont pas vérifiées dans le cas présent. La régression linéaire de $\delta^{18}O$ dans les précipitations en fonction de la température est significative pour des moyennes annuelles aux latitudes tempérées. Faute de trouver une paramétrisation idoine, nous avons appliqué cette relation toute les 6 heures pour prescrire le $\delta^{18}O$ de la vapeur (en supposant l'équilibre isotopique entre l'eau liquide et sa vapeur) sur l'ensemble de la colonne atmosphérique. La deuxième alternative repose sur l'intégration ('nesting' en anglais) de $REMO_{iso}$ dans un modèle hôte qui reproduise explicitement le cycle des isotopes stables de l'eau. Dans le cas présent, $REMO_{iso}$ est 'niché' dans $ECHAM4_{iso}$, contraint par des températures de surface océaniques climatologiques. A l'instar des autres paramètres pronostiques, le $\delta^{18}O$ simulé par ECHAM est assimilé aux limites latérales de $REMO_{iso}$.

La première validation concerne la distribution spatiale du $\delta^{18}O$ en moyennes annuelle et saisonnières. Dans ce but, nous comparons le $\delta^{18}O$ simulé par $REMO_{iso}$ aux mesures mensuelles du réseau GNIP. $REMO_{iso}$ reproduit qualitativement les effets isotopiques classiques. Le $\delta^{18}O$ diminue avec l'altitude et la distance à son lieu d'évaporation (continentalité), ainsi qu'avec la latitude (effet de température). En revanche, la prescription du $\delta^{18}O$ en fonction de la température induit une sous-estimation chronique de -4.5‰ du signal isotopique. Cette disparité est plus marquée durant l'hiver et aux hautes latitudes. En revanche, l'intégration de $REMO_{iso}$ dans $ECHAM_{iso}$ ne présente pas d'erreur systématique, mais l'amplitude saisonnière du signal

†K. Sturm, G. Hoffmann, B. Langmann and W. Stichler (2005), *Hydrological Processes, in press*.

isotopique est amoindrie par rapport aux observations. Pour confirmer ces premiers résultats, nous comparons le δ^{18}O simulé par REMO$_{iso}$ à des mesures quotidiennes effectuées par W. Stichler. Les précipitations journalières ont été analysées en trois stations, réparties à travers l'Allemagne : Nordeney, Arkona et Hohenpeissenberg. La dispersion des δ^{18}O à l'échelle quotidienne augmente en fonction de la continentalité, aussi bien dans les observations que les résultats de REMO$_{iso}$.

En complément de cette étude, sont présentés des résultats préliminaires d'une simulation forcée ('nudged' en anglais) de REMO$_{iso}$. En premier lieu, M. Werner a appliqué à ECHAM$_{iso}$ le forçage aux réanalyses ERA-15 du ECMWF. En deuxième lieu, la technique du forçage spectral a été appliquée a REMO$_{iso}$. Elle réside dans une assimilation des vents aux hautes altitudes dans REMO$_{iso}$ envers la circulation synoptique simulée par le modèle hôte (en l'occurrence, ECHAM$_{iso}$ forcé par ERA-15). Cette technique de double forçage permet de conjuguer une représentation réaliste de la circulation observée à grande échelle avec une simulation explicite du cycle des isotopes stables de l'eau, i.e. de faire la synthèse entre les deux formulations des conditions aux limites latérales décrites précédemment. L'amélioration est constatée en comparant la nouvelle simulation aux mesures quotidiennes de δ^{18}O effectuées à Saclay par J. Jouzel. Il est ainsi possible d'analyser non seulement la climatologie du cycle des isotopes de l'eau, mais également une le signal isotopique lors d'une situation météorologique particulière.

Zusammenfassung

Dieses Kapitel präsentiert die ersten Ergebnisse des regionalen Klimamodells REMO$_{iso}$ mit dem Zyklus stabiler Wasserisotope. Dies ist der Abschluß der Entwicklung und Regelung des Isotopenmoduls von REMO, für die anderthalb Jahr benötigt wurden. REMO$_{iso}$ wurde hier zuerst für eine zweijährige Simulation über Europa benutzt. Es war folgerichtig, REMO$_{iso}$ dort zu validieren, wo schon REMOs Grundversion ohne Wasserisotope am häufigsten angewandt worden ist. Darüber hinaus verfügt Europa über die höchste räumliche Dichte an zuverlässigen Wasserisotopenmessungen in dem 'global network of isotopes in precipitation' (GNIP).

Zwei Methoden für die Bestimmung der vorzuschreibenden Wasserisotopenzusammensetzung an REMOs seitlichen Rändern werden hier getestet. Die erste Methode besteht darin, daß REMOs Randbedingungen von Analysen des European Centre for Medium-Range Weather Forecasts (ECMWF) eingelesen werden. Da diese keine Information über Wasserisotope enthalten, wurde δ^{18}O an REMOs seitlichen Rändern durch eine von W. Dansgaard empirisch erstellte lineare Beziehung zwischen δ^{18}O und Temperatur festgesetzt. Es muss jedoch beachtet werden, daß die dieser empirischen Beziehung unterliegenden Bedingungen im Allgemeinen nicht erfüllt sind. Dansgaards lineare Regression ist lediglich für die Jahresmittel des Niederschlags-δ^{18}O gültig. In Ermangelung einer angemessenen, für kürzere Zeiträume gültigen Parametrisierung wurde Dansgaards Regression angewandt, um die 6-stündigen Randbedingungen für Dampf-δ^{18}O in Abhängigkeit von der amtosphärischen Temperatur vorzuschrieben, wobei isotopisches Gleichgewicht zwischen Wasserdampf und Wolkenwasser unterstellt wurde. Die zweite Methode besteht in dem Einnisten von REMO$_{iso}$ in einem Hostmodell, das explizit den Wasserisotopenzyklus berechnet. In unserem Fall handelte es sich um ECHAM$_{iso}$ mit klimatologischen Meeresoberflächentemperaturen, dessen δ^{18}O wie andere prognostische Parameter an den seitlichen Rändern von REMO$_{iso}$ assimiliert wurde.

Eine erste Validation von REMO$_{iso}$ besteht im Vergleich der räumlichen Verteilung des von REMO$_{iso}$ simulierten δ^{18}O mit jährlich und jahreszeitlich gemittelten GNIP-Messungen. REMO$_{iso}$ bildet klassische Isotopeneffekte nach. δ^{18}O nimmt sowohl mit Höhe und Entfernung vom Verdampfungsort (Kontinentaleffekt) als auch mit der geographischen Breite (Temperatureffekt) ab. Jedoch führt die Benutzung von Dansgaards Regressionsmodell zu einer systematischen Unterschätzung des δ^{18}O von -4.5$^{\circ}/_{\circ\circ}$. Die Diskrepanz tritt verstärkt im Winter und in hohen geographischen Breiten auf. Dagegen zeigt das Einnisten von REMO$_{iso}$ in ECHAM$_{iso}$ keine systematische Abweichung, wenngleich die jahreszeitliche Schwingungsbreite des δ^{18}O in REMO$_{iso}$ gedämpft wiedergegeben wird. Zur Bekräftigung dieser ersten Ergebnisse wurde REMO$_{iso}$s Out-

put mit täglichen $\delta^{18}O$-Messungen verglichen, die von W. Stichler an drei deutschen Stationen ausgeführt wurden: Nordeney, Arkona und Hohenpeissenberg. Sowohl in den Beobachtungen wie in den Simulationen mit $REMO_{iso}$ wächst die Streuung der täglichen Werte des Niederschlags-$\delta^{18}O$.

Als Ergänzung zu dieser Studie werden vorläufige Ergebnisse einer geführten (engl. nudged") $REMO_{iso}$ Simulation gezeigt. Als erster Schritt wurde die Nudgingprozedur von M. Werner an $ECHAM_{iso}$ angepasst. Nach dieser Vorgehensweise werden die ERA-15 Reanalysen in die von ECHAM simulierte Zirkulation assimiliert, ohne daß der Wasserisotopenzyklus dabei abgeändert wird. Als zweiter Schritt wird $REMO_{iso}$ spektral "genudged", d.h. die von REMO simulierten Windfelder in der hohen Atmosphäre werden der großskaligen Hostmodellzirkulation angepaßt. Damit kann eine explizite Berechnung des Wasserisotopenzyklus mit einer wirklichkeitstreuen atmosphärischen Zirkulation vereinigt werden; die Synthese der zwei zuvor beschriebenen Methoden der Formulierung der isotopischen Randbedingungen wird somit erreicht. Ein Vergleich der Ergebnisse dieser doppelt "genudgtenSSimulation mit von J. Jouzel in Saclay ausgeführten, täglichen Dampf-$\delta^{18}O$-Messungen zeigt eine deutliche Verbesserung gegenüber den nicht "genudgtenSSimulationen. Die Analyse des simulierten Wasserisotopenzyklus ist somit nicht auf dessen Klimatologie beschränkt, sondern sie kann auf Untersuchungen bestimmter meteorologischer Situationen erweitert werden.

3.1 Introduction

High resolution modelling of the isotopic water cycle reacts on two specific needs when analysing the increasing amount of water isotope observations. Numerous case studies have been conducted measuring the isotopic composition on an event basis. State-of-the-art atmospheric GCMs are not capable to reproduce the observed rapid and large variations of the water isotope signal and to represent the underlying physical processes. Moreover, geographically challenging situations ask for a high resolution modelling approach. High altitude ice-core data, for example, are strongly influenced by surrounding orography. Their quantitative interpretation is typically hampered by a lack of long-term meteorological observations near the drilling site and their extreme position on the top of a steep mountain area.

The present article describes the first development and validation of the stable water isotope module in the REMO regional circulation model. First, we briefly introduce the concept of the various effects and physics of the water isotope as they were introduced by Dansgaard [1964]. This provides us with the necessary concepts to validate afterwards the model. We then introduce a new approach in meso-scale water isotope modelling, applied in a case study over Western Europe in 1997 - 1998. The model output is validated on a monthly basis against the global network of isotopes in precipitation (GNIP) database [IAEA and WMO, 2001]. For more robust testing of the physical parameterisation scheme, an analysis of the diurnal variability of the δ^{18}O signal is performed at three German GSF stations (Gesundheit für Umwelt und Gesundheit). Special attention is given to the sensitivity of the model to boundary conditions. Finally, we conclude by indicating new possibilities which REMO$_{iso}$ rises in investigating the water isotope cycle.

3.1.1 Empirical analyses and identification of isotope 'effects'

Mass-dependent fractionation of water molecules between heavier isotopomers (oxygen $H_2^{18}O$ and hydrogen $HD^{16}O$) and the lighter standard water molecule ($H_2^{16}O$) occurs both under equilibrium (thermodynamic Al) and non-equilibrium (kinetic) conditions; it is expressed as a deviation (δ^{18}O) from the Vienna Standard Mean Ocean Water (V-SMOW) ratio: $\delta^{18}\mathrm{O} = \frac{\left([H_2^{18}O]/[H_2^{16}O]\right)_{sample}}{\left([H_2^{18}O]/[H_2^{16}O]\right)_{V-SMOW}} - 1$ in $^{\circ}/_{\circ\circ}$. From the evaporation to the precipitation site, the water isotopes undergo a number of different processes influencing the final isotopic signal in precipitation. Though condensation temperatures play a leading role, in particular in high latitudes, several other climate parameters such as the cloud type, moisture origin and mixing along different atmospheric pathways or re-evaporation from vegetation covered continental surfaces equally affect the water isotopes. This already points to the need of a comprehensive representation of the hydrologic cycle in order to fully understand water isotopic variability on different time scales.

The International Atomic Energy Agency (IAEA) in cooperation with the World Meteorological Organisation (WMO) launched in 1961 the Global Network of Isotopes in Precipitation (GNIP) [IAEA and WMO, 2001], consisting in a world-wide survey of the isotopic composition of monthly precipitation [Schotterer et al., 1996]. This global coherent data-base served as a major basis for identifying empirical relations, known as 'effects', which provide a first interpretation of the isotopic signal.

The *temperature effect* accounts for the observed general decrease in δ^{18}O with decreasing temperature. A first quantification is given in [Dansgaard, 1964], computing a linear regression of annual mean $\overline{\delta^{18}\mathrm{O}}$ in precipitation to the mean annual surface temperature $\overline{T_{surf}} < 15^{\circ}C$ at North Atlantic coast and Greenland ice cap stations:

$$\overline{\delta^{18}\mathrm{O}} = 0.69\,\overline{T_{surf}} - 13.6\,^{\circ}/_{\circ\circ} \tag{3.1}$$

Taking amount-weighted averages over at least a decade of GNIP station data, Yurtsever [1975] gave a similar relation: $\overline{\delta^{18}\mathrm{O}} = (0.521 \pm 0.014)\ \overline{T_{surf}} - (14.96 \pm 0.21)\,^{\circ}/_{\circ\circ}$. In [Rozanski et al., 1993], a linear fit for all non-polar stations of the IAEA networks gives : $\overline{\delta^{18}\mathrm{O}} = 0.58\ \overline{T_{surf}} - 13.64\ ^{\circ}/_{\circ\circ}$. Yet analysis of the inter-annual variability shows that temporal isotope-temperature gradients are not necessarily identical to the spatial temperature effect. Mook et al. [2001] for instance found often less negative δ^{18}O than expected by the above mentioned relations. A seasonal temperature pattern is clearly followed by all but some marine GNIP stations, with generally a lower $\delta^{18}\mathrm{O} - T$ regression slope than that of

mean annual values.

The *continental effect* accounts for the progressive depletion of $H_2^{18}O$ in precipitation with increasing distance from the coast (that is, the main source of moisture) related to land-inwards rain-out. E.g. an average depletion of 7 $‰$ is observed during the passage over Europe, from the Irish coast to the Ural mountains. The effect in summer is only about one fourth of the effect in winter, due to non-fractionating evapo-transpiration by vegetation. Rozanski et al. [1993] reports a quantification of the continental effect for western Europe in winter, i.e. the $\delta^{18}O$ decrease as a function of the distance from the Atlantic Coast. The gradient equals -3.8 $‰$ / 1000 *km* for longitudes in [17°E; 20°E]; further eastwards, additional moisture supply from southern, secondary water vapour sources (Mediterranean, Black and Caspian Seas) tends to diminish the slope to -1.6 $‰$ / 1000 *km*. Accordingly, the extent to which a continental effect occurs probably depends on the prevailing direction of the air masses movement, rather than simply on distances from the coast [Mook et al., 2001].

The *altitude effect* accounts for the observed lowering of $\delta^{18}O$ in precipitation with increasing altitude. It is physically related to a temperature controlled rain-out process when air masses are lifted up at orographic obstacles [Moser and Stichler, 1971]. Resulting altitude dependence vary from -0.1 $‰$ to -0.6 $‰$ / 100 *m*, often decreasing at higher altitudes [Vogel et al., 1975]; regional studies by Siegenthaler and Oeschger [1980] give a similar range of -0.16 $‰$ to -0.4 $‰$ / 100 *m*.

3.1.2 Modelling the isotopic composition of precipitation

In the following we present a non-exhaustive list of water isotope models in growing complexity. It is beyond the scope of this article to describe them in all details, hence only their major characteristics and performance are briefly recalled.

A first conceptual model was constructed by Dansgaard [1964]. He assumed that a vapour mass is displaced from its oceanic origin to the condensation site without further mixing. The two-phase system (vapour/liquid) fractionates water isotopes successively during formation of liquid water, which is directly extracted from the system without further isotopic exchange (open system). The isotopic composition of the remaining vapour fraction is therefore principally controlled by the rain-out intensity, which is in turn controlled by the temperature gradient between the source and the precipitation site. Such simple Rayleigh models have been continuously improved by including kinetic processes during evaporation from the sea surface [Merlivat and Jouzel, 1979] or during the formation of ice crystals [Jouzel and Merlivat, 1984]. In their most advanced version they describe in very detail cloud internal processes during the synchronous existence of three phases (vapour/solid/liquid) [Ciais et al., 1995] and allow even the computation of realistic atmospheric pathways [Kavanaugh and Cuffey, 2003]. All these studies compute realistically the high-latitude temperature dependence of the water isotopes (in the order of 0.6 $‰ \cdot {}^0C^{-1}$) which is of crucial importance for the use of the water isotopes as paleo-thermometer [Jouzel et al., 1997]. However, still these Rayleigh models do not describe the full complexity of the hydrologic cycle - e.g. they do not include the mixing of different air masses, the influence of evapo-transpiration over continental surfaces or the complex behaviour of convective cloud processes.

Therefore, in a next step the fractionation processes were built into Atmospheric General Circulation Processes (AGCMs). These models solve the full set of equations (primitive equations) including the conservation of mass, momentum and energy on a discretised three dimensional grid. Fractionation processes are taking into account for each phase change within the hydrologic cycle of the AGCM. Hoffmann et al. [2000] summarizes the existing GCM with water isotope diagnostics : Joussaume et al. [1984] built the first water isotope module into the LMD (Laboratoire de Météorologie Dynamique) GCM, with a coarse resolution [Joussaume et al., 1984], followed by Jouzel et al. [1987] with the GISS (Goddard Institute of Space Sciences) GCM with an horizontal resolution of $\sim 9^\circ$ and 9 vertical levels. More recently [Hoffmann et al., 1998] included a water isotope module in the ECHAM (European Centre model HAMburg) GCM with a horizontal resolution of $\sim 2.8^0$ and 19 vertical levels, as did D. Noone in the MUGCM (Melbourne University GCM) with a T31 spectral resolution and 9 vertical levels[Noone and Simonds, 2002].

The major drawback of GCMs in representing the water isotope cycle is their relatively coarse resolution for regional studies, and the corresponding parameterisation for sub-scale processes. As stated in [IPCC, 2001], 'regional models consistently improve the spatial details of simulated climate compared to AGCM'. Following this incentive, we introduce

the water isotope module in the regional circulation model (RCM) REMO (REgional MOdel).

3.2 Description of REMO$_{iso}$

The regional circulation model REMO 5.0 (REgional MOdel) is a modified version of the numerical weather forecast model system EM/DM from the German Weather Service [Majewski, 1991]. In its current version, it uses the same physical parameterisation as the ECHAM-4 general circulation model [Roekner et al., 1996]. A complete description of the model features can be found in [Jacob, 2001, Jacob et al., 2001]. In the following, we briefly summarise the relevant model characteristics, focusing on the water cycle.

3.2.1 Standard climatic settings for REMO

The horizontal discretisation of REMO relies on a rotated Arakawa-C grid, allowing a nearly uniform cell size all over the study domain, while the vertical discretisation occurs on hybrid altitude-pressure, so called η-levels. The current study domain spans over entire Europe, from the Mediterranean coast of Northern Africa in the South to the Barents Sea in the North, and from the Atlantic Ocean in the West to the Anatolian Plateau in the East (Figure 3.1). In the present experiment, REMO was set up with a 0.5° ($\sim 55\ km$) horizontal resolution on a 81x91 grid, with 19 vertical levels. Water vapour, cloud liquid water and water isotope tracers are prognostic variables in the model, using a leap-frog scheme with semi-implicit correction and Asselin-filter. At the lateral boundaries of the domain, the model assimilates prognostic variables (pressure, temperature, wind speed, water vapour and cloud water) from the host model, within a 8-grid box buffer zone. The host model, either ECMWF analyses data [Norris, 1997] or ECHAM simulations, provides boundary data at (00:00, 06:00, 12:00 and 18:00 UTC). These boundary conditions are linearly interpolated, and assimilated by REMO at every time-step. The boundary conditions are presented later in 3.2.2.

Critical hydrological processes are parameterised as sub-grid scale processes. The cumulus convection, subdivided in shallow, middle and deep convection, follows the bulk mass concept of [Tiedtke, 1989], adapted according to [Nordeng, 1994]. Organised detrainment, computed for a spectrum of clouds detraining at different heights, is related to buoyancy instead of moisture convergence. Cloud water detrained at the top of cumulus clouds enters as a source term in the stratiform cloud equation. Stratiform cloud water is computed as a function of phase changes (source) and precipitation formation (sinks). The latter depends on coalescence of cloud droplets and gravitational settling of ice crystals [Roekner et al., 1996]. Three type of water reservoirs are considered in the soil module : (bucket-type) soil wetness, snow layer and interception of rain by the canopy. The stomatal control of evapo-transpiration is addressed, although schematically. Turbulent fluxes at the surface are calculated from the Monin-Obukhov similarity theory with a higher-order closure scheme. The eddy diffusion coefficients are calculated as functions of the turbulent kinetic energy [Brinkop and Roeckner, 1995].

3.2.2 Isotopic settings in REMO

The stable water isotopes were first implemented into ECHAM-3 global circulation model by [Hoffmann et al., 1998], later updated to ECHAM-4 by [Werner et al., 2000]. Fractionation and transport processes are embedded at all stages of the hydrologic cycle by defining isotopic counterparts to all water related variables. Hence the species $H_2^{18}O$ and HDO are treated independently from the predominant $H_2^{16}O$, but undergo the same processes, to which both equilibrium and kinetic fractionations were included. A complete description of the water isotope cycle as included in ECHAM can be found in [Hoffmann et al., 1998]. During evaporation from the ocean, the vapour is considered to be saturated, in a temperature-dependent equilibrium [Majoube, 1971] with a slightly enriched water phase ($\delta^{18}\mathrm{O} = 0.5\ ‰$), which is then corrected for wind-speed dependent kinetic effects [Merlivat and Jouzel, 1979]. Condensation into droplets or ice crystals is treated as an equilibrium fractionation under temperate conditions. At low temperatures ($T < -20^\circ C$), the slower diffusion of heavy isotopes through the microscopic boundary layer around snow flakes is taken into consideration. Partial re-evaporation of rain drops below the cloud base and the resulting kinetic fractionation is treated differently for stratiform and convective

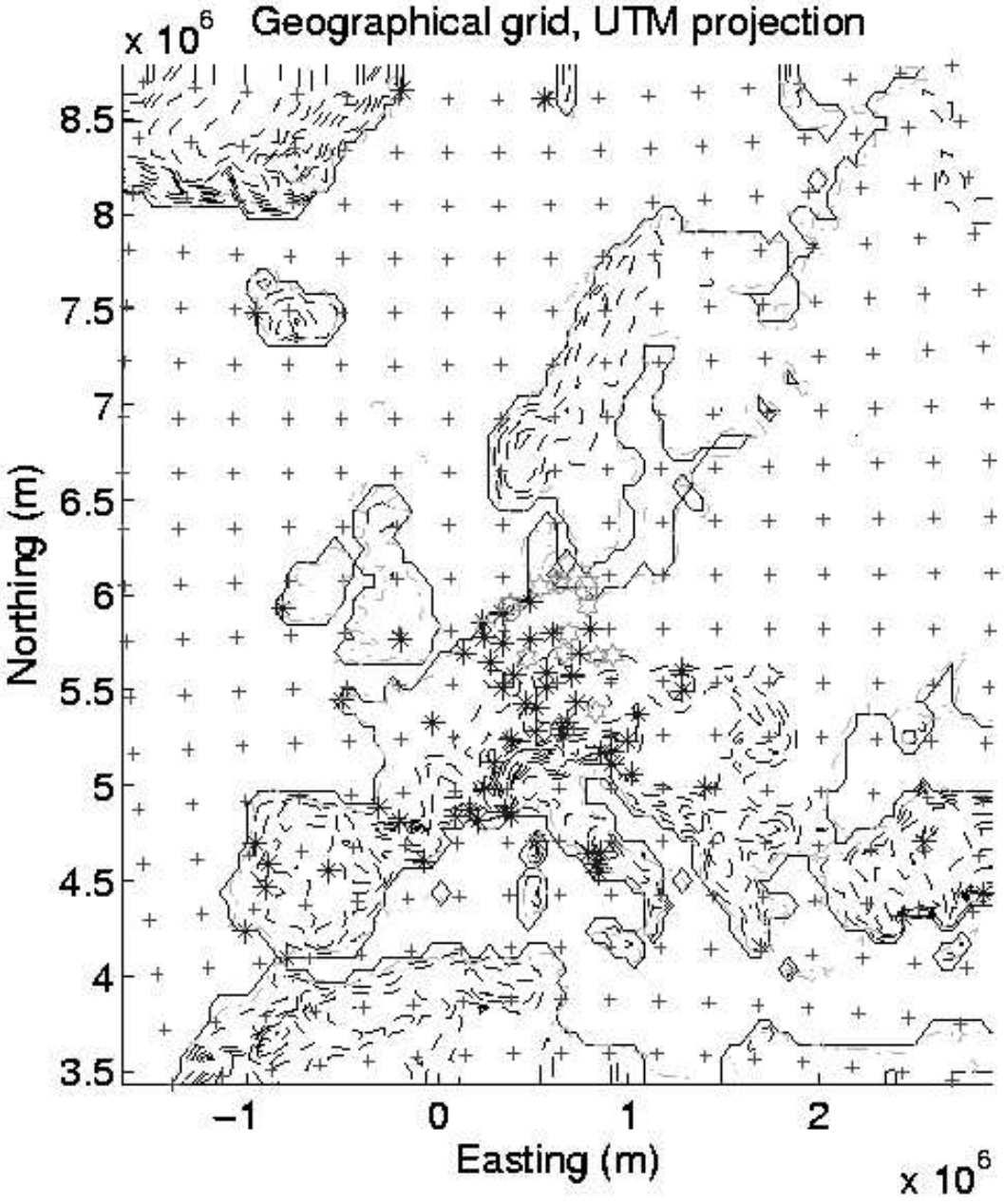

Figure 3.1: Study domain for REMO 81x91, in the area-true Universal Tranverse Mercator (UTM) projection. As an indication for the 0.5° resolution, the coastline and 300m isolines are plotted. The crosses represents every fifth grid point. The location of IAEA stations are marked with stars, GSF stations with hexagonals. The three GSF stations with daily measurements (Arkona, Nordeney and Hohenpeissenberg) are represented as circles.

clouds, identically to the ECHAM parameterisation [Hoffmann et al., 1998]. For stratiform rain, the smaller drop radii, hence lower falling speed is assumed to cause an isotopic re-equilibration of 95% with surrounding vapour, while it occurs only to 45% for convective rain. Considering the bucket-type surface scheme, evapo-transpiration from the unique soil reservoir by the vegetation is considered non-fractionating, while the remaining flux is treated as fractionating bare-soil evaporation (with no explicit representation of hydrological features such as runoff, lakes...).

Initial and boundary conditions are critical issues when using a regional circulation model. According to the standard procedure [Hoffmann et al., 2000], the initial atmospheric water vapour is set to $\delta^{18}O = -80\ ‰$, while soil reservoirs are initialised using the [Dansgaard, 1964] $\delta^{18}O$-temperature regression given in Equation 3.1 with soil temperature at 3 metres depth. In the first model set-up (referred to as ECMWF-nested simulation hereafter), ECMWF analysis are used as boundary conditions. Since no isotopic information is available in ECMWF analyses, the water vapour in air-masses entering the domain were assigned an isotopic composition in equilibrium with liquid water following the Dansgaard equation. The formulation of the boundary conditions is given in Equation 3.2, where $\delta^{18}O_l$ stands for the liquid water isotopic composition, $\delta^{18}O_v$ for water vapour composition, T for temperature in $^\circ C$ and $\alpha(T)$ for the temperature dependent equilibrium factor [Majoube, 1971].

$$\begin{cases} \delta^{18}O_l = 0.69 \cdot T - 13.6\,‰ & \text{for T } \leq 13.9^o C \\ \delta^{18}O_l = -4\,‰ & \text{for T } > 13.9^o C \\ \delta^{18}O_v = \frac{\delta^{18}O_l + 1}{\alpha(T)} - 1 & \forall T \end{cases} \tag{3.2}$$

In a second step, $REMO_{iso}$ is nested into an $ECHAM_{iso}$ simulation, assimilating isotopic boundary conditions identically to other prognostic atmospheric variables. The $ECHAM_{iso}$ simulation used the AMIP 1979-1994 SST climatology as boundary condition. The $REMO_{iso}$ simulation obtained with these settings is referred to as ECHAM-nested simulation thereafter.

3.3 Results and discussion

Here we present the results of a two-year case study for the ECMWF and ECHAM simulations, from January 1997 to February 1999, without considering the first two spin-up months. In the following, we analyse the isotopic features displayed by REMO and how it compares to $\delta^{18}O$ measurements in precipitation at yearly, monthly [IAEA and WMO, 2001] down to event time-scales. The validation of REMO for climatic parameters such as temperature and total precipitation amounts is beyond the scope of this case study. REMO has been intensively used over Europe and reaches among the best scores in RCM inter-comparisons performed as part of the BALTEX project [Jacob et al., 2001].

Seasonality appears to play a major role in all isotopic fractionation processes, primarily because of their dependence on temperature. In the present article, seasonality is considered to be best represented by the amplitude of the signal, assuming that it has a sinusoidal shape with one-year periodicity and a maximum on July the 21^{st} *. This presentation of the isotope seasonality is in good agreement with observations in the study area. The mean isotopic composition of precipitation, $\overline{\delta^{18}O}$, as well as its seasonal amplitude A, are computed by fitting a time-dependent cosine function of prescribed period $\mathcal{T}$ and phase τ to the observations, according to equation 3.3.

$$\begin{cases} \delta^{18}O = A \cdot \cos\left(\frac{(t-\tau)\cdot 2\Pi}{\mathcal{T}}\right) + \overline{\delta^{18}O} \\ \text{data sets} : \delta^{18}O \text{ monthly data set}, t \text{ time in days} \\ \text{prescribed parameters} : \mathcal{T} = 365\,days, \tau = \text{July } 21^{th} \\ \text{least square regression} : A \text{ seasonal amplitude}, \overline{\delta^{18}O} \text{ mean } \delta^{18}O \end{cases} \tag{3.3}$$

In the next section, we focus on the differences between REMO simulations (ECMWF and ECHAM nested runs) and the

*Not only this formulation quantifies the intuitive notion of seasonality in terms of the seasonal amplitude of the $\delta^{18}O$ signal, but also it has the advantage of being insensitive to missing values in determining the long-term mean. Yet its statistical relevance can be questioned with regard to the short study period (2 periods of the signal).

GNIP measurements.

3.3.1 Mean annual $\delta^{18}O$ in precipitation

The map of mean annual values for $\delta^{18}O$ in precipitation in the ECHAM-nested run is shown in Figure 3.2. Values in the 8-grid cell buffer zone at the lateral boundary of the model are to be discarded, as numerical noise is produced by the boundary condition assimilation scheme.

The latitudinal, or *annual temperature effect* appears as being the predominant trend governing the spatial distribution of water isotopes in precipitation : the North to South increase in mean annual temperatures induces a strong increase in $\delta^{18}O$. Figure 3.3 displays a scatter plot of annual $\delta^{18}O$ versus annual temperature for available GNIP $\delta^{18}O$ and T series. The temperature-$\delta^{18}O$ gradient computed from the selected GNIP stations is equal to $0.46\ ‰.^0C^{-1}$. A similar computation - for model output at the corresponding GNIP stations - yields gradients of $0.44‰.^0C^{-1}$ for the ECMWF-nested run, and $0.56‰.^0C^{-1}$ for the ECHAM-nested run [†]. The two first gradients are slightly weaker than literature values for non-polar stations ranging from 0.5 to 0.6 $‰.^0C^{-1}$ (cf. Section 3.1.1), which the ECHAM-nested run agrees well with. While the slope agrees well between modelled and measured values, there is an average $-4.5\ ‰$ offset between absolute $REMO_{ECMWF}$ and GNIP values. No offset is observed between $REMO_{ECHAM}$ and GNIP.

Figure 3.4 shows the spatial distribution of modelled versus the observed $\delta^{18}O$ values. The represented parameter is the best-estimate yearly mean in precipitation $\overline{\delta^{18}O}$ at the location of GNIP stations, according to Equation 3.3. Circle radii are proportional to the value at a given site, while black stands for GNIP observations, green for $REMO_{ECHAM}$ and red for $REMO_{ECMWF}$. The $\overline{\delta^{18}O}$ values for each GNIP station are given in Table 3.1. In the GNIP observations, both the latitudinal gradient, decreasing from South to North, and the continental gradient, decreasing from coast to land-inwards stations are clearly identified. Although the GNIP data set comprises too few mountain stations, there is a clear indication of the altitude effect when looking at the gradient between plain and mountain stations. Analysing the ECHAM-nested simulation, only 9 stations out of 57 have a $\overline{\delta^{18}O}$ diverging by more than $1.5‰$ from GNIP values, considering that the standard deviation of annual $\delta^{18}O$ averages in the GNIP dataset is $0.7‰$. Most of the discrepancies can be explained by altitude difference exceeding 500m between the actual station and the 50-km averaged topography around it, as seen by REMO (for Carpentras-F, Klagenfurt-A, Penhas Douradas-P, Vienna-A, Villacher Alpe-A, Wasserkuppe-D). Table 3.1 exhibits the same offset for $REMO_{ECMWF}$ as presented in the previous paragraph, with the largest bias at coastal stations (Brest-F, De Bilt-NL, Emmerich-D, Montpelier-F, Valentia Observatory-IRL). As for GNIP, the classical temperature, continental and altitude effects are well reproduced as similar gradients in REMO simulations.

The principal mountain massif in the study domain, i.e. the Alps, appears clearly on the map, as do smaller mountain ranges as the Transylvanian Carpathes and the Fenno-Scandinavian range. This *altitude effect* appears as a combination of temperature and amount effects introduced in section 3.1.1. Even smaller mountain ranges such as the Fenno-Scandinavian range, and to a lesser extent for the Grampian Mountains in the Scottish Highlands, the Cordillera Cantabrica on Spain's north Atlantic coast or the Rhodope Mountains on the Greek-Bulgarian border are marked by a clearly depleted isotope signal in $REMO_{iso}$ simulations. On the other hand, mountain ranges that do not stand as an obstacle to the general atmospheric motion have a reduced altitude effect, such as the Pyrenees on the French-Spanish boarder or the relatively poor effect of the Alps. On Figure 3.5, the variation of $\delta^{18}O$ with altitude is shown on different latitudinal bands (corresponding to the Greenland icesheet, the Scandinavian mountain range and all mid-European mountain ranges), for all grid points with an altitude exceeding 500m. The vertical gradient of $\delta^{18}O$ is in the order of $0.4‰/100m$ for both Greenland ($R^2 = 0.69$) and mid-European mountain ranges ($R^2 = 0.42$). The correlation coefficient is lower in the second case, because of the merging of different mountain ranges in the second category, as compared to the rather uniform Greenland climatic context. Apparently, the vertical gradient is two times smaller in the case of the Scandinavian mountain range, down to $0.2‰/100m$. Yet the scatter is very large ($R^2 = 0.12$, although only a single mountain range is considered).

[†]The selected GNIP stations, located in the REMO domain, have $\delta^{18}O$ and T_{surf} series without gaps exceeding 6 months over the study period. Out of the 57 GNIP stations analysed for monthly data, only 30 satisfy the criteria for computing a valid yearly mean. Yet, the linear least-square regression does not take into account the spatial inhomogeneity of the selected stations, hence it is questionable whether this station sampling is significant for the temperature effect over Europe.

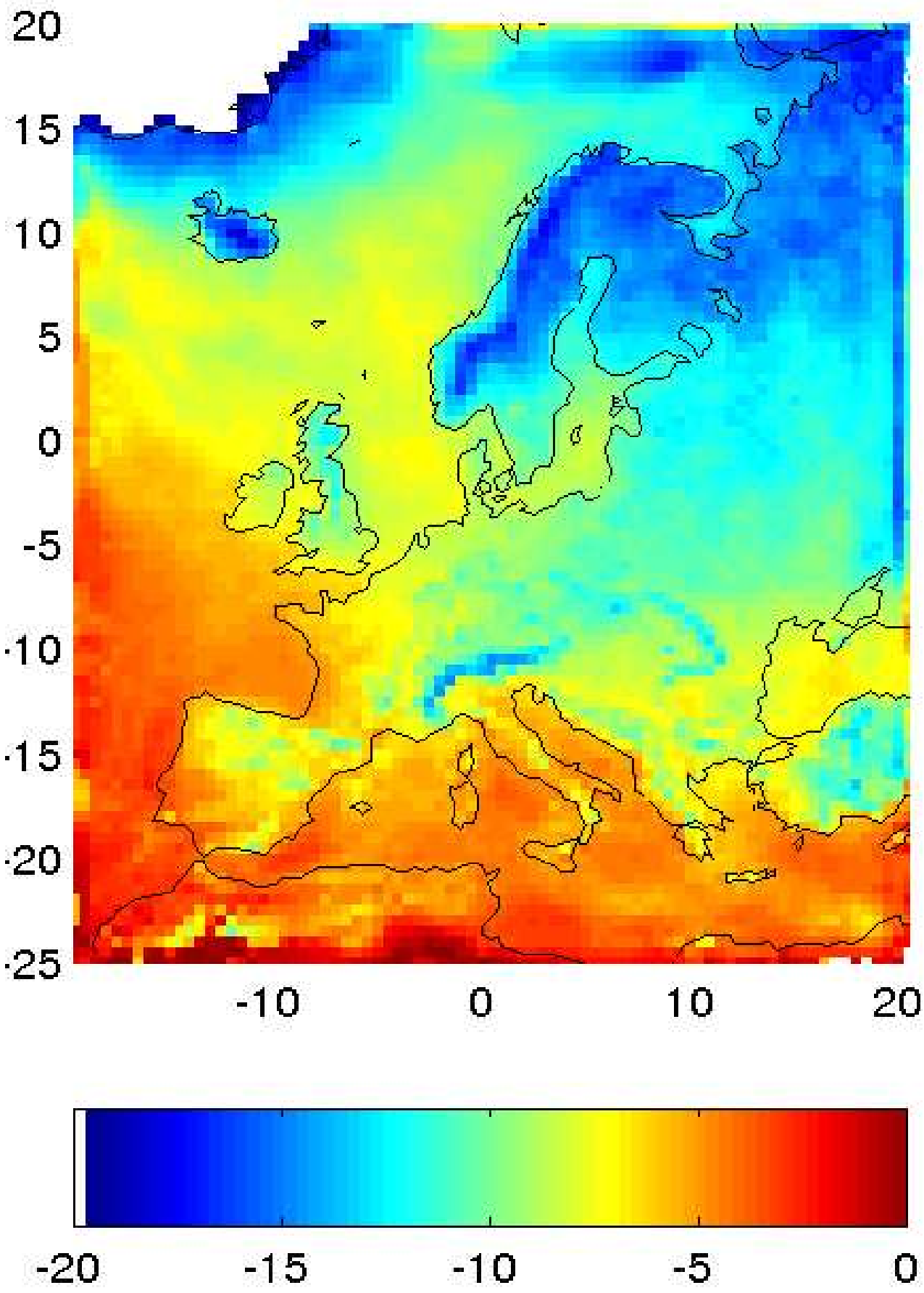

Figure 3.2: Yearly mean $\delta^{18}O$ in $^0/_{00}$ for $REMO_{iso}$, nested inside $ECHAM_{iso}$ boundary conditions. Results in the 8-grid cell boundary buffer zone should be discarded as numerical noise produced by the assimilation scheme.

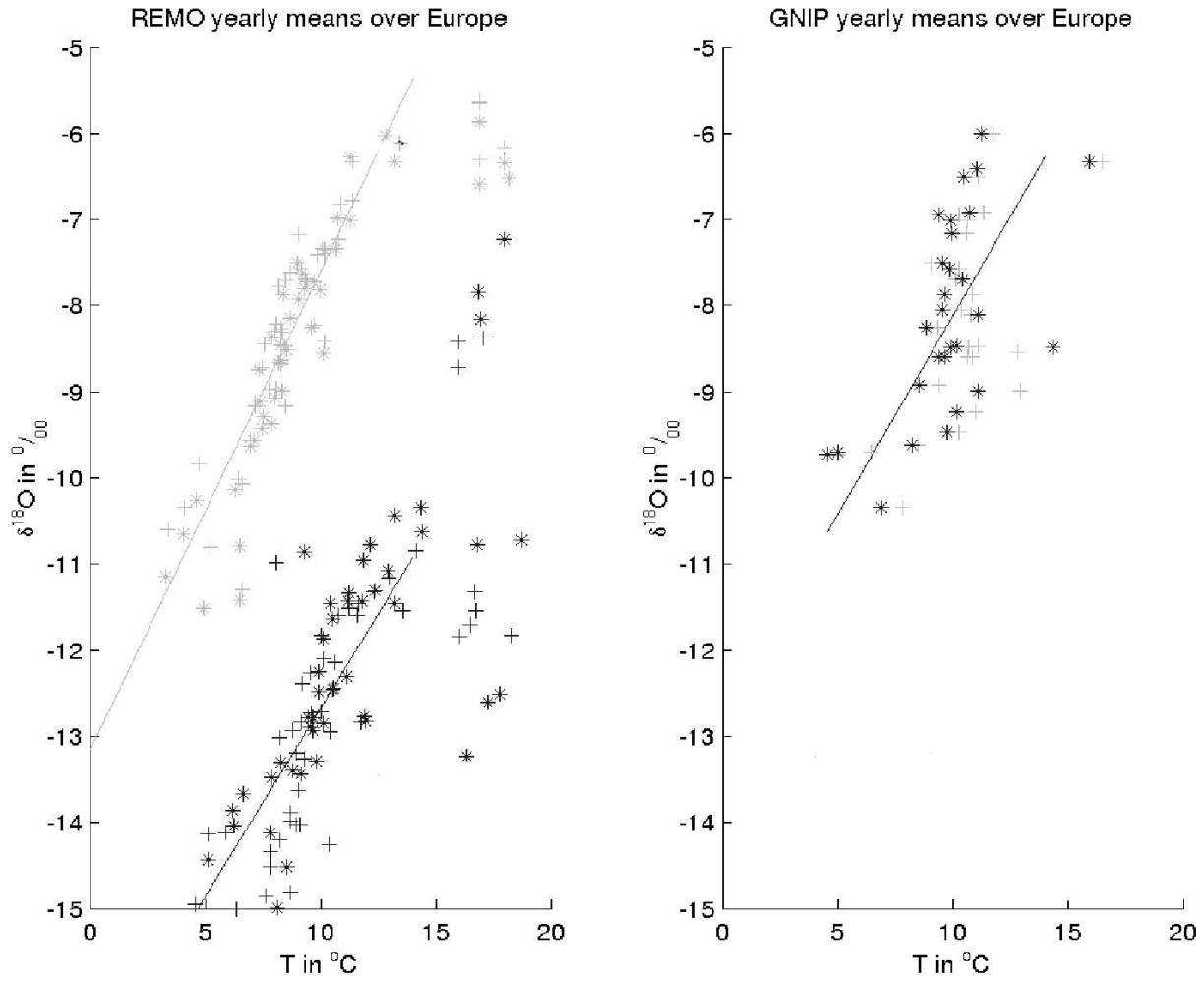

Figure 3.3: Annual correlation between $\delta^{18}O$ and temperature for REMO (left panel) and IAEA-GNIP (right panel) stations. ECMWF (ECHAM) nested REMO is represented as dark (light) grey symbols. Least-square regression for REMO nested in ECMWF (ECHAM): $\overline{\delta^{18}O} = 0.56\,(0.44)\ \overline{T} - 13.2\,(-17.1)\ ^{\circ}/_{\circ\circ}$, with a correlation coefficient of $R = 0.94\,(0.82)$. Least-square regression for IAEA stations : $\overline{\delta^{18}O} = 0.46\ \overline{T} - 12.7\ ^{\circ}/_{\circ\circ}$, with a correlation coefficient of $R = 0.60$.

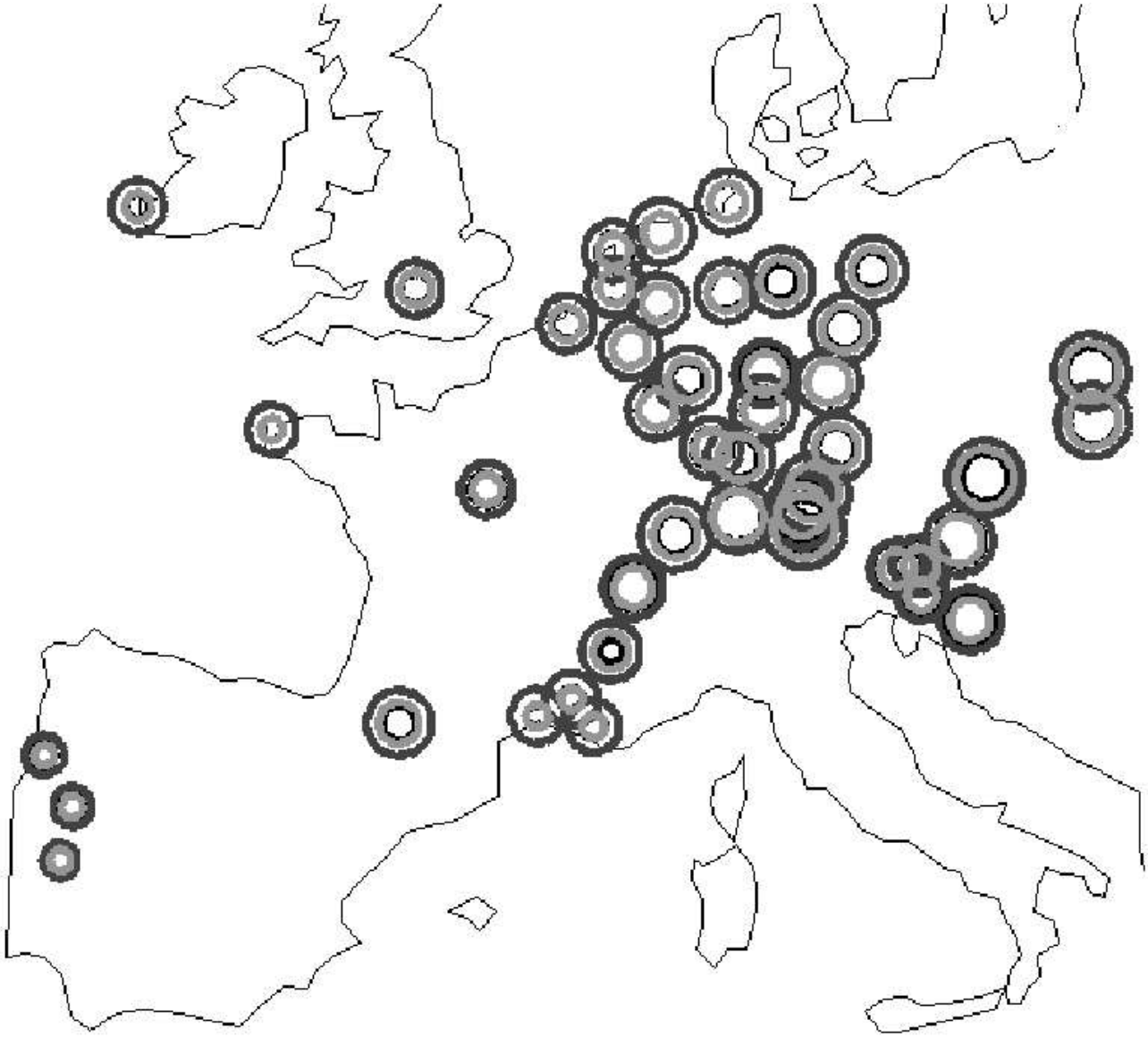

Figure 3.4: Long-term means $\overline{\delta^{18}O}$ as defined in Equation 3.3, for all GNIP station locations. The value at a site is indicated by the circle radius. Black circles stand for GNIP stations, dark grey circles for ECMWF-nested REMO and light grey circles for the ECHAM-nested REMO.

Station name	Longitude (degree)	Latitude (degree)	Altitude GNIP (masl)	Altitude REMO (masl)	$\overline{\delta^{18}O}$ GNIP (‰)	$\overline{\delta^{18}O}$ ECHAM (‰)	$\overline{\delta^{18}O}$ ECMWF (‰)	Precip GNIP (mm)	Precip ECHAM (mm)	Precip ECMWF (mm)
AVIGNON	4.82	43.95	30	0	-4.753	-4.562	-10.66	35.85	48.8	47.43
BAD SALZUFLEN	8.73	52.1	100	173.68	-7.468	-7.971	-11.99	112	89.63	76.3
BEEK	5.78	50.92	111	245.98	-7.442	-7.448	-11.88	128.7	93.12	67.45
BERLIN	13.4	52.47	50	91.98	-7.433	-8.701	-13.13	63.21	54.12	49.13
BRAAKMAN	3.75	51.3	2	25.34	-6.265	-6.715	-11.03	73.97	65.91	66.14
BRAUNSCHWEIG	10.45	52.3	88	191.1	-7.173	-8.763	-13.12	78.9	67.01	61.21
BREST PLOUZANE	-4.57	48.36	80	0	-4.408	-4.596	-9.803	112.3	87.94	88.58
CAMPISTROUS	0.38	43.12	600	1236.86	-7.117	-8.27	-13.06	74.22	79.65	98.78
CARPENTRAS	5.78	44.95	99	647.11	-4.986	-7.362	-11.77	57.8	52.78	38.87
CUXHAVEN	8.72	53.87	12	3.91	-7.125	-7.285	-12.3	86.61	81.37	77.5
DE BILT	5.18	52.1	2	8.35	-6.698	-6.817	-11.38	79.53	70.4	71.79
EMMERICH	6.6	51.83	43	28.6	-7.004	-7.077	-11.39	95.67	78.82	74.21
GARDANNE	5.45	43.45	215	0	-4.797	-4.698	-10.34	30.07	45.04	38.35
GARMISCH-PARTENKIRCHEN	11.07	47.48	720	1881.13	-11.01	-12.46	-16.12	153.8	139.9	120
GRAZ UNIVERSITAT	15.45	47.07	470	677.17	-10.05	-9.54	-13.78	81.3	60.07	68.63
GRONINGEN	6.55	53.23	1	0.91	-7.157	-7.187	-12.59	88.92	88.88	63.68
HOF-HOHENSAAS	11.88	50.32	567	333.76	-8.671	-8.57	-12.66	105.4	76.34	66.42
HOHENPEISSENBERG	11.02	47.8	977	972.17	-11.74	-10.08	-14.55	204.2	163.4	75.13
KARLSRUHE	8.38	49.02	120	210.61	-7.676	-7.262	-11.84	150.2	100.8	57.98
KLAGENFURT FLUG-PLATZ	14.32	46.63	900	244.39	-10.74	-6.976	-11.37	129.9	95.19	70.17
KOBLENZ	7.58	50.35	97	362.06	-7.104	-8.218	-12.71	83.32	58.44	54.88
KONSTANZ	9.18	47.68	447	1165.63	-9.937	-10.21	-13.89	200.9	158.9	62.96
KRAKOW (WOLA JUS-TOWSKA)	19.88	50.07	205	680.07	-10.09	-11.35	-15.04	101.8	72.15	64.71

Table 3.1: Mean $\delta^{18}O$ and precipitation at the GNIP stations.

Station name	Longitude (degree)	Latitude (degree)	Altitude GNIP (masl)	Altitude REMO (masl)	$\overline{\delta^{18}O}$ GNIP (‰)	$\overline{\delta^{18}O}$ ECHAM (‰)	$\overline{\delta^{18}O}$ ECMWF (‰)	Precip GNIP (mm)	Precip ECHAM (mm)	Precip ECMWF (mm)
LEIPZIG	12.43	51.35	125	271.14	-8.217	-9.012	-13.11	75.45	59.82	41.83
LIPTOVSKY MIKULAS-ONDRASOVA	19.73	49.12	570	552.54	-9.979	-10.59	-14.47	67.16	48.33	54.4
LJUBLJANA	14.31	46.04	299	0	-7.878	-6.074	-10.11	108.6	61.04	102.8
MONTPELLIER	3.95	43.57	45	0	-4.54	-4.732	-10.76	42.85	54.97	54.68
NEUHERBERG	11.33	48.15	489	1245.3	-9.708	-10.7	-14.84	154.9	141.5	70.97
ORLEANS-LA-SOURCE	1.9	47.9	109	124.81	-6.637	-6.015	-10.58	75.26	60.51	56
PENHAS DOURADAS	-7.33	40.25	1380	289.37	-6.697	-4.431	-8.051	41.3	74.75	135.3
PORTALEGRE	-7.25	39.17	597	248.32	-4.746	-4.402	-7.218	21.59	39.91	77.18
PORTO	-8.36	41.08	93	132.46	-4.771	-4.054	-8.051	114.7	104.2	126.6
REGENSBURG	12.07	49.02	377	455.4	-8.2	-8.947	-13.22	81.5	71.06	51.88
REYKJAVIK	-21.93	64.13	14	0	-8.717	-9.003	-13.42	83.13	103.1	66.33
STUTTGART (CANNSTATT)	9.2	48.83	315	604.42	-7.946	-8.96	-13.29	102.2	82.69	51.75
THONON-LES-BAINS	6.28	46.22	385	604.29	-8.833	-7.907	-12.14	204.6	150.2	77.88
TRIER	6.7	49.75	273	274.1	-7.658	-7.414	-11.85	105.2	75.36	65.29
VALENTIA (OBSERVA-TORY)	-10.25	51.93	9	0	-5.271	-5.518	-10.58	116.6	109.3	134.2
VIENNA (HOHE WARTE)	16.37	48.25	203	708.32	-9.618	-11.56	-14.9	66	56.14	65.73
VILLACHER ALPE	13.67	46.6	2135	119.19	-10.62	-7.108	-11.23	117	84.75	103
WALLINGFORD	-1.1	51.6	48	63.05	-6.158	-6.704	-10.84	73.9	65.79	52.63
WASSERKUPPE RHOEN	9.95	50.5	921	262.47	-9.708	-8.178	-12.56	87.2	65.82	98.54
WEIL AM RHEIN	7.4	47.3	249	841.64	-8.271	-9.362	-14.03	127.6	98.5	62.04
WIERINGERWERF	5.05	52.8	-4	0	-6.784	-6.499	-11.73	77.29	77.54	61.63
WUERZBURG	9.9	49.8	259	329.88	-8.454	-8.091	-12.74	82.88	64.85	46.88
ZAGREB	15.59	45.49	165	635.18	-9.399	-8.034	-12.61	82.21	59.5	75.11
Average					-7.73	-7.73	-12.15	96.47	81.27	71.59

Table 3.2: Table 3.1 continued...

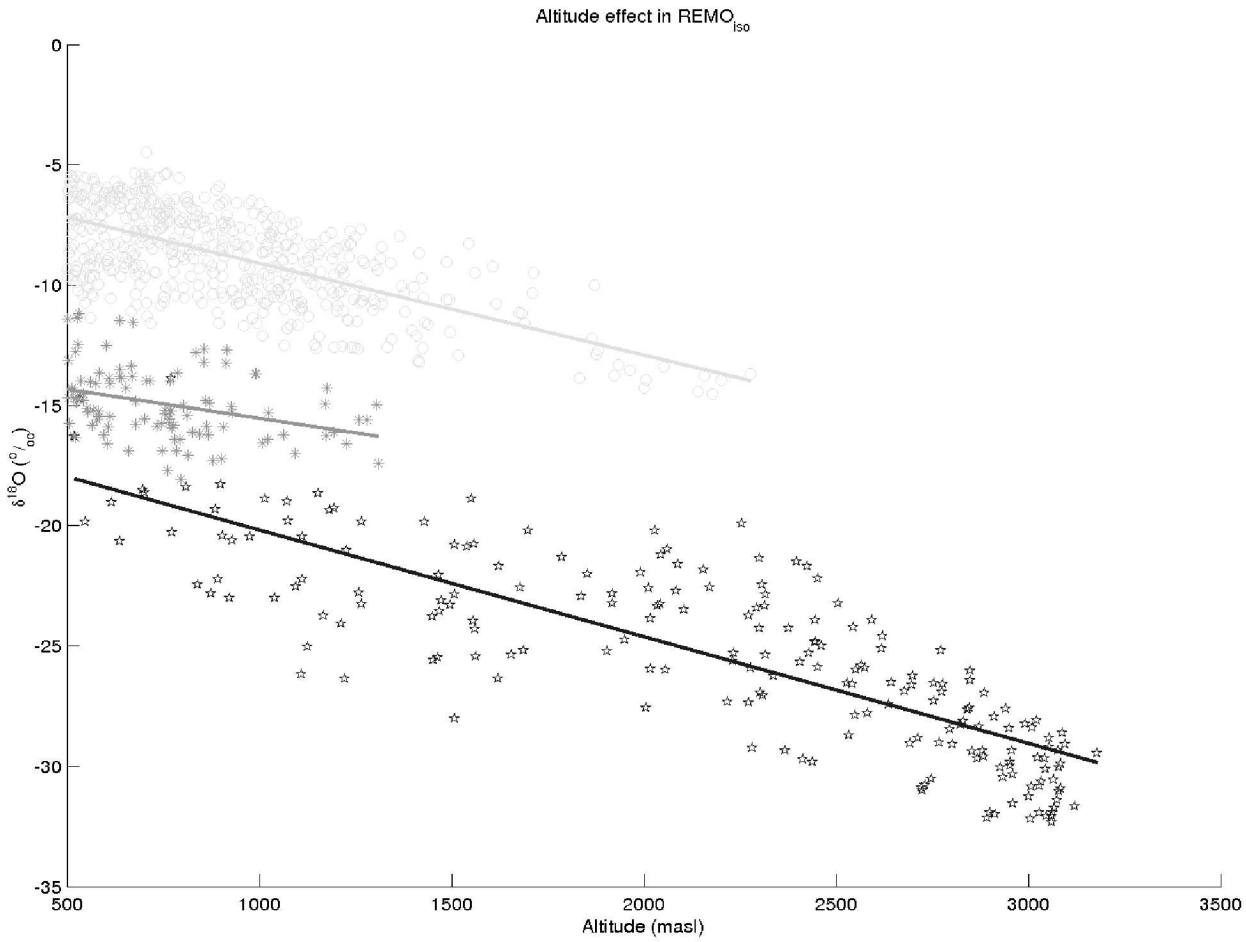

Figure 3.5: Variation of $\delta^{18}O$ with altitude over the entire model domain, for the ECHAM-nested REMO simulation. Black pentograms stand for Greenland, with a $\delta^{18}O = -4.43\ 10^{-3} \cdot h - 15.8\,‰$ and a $R^2 = 0.691$. Dark grey stars stand for the Scandinavian mountain range, with a $\delta^{18}O = -2.39\ 10^{-3} \cdot h - 13.1\,‰$ and a $R^2 = 0.116$. Light grey circles stand for central Europe massifs, with a $\delta^{18}O = -3.82\ 10^{-3} \cdot h - 5.27\,‰$ and a $R^2 = 0.421$.

Relating to Figure 3.2, we suggest that the higher $\delta^{18}O$ values correspond to the windward mountain side, with a similar vertical gradient around $0.4\,‰/100m$. On the lee side, the vertical rain-out rate is less pronounced, and the continental effect dominates. Hence, the altitude effect is not as pronounced in the more depleted values. Further information on the altitude effect is gained from model-measurement comparisons at higher time resolution, as discussed in the next sections.

Thirdly, the *continental effect* appears clearly in Figure 3.2, with a continuous decrease in mean precipitation $\delta^{18}O$ from the Atlantic coast land-inwards to the central European lowlands. The difference in the REMO results matches well the $-7\,‰$ difference mentioned in Section 3.1.1. The continental effect is further marked by a clearly defined seasonal behaviour, being more pronounced in winter than in summer. This aspect will be addressed in the next section. Finally, a notable difference in precipitation $\delta^{18}O$ values appears on Figure 3.2 between the continent and the ocean. This points out the importance of soil-atmosphere processes on the isotopic re-equilibration of falling rain drops with the surrounding moisture. Since all GNIP stations are located on land, no experimental evidence was available to this study for validating the isotopic signal of land versus sea precipitation as simulated by REMO$_{iso}$.

In conclusion, the annual average of precipitation $\delta^{18}O$ in the ECHAM-nested simulation agrees well with the GNIP dataset at all but two stations, whereas the ECMWF-nested one, although representing correctly temperature, altitude and continental gradients, has a generalised negative bias of $-4.5\,‰$. In the following section, the model's output is further analysed on monthly time-scale.

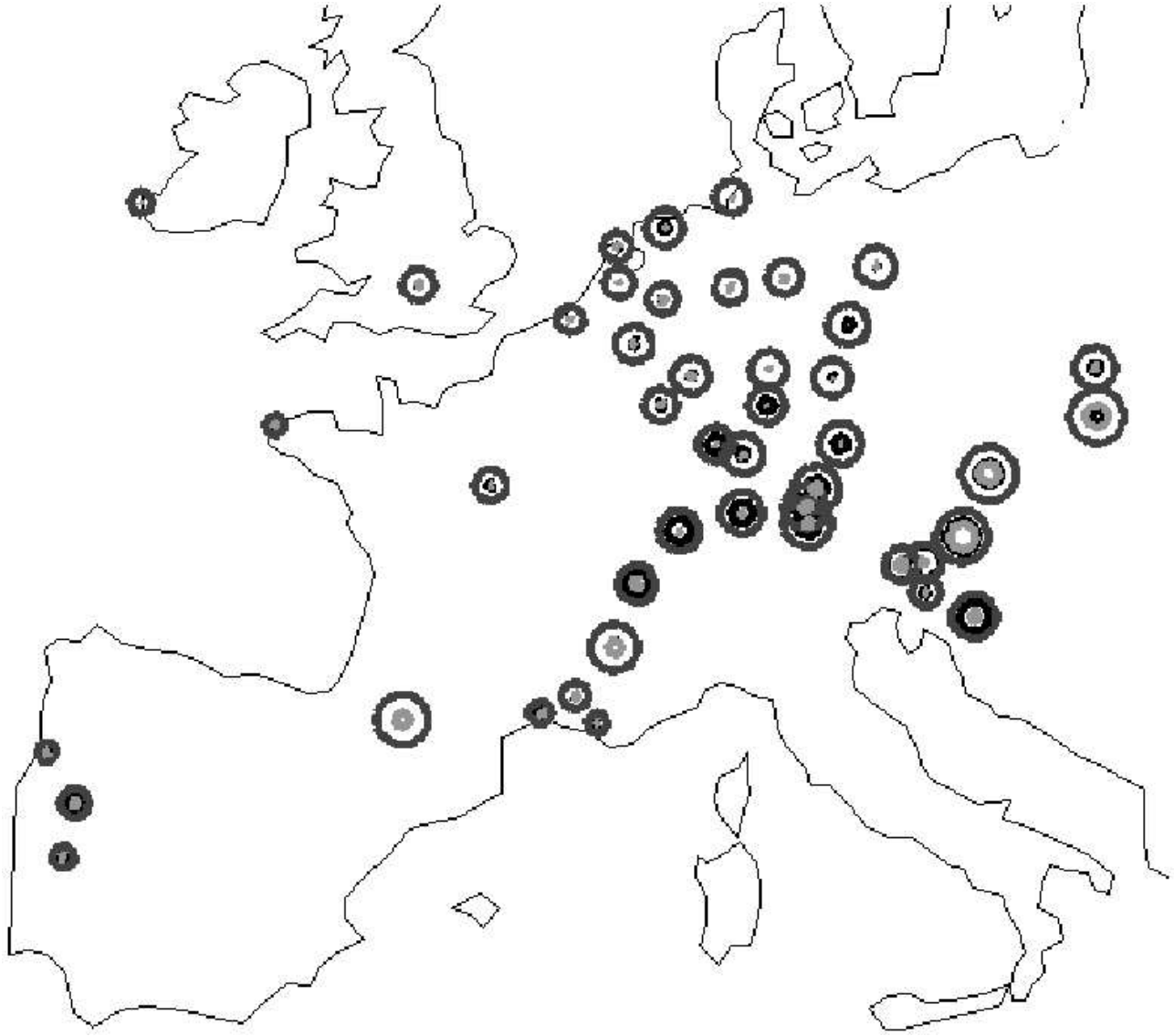

Figure 3.6: Seasonal amplitude A as defined in Equation 3.3, at all GNIP station locations. The colour legends are equivalent to Figure 3.4: Black stands for GNIP, light grey for ECHAM-nested REMO and dark grey for ECMWF-nested REMO.

3.3.2 Monthly time series at GNIP-IAEA stations

The output of REMO simulations are tested against monthly GNIP data. Over the experiment period (March 1997 - February 1999), 57 GNIP stations were in operation inside the study domain, as defined in Figure 3.1.

Figure 3.6 displays the seasonal amplitude A of $\delta^{18}O$ in precipitation, as obtained from Equation 3.3. As expected from temperature variations, the seasonal amplitude in observed precipitation $\delta^{18}O$ increases with distance from the coast and with altitude. The average seasonal amplitude for all stations is $1.23\,‰$ for GNIP data, $0.63\,‰$ for the ECHAM-nested run and $3.56\,‰$ for the ECMWF-nested run. The tendency of increasing amplitude with continentality and altitude is well reproduced by REMO$_{iso}$, although the seasonal amplitude is over-estimated by a factor 2 in the ECMWF-nested run, and under-estimated by a factor 2 in the ECHAM-nested run.

In Figure 3.7, a 2-year record of $\delta^{18}O$ and precipitation amounts is plotted for two stations. Graz University is representative of most mountain stations, with a strong seasonality in both $\delta^{18}O$ and precipitation amounts. The seasonal amplitude A for GNIP/ ECHAM-nested/ ECMWF-nested datasets is respectively $3.26/2.57/5.17\,‰$. The ECHAM-nested run hence shows a good agreement with GNIP data for both $\overline{\delta^{18}O}$ and A, with slightly too enriched $\delta^{18}O$ values

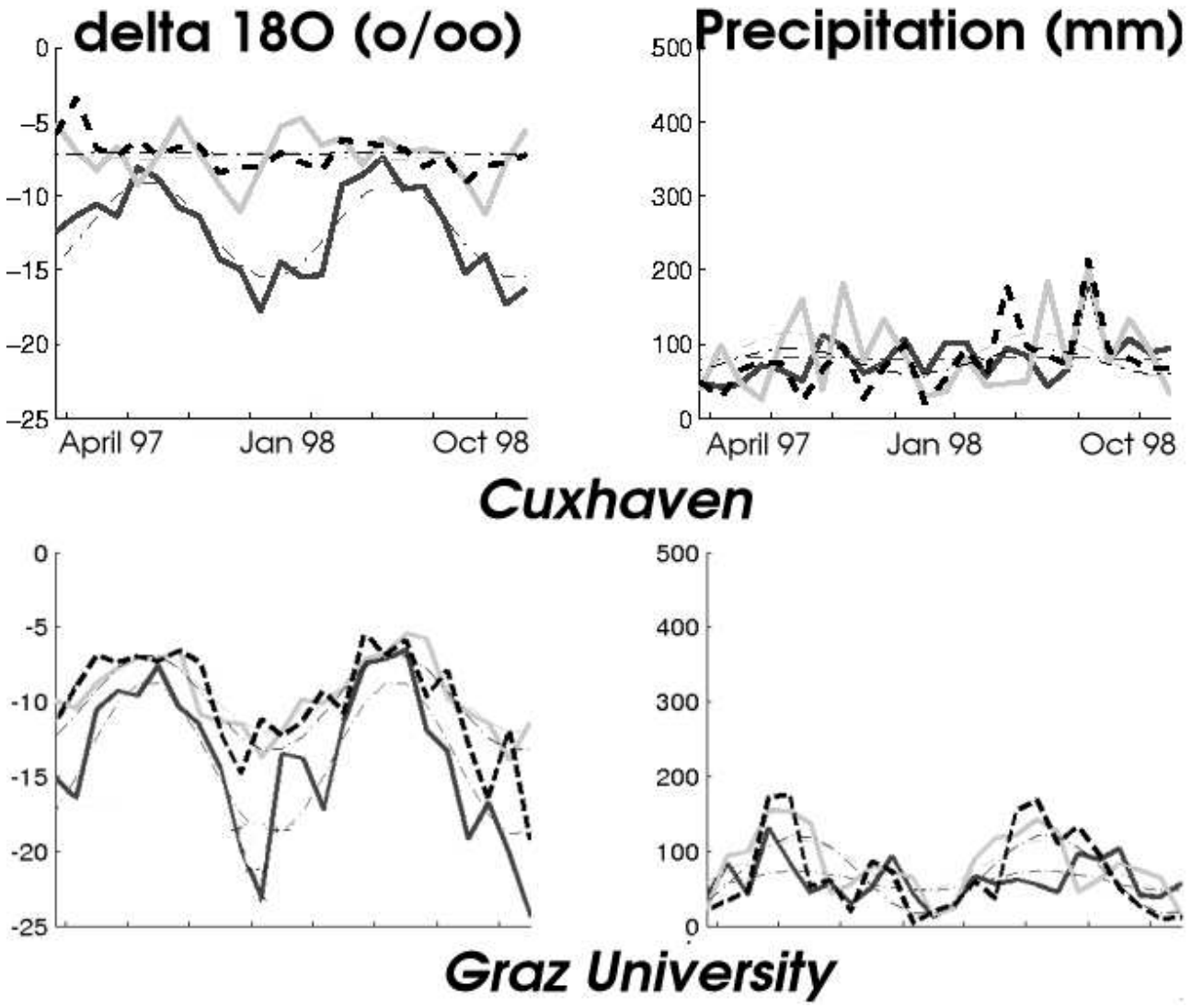

Figure 3.7: $\delta^{18}O$ and total precipitation amounts at Cuxhaven [8.72, 53.87, 12] and Graz University [15.45, 47.07, 470]. Observations are in black (thick dashed line), ECHAM-nested REMO run in light grey and ECMWF-nested REMO in dark grey. The best-fit sinusoidal function, according to Equation 3.3, is plotted in the same colour as a dotted line.

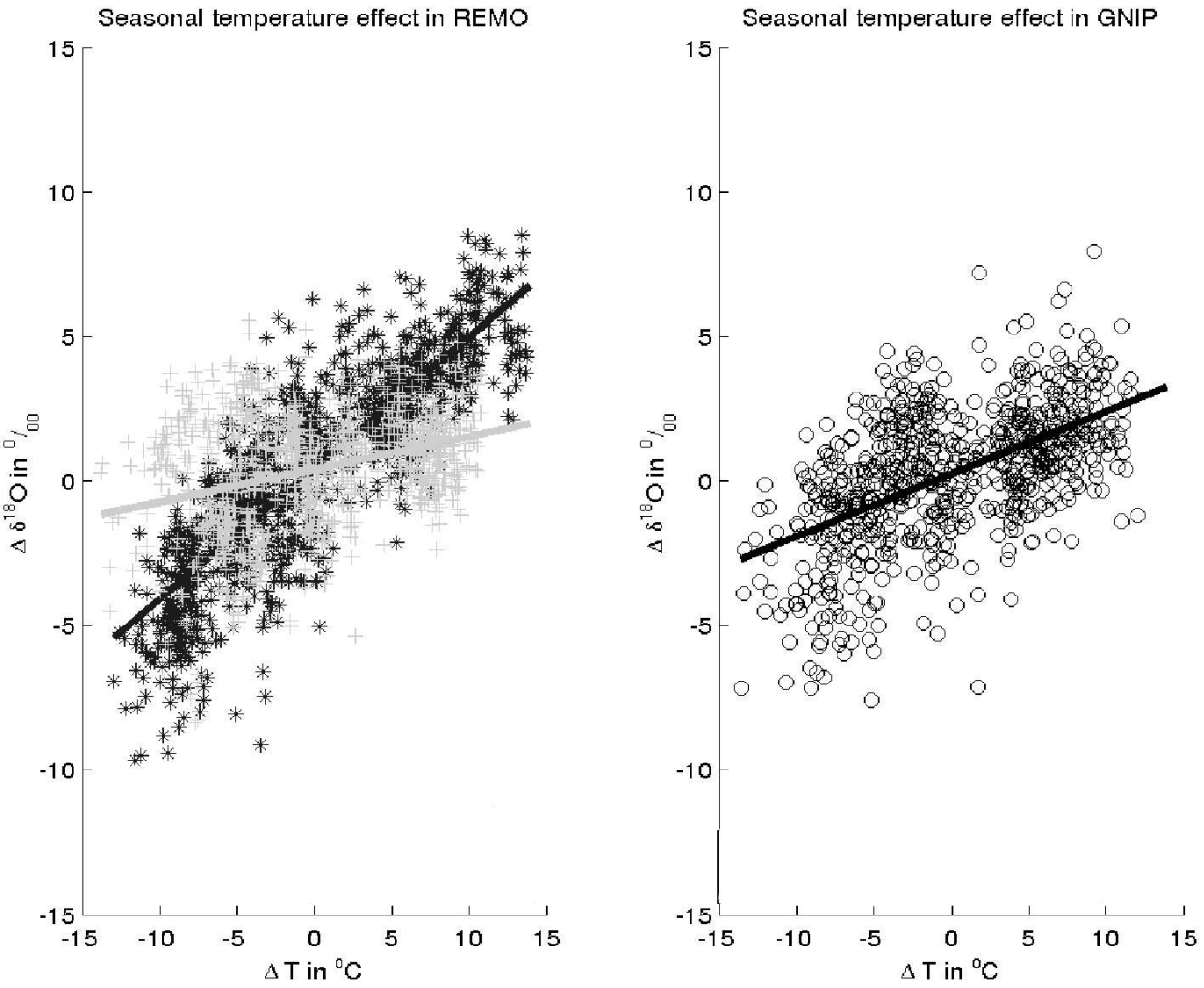

Figure 3.8: Seasonal correlation between δ^{18}O in precipitation and temperature for REMO (left panel) and IAEA-GNIP (right panel) stations. ECHAM-nested REMO is plotted in light grey, ECMWF-plotted REMO in dark grey, GNIP in black. The deviation of monthly values from yearly means for δ^{18}O, noted $\Delta\delta^{18}$O, are plotted against the equivalent for temperature, noted ΔT. Least-square regression for REMO : $\Delta\delta^{18}\mathrm{O} = 0.11\,(0.45)\ \Delta T + 0.41\,(0.45)\ ‰$, with a correlation coefficient $R = 0.33\,(0.84)$. Least-square regression for IAEA-GNIP stations : $\Delta\delta^{18}\mathrm{O} = 0.22\ \Delta T + 0.25\ ‰$, with a correlation coefficient $R = 0.55$.

in winter, causing a lesser amplitude value. On the other hand, the ECMWF-nested run has an overall underestimation of δ^{18}O values, reaching up to $-10\,‰$ in winter but usually less than $-3\,‰$ during summer, resulting in exaggerated seasonality. Cuxhaven stands for coastal stations, without any distinct seasonality neither in δ^{18}O nor in total precipitation. The δ^{18}O values in the GNIP record mainly oscillates around a mean at $-7.01\,‰$ with an amplitude of $0.57\,‰$. This behaviour is well reproduced by the ECHAM-nested run, with a $\overline{\delta^{18}\mathrm{O}}$ of $-7.08\,‰$ and an A of $-0.58\,‰$. The different sign for the fitted amplitude parameter has no real significance, due to the absence of clear seasonality. The ECMWF-nested run simulates a strong seasonality ($A = 3.03\,‰$), resulting in a gross underestimation of the mean value ($\Delta\overline{\delta^{18}\mathrm{O}} = -4.4‰$). It is yet worth noticing that the differences in $\overline{\delta^{18}\mathrm{O}}$ and A between the mountain and stations are very similar for all three datasets. The mean value decreases from Cuxhaven to Graz by $2.4\,‰$ for both REMO runs versus $3.0\,‰$ for GNIP, and the seasonality increases respectively by $2.1\,‰$ versus $2.6\,‰$. The statement is valid for most other stations: REMO reproduces qualitatively both the spatial and temporal gradients of the δ^{18}O signal, but these trends are weaker than what is observed in the GNIP data-set.

Finally, the seasonal temperature effect is investigated with the available data, according to the method exposed in

[Rozanski et al., 1993]. Instead of plotting the absolute values of $\delta^{18}O$ against those of temperature (causing enormous scattering), the difference for each station between the monthly values and the annual mean is plotted for both parameters . The scatter-plot, as well as the regression lines, are shown on Figure 3.8. The slope of the linear regression for the GNIP monthly data, $\frac{\Delta\delta^{18}O}{\Delta T} = 0.22\,‰\cdot{}^{0}C^{-1}$, is similar to gradient reported by [Rozanski et al., 1993]. The slope coefficient for the ECMWF-nested run is higher by a factor of 2 (at $\frac{\Delta\delta^{18}O}{\Delta T} = 0.45\,‰\cdot{}^{0}C^{-1}$) whereas that of the ECHAM-nested run is lower by a factor 2 (at $\frac{\Delta\delta^{18}O}{\Delta T} = 0.11\,‰\cdot{}^{0}C^{-1}$). In accordance with conclusions from Figure 3.6, the stronger (weaker) slope for the ECMWF (ECHAM)-nested run as compared to GNIP show the higher (lower) dependency of $\delta^{18}O$ to temperature. This is further highlighted by the correlation coefficient for the ECMWF (ECHAM)-nested run, which is significantly higher (lower) than for the GNIP measurements (respectively $R = 0.84/0.33/0.55$).

Figure 3.9 displays the mean annual, summer and winter $\delta^{18}O$ against the longitudinal distance from the coast for all GNIP stations included in the study domain and period. Here we only focus on the slope of the regression lines, since the shift in absolute $\delta^{18}O$ values relates primarily to their dependence on temperature. As mentioned in section 3.1.1, the continental effect in winter is about 4 times stronger than in summer, which is consistent with the slopes obtained in Figure 3.9 for GNIP data. Although being limited to stations included in the study domain and period, the continental gradient computed from the GNIP data agrees well with more robust statistical evidence from [Rozanski et al., 1993] : the winter/annual/summer gradients for the selected stations are equal to $\frac{\Delta\delta^{18}O_s}{\Delta\lambda} = -3.27/-2.15/-1.04\,‰\cdot(1000km)^{-1}$. Both the ECHAM- (respectively $\frac{\Delta\delta^{18}O_s}{\Delta\lambda} = -2.96/-1.98/-1.00\,‰\cdot(1000km)^{-1}$) and the ECMWF-nested runs (respectively $\frac{\Delta\delta^{18}O_s}{\Delta\lambda} = -2.91/-1.85/-0.782\,‰\cdot(1000km)^{-1}$) show similar features, which truly identifies physical processes inside the study domain (independently from boundary conditions). As compared to GNIP observations, the continental gradient agrees well but the winter gradient is underestimated by 10%.

In conclusion, the analysis of monthly $\delta^{18}O$ and temperature values over a large number of stations enables to discriminate between misfits related to inappropriate boundary conditions on one hand, and to $REMO_{iso}$ physical parameterisation on the other hand. The ECMWF-nested run displays a general offset of $-4.5\,‰$, with a stronger bias during winter and a too high dependency on temperature; this can clearly be linked to the T-dependent Dansgaard parameterisation of the isotopic boundary conditions. The ECHAM-nested run, albeit representing climatological conditions, is much closer to the GNIP 1997-1999 dataset: it does not display any generalised, boundary induced bias on a yearly basis. The monthly dependency of the $\delta^{18}O$ signal to temperature is yet too weak, which would point to a similar underestimation in the host model ECHAM. Nevertheless as revealed by very similar gradients in both simulations, REMO fails to reproduce the continental and altitude effects in their observed extent, with less depleted results in winter.

3.3.3 Precipitation event records at GSF stations

The record of single precipitation amount and their $\delta^{18}O$ at the Nordeney, Arkona and Hohenpeissenberg stations represent a unique data-set to investigate the short time variability of precipitation $\delta^{18}O$. From their geographic characteristics, the two coastal and one mountain stations are representative of varyingly maritime to continental/altitude influenced climatic situations. The sampling procedure for the high resolution stations Nordeney, Arkona and Hohenpeissenberg is as follows. Daily precipitation is sampled by the German weather service (Deutscher Wetterdienst, DWD) and sent to the GSF. The $H_2^{18}O$ isotopic composition of the precipitation samples is measured with standard CO_2 equilibration techniques.

On Figure 3.10, the $\delta^{18}O$ measurements are displayed as black crosses and their one-month running mean as the black line , while the monthly accumulated precipitation amounts are displayed as black bars. Similarly, modelled $\delta^{18}O$ values are depicted as green stars for the ECMWF-nested run (red for the ECHAM-nested one), with the one-month running mean line and cumulated precipitation bars in the same colour. The model values are areal means from the 50x50km grid cell comprising the station's location, without any further downscaling diagnostics.

In these experiments, REMO is running in a climate mode: apart from initialisation, it is constrained by the host model (either ECMWF or ECHAM) only in the buffer zone. It is not meant to reproduce a given meteorology situation by assimilating atmosphere observations (as in the forecast mode). Accordingly, the modelled precipitation cannot correspond to observed daily precipitation. In other words, the inherent variability in daily precipitation generated by

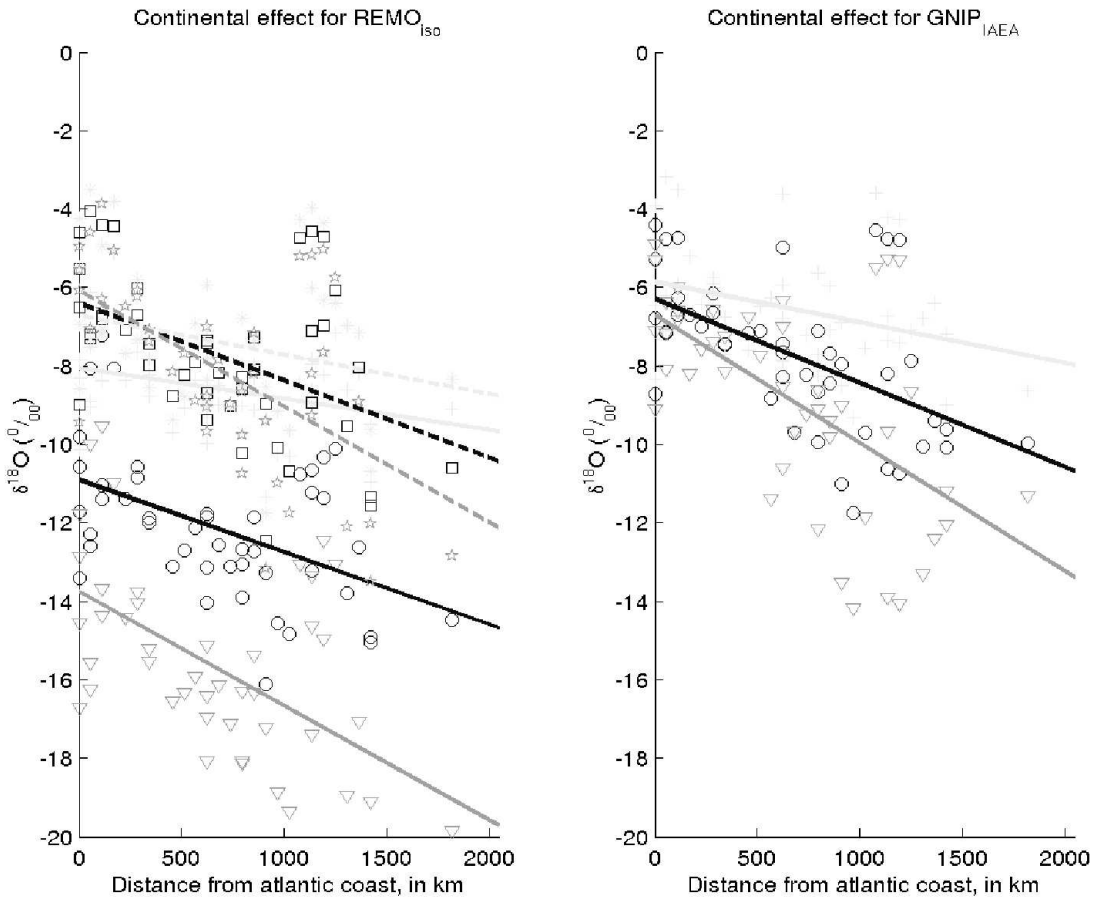

Figure 3.9: Annual (black), summer (light grey) and winter (dark grey) mean $\delta^{18}O$ are plotted as a function of the longitudinal distance to the Atlantic coast, for REMO (left panel) and GNIP (right panel). The longitudinal distance λ is expressed as the distance between the station and the nearest point on the Atlantic coast at the same latitude, reflecting the mean trajectory of air masses over Europe. The seasonal variations are computed with the seasonal amplitude factors as in Equation 3.3. Linear regression yields following values for the continental gradient : for GNIP/control run/sensitivity test respectively, $\frac{\Delta\delta^{18}O_a}{\Delta\lambda} = -2.15\ /\ -1.97\ /\ -1.85\ ‰\ \cdot\ (1000km)^{-1}$, with an offset of $-6.25\,/\,-6.40\,/\,-10.9‰$ in annual mean, $\frac{\Delta\delta^{18}O_s}{\Delta\lambda} = -1.04\ /\ -1.00\ /\ -0.078\ ‰ \cdot (1000km)^{-1}$ with an offset of$-5.85\ /\ -6.70\ /\ -8.06‰$ in summer, $\frac{\Delta\delta^{18}O_w}{\Delta\lambda} = -3.27\ /\ -2.96\ /\ -2.91\ ‰ \cdot (1000km)^{-1}$ with an offset of $-6.71\ /\ -6.08\ /\ -13.8‰$ in winter.

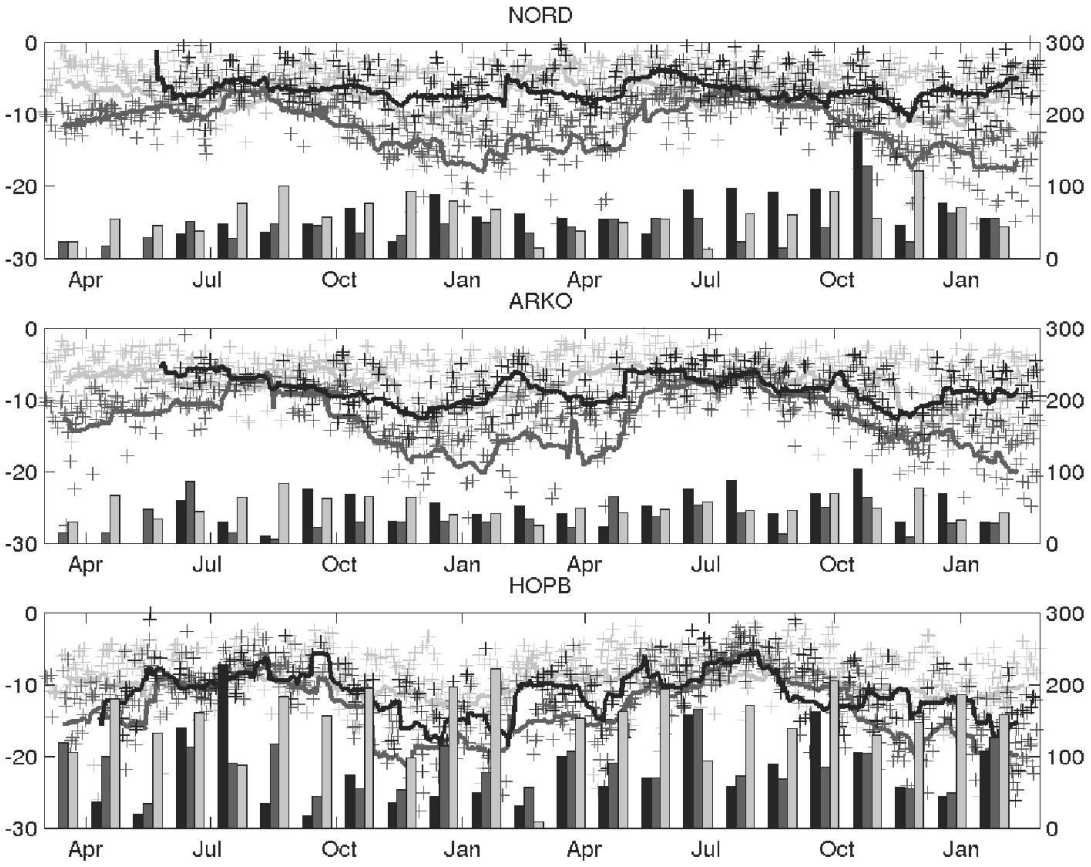

Figure 3.10: Comparison of daily precipitation and $\delta^{18}O$ for GSF stations Nordeney (7.09°E, 53.43°N, 16m, upper row), Arkona (13.26°E,54.41°N, 41m, middle row) and Hohenpeissenberg (11.02°E, 47.80°N, 977m, lower row). The ECHAM-forced REMO run is plotted in light grey, the ECMWF-forced one in dark grey and GSF observations in black, with their respective 30-days moving average.

REMO is so large that 'realistic' boundary conditions (i.e. the ECMWF-nested run) hardly improves the daily simulated precipitation amounts, as compared to 'climatological' boundary conditions (i.e. the ECHAM-nested run). Hence, no day-to-day comparison can be made between the REMO simulations and the GSF data-sets; thereafter, we present the analysis of long-term parameters taken from daily series. The mean $\delta^{18}O$ and its seasonal amplitude *A* is computed from the daily record according to Equation 3.3. The stochastic behaviour of daily precipitation is represented by the standard deviation σ between the actual daily measurements and the sine fitting is defined in Equation 3.4.

$$\sigma = \sqrt{\sum \left(\delta^{18}O_i - \left(A \cdot sin\left(\frac{(t_i - \tau) \cdot 2\pi}{\mathcal{T}} \right) + \overline{\delta^{18}O} \right) \right)^2} \tag{3.4}$$

Nordeney is located (7.09°E, 53.43°N, 16m) on an East-Friesland island, off the German coast of the North Sea. Over the 2-year study period, the daily $\delta^{18}O$ in precipitation shows hardly any seasonality, being nearly constant at $-5.72\,‰$. The daily scatter ($\sigma = 2.79\,‰$) is much larger than the seasonal amplitude ($A = 0.84\,‰$). This stationary behaviour is typical for a pure maritime climate, with air moisture directly originating from the Atlantic Ocean, similar to GNIP coastal stations such as Braakman (NL), Brest (F), Cuxhaven (D), De Bilt (NL), Emmerich (D), Valentia Observatory (IRL), Wieringerwerf (NL).

The daily $\delta^{18}O$ as simulated in the ECHAM-nested run are very similar to measured values: it oscillates around $-6.04\,‰$, with no seasonality ($A = 0.79\,‰$) but even higher scattering than the GSF dataset ($\sigma = 4.03\,‰$). The ECMWF-nested run shows the typical underestimation of the mean value at coastal stations, with an exaggerated seasonality ($A = 3.76\,‰$), but a similar scattering as the observations ($\sigma = 2.86\,‰$) . In late summer, modelled values agree well with observations, but $\delta^{18}O$ are largely underestimated throughout the rest of the year, which results in a mean annual $\delta^{18}O$ of $-11.2\,‰$. The running mean is less smooth than observations, with 'bumps' up to $-3\,‰$ over a few days. This indicates that the model is inaccurately sensitive to synoptic perturbations.

Arkona is located (13.26°E, 54.41°N, 41m) on the island of Rügen, off the German coast of the Baltic Sea. The running mean in the observations shows a weak seasonality with an amplitude of $1.44\,‰$ around the mean value at $-7.89\,‰$. The scatter in daily values remains equivalent to Nordeney at $\sigma = 2.75\,‰$. The seasonality can be explained by a less maritime climate at Arkona : although situated at the coast, air masses are influenced both by the Danish peninsula to the West and Scandinavia to the North.

The ECHAM-nested run does not differ significantly from observations, although it does not capture the increase in continentality from Nordeney to Arkona. Hence, the mean $\delta^{18}O$ is higher ($-6.68\,‰$) and the seasonal amplitude lower ($1.07\,‰$) than observed. In opposition to the two other datasets, the daily scatter is reduced between Nordeney and Arkona ($\sigma = 3.48\,‰$). As for Nordeney, the ECMWF-nested run underestimates $\delta^{18}O$ in all but late summer months, resulting in a very low mean annual value of $-12.0\,‰$. The seasonal amplitude of $4.04\,‰$ is stronger than at Nordeney as in the observations. However it is still overestimated. The scatter of simulated daily $\delta^{18}O$ increases with regard to Nordeney ($\sigma = 3.89\,‰$). [‡] We can further look at the differences, for each data-sets, between Nordeney and Arkona. Both simulations display a similar limited continental effect from Nordeney to Arkona, with mean lowered by $-0.8\,‰$ and seasonality increased by $0.3\,‰$. These parameters are slightly lower than in the observations (respectively $-2.1\,‰$ and $0.6\,‰$).

Hohenpeissenberg is located (11.02°E, 47.80°N, 977m) on the Northern foothills of the German Alps. The seasonality in observations is strong, with an amplitude of $3.27\,‰$ and a mean of $-10.8\,‰$. The daily scatter is higher than at coastal stations ($\sigma = 3.84\,‰$). The behaviour is typical for continental, mountain climate and is similar to GNIP station records at Graz (A), Klagenfurt (A), Konstanz (D/CH), Thonon-les-Bains (F), Villacher Alpe (A) or Zagreb (CRO).

The ECHAM-nested run largely underestimates the continentality and altitude effect at Hohenpeissenberg, resulting in an overestimated average ($-8.82\,‰$) and an underestimated seasonal amplitude ($1.62\,‰$). In agreement with the observations, the daily variability increases compared to coastal stations up to $3.80\,‰$. Here the ECMWF-nested run is closer to observations, with a mean at $-12.6\,‰$ and a seasonal amplitude at $5.16\,‰$. However it mostly reflects the com-

[‡] Daily scatter of precipitation $\delta^{18}O$ is significantly larger during winter than any other season. In fact, snow precipitation does not partially equilibrate with surrounding moisture by re-evaporation (as does rain), and reproduces thus the isotopic variability in clouds unaltered.

bination of the exaggerated seasonality at its boundaries and the underestimated continental and/or altitude effect in the REMO domain. The scatter too increases to $4.05\,‰$ as compared to its coastal values. As for Arkona, the differences in mean value (respectively $-2.8/-1.1\,‰$) and seasonal amplitude (respectively $0.9/1.4‰$) between Hohenpeissenberg and Nordeney lie largely under the observed parameters ($\Delta\overline{\delta^{18}O} = -5.0\,‰$ and $\Delta\sigma = 2.4\,‰$). As stated from monthly GNIP results, REMO performs better at other mountain stations than Hohenpeissenberg, possibly because of sub-grid topography effects not well accounted for in the model in that particular grid-cell.

In conclusion, the daily results at the GSF sampling sites Nordeney, Arkona and Hohenpeissenberg confirm previous remarks on monthly GNIP records. The ECHAM-nested run is physically more consistent, and in fact closer to $\delta^{18}O$ measurements than the ECMWF-nested one. Furthermore REMO reproduces correctly in both setups the tendencies related to isotopic effects, but fails to simulate their magnitude on an annual and seasonal level. Finally, the inter-diurnal variability of $\delta^{18}O$ in precipitation is larger than its seasonal variability, and increases with altitude and/or continentality.

In this case study, REMO is used in a climate mode, as opposed to forecast mode. It means that the model evolves freely and diverges almost certainly from observed meteorological conditions, even when nested in ECMWF-reanalyses. A more detailed analysis of the daily signal in the frequency domain, using Fourier transforms and cross-histograms for $\delta^{18}O$, precipitation and temperature, will be presented in a specific article, taking better into account the stochastic behaviour of precipitation. Nevertheless, the good agreement in daily variability and frequency distribution between REMO$_{iso}$ and observations constitutes a more robust validation of the isotopic physical scheme than on the usually performed monthly basis.

3.4 Conclusions and outlooks

3.4.1 Summary of REMO$_{iso}$ performances

The present article introduces REMO$_{iso}$, the first regional circulation model including the stable water isotope cycle, and its validation over Europe. Special attention is paid to the sensitivity of REMO$_{iso}$ results to the boundary conditions. The mean residence time of a water molecule in the atmosphere ranges from 8 to 10 days, whereas depressions swift over the whole study domain in only 3-4 days; therefore boundary conditions are a crucial issue to regional models.

Two experimental settings are tested: the RCM is nested either in the ECHAM4$_{iso}$ GCM, or in the ECMWF analyses. On one hand, REMO$_{iso}$ uses as boundary conditions atmospheric (pressure, wind speed, liquid and vapour water content) variables and their isotopic counterparts from ECHAM$_{iso}$, a general circulation model including the stable water isotope cycle. Thus the isotopic signature of air-masses entering the model domain is physically consistent with the meteorological boundary conditions. However, the simulation has no strong connection with the actual synoptic situations of the years 1997-1999 since mid-latitude weather is weakly controlled by sea surface temperatures. On the other hand, REMO$_{iso}$ assimilates at its boundaries the best approximate of 1997-1999 meteorology from the ECMWF analyses, parameterising the isotopic composition with help of the Dansgaard $\delta^{18}O$-temperature relation (cf. Equation 3.1). The physical basis underlying this approach is highly questionable, since the Dansgaard relation was established for mean annual values in precipitation, but has been used here for water vapour on the entire atmospheric column on a 5 minute time-step.

In both runs, the gridded output shows on Figure 3.2 a high-resolution signal of $\delta^{18}O$ in precipitation, reproducing qualitatively the major isotopic effects: temperature, continental and altitude effects. The simulated $\delta^{18}O$ in precipitation is highly dependent on the boundary dataset, at annual, seasonal to event time-scales. The mean annual values of $\delta^{18}O$ are globally well reproduced by the ECHAM-nested run (cf. Figures 3.3 and 3.4), whereas the ECMWF-nested run has a generalised offset of $-4.5\,‰$. The same observation holds at the monthly time-scale. For most stations, the seasonal amplitude (as defined in Equation 3.3) in the ECHAM-nested run agrees reasonably well with observations on Figure 3.6. However, the seasonal amplitude is often underestimated. This is confirmed by the underestimated seasonal $\delta^{18}O$-T regression coefficient on Figure 3.8, and reflects an underestimation of the seasonal contrast in the ECHAM$_{iso}$ model over Europe. On the whole, the ECHAM$_{iso}$ boundary conditions appear as being better suited than ECMWF with T-dependent parameterisation. The ECMWF-nested run displays a systematic exaggeration of the seasonal amplitude over

Data set	$\overline{\delta^{18}O}$	A	σ
Nordeney			
GSF	-5.724	0.836	2.788
ECHAM nested	-6.041	0.789	4.026
ECMWF nested	-11.155	3.757	2.855
Arkona			
GSF	-7.887	1.443	2.752
ECHAM nested	-6.680	1.074	3.481
ECMWF nested	-12.017	4.040	3.885
Hohenpeissenberg			
GSF	-10.760	3.266	3.836
ECHAM nested	-8.823	1.622	3.802
ECMWF nested	-12.607	5.158	4.049

Table 3.3: Mean, amplitude and scattering of the $\delta^{18}O$ [$^{\circ}/_{\circ\circ}$] in precipitation, according to equations 3.3 and 3.4. The GSF daily precipitation samples were collected at following stations: Nordeney, Arkona and Hohenpeissenberg.

the entire domain, reflecting the annual cycle of temperature at the domain's boundaries. From the latter we can conclude that REMO$_{iso}$ proved to be very sensitive to boundary conditions, both in annual means and seasonal variations. Our objective is to combine the advantages of the ECHAM and ECMWF datasets, by nesting REMO into an ECMWF-nudged version of ECHAM$_{iso}$. Dynamical variables (e.g. wind speed, pressure, temperature) of the GCM are constrained to fit the nudging dataset, while the (isotopic) water cycle is left untouched. Thus, the physical coherence between isotopic and meteorological variables can be preserved, while the GCM would be forced to reproduce a given synoptic situation. Similarly, REMO itself will be nudged at its upper boundary by winds from the ECMWF reanalyses, applying the spectral nudging technique [von Storch et al., 2000].

Albeit the influence of the boundary conditions, strong similarities are identified between both runs in relative features, revealing physical processes taking place inside the study domain. The increase of seasonal amplitude between coastal and mountain stations across Germany is similar for both runs on Figure 3.6 and Table 3.3, but not as strong as GNIP and GSF observations indicate it. As another example, the $\delta^{18}O$-distance from coast regression lines are nearly parallel for both runs on Figure 3.9, but the GNIP regression lines are steeper. Hence REMO$_{iso}$ fails to simulate the correct amplitude of the continental effect. Further investigation is needed to determine the causes of this misfit. Comparing ECHAM results at different resolutions (T30, T106) with REMO standard $1/2^{o}$ resolution, and possibly extending the analysis to REMO $1/6^{o}$ resolution, could reveal how sensitive the simulated continental effect is to resolution. Comprehensive experimental data, such as near-surface vapour sampling or in-clouds sampling would enable to discriminate between misfits in the parameterisation of cloud or surface processes.

3.4.2 Downscaling of isotopic precipitation

The major improvement of regional modelling of water isotopes as compared to global modelling is the enhanced horizontal resolution, thus the finer representation of orography. A remarkable consequence of the latter is that processes taking place exclusively in mountain areas appear clearly in REMO simulations with a resolution of $\sim 50km$. The mountain effect is likely to appear more distinctly when REMO is run at 18-km resolution. Yet, this improvement is still regarded insufficient for resolving local effects. The comparison to observation series could improve if proper downscaling is applied to the mean grid-cell output. Previous work was performed with dynamical and statistical downscaling of rain fall, especially in mountain areas [Brasseur et al., 2002]. This effort needs to be extended to isotopic signature of this downscaled precipitation. Such downscaling techniques could lower the resolution in simulated precipitation down to a kilometric scale, which would be suitable to e.g. snow deposition at ice-core drilling sites or surface runoff modelling.

3.5 Preliminary results of a spectral nudged REMO$_{iso}$ simulation over Europe: improvements in simulated temperature, precipitation and $\delta^{18}O$ †

This section is not present in the original article [Sturm et al., 2005], revised in November 2004, which constitutes the major part of the present chapter. Shortly later, a new simulation by spectral nudged REMO$_{iso}$ was performed over Europe, with boundary conditions from the ERA-15 nudged ECHAM$_{iso}$ v.4.5. Jean Jouzel kindly contributed by granting access to daily vapour $\delta^{18}O$ measurements from Saclay. The present analysis was performed mainly by G. Hoffmann and M. Kelley, and later presented at the annual meeting of the AlpIMP project funded by the European Union. The section thereafter summarises their major findings. This case-study should be regarded as preliminary results from the nudged REMO$_{iso}$ simulation over Europe. A thourough analysis, in support to the interpretation of daily measurements, is currently in preparation.

3.5.1 Limits in comparing GCM output to station observations: example of ECHAM3$_{iso}$ in Heidelberg

Water isotope modelling using general circulation models (GCM) has now been used since about 20 years [Joussaume et al., 1984, Jouzel et al., 1987, Hoffmann et al., 1998, 2000, Noone and Simonds, 2002]. This approach was extremely successful providing better understanding in the controlling factors and processes of the global water isotope cycle. Annual mean and geographic distribution as well as the seasonal cycle and inter-annual variability were reproduced and analysed by various GCMs. In many of these studies the relationship between mean (i.e. annual or seasonal) temperature and/or local precipitation and the corresponding isotope signal was a central point of interest since it is these kinds of "modern analogues" which are used in paleo-climatology to derive past climate parameters.

However, the temperature/isotope relation which is key for the use of the water isotopes as paleo-thermometer in high-latitude ice core records is the result of highly variable synoptic systems. These systems transport water vapour from low to high latitudes and form clouds and condensate thereby fractionating the stable water isotopes. Global GCMs are capable to reproduce the statistical correlation between local climate parameters, in particular temperature and precipitation, and the water isotopes, but it is difficult to test if these model are doing this for the right reason, that is if they are correctly simulating the isotope signal of individual air masses within storms or passing fronts. Figure 3.11 illustrates the capacity of global GCMs to simulate the seasonal cycle of the water isotopes, $\delta^{18}O_{vapour}$. As reported in Jacob and Sonntag [1991], $\delta^{18}O$ in vapour and precipitation were was measured daily at Heidelberg, Germany. However, this comparison shows also that there are problems in the synoptic time domain (<10days). The ECHAM4$_{iso}$ model, which was used in this analysis, systematically overestimates variability of the water isotopes in the time range of roughly between 1 to 6 days. Many different explanations are possible for a systematic bias between the model and observations, such as the coarse spatial model resolution (here we show results of a T42 simulation corresponding to a $2.8^\circ \times 2.8^\circ$ resolution on the physical grid), the poor representation of spatial heterogeneity of the land surface or the damped inter-annual variability in a simulation forced with climatological SSTs. However, most of these mechanisms rather point to under- instead of overestimated variability in a GCM. In fact synoptic variability of temperature and precipitation is correctly reproduced by the model which makes processes specifically linked to the water isotope cycle more probable as the origin of the overestimated variability shown in Figure 3.11.

Furthermore, a direct comparison between the model and observations for specific storms is not possible as long as the global model is run in a climatological (that is forced by long term mean "climatological" SSTs) mode or even forced by observed SSTs of a specific year. Internal atmospheric variability dominates the water isotope signal entirely as demonstrated in Figure 3.11. For instance, the most depleted values of the isotopic composition of water vapour at Paris are generally not in phase when comparing the model and the observations. Obviously the numerous high-frequency peaks and lows in the records associated with the passage of atmospheric fronts are not in phase (and they shouldn't because of the high internal variability correctly captured by the GCM).

† J. Jouzel, G. Hoffmann, K. Sturm, M. Kelley, *Extended abstract of an oral presentation at the AlpIMP meeting, Bologna, April 2005*

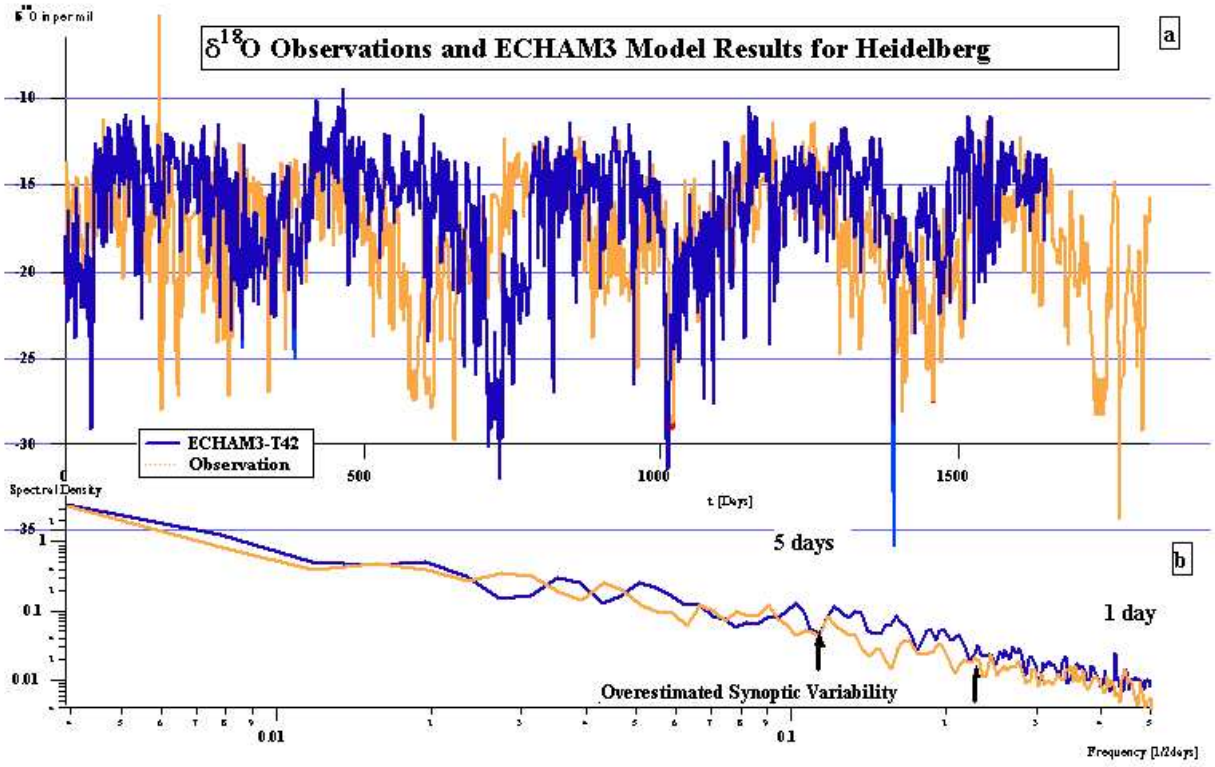

Figure 3.11: Comparison of $\delta^{18}O_{vapour}$ between ECHAM3 and observations in Saclay. Upper graph shows a comparison of daily records over 5 years. Lower graph shows the power spectrum of FFT analysis for both data sets.

3.5.2 Nudging of the ECHAM3 GCM to ERA 15

Therefore we developed a two-step model approach specifically aimed at analysing high frequency isotope records. In a first step, the global GCM ECHAM4$_{iso}$ was nudged to meteorological re-analysis wind fields provided by the European Centre, ECMWF, Reading. These re-analysis data sets, - here we use the ERA15 data set - guarantee both a close correspondence to the observations and a physically consistent three-dimensional flow field. The term "nudging" here means a continuous but small modification of the computed wind field of the ECHAM4 to achieve a close similarity with the ERA15 data. Technically, this nudging is done in a way that the GCMs physics is only slightly influenced. The hydrological cycle, for instance, still is computed independently by the ECHAM4. Moreover, the nudging is only done with the large-scale components of the wind field, therefore small scale features are still produced by the GCM itself. A detailed description of the nudging technique is given in Timmreck and Schulz [2004]. We started the ECHAM4 simulation in the nudging mode at 1980 and stopped at 1984. It is planned to continue this simulation until 1993 (end of the ERA15 data set) and, afterwards, even until 2003 using the more recent ERA40 data.

3.5.3 Spectral nudging of REMO nested in ECHAM

The global nudging procedure provided us the necessary meteorological and isotopic boundary condition for the second step of our approach. The regional climate model REMO is forced at its boundary with the climate and water isotopes simulated before by the ECHAM4 model. Moreover, within the model domain (here we have chosen Central Europe where the largest number of high-frequency water isotope records is available) the REMO model in the 0.5°standard resolution is again nudged to the re-analysis data. The details of the spectral nudging technique are reported in von Storch et al. [2000]. It is important that the water isotopes as part of the hydrological cycle are freely computed by both models, ECHAM4

and REMO, and there is no direct influence on the water isotopes by the nudging procedure.

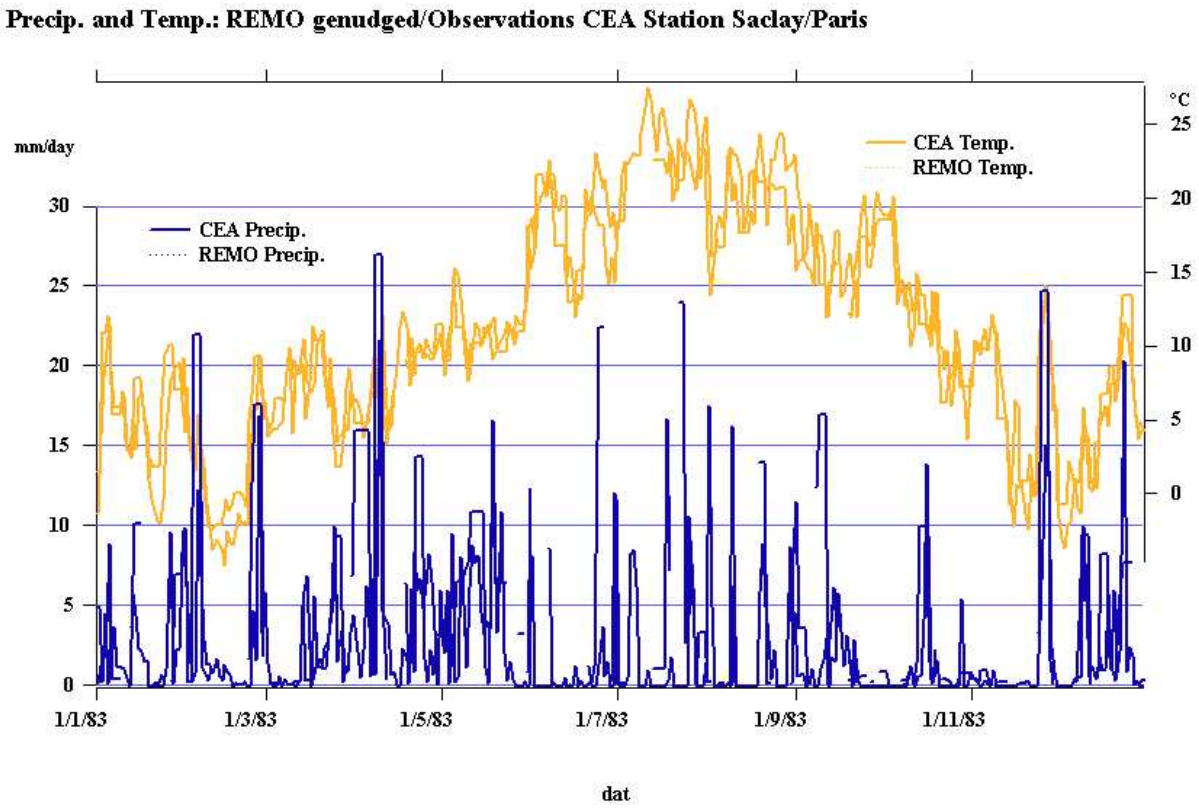

Figure 3.12: Comparison of daily temperature and precipitation observations in Saclay with the nudged REMO$_{iso}$. The data sets both cover one year, from January to December 1983.

Figure 3.12 shows the REMO results for temperature and precipitation for the year 1983 for the water vapour sampling station at the LSCE, Saclay (near Paris). Obviously, the model captures even second order features of the temperature evolution of this specific year. We point particularly to the persistently very cold period in the second half of February, 1983. Precipitation distribution of the grid point including the Saclay measuring site is in fair agreement with the observation. Small-scale land surface features probably are responsible for simulated precipitation amounts different from the station measurements.

3.5.4 Case study in February 1983

The REMO results are a logical consequence of the different spatial correlation length of temperature and precipitation. In this respect, the water isotopes (Figure 3.13) are situated in between the "large-scale" temperature field and - as part of the hydrological cycle - the "small-scale " precipitation field. Timing of most of the peaks and lows in the $\delta^{18}O_{vapour}$ record is correctly captured, though sometimes with a slightly underestimated amplitude. The February cool period is even much more intense in the observed isotope record. The model isotope signal at that time is the most-depleted, in the sense of the isotope/temperature relation "isotopically coldest", and long lasting period. The model however underestimates by a factor of two the isotope amplitude. Obviously, when comparing with the temperature record from Figure 3.12, the isotope signal is not only influenced by local temperature (the temperature signal is clearly less strong than the isotope signal) or by local precipitation (the corresponding period is very dry) but is also affected by the advection of very depleted air masses. Figure 3.14 shows the wind field of February 10, 1983, and clearly confirms this hypothesis. The Paris area is under the influence of a strong anomalous east circulation advecting cold and isotopically depleted air masses westward.

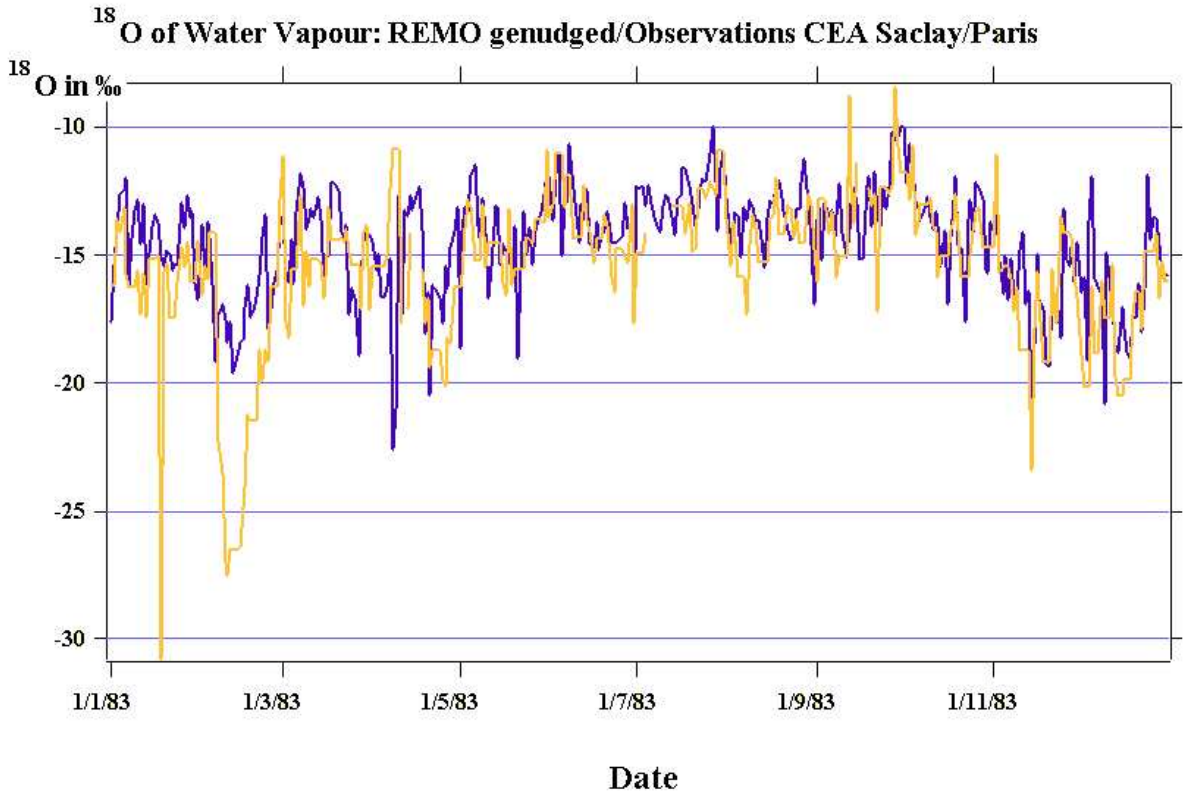

Figure 3.13: Comparison of water vapour observations in Saclay with the nudged REMO$_{iso}$. The data sets both cover one year, from January to December 1983.

It is planned to extend the above case study into a more systematic analysis of the relation between circulation patterns and isotope signals. Leading weather patterns are accompanied by typical isotope levels. The interpretation of inter-annual or decadal shifts in the water isotopic composition of precipitation can be based on such a weather pattern/isotope classification instead of using just empirical temperature/isotope relationships.

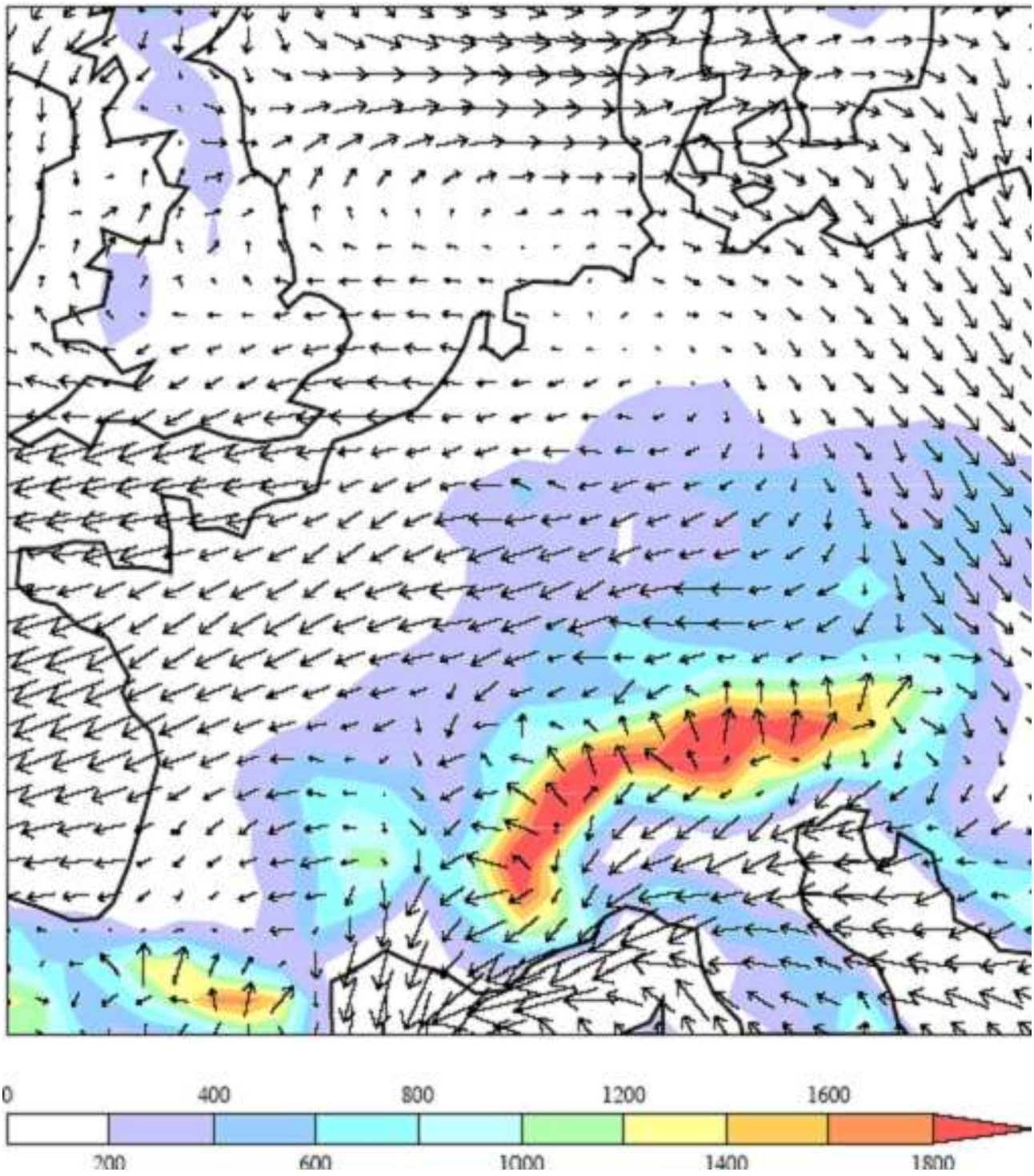

Figure 3.14: Horizontal wind field over Europe on February 10, 1983. Arrows represent the wind field, and shadings indicate the orography.

Bibliography

O. Brasseur, H. Gallée, D. Creutin J, T. Lebel, and P. Marbaix. High resolution simulations of precipitation over the Alps with the perspective of coupling to hydrological models. *Advances in Global Change Research*, 10:75 – 100, 2002. 52

S. Brinkop and E. Roeckner. Sensitivity of a general circulation model to parametrization of cloud-turbulence interactions in the atmospheric boundary layer. *Tellus*, 47A:197 – 220, 1995. 34

P. Ciais, C.J.W. White, J. Jouzel, and J.R. Petit. The origin of present-day Antarctic precipitation from surface snow deuterium excess data. *Journal of Geophysical Data*, 100:18 917 – 18 927, 1995. 33

W. Dansgaard. Stable isotopes in precipitation. *Tellus*, XVI:436 – 468, 1964. 32, 33, 36

G. Hoffmann, J. Jouzel, and V. Masson. Stable water isotopes in atmospheric general circulation models. *Hydrological Processes*, 14:1385 – 1406, 2000. 33, 36, 53

G. Hoffmann, M. Werner, and M. Heimann. Water isotope module of the ECHAM atmospheric general circulation model: A study on timescales from days to several years. *Journal of Geophysical Research*, 103(14):16 871 – 16 896, 1998. 33, 34, 36, 53

International Atomic Energy Agency IAEA and World Meteorological Organisation WMO. The Global Network of Isotopes in Precipitation (GNIP) database. *"http://isohis.iaea.org"*, 2001. 32, 36

Intergovernmental Panel on Climate Change IPCC. Climate Change 2001: The Scientific Basis – Contribution of Working Group I to the Third Assessment Report of IPCC. *UNEP/WMO Publications*, 2001. 33

D. Jacob. A note to the simulation of the annual and inter-annual variability of the water budget over the Baltic Sea drainage basin. *Meteorology and Atmospheric Physics*, 77:61 – 73, 2001. 34

D. Jacob, U. Andrae, G. Elgered, C. Fortelius, L.P. Graham, S.D. Jackson, U. Karstens, C. Koepken, R. Lindau, R. Podzun, B. Rockel, F. Rubel, H.B. Sass, R.N.D. Smith, B.J.J.M. Van den Hurk, and X. Yang. Comprehensive Model Intercomparison Study Investigating the Water Budget during the BALTEX-PIDCAP Period. *Meteorology and Atmospheric Physics*, 77:19 – 43, 2001. 34, 36

H. Jacob and C. Sonntag. An 8 year record of the seasonal variation of ^{2}H and ^18O in atmospheric water vapor and precipitation at Heidelberg, Germany. *Tellus*, 43(B):291 – 300, 1991. 53

J. Joussaume, R. Sadourny, and J. Jouzel. A general circulation model of water isotope cycle in the atmosphere. *Nature*, 311:24 – 29, 1984. 33, 53

J. Jouzel, R.B. Alley, K.M. Cuffey, W. Dansgaard, P. Grootes, G. Hoffmann, S.J. Jonsen, R.D. Koster, D. Peel, C.A. Shuman, M. Stievenard, M. Stuiver, and J.W.C. White. Validity of the temperature reconstruction from water isotopes in ice cores. *Journal of Geophysical Research*, 102:26471 – 26487, 1997. 33

J. Jouzel and L. Merlivat. Deuterium and oxygen 18 in precipitation: modeling of the isotopic effects during snow formation. *Journal of Geophysical Research*, 89:11 749 – 11 757, 1984. 33

J. Jouzel, G.L. Russel, R.J. Suozzo, R.D. Koster, J.W.C. White, and W.S. Broecker. Simulations of the *HDO* and $H_2^{18}O$ atmospheric cycles using the NASA/GISS general circulation model: the seasonal cycle for present-day conditions. *Journal of Geophysical Research*, 92:14 739 – 14 760, 1987. 33, 53

J. Kavanaugh and K. Cuffey. Space and time variation of $\delta^{18}O$ and δD in Antarctic precipitation revisited. *Global Biogeochemical Cycles*, 17:1017 – 1031, 2003. 33

D. Majewski. The Europa-Modell of the Deutscher Wetterdienst. *ECMWF Seminar on numerical methods in atmospheric models*, 2:147 – 191, 1991. 34

M. Majoube. Fractionnement en oxygène 18 et en deutérium entre l'eau et sa vapeur. *Journal of Chemical Physics*, 10: 1423 – 1436, 1971. 34, 36

L. Merlivat and J. Jouzel. Global climatic interpretation of the deuterium-oxygen 18 relationship for precipitation. *Journal of Geophysical Research*, 84:5029 – 5033, 1979. 33, 34

W.G. Mook, J. Gat, K. Rozanski, W. Stichler, M. Geyh, K.P. Seiler, and Y. Yurtsever. Environmental isotopes in the hydrological cycle, principles and applications. *Vol. I & II, UNESCO/IAEA Series*, 2001. http://www.iaea.org/programmes/ripc/ih/volumes/volumes.htm. 32, 33

H. Moser and W. Stichler. Die Verwendung des Deuteriums und Sauerstoff-18 Gehalts bei hydrologischen Untersuchungen. *Geologia Bavarica*, 64:7–35, 1971. 33

D. Noone and I. Simonds. Association between 18O of water and climate paramters in a simulation of atmospheric circulation for 1979-95. *Journal of Climate*, 15:3150 – 3169, 2002. 33, 53

T.E. Nordeng. Extended versions of the convective parametrization scheme at ECMWF and their impact on the mean and transient activity of the model in the tropics. *ECMWF Research Department, Technical Memorandum No. 206*, 1994. 34

B. Norris. Change of the operational forecasting system. *ECMWF Newsletter*, 74, 1997. 34

E. Roekner, E.K. Arpe, L. Bengtsson, M. Christoph, M. Claussen, L. Dümenil, M. Esch, M. Giorgetta, U. Schlese, and U. Schulzweida. The atmospheric circulation model ECHAM-4: model description and simulation of the present day climate. *Max-Planck-Institute für Meteorologie Report*, 218, 1996. 34

K. Rozanski, L. Araguás-Araguás, and R. Gonfiantini. Isotopic patterns in modern global precipitation. *AGU Monograph*, 78:1–37, 1993. 32, 33, 47

U. Schotterer, F. Oldfield, and K. Fröhlich. GNIP : Global Network of Isotopes in Precipitation. *IAEA/PAGES/WMO/ IAHS publication*, 1996. "http://www.iaea.org/programs/ri/gnip/1stpage.html". 32

U. Siegenthaler and H. Oeschger. Correlation of ^{18}O in precipitation with temperature and altitude. *Nature*, 285:314, 1980. 33

K. Sturm, G. Hoffmann, B. Langmann, and W. Stichler. Simulation of $\delta^{18}O$ in precipitation by the regional circulation model REMO_{iso}. *Hydrological Processes – in press*, 2005. 53

M. Tiedtke. A comprehensive mass flux scheme for cumulus parametrizations in large-scale models. *Monthly Weather Review*, 117:1779 – 1800, 1989. 34

C. Timmreck and M. Schulz. Significant dust simulation differences in nudged and climatological operation mode of the AGCM ECHAM. *Journal of Geophysical Research*, 109(13), 2004. 54

J.C. Vogel, J.C. Lerman, and W.G. Mook. Natural isotopes in surface and groundwater from Argentina. *Hydrological Science Bulletin*, XX:203 – 221, 1975. 33

H. von Storch, H. Langenberg, and F. Feser. A Spectral Nudging Technique for Dynamical Downscaling Purposes. *Monthly Weather Review*, 128:3664–3673, 2000. 52, 54

M. Werner, U. Mikolajewicz, M. Heimann, and G. Hoffmann. Borehole versus isotope temperatures on Greenland : seasonality does matter. *Geophysical Research Letters*, 27:723 – 726, 2000. 34

Y. Yurtsever. Worldwide survey of isotopes in precipitation. *IAEA report, Vienna*, 1975. 32

Chapter 4

Simulation of the stable water isotopes in precipitation over South America: comparing regional to global circulation models †

Résumé

Dans le précédant chapitre, le modèle de circulation régional REMO intégrait pour la première fois le cycle des isotopes stables de l'eau. Poursuivant les objectifs généraux de la thèse, nous avons transféré le domaine d'étude de l'Europe vers L'Amérique du Sud. Contrairement au cas précédant, il n'était pas *a priori* acquis que REMO$_{iso}$ serait capable de reproduire le climat tropical et sub-tropical de l'Amérique du Sud. De plus, traiter les dénivelés abrupts de la Cordillère des Andes était, au vu de la condition hydrostatique, un défi pour la dynamique du modèle. Avant d'analyser le signal isotopique en Amérique du Sud, il nous a paru nécessaire de considérer dans un premier temps la validité du cycle hydrologique 'standard', ainsi que les caractéristiques de la circulation atmosphérique sud-américaine. Cette évaluation requise donnait en outre l'occasion d'aborder la sensibilité des paramétrisations physiques (dont celles portant sur le fractionnement isotopique) à la résolution horizontale des modèles. C'est dans ce cadre que se situe l'étude suivante.

Pour établir la validité de REMO$_{iso}$ en contexte tropical, cette étude se focalise sur la représentation du cycle saisonnier standard, i.e. climatologique. Pour minimiser les variations inter-annuelles induites par l'océan, les températures de surface de l'océan (sea-surface temperatures – SST), sont prescrites dans REMO$_{iso}$ et son modèle hôte ECHAM$_{iso}$ T30 pour représenter une année moyenne, se répétant perpétuellement. Ainsi les 5 années de simulations peuvent être considérées comme autant de réalisations du cycle annuel représentatif des 2 dernières décennies (simulations d'ensemble). Le cycle annuel moyen sur ces 5 années de simulation est comparé à des climatologies analogues, construites à partir des autres modèles et observations.

Primo, les précipitations simulées par REMO$_{iso}$, avec une résolution au sol de $0.5^\circ (\sim 54km)$, sont comparées à ECHAM$_{iso}$ en résolution T30 ($3.75^\circ \sim 420km$) et T106 ($1.125^\circ \sim 125km$), à l'aune de plusieurs observations spatialisées. L'alternance entre saison sèche et humide est raisonnablement capturée par les modèles, malgré une divergence dans la position des maxima printaniers (Andes équatoriennes au lieu de l'embouchure de l'Amazone). REMO$_{iso}$ offre une meilleure prise en compte des précipitations orographiques, mais hérite des déficiences de son modèle hôte. De plus, les précipitations sont globalement surestimées de

† K. Sturm, G. Hoffmann and B. Langmann, *submitted to Journal of Climate*.

30% sur l'ensemble du domaine. En cela, REMO$_{iso}$ rejoint les autres modèles de circulations régionaux appliqués en Amérique du Sud. Secundo, les caractéristiques de la circulation atmosphérique régionale sont correctement représentées par REMO$_{iso}$, notamment la dépression du Chaco, l'anti-cyclone Bolivien et l'advection induite. Tertio, le signal isotopique simulé est comparé aux mesures des stations éparses du réseau mondial de collecte des isotopes dans les précipitations (global network of isotopes in precipitation – GNIP). L'affinement progressif de la résolution horizontale améliore indubitablement la simulation du δ^{18}O en relief accidenté (illustré par la Cordillère des Andes). D'autres phénomènes méso-échelles sont également résolus avec plus de détail, ce qui facilite la comparaison entre modèles et données.

Dès lors que REMO$_{iso}$ reproduit une image fiable du climat sud-américain, il est justifié d'explorer de nouveaux éléments pour l'interprétation du δ^{18}O en tant que proxy climatique. En particulier, REMO$_{iso}$ donne lieu à une interprétation plus fine de l'effec d'altitude (diminution de δ^{18}O avec l'altitude) que ne l'autorise ECHAM$_{iso}$. De même, nous nous intéressons au gradient continental atypique du δ^{18}O à travers le bassin amazonien sur la base des données REMO$_{iso}$, ECHAM$_{iso}$ et GNIP. Enfin, nous adoptions un référetiel Lagrangien pour décrire l'évolution du contenu isotopique des précipitations le long de leur trajectoire.

Zusammenfassung

Im vorherigen Kapitel wurde die Erweiterung des regionalen Klimamodells REMO um den Wasserisotopenzyklus beschrieben. Dem allgemeinen Ziel dieser Arbeit folgend wurde daraufhin das Augenmerk auf Südamerika verlegt. Im Gegensatz zur ersten Studie war *a priori* nicht gesichert, daß REMO$_{iso}$ im Stande war, das sub- und tropisches Klima Südamerikas nachzubilden. Zudem stellen die steilen Höhenunterschiede der Anden eine Herausforderung an die Modelldynamik dar, insbesondere angesichts der hydrostatischen Annahme, die deren Formulierung zugrunde liegt. Vor der Analyse des simulierten Isotopensignals erschien es zunächst nötig, die simulierte Wasser- und Luftzirkulation zu validieren. Dies bot zudem die Gelegenheit, die Sensitivität der physikalischen Parametrisierungen (u.a. der isotopischen Fraktionierungsprozesse) von der horizontalen Modellauflösung zu untersuchen. Die folgende Studie verläuft in diesem Rahmen.

Um festzustellen, inwiefern REMO für den tropischen Klimakontext geeignet ist, konzentriert sich diese Studie auf den langjährig gemittelten (d.h. klimatologischen) Jahreszyklus. Um die vom Ozean angetriebene inter-annuale Variabilität außer Kraft zu setzen, wurde für die Meeresoberflächentemperaturen (sea-surface temperature – SST) gemäß ein klimatologisches Jahreszyklus festgesetzt. So können die 5 Jahre der REMO$_{iso}$ Simulation als einzelne Realisierungen des für die letzten 2 Jahrzehnte repräsentativen Jahreszyklus angesehen werden (Ensemblelauf). Aus dem 5-jährigen Experiment wurde eine REMO$_{iso}$ Klimatologie erstellt, die mit ähnlich aus Modell- und Beobachtungsdatensätzen zusammengestellten Klimatologien verglichen wird.

Als Erstes wird der von REMO$_{iso}$ in $0.5^\circ(\sim 54km)$ Auflösung produzierte Niederschlag mit dem von ECHAM$_{iso}$ T30 ($3.75^\circ \sim 420km$) und T106 ($1.125^\circ \sim 125km$) anhand von beobachteten Niederschlagsrasterdatensätzen bewertet. Die Abwechslung von Trocken- und Regenzeit wird in den Modellen qualitativ nachgebildet, trotz einer merkbaren Abweichung in der Lage des frühjährlichen Maximums über den equatorianische Anden anstatt über der Amazonasmündung. REMO erlaubt eine verbesserte Berücksichtigung des orografischen Niederschlags, aber es übernimmt von seinem Hostmodell den oben erwähnten systematischen Fehler. Dazu ist der Niederschlag gebietsweit um 30% überschätzt, was ein für Studien mit regionalen Klimamodellen häufiges Problem ist.

Daraufhin wird gezeigt, daß die typischen Merkmale der Luftzirkulation über Südamerika von REMO$_{iso}$ wirklichkeitstreu nachgebildet werden, insbesondere die Chaco-Tief, das Bolivianische Hochdruckgebiet und die dadurch verursachte Windströmung.

Drittens wird das simulierte stabile Wasserisotopensignal mit den wenigen Stationen des 'global network of isotopes in precipitation' (GNIP) verglichen. Unzweifelhaft verbessert die schrittweise feinere Auflösung die δ^{18}O-Darstellung im Hochgebirge (Andinische Kordilleren). Weitere meso-skalige Phänomene sind ebenfalls besser aufgelöst, wodurch der Vergleich von Modell- und Beobachtungsserien erleichtert wird.

Da $REMO_{iso}$ eine wirklichkeitstreue Nachbildung des südamerikanischen Klimas liefert, ist es möglich, weitere Interpretationselemente des $\delta^{18}O$-Signals als Klimaproxy zu erforschen. Insbesondere bietet sich $REMO_{iso}$ zu einer ausführlicheren Analyse des Höheneffektes ($\delta^{18}O$-Verringerung mit zunehmender Höhe), als es $ECHAM_{iso}$ ermöglicht. Ähnlich kann $REMO_{iso}$ weiterreichende Einblicke über den atypischen $\delta^{18}O$-Kontinentgradient verschaffen. Zuletzt wird in einem Lagrange-Bezugssystem der Verlauf des $\delta^{18}O$ entlang typischer Luftmassen-Zirkulationslinien geschildert.

4.1 Introduction

Tropical ice-cores recovered from several Andean summits represent a unique archive of climate variability in the inter-tropical belt [Thompson et al., 2000, Ramirez et al., 2003, Ginot et al., 2002]. Yet the interpretation of their isotopic signal is more complicated than in the case of polar ice-cores. Unlike the latter, precipitation at tropical latitudes is predominantly convective, hence the isotopic signal is less sensitive to local temperature conditions. Further differences include a broader variability in moisture origin, large feedback of vegetation on the hydrological cycle and local effects caused by the steep surrounding topography.

As a consequence, simple trajectory-based Rayleigh distillation models are not able to account for observed variations in the isotopic ice-core composition. Stable water isotope enabled global circulation models shed a new light on the matter. Recently, Vuille et al. [2003b] conducted a comprehensive study with the ECHAM$_{iso}$ and the $_{iso}$GISS II GCMs to investigate the climatic controls on the isotopic signal over South America. The authors focus on the inter-annual, and to a lesser extent the seasonal variability of the simulated isotopic signal. In a compagnon article, Vuille et al. [2003a] report that the inter-annual isotopic signal in tropical Andean ice-cores records Pacific sea-surface temperature anomalies. Similarly, Bradley et al. [2003] reports that stable water isotope variations in Andean ice-cores are primarily related to the El Niño Southern Oscillation (ENSO) phenomenon.

On the other hand, experimental evidence from a isotopic precipitation sampling network across Bolivia demonstrated that local temperatures have limited influence on the isotopic composition [Vimeux et al., -]. Furthermore, back-trajectory analysis shows that, under prevailing inter-tropical easterlies, the origin of moisture precipitating over eastern Andean summits is located in the Atlantic. Using a centennial simulation by the ECHAM$_{iso}$ GCM, Hoffmann et al. [2003] demonstrates that precipitation and recycling by vegetation over the Amazon basin primarily controls the isotopic signal in Andean ice-cores. As a further evidence, the isotopic signals in Andean ice-cores reveal a high level of similarity, which acknowledges their common moisture origin. Taking profit of the high resemblance, the authors define a common Andean isotope index (AII). Hoffmann [2003] reports that the AII is in good agreement with the first principal component of global precipitation.

Hence, the simulated stable water isotope signal over the tropical Andes gives rise to divergent interpretation. One reason for uncertainty might be coarse resolution of GCM, which greatly underestimates the Andean topography E.g. at the common T30 resolution, the smoothed Andean orography culminates at 1500 masl instead of the actual > 6000 masl high peaks and 4000 masl elevated Altiplano. To overcome this limitation, we applied the regional circulation model REMO$_{iso}$, fitted with stable water isotope diagnostics, to tropical South America.

The present article introduces a 5-year simulation by REMO$_{iso}$ at a horizontal resolution of 0.5°. The study domain extends from 100°W to 20°W in longitude and 35°S to 15°N in latitude. We first compare the annual cycle of precipitation simulated by REMO to ECHAM simulations at T30 ($3.75^\circ \sim 420km$) and T106 ($1.125^\circ \sim 125km$) resolutions. Simulated precipitation is evaluated against gridded precipitation observations. We then assess the ability of REMO$_{iso}$ to reproduce typical features of the South American atmospheric circulation, as the Bolivian high and Chaco low. Finally we investigate the benefits of improved resolution for the simulation the stable water isotope signal across South America. The discussion on the simulated isotope signal focuses on the analysis of the simulated altitude effect, as well as the anomalous continental gradient across the Amazon basin. Finally, we adopt a Lagrangian referential to describe the joint evolution of precipitation and its isotopic signature along the air mass trajectory.

4.2 Model and data

The present section introduces simulations by the stable water isotope enabled regional circulation model REMO$_{iso}$, and the global model ECHAM$_{iso}$ at the resolutions T106 and T30. For the present study, REMO was integrated over 5 years. Longer data series exist both of ECHAM runs and observations, but we restrict their analysis to a 5 year period for the sake of statistical consistency with the REMO simulation. Model results of synoptic scale meteorological parameters, total precipitation and isotopic signal in precipitation are compared to gridded and station observations.

4.2.1 Model description and experiment set-up

Two atmospheric circulation models, developed at the Max Planck Institute for Meteorology (Hamburg), were enabled with stable water isotope diagnostics. The global circulation model ECHAM-4 is optimised to run at six spectral resolutions from T21 to T106; we selected two runs at T30 (3.75 °, i.e. $\sim$ 420 km at the Equator) and T106 (1.125 °, i.e. $\sim$ 125 km at the Equator) resolution for this study, with 19 vertical levels each. Apart from the resolution, the two runs differ by the boundary conditions used to specify the sea-surface temperatures (SST). The ECHAM T30 run uses the GlSST climatology [Rayner et al., 1994], representing the mean annual SST cycle over the 1979-1998 period. After a 3 year spin-up, this T30 simulation covers 10 years, of which the 5 first were analysed in the present study. The ECHAM T106 run uses observed, yearly varying SST from 1979 to 1998, of which 5 years from 1985 to 1989 were analysed. The selection of the years 1985 to 1989 are motivated from the analysis of different observational data sets, as described in the next section. Further details about the water isotope enabled ECHAM model can be found in Hoffmann et al. [1998] and Werner et al. [2000].

The regional circulation model REMO, fitted with stable water isotope diagnostics, was run at 0.5 ° ($\sim$ 53 km) resolution, with 19 vertical levels. The study domain ranges from 100°W to 20°W in longitude and 35°S to 15°N in latitude. REMO was nested into the ECHAM T30 run mentioned above, with climatological SST conditions. After a 1 year spin-up, the model was integrated over 5 years, corresponding to the 5 years from the ECHAM T30 run mentioned above. The physical parameterisations and corresponding isotopic fractionation processes were adapted from ECHAM-4. The current version of REMO (5.0-EC4) and its water isotope module is extensively described in Sturm et al. [2005a]. The major features of the water isotope module are :

1) the isotopic tracers $H_2^{18}O$ and HDO are treated as prognostic variables both for their liquid and gaseous phase;

2) the soil module includes three prognostic reservoirs for isotopic tracers, (bucket) soil moisture, canopy interception and snow pack;

3) evaporation from the sea-surface includes both equilibrium and wind-drift dependent kinetic fractionation [Merlivat and Jouzel, 1979];

4) no discrimination is made between evaporation and transpiration from the soil moisture, hence considered non-fractionating;

5) 3-phase equilibrium and kinetic effects are accounted for the fractionation in convective and stratiform clouds;

6) partial re-evaporation of rain drops below the cloud induces an isotopic re-equilibration with the surrounding moisture, at a rate of 45% for convective and 95% for large-scale rain.

4.2.2 Gridded precipitation observations and isotopic measurements

Several gridded precipitation data sets are available, differing in the observational sources, the spatial and temporal resolution. It is beyond the scope of this article to analyse the difference of these data sets over South America.

Here, we selected five gridded annual series of monthly precipitation covering the study domain, summarised in table 4.1. A brief description of all data sets follows:

1) the WML data set [Willmott and Matsuura, 2001, version 1.02] was obtained applying the climatologically aided interpolation (CAI) method [Willmott and Robeson, 1995] from station records in the global historical climatology network (GHCN). It has a resolution of 0.5° and contains land precipitation only.

2) the GPCP data-set [Huffman and Bolvin, 2004, version 2] was produced as part of the Global Precipitation Climatology Project. It combines SSMI, TOVS satellite estimates of precipitation with rain gauge measurements from the GHCN, CAMS and GPCC networks [Huffman, 1997]. Its resolution is 2.5° and it covers both land and ocean precipitation.

3) the CMAP data set [Xie and Arkin, 2002] stands for 'CPC merged Analysis of Precipitation'. It combines satellite estimates of precipitation, gauge measurements and NCEP re-analyses [Xie and Arkin, 1997]. As for the GPCP data set, its resolution is 2.5° over both land and ocean.

4) the CRU data set [Hulme et al., 1998, New et al., 2000] was produced by the Climate Research Unit at University of

Name	Resolution (°)	Source	Period	Total (mm)	Reference
Models					
REMO	0.5 x 0.5	clim. SST	5 years	2195	present paper
ECHAM T30	3.75 x 3.75	clim. SST	5 years	1577	Hoffmann et al. [1998]
ECHAM T106	1.125 x 1.125	obs. SST	1985-1989	1400	Werner, personal comm.
Observations					
WML	0.5 x 0.5	gauge on land	1985-1989	1660	Willmott and Matsuura [2001]
GPCP	2.5 x 2.5	gauge/sat.	1985-1989	1703	Huffman and Bolvin [2004]
CMAP	2.5 x 2.5	gauge/sat.	1985-1989	1630	Xie and Arkin [2002]
CRUtrop	3.75 x 2.5	gauge/sat.	1985-1989	1501	Doherty et al. [1999]
CRU	3.75 x 2.5	gauge on land	1985-1989	1501	Hulme et al. [1998]
GNIP	43 stations	monthly clim.	1960-2000	-	IAEA and WMO [2001]

Table 4.1: Specifications of the modelled and observed data-sets used in the present article.

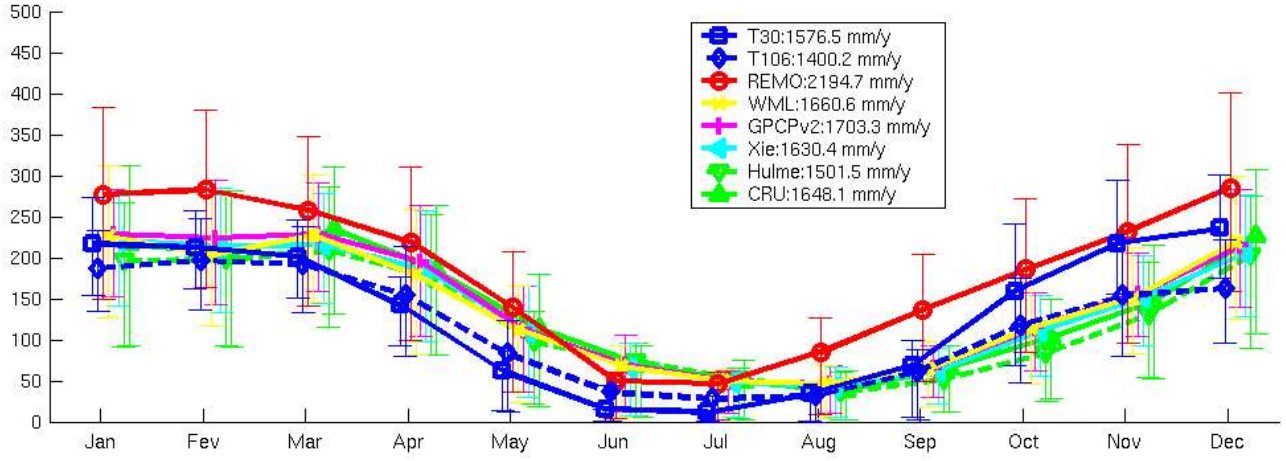

Figure 4.1: Mean precipitation (in mm/month) over land for the data sets listed in table 4.1. The data sets are averaged over the 1985-1989 period, at a latitude between 0 deg and 23.5 deg S (i.e. between the Equator and the Capricorn tropic). Bars show the 25% and 75% percentiles over the averaged domain.

East Anglia. It applies a Thiessen polygon weight interpolation of station records from CRU/US DoE and GHCN stations. 5) the CRUtrop data set [Doherty et al., 1999] is a refined version of the precedent over the extended tropics, incorporating remote-sensed OLR for a best estimate of tropical convective precipitation.

All data-sets cover a 20 year period from 1979 to 1998, corresponding to the ECHAM T106 experiment, apart from Doherty et al. [1999] that spans from 1975 to 1994. In that period, we identified a period of five consecutive years which deviated the least from the 20 year mean over the study domain. As such, the five year precipitation data-sets can be compared to the REMO simulation in a statistically consistent manner. It is believed that the use of climatological SST in REMO/ECHAM T30 improves the climatological representativeness of precipitation over a short (5 year) integration period.

For each data-set, the mean precipitation over 1985 to 1989 was less than 5% wetter than the 20-year average, apart from the CRU data set (9.6%). Moreover, no extreme anomaly occurred, as the 1986-87 El Niño did not affect precipitation over South America as drastically as the 1982-83, 1992-93 or 1997-98 events. Hence, the period from Jan 1985 to Dec 1989 is considered to be representative of the late XX^{th} century conditions over the study domain.

Monthly mean sea-level pressure and surface temperature were retrieved from the ERA40 data server [ECMWF and Raoult, 2003]. As for the precipitation data sets, the selected period runs over 5 years, from January 1985 to December 1989, with a horizontal resolution of 2.5°. The reanalysis project, completed in 2004, assimilates remote-sensed measurements from 7 satellites as well as numerous radiosonde and station meteorological data.

Evaluation of modelled isotopic precipitation over South America is complicated because of sparse station measurements in the global network for isotopes in precipitation (GNIP). In order to maximise the number of stations, we compare model results to the GNIP climatology [IAEA and WMO, 2001]. A mean annual cycle is constructed for all GNIP stations that were in operation at least three years, between 1961 and 2001. The GNIP data set is the only one to derogate from the '5 year' rule.

4.3 Evaluation against observations

In this section, we evaluate some climatic features of the model simulations, as compared to observations. In particular, we concentrate on precipitation amounts, distribution and seasonality, as well as meteorological features controlling the regional atmospheric circulation (e.g. Bolivian high, Nord-este low, and the induced vapour transport).

4.3.1 Precipitation

The figure 4.1 shows the mean annual cycle of precipitation for both models and observations, as listed in table 4.1. The spatial average was taken over land only (to be consistent with the WML data set), for all latitudes of the domain comprised between the Equator and the Capricorn (Southern) tropic, i.e. a domain limited to [100°E;20°E] in longitude and [0°;23.5°S] in latitude. Hence, the seasonal behaviour of precipitation is clearly revealed, which is masked if averaging over both hemispheres. The Southern tropics experiences a dry season from May to September (austral winter) and a wet season from October to April (austral summer), concentrating about 80% of the annual precipitation. Since the spatial distribution of rainfall is far from Gaussian, we preferred to plot the 25% and 75% percentiles (first and third quartile) in bars around the mean instead of the standard deviation.
All observational data sets display a similar behaviour, reaching maximum values of 200 - 250 mm/month in January and March, and its minimum of 50 mm/month in August. The CRUtrop data set gives a 10% smaller estimate of austral summer precipitation, summing up to 1500 mm/year as compared to an average 1650 mm/year for the WML, GPCP, CMAP and CRU data sets. The interpolation methods produce fairly uniform data sets, since both the first and third quartile do not differ from the mean by more than 50%.

The T106 simulation by ECHAM is in good agreement with the observational data sets, apart from underestimating precipitation in the late wet and dry season (April to July). It fails also to reproduce the double maxima in the wet season. As a consequence, the annual precipitation amounts to 1400 mm/year, which underestimates by 15% the mean of the observations.
Although the total annual precipitation by the ECHAM T30 simulation is closer to the observations (1570 mm/year, i.e. only 5% underestimation), its seasonality seams to be shifted by 1-2 months. The precipitation minimum falls in June-July instead of August, and it misses the second maximum in March. Accordingly, the precipitation in March-Jun are underestimated by up to 70%, whereas they are overestimated during October to December. Common for both ECHAM simulations is a gross underestimation of dry season precipitation, with average values in July below 30 mm/month for T106 and below 10 mm/month for T30.
REMO inherits the shifted seasonality of its host model, ECHAM T30. Nevertheless, it reproduces the double maxima shape in the wet season, one month ahead of the observations (December and February). Precipitation amounts are overestimated all year round, summing up to nearly 2200 mm/year (33% more than the observations). The third quartile values are significantly higher for REMO than for both models and observations, which indicates that a large number of extreme monthly precipitation tend to lift the mean, although the first quartile values are reasonable. Overestimation of precipitation is even more severe over the ocean. In connection with the Pacific inter-tropical convergence zone (ITCZ), REMO simulates precipitation that exceed 4000 mm/month, whereas CMAP observations never exceed 500 mm/month.

The discrepancies in the annual cycle of mean precipitation are related to a mismatch in their spatial distribution. The maps of mean annual precipitation for the REMO, ECHAM T106 and T30 simulations, compared to the WML, GPCP and CMAP observations are shown in figure 4.2. Generally one observes that local precipitation maxima increase with resolution, both in the simulations (related to increased orographic precipitation) and the observations (according to the CAI interpolation technique by Willmott and Robeson [1995]). Grid cells with precipitation occasionally exceeding 1000 mm/month are found in all data sets but ECHAM T30, GPCP and CMAP. In WML and ECHAM T106, the maximum occurs over the isthmus of Panama ($\sim [80°E;7°N]$). CRU and CRUtrop locate it on the Eastern slope of the Equatorian Andes ($\sim [79°E;2°S]$). REMO clearly overestimates precipitation in steep relief, all over the study domain. Over 60 grid cells exceed 1000 mm/month, on the Eastern slope of the Peruvian Andes, both sides of the Equatorian and Columbian cordilleras, the Northern Guiana highlands, and reaching an unrealistic maximum of 3200 mm/year over the Cordillera de Talamanca (Panama). These extreme values occur in the tropically fitted REMO simulation as well. The WML data set alone shows spot-wise maxima over the central Andes $[65°E;18°S]$ exceeding 800 mm/month. Other local maxima are observed over the Guiana [68°W;5°N] and south Brazilian [43°W;20°S] highlands. Such extreme precipitation in the WML data set remain local probably due to the scarcity of station records in such regions. It is thus questionable whether the CAI algorithm sufficiently accounts for orographic effect on precipitation, which is entirely overseen in

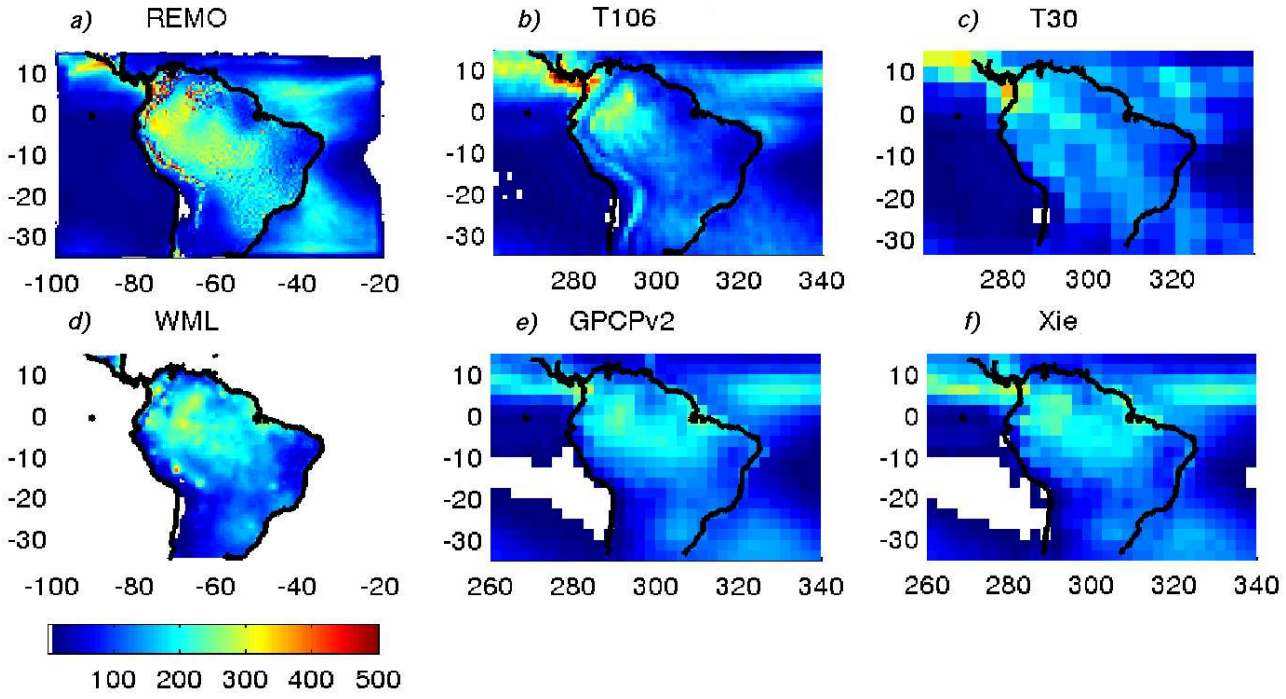

Figure 4.2: Mean annual precipitation in mm/month simulated by REMO (a), ECHAM T106 (b) and T30 (c) as compared to gridded observations from WML (d,[Willmott and Matsuura, 2001]), GPCP (e,[Huffman and Bolvin, 2004]) and CMAP (f,[Xie and Arkin, 2002])

coarser resolution sets as GPCP, CMAP and CRU.

Notwithstanding extreme values, the precipitation patterns differ between observations and simulations, as depicted on figure 4.2. All models produce high precipitation amounts on the North-West Amazon basin, including the Guiana highlands, reaching 4000 mm/year. This agrees with WML, but neither GPCP nor CMAP exceed 2500 mm/year in this area. On the other hand, all three models underestimate precipitation around the Amazon mouth, with less than 1500 mm/year. All observations agree on a 3000 mm/year average, i.e. about twice as much. This discrepancy is enhanced when looking at the months of March to May. Both models and observations produce local maxima of 450 mm/month. All three models locate the maximum over the ocean ($\sim [35°E; 5°S]$), whereas observations locate it on the coast ($\sim [45°E; 5°S]$). In the simulations, the moisture is transported further inland, to produce a second rainout maximum at the topographic barrier of the Andes. This discrepancy is common to several modelling studies [Rojas and Seth, 2003]. The increased precipitation on the east flank of the Cordillera is marked in regional circulation models, as moisture converges due to low-level jets (LLJ [Vernekar et al., 2003]). The different location of precipitation maxima is responsible for the apparent shifted seasonality in figure 4.1.

Similar discrepancies in simulated precipitation patterns are found in other studies. Costa and Foley [1998] indicate that re-analyses overestimate precipitation over Central and Eastern Amazon Basin. Both GSFC and NCEP re-analyses reach maxima in annual values of 3 m/year and above, as does REMO. Lenters and Cook [1999] report precipitation maxima of 420 mm/month during austral summer (DJF), located 55°W and 10°S, in the global precipitation index (GPI) data set, which even exceeds values by REMO. The presence of relief in a GFDL GCM control simulation produces a local maximum of 450 mm/month at (78°W, 3°N), which is shifted 5 degrees to the east with zonally uniform instead of observed SST, but vanishes in the no-mountain experiment [Lenters and Cook, 1995]. The NCEP η model over South America, driven by NCEP re-analyses, locates correctly the mean precipitation over the Amazon delta, but shows a similar excess as REMO over the Central Amazon basin; similarly to REMO, it produces excessive rainfall on the Eastern slope of the Andes (75°W, 5°S), due to increased moisture flux land inwards [Vernekar et al., 2003, Chou et al., 2000]. Rojas and Seth [2003] nested RegCM in CCM3 over South America. As in our case, both the GCM and the RCM

overestimate precipitation in the western Amazon, but underestimates it in the eastern part. Furthermore, the RCM also produces extreme rainfall (>500 mm/month) at [75°W;5°S], as over the Brazilian highland in extreme wet conditions.

To test the sensitivity to convection parameterisation, we performed a one year integration of REMO with parameters optimised for tropical conditions. According to sensitivity studies by Aldrian [2003], the minimum cloud thickness over land was raised from 75 hPa to 300 hPa, the relative humidity threshold to launch condensation was raised from 80% to 90% and the rain condensation efficiency was lowered from .02 to .0006. This tropical sensitivity experiment points out some explanation to the above cited deficiencies: maximum precipitation located over the ocean instead of the Amazon mouth. The tropical fit for convection reduces precipitation over the ocean by 30% in the inter-tropical convergence zone (ITCZ). The decrease of ocean precipitation by the tropical convection parameterisation confirms previous studies with REMO in Indonesia [Aldrian, 2003]. Concurrently, convection is enhanced by 50% at the point where maritime air masses first penetrate the continent, that is over the Amazon delta, in agreement with the observations. Since this experiment was limited to one year, it cannot be concluded whether the 15% decrease in precipitation at the Andean foothills is significant, since it is in the same order of magnitude as REMO's atmospheric internal variability.

In conclusion, deficiencies noted in REMO and ECHAM are widely shared in other circulation model studies over South America. REMO produces an general overestimation of precipitation throughout the year, however neither the seasonal variations nor the regional relative patterns are severely affected. The convective parameterisation overestimated precipitation in the Tropics. Due to intense evapo-transpiration, atmospheric moisture is recycled over the Amazon basin. Hence, precipitation is maintained at high levels downstream. Nevertheless, REMO reproduces increased orographic precipitation over the Andes that is physically consistent. The latter is not captured by the gridded observation data sets. The most severe discrepancy (maxima at [75°W;5°S] instead of [50°W;5°S] in March) is inherited from the host simulation by ECHAM T30, and could possibly be improved with nudging procedures [von Storch et al., 2000, Seth and Rojas, 2003].

4.3.2 Atmospheric circulation

The isotopic signature of a given rain-fall is not only sensitive to local precipitation, but to its integrated history along the parcel trajectory. Hence, a good knowledge of the regional circulation is essential for the interpretation of δ^{18}O records. In the present section, we demonstrate how REMO reproduces typical characteristics of atmospheric circulation over South America, before looking at the isotopic signal in the following section. Previous studies have shown the improved simulation of South American climate using a regional circulation model [Chou et al., 2000, Vernekar et al., 2003, Seth and Rojas, 2003, Rojas and Seth, 2003].

At first, we look at the mean sea-level pressure (MSLP) in REMO and ECHAM T30, compared with re-analyses data from ERA40 [ECMWF and Raoult, 2003]. The ERA40 MSLP [White, 2002] is computed using the standard approach (also referred to as Sheull method). The vertical profile of temperature below the surface is extrapolated from the temperature in the first level, based on the standard tropospheric lapse rate $\partial T/\partial z = -6.5K \cdot km^{-1}$ (with corrections for extreme cold/warm conditions). By this method, the Andes are represented with an MSLP higher by 2 hPa than surrounding lowlands. The computation of MSLP in ECHAM, based on the same principle [Kornblüh et al., 2003], produces a negative bias of -2 hPa.
This method is not well suited for RCMs, because this altitude bias is enhanced due to the improved representation of orography. For the present study, we developed a new method, extending the membrane SLP deduction method (suggested by Mesinger [1996]) to the 3-D case. The bias over highlands cannot be corrected entirely, but its amplitude is reduced to 0.5 hPa. A detailed discussion of SLP computation is given in the appendix (p. 136).

Figure 4.3 shows the mean sea-level pressures for REMO, ECHAM T30 and ERA40. All data sets agree in reproducing the general patterns of MSLP both over land and ocean, as well as their seasonal variations. As in the re-analyses, two zones of high pressure are found over sub-tropical oceans, between $25°S$ and $30°S$. They represent the descending branch of the Hadley cells. Subsidence over the Pacific is stronger in austral summer (DJF) than over the Atlantic, but weaker in austral winter (JJA). REMO underestimates by up to 1 hPa the MSLP over the tropical oceans in areas with precipitation maxima. This is consistent with the sensitivity test on convection parameterisation: the standard parameterisation

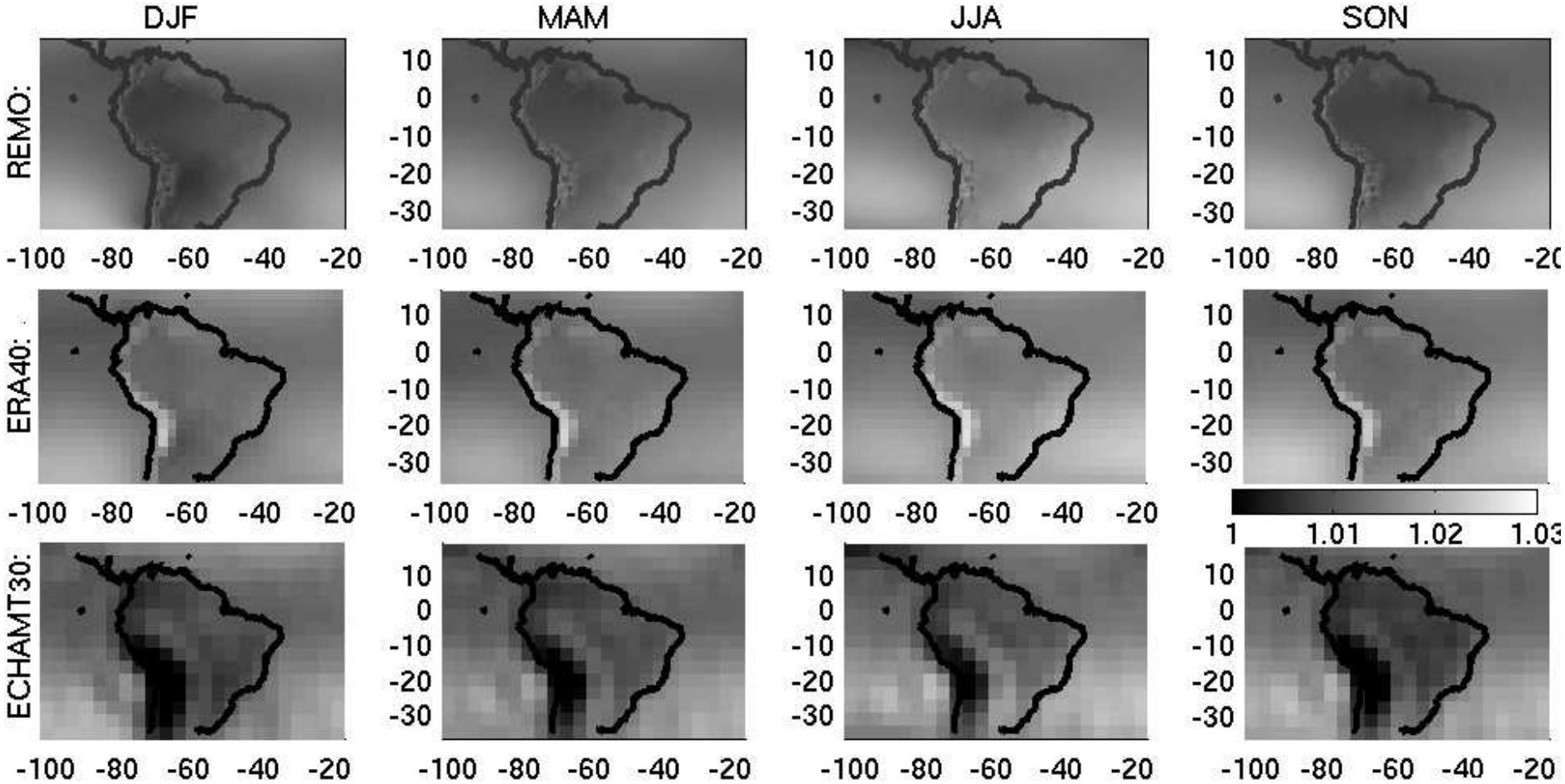

Figure 4.3: Mean sea level pressure (MSLP) in Pascals for austral summer (DJF), autumn (MAM), winter (JJA) and spring (SON). REMO MSLP are represented in the upper row, ERA40 [ECMWF and Raoult, 2003] in the middle row and ECHAM T30 in the lower row. The location of the Chaco Low is marked by 'CL' during DJF.

produces excessive precipitation over the ocean, hence stronger down-drafts and reduced pressure under the ITCZ.
Unlike over the ocean, MSLP in REMO/ECHAM T30 have a generalised negative bias over land. Despite this underestimation, the relative patterns of MSLP, and thus the gradients guiding the geostrophic flows, are well reproduced in REMO. In particular, the build-up of high temperatures east of the Andes during austral spring result in a distinct thermal low during summer. In agreement with the ERA40 data set, the structure (referred to as Chaco low) develops in austral summer (DJF) at the eastern edge of the Andes. REMO locates it at [60°W; 25°S], slightly higher North than the re-analyses.

Several modelling studies show discrepancies in MSLP as observed in REMO [Lenters and Cook, 1995, Rojas and Seth, 2003]. The GFDL GCM overestimates by up to 30m the geopotential at 1000 hPa over the ocean, which corresponds to an underestimation of MSLP by up to 3 hPa. This is in the same range as REMO's error over the ocean.
Rojas and Seth [2003] analyses the MSLP bias in several RCM runs, which show a similar land/sea contrast. The bias is larger in Amazon and Southeast Brazil than in the Nordeste. The bias reaches 4 hPa, with MSLP values lower than re-analyses in austral summer (DJF), and higher in austral autumn (MAM). Due to the different methods in computing MSLP, no direct comparison is possible between these results and observations with REMO. Nevertheless, the seasonal variations of the bias is consistent between RegCM and REMO runs. In general, Christensen et al. [1997] reports MSLP errors by different RCM that commonly reach 3 hPa, with generally negative bias over land. Under such perspectives, MSLP simulated by REMO is in reasonably good agreement with re-analyses.

The Bolivian High (BH), and its counterpart the Nordeste Low (NL), are characterised by their geopotential heights. Figure 4.4 shows the vertical cross section at $\sim 12°S$ of geopotential and temperature deviations from their zonal mean. The Bolivian High builds up during austral spring (SON), to reach its maximum in austral summer (DJF). As described in Lenters and Cook [1997], the BH is then marked by a 50 m increase in geopotential, centred at 200 hPa and $\sim 65°W$. This is the result of a warm core at 400 hPa, topped by a cold lens at 100 hPa. The Nordeste low, located at $\sim 20°W$ has an inverted structure: a cold core at 400 hPa produces a decrease by 40 m in geopotential height at 200 hPa, topped by a warm core at 100 hPa.
Similar to the GFDL GCM used by Lenters and Cook [1997], the warm core simulated by REMO is lower than in the observations (300 hPa). The latter points out an underestimation of deep convection with REMO's standard parameterisation, in agreement with the tropical sensitivity run. In absence of intense convection over the Amazon, the BH-NL vanishes during austral autumn (MAM) and winter (JJA). The remaining radiative heating over the Altiplano, and associated geopotential anomaly, leaves the 200 hPa wind field unaltered.

The mean seasonal geopotential height, wind field and divergence at 200 hPa are shown on figure 4.5. It is possible to identify during austral summer (DJF) a synoptic maximum of geopotential, which lies 5°North of the minimum of MSLP at [63°W;19°S], and marks the Bolivian High. The BH is further stressed by the anti-cyclonic (counter clockwise) vortex developing around it. On the opposite, the Nordeste Low, located at [22°W;20°S], is characterised by a 100m decrease in geopotential height, which coincides with a cyclonic (clockwise) wind circulation. The major domain of divergence at 200 hPa (corresponding to lower troposphere convergence) is located to the North and the East of the BH. The areas of maximum 200 hPa convergence correspond to high precipitation (as compared to Figures 4.2, 4.7, and 4.8). Strong convergence extends to the North-East over the Atlantic, joining the Inter-Tropical Convergence Zone (ITCZ). A second zone of convergence forms at [30-40°W;30°S], known as the South-Atlantic Convergence Zone (SACZ). In austral winter (JJA), the geopotential height in the Southern Hemisphere adopts a zonal distribution, where both the BH and the NL vanish. The wind field, in geostrophic equilibrium, is perpendicular to the gradient of geopotential, i.e. it flows as westerlies. The major zone of convergence (ITCZ) lies at 10°S over the Pacific and penetrates across the Andes into Columbia and Ecuador. This high convergence is responsible for the heavy precipitation over the Eastern flank of the Andes. Intermediate seasons (MAM and SON) show the abrupt transition from the winter to the summer mode.

These results are in good agreement with Hastenrath [1997], reporting the location of the Bolivian High at [65°W;15°S] and similar divergence patterns. Lenters and Cook [1997] investigate the origin of the BH using the GFDL GCM. As for REMO, the GFDL GCM locates the BH 5°to the South-East as compared to NASA-DAO analyses. Latent heat release related to high convection over the Amazon is the primary cause of the BH. In second order, Lenters and Cook [1997]

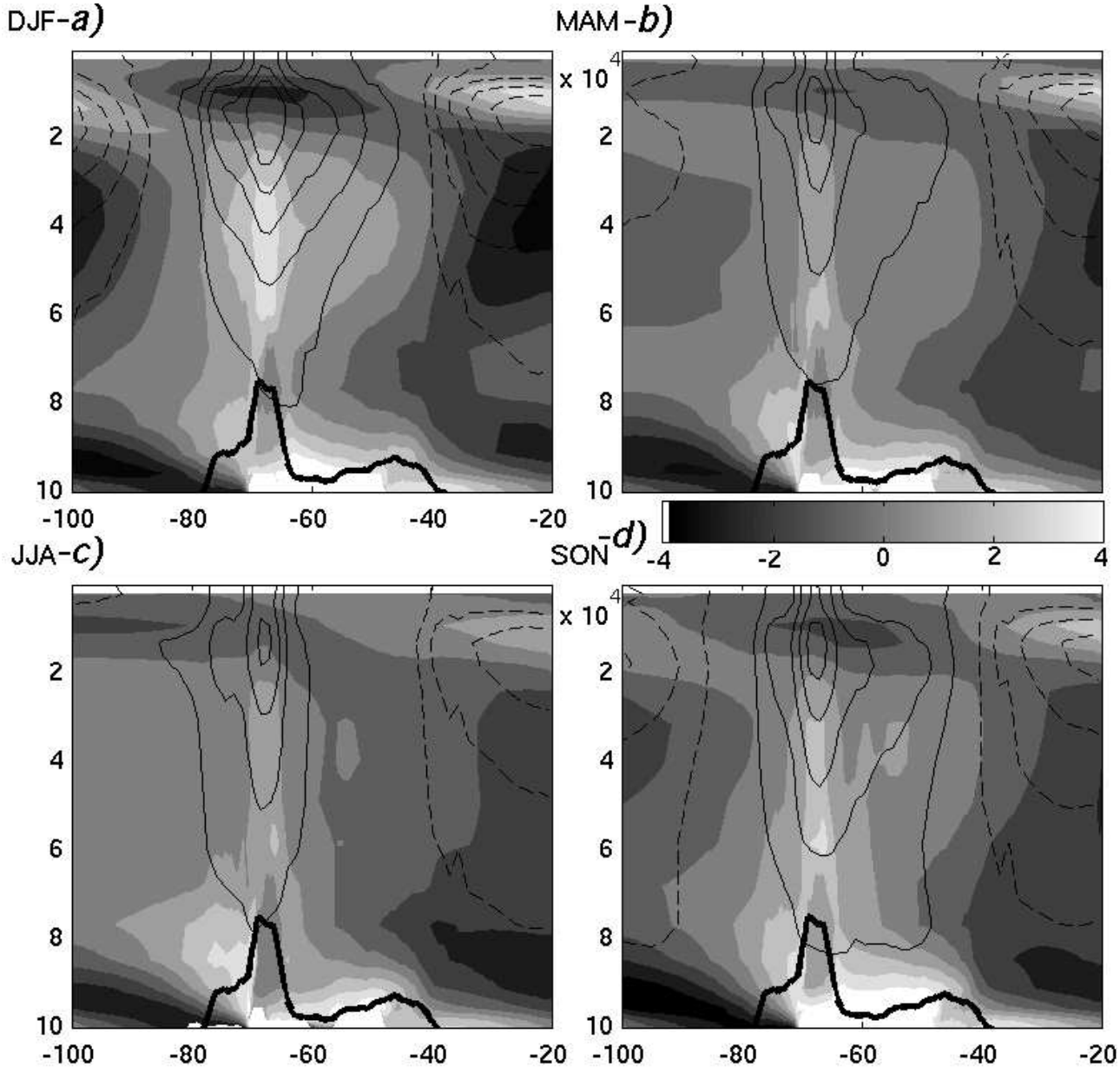

Figure 4.4: Vertical cross section of virtual temperature anomaly (shaded, 1K interval) and geopotential anomaly (contour interval 10m, negative contours dashed) from zonal means, averaged from 10° to 25°S. X-axis represents longitude (degrees), Y-axis the pressure coordinate (100 hPa).

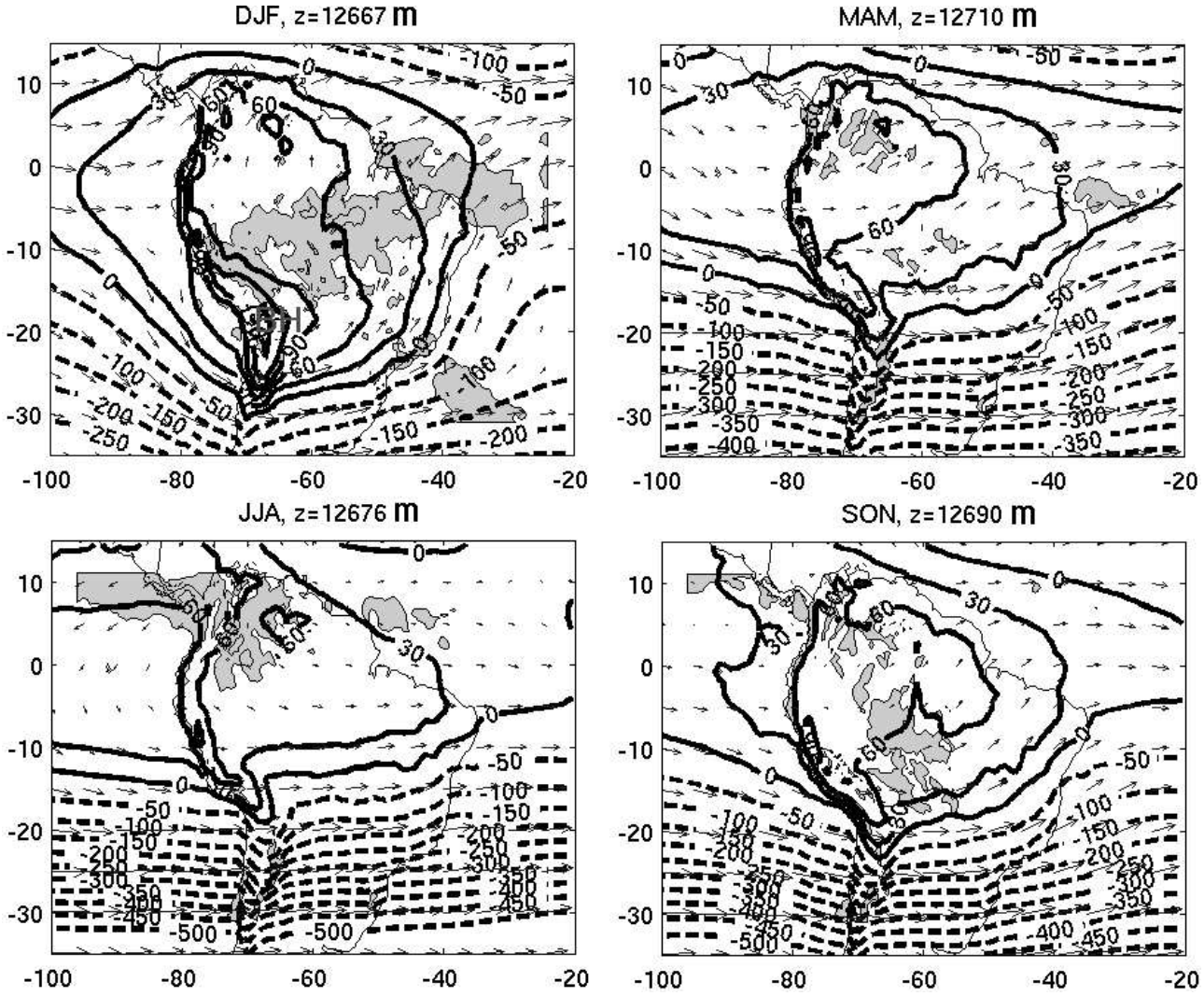

Figure 4.5: Geopotential anomaly from the median $\overline{h}$ in meters at 200 hPa. Values for the median are : in austral summer (DJF) $\overline{h} = 13433m$, in autumn (MAM) $\overline{h} = 13479m$, in winter (JJA) $\overline{h} = 13456m$, and in spring (SON) $\overline{h} = 13456m$. Positive (negative) contours are indicated with continuous (dashed) lines, in a 30 m (50 m) increment. Arrows represent the mean wind field at 200 hPa. Shaded areas indicate wind divergence at 200 hPa exceeding the 75% percentile. The location of the Bolivian High is marked by 'BH' during DJF.

prove that the presence of the Andean relief (at T30 resolution) sharpens the BH and increases its geopotential anomaly by 30m. The higher resolution in REMO confirms the latter, with a geopotential anomaly exceeding 100 m.

4.3.3 Isotopic composition of precipitation

The validity of ECHAM$_{iso}$ has been demonstrated at various resolutions (see [Hoffmann, 2003, Hoffmann et al., 2003, Vuille et al., 2003b]). In the present section, we highlight the similarities and differences between REMO and ECHAM T106/T30 simulations. Evaluation is conducted primarily with the GNIP data set, cited in table 4.1.

The mean annual δ^{18}O in precipitation for all models is shown in figure 4.6. Over the ocean, the ECHAM T106 simulation differs from the climatological ECHAM$_{iso}$ T30 and REMO$_{iso}$. Over the Pacific ocean, the zone of most enriched precipitation lies between [10°S;20°S], symmetrically to its counterpart over the Atlantic Ocean. In both climatological runs (REMO and ECHAM T30), the location of the Atlantic high δ^{18}O is identical, but the Pacific zone is shifted equatorward by 10°.

All three simulations show similar spatial patterns over land, summarised as follows.
1) comparably enriched precipitation over the central Amazon basin, roughly between 5°N and 10°S (e.g. $\overline{\delta^{18}\mathrm{O}} = -3.5‰$ in Manaus, [60.02°W;3.12°S]).
2) moderately depleted precipitation on the highlands of Guiana [65°W;5°N] and Southern Brasil [50°W;20°S], (e.g. $\overline{\delta^{18}\mathrm{O}} = -5‰$ in Campo Grande, [54.67°W;20.47°S]).
3) highly depleted precipitation on the Altiplano and the Andean Cordillera [70°W;15°S], with a magnitude increasing with the models resolution (e.g. $\overline{\delta^{18}\mathrm{O}} = -14.5/-12/-7‰$ for REMO/ECHAM T106/ ECHAM T30 in La Paz, [68.08°W;16.29°S]).
The REMO simulation reproduces identical large-scale patterns to its host simulation, ECHAM T30. This means that no bias in mean annual δ^{18}O is introduced by the regional model. On the other hand, contrasts between highlands and plains are enhanced in the REMO simulation, due to the improved resolution. The next section discusses the physical explanations of the altitude effect (discussion of Table 4.2). Besides the altitude effect, Figure 4.6 reveals an reduced continental gradient over the Amazon basin. The relation between the latter and the neglected fractionation processes in the surface model is discussed in connection with Table 4.3.

Spatial distribution of δ^{18}O strongly varies according to the season. δ^{18}O and precipitation amounts during the wet season (austral summer - DJF) is shown in Figure 4.7; similar maps for ECHAM T106 and T30 can be found in Hoffmann et al. [2003], Vuille et al. [2003b]. δ^{18}O is anti-correlated with precipitation, underlining the amount effect [Dansgaard, 1964].
Furthermore, the rainy season records a NW-SE gradient of decreasing δ^{18}O, from the central Andes to the Paraná region. The horizontal moisture transport $\vec{H}$ in Figure 4.7 shows that Amazonian moisture is transported by strong winds from the Central Andes to the Paraná regions. Brahmananda Rao et al. [1996] reports similar figures for vertically integrated moisture transport throughout the year. This low-level motion is associated with high convergence in summer (shown in Figure 4.5) and increasing precipitation along the path. Meridional flow combines with progressive rain-out to produce the progressive depletion of precipitation between the origin of low-level jets ([70°W;10°S]) and the maximum precipitation associated with the continental extension of the south Atlantic convergence zone (SACZ) at [45°W;20°S]. Advection of moist air along the Andean ridge by LLJ, causing excessive precipitation in the continental SACZ extension, is referred to as South American Monsoon System (SAMS). The NW-SE δ^{18}O gradient proves that stable water isotopes are a good proxy of the SAMS. This aspect is investigated in a separate study [Sturm et al., 2005b].

Austral winter (JJA) climate characteristics are shown in Figure 4.8. The weak continental gradient observed on annual means (Figure 4.6) vanishes, with maximum δ^{18}O around [45°W;7°S]. This is in contradiction with the classical land-inwards depletion of enriched, maritime air masses. High δ^{18}O values (between 0‰ and -2‰) propagate from the Amazon basin along the east flank of the Andes, reaching subtropical latitudes (30°S). δ^{18}O thus marks the persistence of low-level jets (LLJ) during austral winter, albeit with lesser strength than summer [Vera, 2002]. A comparison of the δ^{18}O gradient across the Amazon basin between REMO, ECHAM T106, ECHAM T30 and GNIP is presented in the next

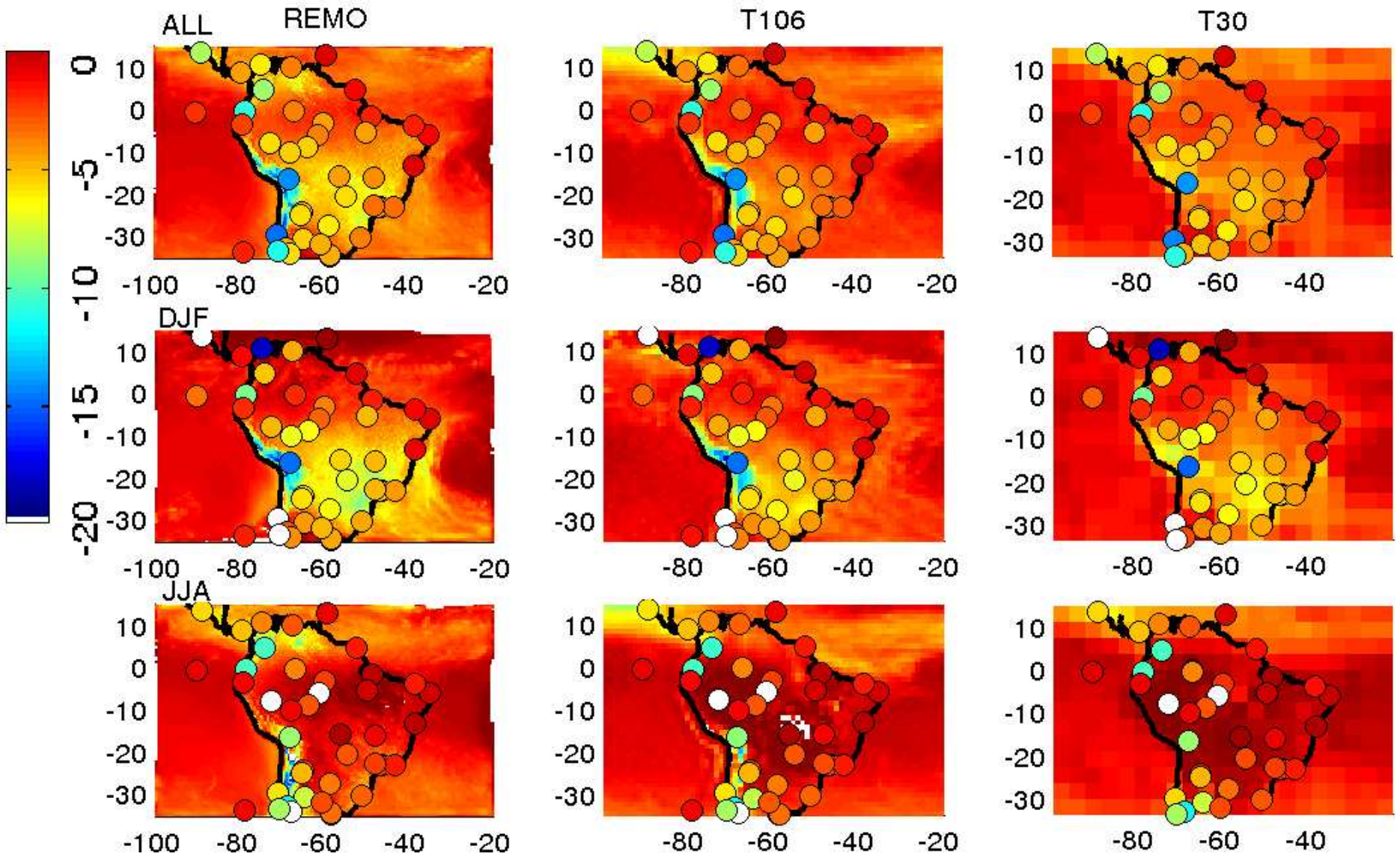

Figure 4.6: Mean annual (upper row), summer (middle row) and winter (lower row) precipitation $\delta^{18}O$ (in ‰) for REMO, ECHAM T106 and T30. Annual means from the GNIP climatology are represented as coloured dots.

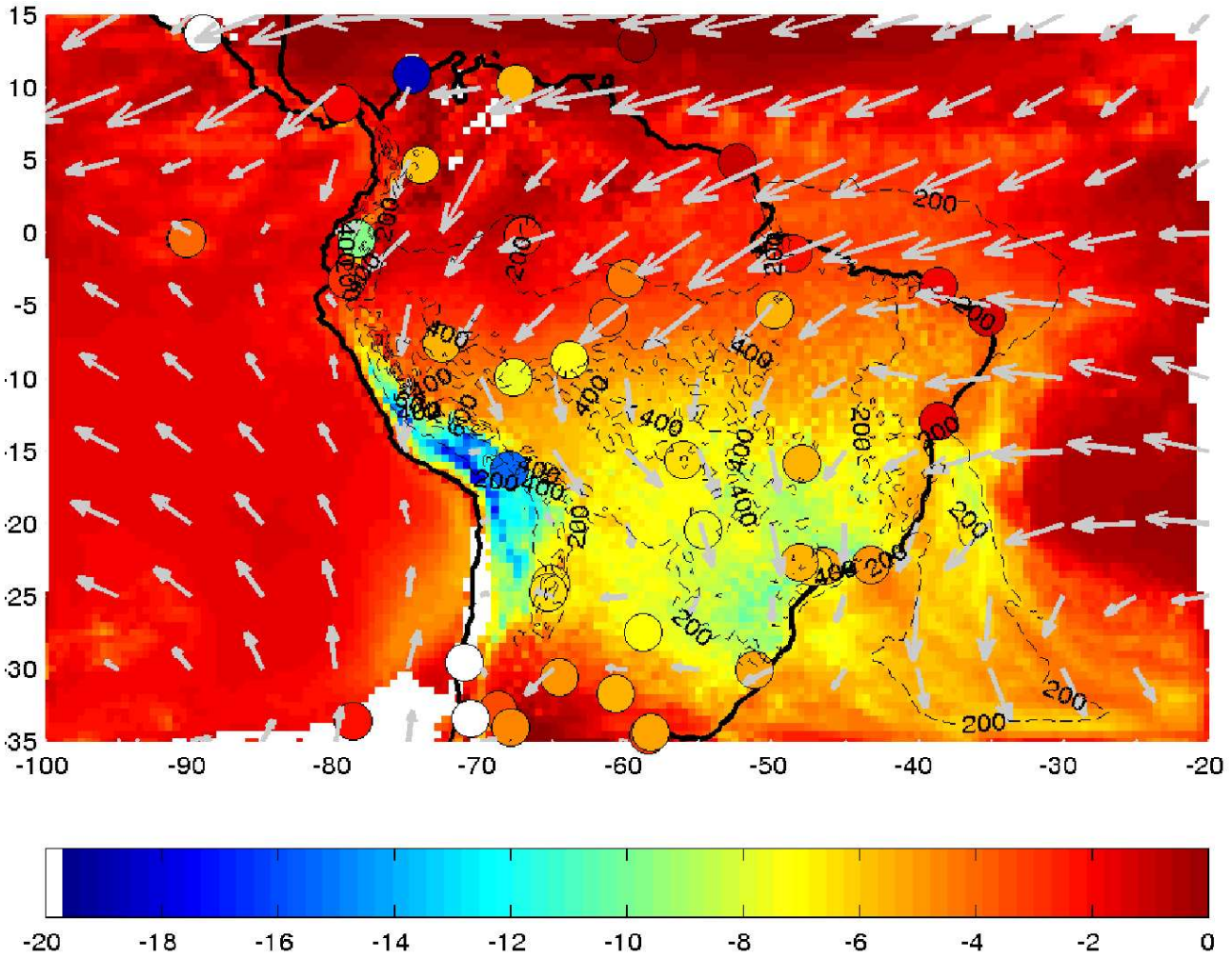

Figure 4.7: Mean austral summer $\delta^{18}O$ in precipitation (in $‰$) for REMO. Contours represent the precipitation amounts (in mm/month), and arrows the horizontal vapour transport. GNIP mean values over the same period are represented as coloured dots.

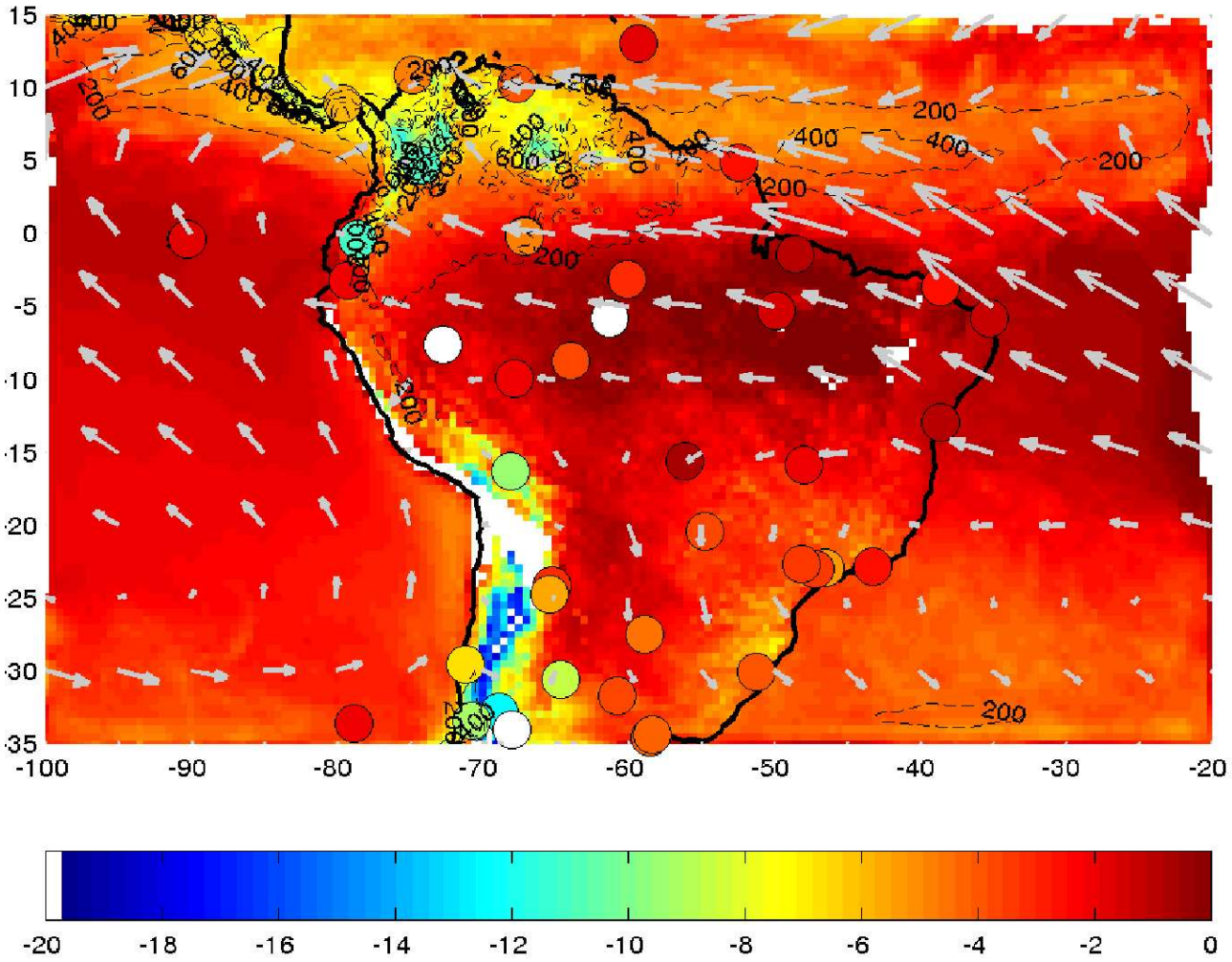

Figure 4.8: Same as figure 4.7, but for the austral winter.

section.

In order to assess the model skill in representing both the mean value and the seasonal variations of the isotopic signal, we computed the figure of merit in time (FMT *) respective to GNIP monthly values. The skills are very similar for all three models: FMT generally lie between 0.6 and 0.8 in the subtropics, but reach their minimum values (0.4) in the Amazon. Resolution improves marginally the skills: the median FMT for ECHAM T30, ECHAM T106 and REMO are respectively 0.515/0.567/0.585.

One limitation of the FMT is that mean grid-cell precipitation at different resolutions are compared to station measurements. A more consistent way of comparing model results with each other is to up-scale at the coarsest resolution prior to comparing the results. We averaged the results over a $5^\circ \times ^\circ$ box: for ECHAM T30, this box covers 2-4, for ECHAM T106 16-25, for REMO 101 grid cells. We compare the average value, the 25% and 75% percentile of model data to the point measurements of stations comprised in the box. We select three locations of particular climatic interest for this study: a coastal area, around Cayenne [52-57°W;0-5°N], an Amazonian area, around Manaus [58-63°W;2-7°S], and an area at the foothills of the Andes around Pôrto Velho [62-67°W;7-12°S]†.

The climatologies of δ^{18}O and precipitation for each region are shown in figure 4.9. The precipitation climatologies reflect the same deficiencies as reported in the previous section (cf. Figures 4.1, 4.2). The GNIP precipitation in Cayenne nevertheless overestimates the precipitation by 33% as compared to the WML data set. It is worth noticing the shift from the inner tropics (Cayenne and Manaus), with a double peak in the wet season, to the outer tropics (Pôrto Velho), with a single peaked wet season.

In the coastal area, all four data-sets have in common a weak seasonal amplitude (difference between maximal and minimal monthly value) of the δ^{18}O signal, although it is well pronounced for precipitation. No significant deviation in δ^{18}O is observed between the three models. Simulated δ^{18}O is underestimated by 3 ‰ from October to January, corresponding to the first peak of the wet season. Furthermore, it is worth noticing that precipitation is more depleted during the first peak, although the local precipitation amounts are larger during the second peak.

In the Amazon region, the seasonal amplitude reaches 6 ‰ for all data sets, increasing as a result of continentality. All models overestimate δ^{18}O by 3 ‰ all year round (once the amount effect is corrected for the excess precipitation from September to December). ECHAM T30 produces more rain during the first peak than during the second one; accordingly, the precipitation is more depleted during the first peak than during the second. The inverse occurs for the ECHAM T106 run, yet precipitation during the second peak is less depleted than expected (for the same reason as above). REMO overestimates precipitation as compared to ECHAM T30, but without being more depleted. It is worth noticing that the minimum δ^{18}O occurs in May, i.e. one month after the maximum in precipitation.

In the Andean foothills, REMO's precipitation agrees best with the GNIP and WML data sets. Remarkably, the δ^{18}O signal conserves a double peaked shape even though precipitation does not exhibit this feature. Models overestimate δ^{18}O by 5 ‰ during the dry season (July to September) and the late wet season (February to April).

Several conclusions can be drawn from these observations. Firstly, the permanent positive bias in δ^{18}O at Manaus is caused by the non-fractionation fractionation fluxes at the surface. Currently, all vapour flux at the surface is considered non-fractionating, assuming that most of it is due to transpiration by vegetation. This study proves that evaporation from the bare water bodies (rivers, ponds, puddles), and the inherent kinetic and thermodynamic fractionation cannot be neglected, especially during the dry season. This underestimation of the continental gradient during the dry season is shared by the by the ECHAM T106 model, as well as isotope-enabled GISS II GCM [Vuille et al., 2003b].

Secondly, analysis of the back-trajectories from Cayenne for water vapour explains the different isotopic signature of the double wet season. In MAM, the ITCZ lies to the South of Cayenne, and air masses are drifted by Northern westerlies. Hence moisture precipitating over Cayenne originates from the nearby tropical Atlantic, with a less depleted initial state. In SON, the ITCZ has travelled North of Cayenne, and the Southern westerlies prevail, Hence moisture originates from

*Figure of merit in time is defined as follows: $FMT = \frac{\sum_{i=1}^{12} \min\left(|\delta^{18}O_{mod}(i)|,|\delta^{18}O_{GNIP}(i)|\right)}{\sum_{i=1}^{12} \max\left(|\delta^{18}O_{mod}(i)|,|\delta^{18}O_{GNIP}(i)|\right)}$, where $\delta^{18}O(i)$ represents the monthly value, 'mod' stands for simulations and 'GNIP' for observations. In case of perfect agreement, FMT equals 1, and decreases towards 0 otherwise.

†Pôrto Velho, in Brasil, is not strictly speaking at the foothills of the Andes. Yet the climatologies are very similar to the southwards shifted box [62-67°W;2-7°S], (Zongo valley in the Yungas). Unfortunately, no GNIP is available in the Zongo box, thus we preferred to show results around Pôrto Velho.

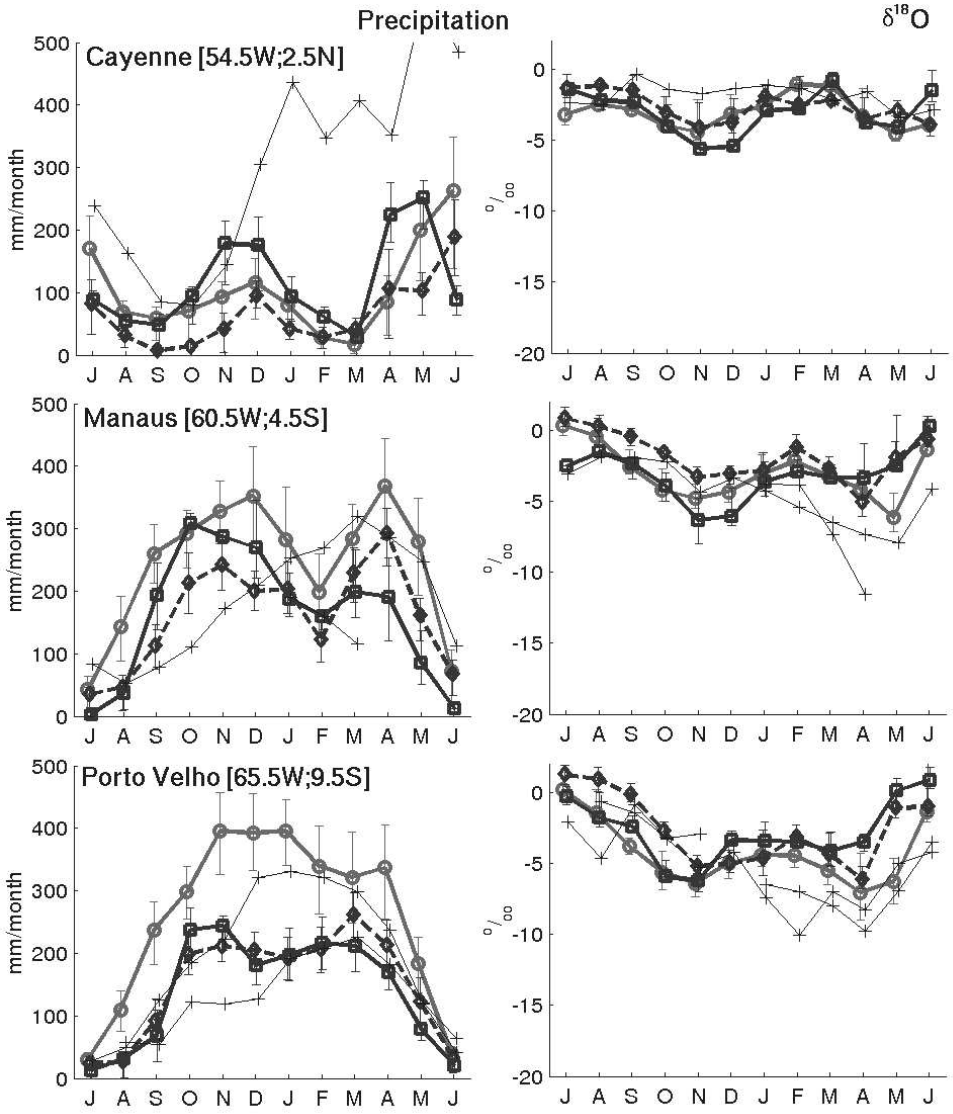

Figure 4.9: Precipitation (on the left panel, in mm/month) and $\delta^{18}O$ (on the right panel, in $^{\circ}/_{\circ\circ}$) climatologies for REMO (light grey circles), T106 (dotted black diamonds), T30 (black squares). Precipitation and $\delta^{18}O$ are averaged over a 5x5 degree box centred respectively at [54.5°W;2.5°N], [60.5°W;4.5°S], [65.5°W;9.5°S]. The error bars show the first and third quartile (i.e. 25% and 75% percentile) for grid cells comprised in the box, covering 5 years of data. GNIP stations comprised in the box (respectively Cayenne, Manaus and Pôrto Velho) are depicted with thin crosses.

	Model	Altitude		Latitude		Longitude		MR
		$\Delta\delta^{18}O/\Delta z$ ($‰/100\,m$)	r_z^2	$\Delta\delta^{18}O/\Delta\lvert\varphi\rvert$ ($‰/10°$)	r_φ^2	$\Delta\delta^{18}O/\Delta\lambda$ ($‰/10°$)	r_λ^2	r_{MR}^2
Annual	GNIP	-0.22	68.93%	-0.26	⋆	0.34	14.84%	73.49%
	REMO	-0.17	52.20%	-0.42	11.36%	-0.15	0.72%	56.35%
	T106	-0.16	67.55%	-0.37	11.30%	0.31	13.55%	72.54%
	T30	-0.051	7.08%	0.081	⋆	0.023	⋆	7.62%
DJF	GNIP	-0.23	60.40%	-0.29	⋆	0.14	⋆	62.27%
	REMO	-0.17	24.36%	-0.84	19.12%	-1.1	10.66%	53.38%
	T106	-0.16	49.75%	-0.7	20.53%	-0.059	1.54%	58.62%
	T30	-0.11	8.64%	-0.25	7.99%	-0.64	9.02%	25.47%
MAM	GNIP	-0.25	66.50%	0.001	⋆	0.41	15.33%	69.46%
	REMO	-0.17	54.67%	-0.48	13.17%	-0.15	0.70%	59.78%
	T106	-0.15	65.71%	-0.13	4.25%	0.44	21.13%	71.60%
	T30	-0.035	7.83%	0.0044	⋆	0.33	14.67%	18.04%
JJA	GNIP	-0.19	44.77%	-0.76	⋆	0.46	16.72%	60.99%
	REMO	-0.16	38.57%	-0.8	10.23%	0.88	17.76%	51.94%
	T106	-0.095	20.82%	-0.42	5.91%	0.34	6.31%	25.18%
	T30	0.076	⋆	-0.57	4.11%	0.45	⋆	15.48%
SON	GNIP	-0.19	55.62%	-0.67	⋆	0.31	14.97%	70.45%
	REMO	-0.14	41.30%	-0.24	3.98%	0.41	11.26%	45.46%
	T106	-0.11	40.91%	0.098	⋆	0.57	26.26%	52.79%
	T30	0.03	9.29%	1.0	39.40%	-0.041	⋆	40.82%

Table 4.2: Multi-variate least-square linear regression of $\delta^{18}O$ against altitude, latitude and longitude. The regression slope against altitude is given by $\Delta\delta^{18}O/\Delta z$, with the squared correlation coefficient r_z^2 between $\delta^{18}O$ and altitude alone. Analogous notations apply to latitude (φ) and longitude (λ). The r_{MR}^2 indicates the squared correlation between $\delta^{18}O$ and the multi-variate (MR) fit. ⋆ replaces correlation coefficients that fail the 95% significance test.

the colder, further sub-tropical Atlantic, with a more depleted initial isotopic composition.
Thirdly, the $\delta^{18}O$ signal clearly appears as an integrated proxy of precipitation: the isotopic signal at Pôrto Velho depends not only on the local precipitation rate, but rather on the cumulated precipitation from Cayenne, over Manaus to Pôrto Velho. The next section investigates further this point, by quantifying the amount effect along an air parcel trajectory.

4.4 Climatic interpretation of the water isotope signal

The previous section demonstrates that REMO$_{iso}$ consistently reproduces the isotopic signal in South America, as compared to GNIP and previously validated ECHAM$_{iso}$ simulations. In the present section, we take profit of the comprehensive gridded climate parameters to investigate their physical relationships with $\delta^{18}O$. These relations can later be applied to interpret station $\delta^{18}O$ measurements as a regional climate proxy.

4.4.1 The simulated altitude effect

Altitude appears as the mean control on the mean annual $\delta^{18}O$ distribution (Figure 4.6). Continentality exerts a second order control, which is most obvious in lowlands (Amazon, Chaco). In order to quantify these controls, a multi-variate linear regression of $\delta^{18}O$ is computed with regard to 3 independent variables: altitude, latitude, longitude. Furthermore $\delta^{18}O$ distribution is proven to display large seasonal variations. Hence the regression was computed both for annual and seasonal means. The regression slopes, along with the squared correlation coefficients are listed in Table 4.2.
The multi-variate regression on geographical coordinates does not succeed in capturing the $\delta^{18}O$ variability simulated by ECHAM T30. Hence this coarse resolution simulation is not discussed further in the present paragraph. Furthermore, the spatial inhomogeneity of GNIP station locations makes the interpretation its regression parameters questionable. In the

following, we concentrate on the REMO and ECHAM T106 simulations.

For all data sets, except the low-resolution ECHAM T30 simulation, more than half of the δ^{18}O variance is controlled by altitude. The annual regression slope $\Delta\delta^{18}O/\Delta z \sim -0.2‰/100m$ is similar for (high resolution) models and GNIP observations. Simulated altitude gradient are in good agreement with observational evidence. Gonfiantini et al. [2001], Roche et al. [1999] report altitude gradients along the Yungas valley (Bolivia) between -0.148 and -0.239 $‰/100m$, which is slightly steeper than gradients observed on Mount Cameroun. Tropical δ^{18}O altitude gradients are among the weaker values world-wide, which range from -0.4 to -0.16 $‰/100m$, [Siegenthaler and Oeschger, 1980]. Vogel et al. [1975] reports altitude gradients in the mid-latitude Argentina between -0.6 and -0.1 $‰/100m$.
Continentality explains at most 5% of the residual variance of mean annual δ^{18}O. Computed continental gradients of $-0.3 \pm 0.1‰/10^\circ$ are one order of magnitude smaller than mid-latitude ones (-3.4$‰/10^\circ$ in Western Europe [Rozanski et al., 1993]).

Although the relative control of the altitude effect varies throughout the seasons, the regression slopes remain remarkably stable ($\pm 0.01‰/100m$). In accordance with Gonfiantini et al. [2001], the altitude gradient is slightly larger during the rainy season (DJFMAM) than the dry season (JJASON).
The altitude control appears to be strongest during austral spring (SON) and autumn (MAM). During austral summer (DJF), the altitude control reaches its minimum for REMO ($r^2 = 24\%$), and second smallest value for ECHAM T106 ($r^2 = 49\%$). As obvious on Figure 4.7, a latitudinal gradient becomes significant. Both simulations show a similar latitudinal gradient ($\Delta\delta^{18}O/\Delta|l| \sim -0.8‰/10^\circ$), i.e. twice the annual gradient.
The altitude control is weak too during austral winter (JJA) (REMO: $r^2 = 39\%$, ECHAM T106: $r^2 = 21\%$). Contrasting with DJF, the δ^{18}O are marked by a longitudinal gradient as secondary control. A specific analysis of the continental effect, focused on the Amazon basin is presented in the next subsection.

The higher resolutions, thus finer orography in REMO and ECHAM T106 permit a closer look in the altitude effect. Roche et al. [1999] evidenced an increased (absolute) gradient $\partial\delta^{18}O/\partial z$ increase with altitude. This behaviour is reproduced by the high resolution simulations, which was not accounted for with the previous linear regression. In this paragraph, we discuss the absolute values of altitude gradient, which is always negative.
The gridded δ^{18}O/altitude gradient is computed according to Equation 4.1.

$$\begin{aligned} \frac{\partial\delta^{18}O}{\partial z}(x,y) &= \frac{||\vec{\nabla}\cdot\delta^{18}O(x,y)||}{||\vec{\nabla}\cdot z(x,y)||} \\ \Leftrightarrow \frac{\partial\delta^{18}O}{\partial z}(x,y) &= \frac{\sqrt{\left(\frac{\partial\delta^{18}O(x,y)}{\partial x}\right)^2+\left(\frac{\partial\delta^{18}O(x,y)}{\partial y}\right)^2}}{\sqrt{\left(\frac{\partial z(x,y)}{\partial x}\right)^2+\left(\frac{\partial z(x,y)}{\partial y}\right)^2}} \end{aligned} \tag{4.1}$$

We select the points above 1500 m, with a mean topographic slope $||\vec{\nabla}\cdot z(x,y)|| > 500m/1000km$. These requirements are met by 346 (84) points from the REMO (ECHAM T106) gridded topography. The corresponding scatter plot is shown in Figure 4.10. Annual and seasonal means are fitted with a second order polynomial, to account for the increase of $\partial\delta^{18}O/\partial z$ with height.

Positive $\partial^2\delta^{18}O/\partial z^2$ is noticeable in ECHAM T106. $\partial\delta^{18}O/\partial z$ lies around 0.2 $‰/100\,m$ below 3000 m, and increases towards 0.4 $‰/100\,m$ above 3500 m. Large scatter exist around the quadratic fit, which accounts for 30% of the variance. At T106 resolution, no significant seasonal dependence of $\partial^2\delta^{18}O/\partial z^2$ can be observed.

REMO records a stronger $\partial^2\delta^{18}O/\partial z^2$ than ECHAM T106. $\partial\delta^{18}O/\partial z$ increases from 0.2 $‰/100\,m$ at 1500 m to 0.6 $‰/100\,m$ at 4000 m. 46% of the mean annual $\partial\delta^{18}O/\partial z$ is captured by the quadratic fit.
Despite of the remaining scatter, significant differences appear between the rainy season (DJF) and the dry season (JJA). During DJF, $\partial^2\delta^{18}O/\partial z^2$ is less steep than for the rest of the year. Austral spring (autumn) displays an intermediate behaviours, recording the dry-wet (wet-dry) transition.

The shape and range of $\partial\delta^{18}O/\partial z$ variations agree well with pure Rayleigh distillation, as modelled in Gonfiantini et al. [2001]. The quadratic fit for DJF resembles the pure Rayleigh distillation, assuming a tropospheric lapse rate of $-6.5°C\cdot km^{-1}$ and initial relative humidity of 80%. The JJA fit agrees best with Rayleigh distillation from an initial 60% relative

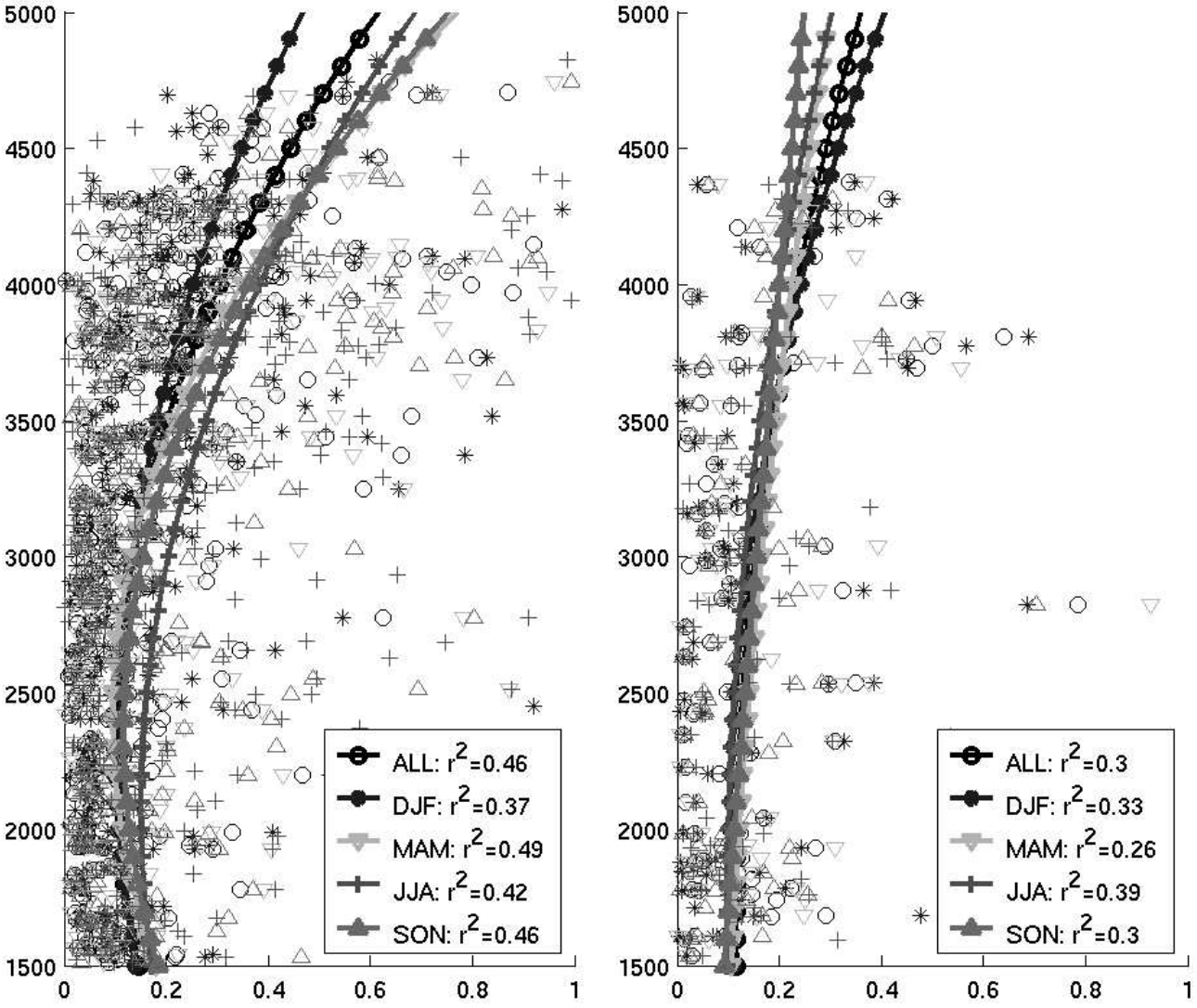

Figure 4.10: Variation of the vertical $\delta^{18}O$ gradient ($\partial\delta^{18}O/\partial z$, in $[‰/100m]$) with altitude (in meters) for REMO (left panel) and ECHAM T106 (right panel). Altitude gradient is given in absolute values. Mean annual values are represented as circles. Mean seasonal values are pictured as follows: DJF - stars, MAM - downwards triangle, JJA - crosses, SON - upwards triangle. Thick lines represent the quadratic fit for annual means and seasonal means. r^2 indicated in the legend indicates the squared correlation coefficient for the quadratic fit.

	Model	$\delta^{18}O$			Precipitation		
		$\overline{\delta^{18}O}$ $‰$	$\Delta\delta^{18}O/\Delta\lambda$ $(‰/10^\circ)$	r^2_δ	$\overline{P}$ mm	$\Delta P/\Delta\lambda$ $mm/10^\circ$	r^2_P
Annual	GNIP	-4.50	-1.1	82.08%	180.46	$\star$	$\star$
	REMO	-4.09	0.13	51.35%	193.66	46	92.73%
	T106	-3.15	0.26	37.01%	130.36	39	82.17%
	T30	-3.94	-0.024	0.77%*	134.50	17	71.22%
DJF	GNIP	-4.05	-1.2	57.63%	212.09	$\star$	$\star$
	REMO	-3.88	0.32	49.82%	270.56	19	43.51%
	T106	-3.16	-0.026	0.73%*	170.87	29	78.33%
	T30	-3.97	0.0028	0.00%*	214.82	-6.7	14.54%*
MAM	GNIP	-6.15	-1.5	92.81%	257.39	$\star$	$\star$
	REMO	-4.80	0.033	2.75%*	261.83	31	76.99%
	T106	-3.93	-0.014	0.06%*	192.66	32	57.70%
	T30	-3.64	-0.025	0.68%*	159.93	5.7	20.02%*
JJA	GNIP	-2.72	-0.39	20.43%*	124.70	$\star$	$\star$
	REMO	-1.33	-0.082	3.92%*	69.86	42	84.68%
	T106	-1.42	1.3	84.94%	56.14	26	53.90%
	T30	-0.62	0.36	45.51	21.67	13	48.56%
SON	GNIP	-2.04	-0.48	21.60%*	106.73	$\star$	$\star$
	REMO	-3.49	-0.94	93.67%	172.37	92	84.58%
	T106	-2.32	-0.24	35.15%	101.76	71	91.12%
	T30	-4.71	-0.088	3.65%*	141.56	57	74.78%

Table 4.3: $\delta^{18}O$ and precipitation continental gradient along the Amazon basin. Results are weighted latitudinally between [0°S; 10°S]. In the case of GNIP, 9 stations comprised in the averaging domain are taken into account. Linear regression with longitude is computed on a [75°W; 35°W] transect. Sign convention is such that a $\Delta/\Delta\lambda > 0$ if it is increasing with continentality. Since easterlies dominate over the Amazon, the continental gradient $\Delta/\Delta\lambda$ is of opposite sign to the longitudinal gradient $\Delta/\Delta L$. For $\delta^{18}O$ (precipitation), the slope in given in $‰/10^\circ$(mm/10°). $\star$ indicate regressions that fail the 95% significance test.

humidity. During the wet season (DJF), relative humidity is higher, which explains the less steep altitude gradient in Figure 4.10.

This is partially confirmed by observation evidence. Vimeux et al. [-] reports that the isotopic signature of air masses lifted along the Zongo valley (Bolivia) can be considered as a closed system, hence Rayleigh distillation can be applied. Nevertheless, the pure Raleigh distillation model yields exaggerated $\partial\delta^{18}O/\partial z$ at high elevations. Observations show that $\partial\delta^{18}O/\partial z$ is stable around 0.4 $‰/100\,m$ above 3500 m. The latter behaviour can be explained by a pseudo-Rayleigh distillation: instead of removing all the condensate from the cloud, 15% of the droplets remain in the cloud, where isotopic equilibrium is reached with the vapour.

According to this interpretation, $\delta^{18}O$ simulated by REMO in steep valleys would follow a pure Rayleigh distillation process, which becomes dominant above 1500 m. REMO fails to represent the pseudo-Rayleigh process, i.e. cloud liquid water would be too low and/or not advected properly along the steep valleys. Considering the hydrostatic assumption and the hybrid $\sigma - P$ vertical coordinate system used by REMO, it is questionable whether atmospheric motion in steep relief is well represented.

4.4.2 Continental gradient across the Amazon basin

The issue of continental effect over South America was briefly addressed in connection with Table 4.2. In the present paragraph, we focus on the longitudinal gradient of $\delta^{18}O$ and precipitation across the Amazon basin.

The longitudinal transect is taken over [75°W;35°W] (which eliminates the effect of the Andes), averaged latitudinally between [0°S;10°S]. For GNIP, 9 stations comprised in the area of interest are used in the calculus. Linear regression of

δ^{18}O and precipitation against continentality (longitude of opposite sign) is shown in Table 4.3. Regression slopes $\Delta/\Delta\lambda$ are of opposite sign to $\Delta/\Delta L$. Hence δ^{18}O decreasing land-inwards have negative $\Delta\delta^{18}O/\Delta\lambda$ values.

The continental δ^{18}O gradient for mean annual GNIP values is negative, which is consistent with the land-inwards depletion of precipitation. The slope for the 9 GNIP stations ($-1.1‰/10°$) is steeper than reported by Salati et al. [1979] ($-0.68‰/10°$), based on 16 stations across the Amazon basin. Annual δ^{18}O gradient for REMO and ECHAM T106 are weakly positive, which contradicts the classical continental effect.
This discrepancy is further observed on seasonal basis. REMO displays a strong positive continental gradient during DJF. Figure 4.6 proves that this artefact is due to a hidden latitudinal gradient: δ^{18}O is most depleted in the south-western part of the transect (high precipitation over the Brazilian highlands in connection with the ITCZ-SACZ), whereas it is most enriched in the north-eastern part (dry conditions in the northern Amazon). Salati et al. [1979] reports continental δ^{18}O gradients during JFM ranging from -1.14 to 0.68 $‰/10°$. The isotopic balance model applied to the Amazon basin [Dall'Olio, 1976] yields a steeper negative gradients during DJF (-2.3 $‰/10°$).
All models display an abnormal continental gradient during JJA. The gradient vanishes for REMO and even becomes positive for ECHAM T106 and T30. Salati et al. [1979] shows a large scatter of δ^{18}O during JJA, showing no distinct continental gradient. Similarly, the isotopic balance model shows an initial depletion of δ^{18}O by $1‰$ between 45°W and 60°W, followed by a re-enrichment of same amplitude at 70°W. Vuille et al. [2003b] reports a vanishing of the δ^{18}O continental gradient across the Amazon in the GISS-II isotope-enabled GCM. Furthermore, the mean δ^{18}O is overestimated in all models as compared to GNIP. Precipitation in ECHAM is underestimated during JJA, but REMO is in good agreement with the WML data set. The non-uniform distribution of GNIP stations infers an exaggerated mean precipitation during JJA.

The present modelling results reinforce the role of transpiration on the weakened of the δ^{18}O continental gradient. During the dry season, precipitation is weak, hence the depletion mechanism is diminished. Water uptake by plants is released to the atmosphere without fractionation. Hence, continuous recycling of moisture by vegetation progressively counter-balances, and locally overcomes the continental rain-out. The latter results in a cancelling of the δ^{18}O continental gradient.
The effect of recycling is enhanced in the models, since all vapour fluxes from the surface are considered non-fractionating. This explains the overestimation of $\overline{\delta^{18}O}$ during JJA. When the latter combines with underestimated precipitation (hence reduced amount effect) as in ECHAM T106, the continental gradient is reversed and becomes positive. As further evidence, the modelled deuterium excess (not shown) has a negative bias at Manaus, reflecting the lack of kinetic fractionation over land.

In conclusion, the discrepancies in the simulated δ^{18}O continental gradient across the Amazon basin underline the need of a better representation of land-atmospheric moisture fluxes in circulation models. Nevertheless, these results confirm the potential use of stable water isotopes as a proxy for moisture recycling by the vegetation. Henderson-Sellers et al. [2002] provide a detailed investigation of that topic.

4.4.3 Evolution of the isotopic composition of moisture along its trajectory

Only a fraction of the δ^{18}O variability is explained by local precipitation: the squared correlation coefficient (r^2) of monthly δ^{18}O with precipitation for REMO/ECHAM T106/ECHAM T30 is respectively equal to 23%/32%/39%. This limitation underlines the integrative character of the isotopic signal. It is hence more appropriate to look at the fractionation processes in a Lagrangian referential (i.e. following an air parcel), instead of the traditional Eulerian referential (i.e. station location).
Monthly wind fields from REMO were used to compute the streamline that reach Pôrto Velho [65.5°W;9.5°S] and Ceara Minim [37.5°W;3.5°S]. We make the assumption that streamlines represent the monthly standard back-trajectories. This is justified only if the upstream wind fields are close to stationary. To test it, we computed the wind directional constancy

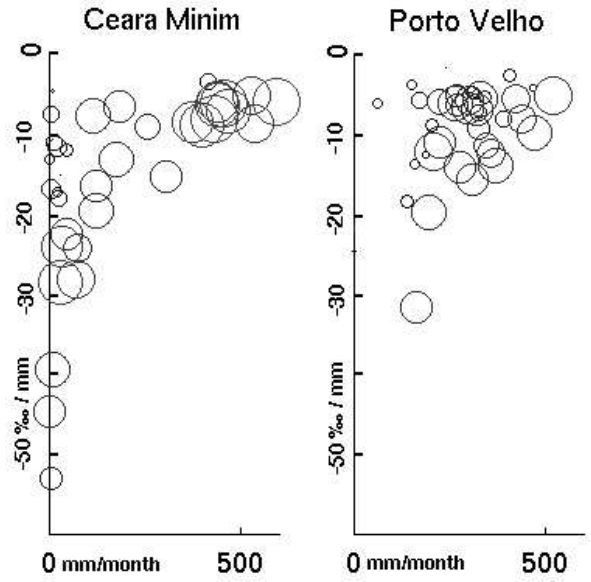

Figure 4.11: Quantification of the amount effect coefficient at a coastal station (Ceara Minim, [37.5°W;3.5°S]) and a continental station (Pôrto Velho, [65.5°W;9.5°S]). Total monthly precipitation is plotted on the X-axis (mm/month), the amount effect coefficient $\partial\delta^{18}O/\partial P$ on the Y-axis (in $‰ \cdot m^{-1}$). The circle size is proportional to the squared correlation coefficient r^2.

on 6-hourly wind fields.

$$D_c = \frac{||\overline{\vec{H}}||}{||\vec{H}||} = \frac{\sqrt{\overline{H_u}^2 + \overline{H_v}^2}}{\sqrt{\overline{H_u^2 + H_v^2}}} \tag{4.2}$$

In case of steady winds, $D_c = 1$, whereas it decreases towards 0 if its direction is very variable. In the present case, $D_c > 0.8$ over tropical South America. Furthermore, the computed streamlines agree well with back-trajectories computed with 6-hr NCEP reanalyses for each calendar month [Vimeux et al., -]. Based on ERA40 reanalyses, Brahmananda Rao et al. [1996] report that vapour transport by transient eddies are negligible north of 30°S (20 °S) during austral summer (winter). Hence mean motion is the dominant vapour advection in tropical South America. All three arguments demonstrate that the assumption above is valid. In the following, trajectories are assimilated to the corresponding streamlines.

A regression of $\delta^{18}O$ against precipitation along the trajectory is performed. Figure 4.11 shows the variation of amount effect coefficient ($AE = \partial\delta^{18}O/\partial P$, in $[‰ \cdot m^{-1}]$) for a typical maritime station, Ceara Minim, and a typical continental station, Pôrto Velho. The squared correlation coefficient r^2 is higher for the maritime station than over land. The squared correlation coefficient r^2 is proportional to the symbol radius. The AE tends to reach its maximum values ($r^2 \leq 0.8$) during the wet season, when precipitation exceeds 500 mm/month.
The variation of AE displays an hyperbolic shape, which is coherent with the Rayleigh distillation theory. During the dry season, the relative degree of distillation is high: even small precipitation events can deplete significantly the cloud vapour. Hence the AE reaches down to $-50‰ \cdot m^{-1}$. During the wet season, AE stabilises at $-7‰ \cdot m^{-1}$, both over land and ocean. The mean value of AE in figure 4.11, calculated in the Lagrangian referential, is in good agreement with $\overline{\partial\delta^{18}O/\partial P} = -9.17‰ \cdot m^{-1}$ calculated in the Eulerian referential. Similar slopes are reported for ECHAM T106/ECHAM T30/GNIP, respectively $\overline{\partial\delta^{18}O/\partial P} = -10.7/-11.5/-9.23‰ \cdot m^{-1}$.

Figure 4.12 shows the back-trajectories from Pôrto Velho in January. They first cross the convergence zone located off Brazil's North Coast, with precipitation peaks exceeding 200 mm/month. This implies a depletion of cloud $\delta^{18}O$ by 1-2 ‰, which is quickly compensated by enriched evaporation over the ocean. Over the continent, the precipitation is steadily increasing with time, producing a gradual decrease of $\delta^{18}O$ by 3-5‰. It is worth noticing that atmospheric motion and convergence zones have a significant inter-annual variability, both in location and intensity. Yet, the AE is

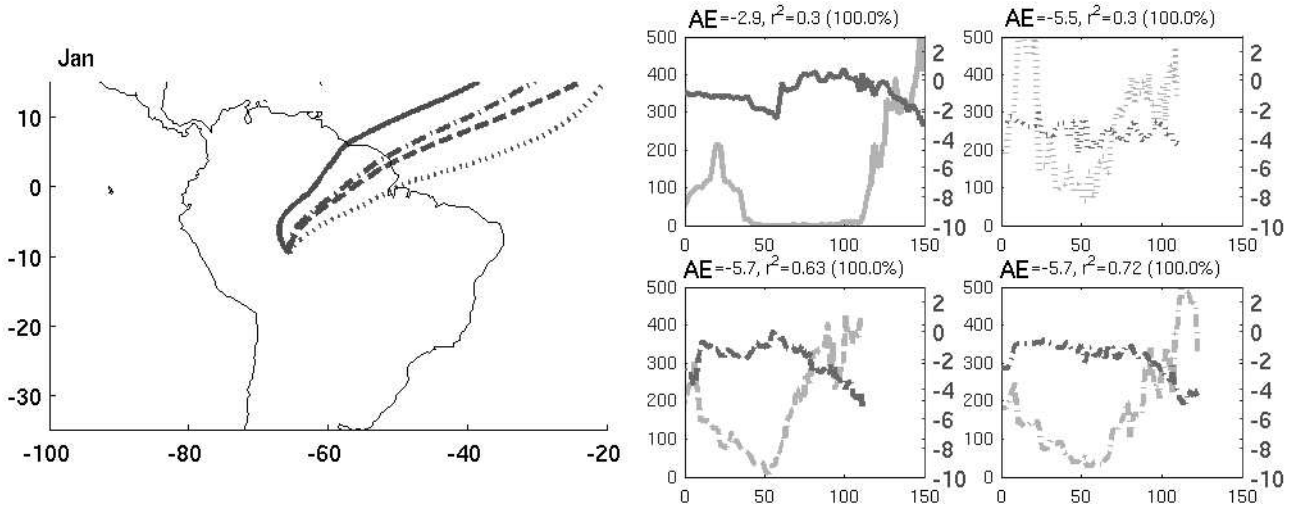

Figure 4.12: The left-hand size panel shows back-trajectories from Pôrto Velho [65.5°W,9.5°S] in January (years 2 to 5). On the right-hand size panel shows, for each year, the evolution of $\delta^{18}O$ (in $‰$, dark grey, Y-axis on the right) and precipitation (in mm/month, light grey, Y-axis on the left) along the trajectory (X-axis, in hours). The 'amount effect' AE (in $‰ \cdot m^{-1}$) is indicated for each case, as well as the squared regression coefficient r^2, and its significance.

fairly constant at $-6‰ \cdot m^{-1}$, with r^2 reaching up to 72%. The continental rain-out is well described by the assumption of a Rayleigh distillation, with condensate (rain) being instantly removed from the reservoir (cloud vapour), without major further inputs (evaporation). Salati et al. [1979] also reports Rayleigh-type distillation processes across the Amazon basin (from Amapá over Manaus to Pôrto Velho) in JFM, where moisture recycling by the vegetation is negligible. It further indicates that the positive $\delta^{18}O$/longitude gradient in DJF for REMO (cf. Table 4.3) is an artefact due to the projection of the trajectory on the X-axis.

Figure 4.13 displays the analogous situation for July, during the dry season. Hardly any precipitation occurs along the trajectory (apart from some orographic precipitation upon reaching the foothills and lowering there the $\delta^{18}O$). Large variations in $\delta^{18}O$ occur, with a positive trend over the continent, reaching positive values. Salati et al. [1979] reports the vanishing of the continental effect during austral winter (JJA). A simple isotopic model taking into account re-evaporation effects locally produces positive continental gradients [Dall'Olio, 1976]. This further reinforces the positive $\delta^{18}O$/longitude gradient reported in Table 4.3.

During the dry season, precipitation no longer controls the isotopic signal. The $\delta^{18}O$ is determined by the isotopic equilibrium at the surface. Non-fractionating transpiration by the vegetation increases the $\delta^{18}O$ of surface vapour. The partial re-equilibration of falling rain droplets with surrounding moisture explains the anomalous high $\delta^{18}O$ values in the heart of the Amazon. This phenomenon is further enhanced in REMO/ECHAM, since all evaporation from the surface is considered non-fractionating.

4.5 Conclusion and perspectives

The present study introduces a simulation of the stable water isotope signal by the regional circulation model $REMO_{iso}$ over tropical South America. The numerical integration is conducted at an horizontal resolution of $0.5°(\sim 53km)$ over a five year period, forced with climatological sea surface temperatures (SST).

The simulated precipitation patterns and their seasonal variability are in good agreement with interpolated rain gauge and satellite observations. The Southern tropics experience a wet season during austral summer (DJF) and a dry season during austral winter(JJA). REMO overestimates precipitation by 30% all year around, but reproduces correctly the distribution of rainfall over the continent. Both ECHAM simulations underestimate precipitation during the dry season (JJA). The major discrepancy between models and observations happens during austral autumn (MAM). Common in REMO

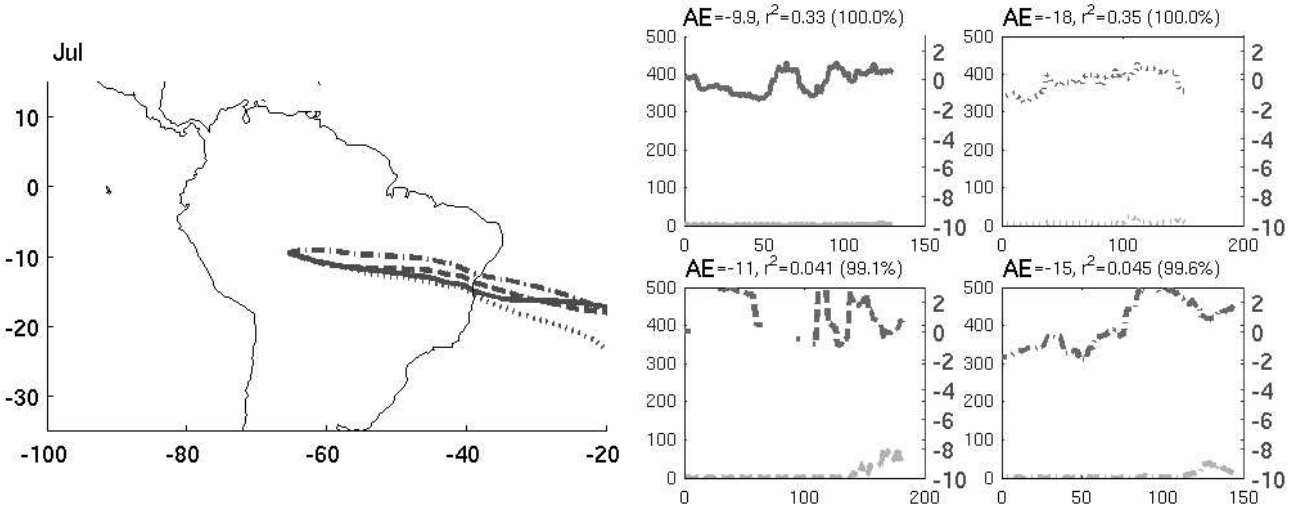

Figure 4.13: As for figure 4.12, but for July.

and ECHAM is exaggerated precipitation over the ocean (in connection with the inter-tropical convergence zone). In opposition to observations, the models locate the maximum of precipitation on the east flank of the Andes instead of the Amazon mouth.

Furthermore, typical meteorological features of the South American climate are well represented in REMO. During austral summer (DJF), the mean sea-level pressures denote a thermal low at [60°W; 25°S] (Chaco low), in agreement with the ERA40 reanalyses. Vertically integrated moisture transport shows a important advection across the Amazon basin, diverted by the Andean Cordillera in a north-west south-east flow towards the Paraná region. Latent heat release by convection over the Amazon basin cause a 4 K warm anomaly at 300 hPa. The latter is responsible for a local maximum of geopotential at 200 hPa around [63°W;19°S] (Bolivian high). The 200 hPa convergence field indicates, besides the inter-tropical convergence zone (ITCZ), the sub-tropical south Atlantic convergence zone (SACZ) at [35°W;30°S].

The δ^{18}O signal in precipitation is in good agreement with isotopic observations (GNIP climatology), as well as coarser resolution general circulation models (ECHAM$_{iso}$ T106 and T30), both on annual and seasonal basis. The three models are compared to GNIP station measurements in a $5^\circ \times 5^\circ$ boxes, located at the coast (Cayenne), in the Amazon basin (Manaus) and at the foothills of the Andes (Pôrto Velho). The simulated isotopic composition is close to observations at the coast, but is overestimated (particularly during the dry season) over the Amazon basin. At Pôrto Velho, precipitation adopts a single maximum distribution typical of the outer tropics, but the δ^{18}O signal inherits the upstream double maxima shape. This underlines the integrative character of the water isotope proxy.

Simulated mean annual δ^{18}O is anti-correlated with altitude for REMO$_{iso}$ and ECHAM$_{iso}$ T106. A closer investigation, using multi-variate regression of δ^{18}O on latitude, longitude and latitude reveals that altitude is the main control of δ^{18}O distribution for all seasons. The simulated δ^{18}O altitude gradient ($\Delta\delta^{18}\mathrm{O}/\Delta z = -1.7‰/100m$) matches reported observed gradients in literature. Only REMO is able to capture the increase of the altitude gradient with height, which suggests that REMO correctly reproduces the lifting of moisture along the Andean slopes as a Rayleigh distillation process.

The compared analysis of a δ^{18}O transect across the Amazon basin reveals that the continental gradient is much weaker than in mid-latitudes. This underlines the importance of moisture recycling by the vegetation, especially during the dry season. Since all evapo-transpiration is considered non-fractionating in the models, the continental gradient vanishes in REMO and even becomes positive in ECHAM T106.

Seasonal maps, as well as box average reinforce the integrative character of δ^{18}O: the isotopic signal in the tropics is a proxy of cumulated precipitation along the trajectory rather than local precipitation. To assess the latter, we identify the common evolution of precipitation and δ^{18}O along the parcel trajectory. This Lagrangian analysis yields a similar

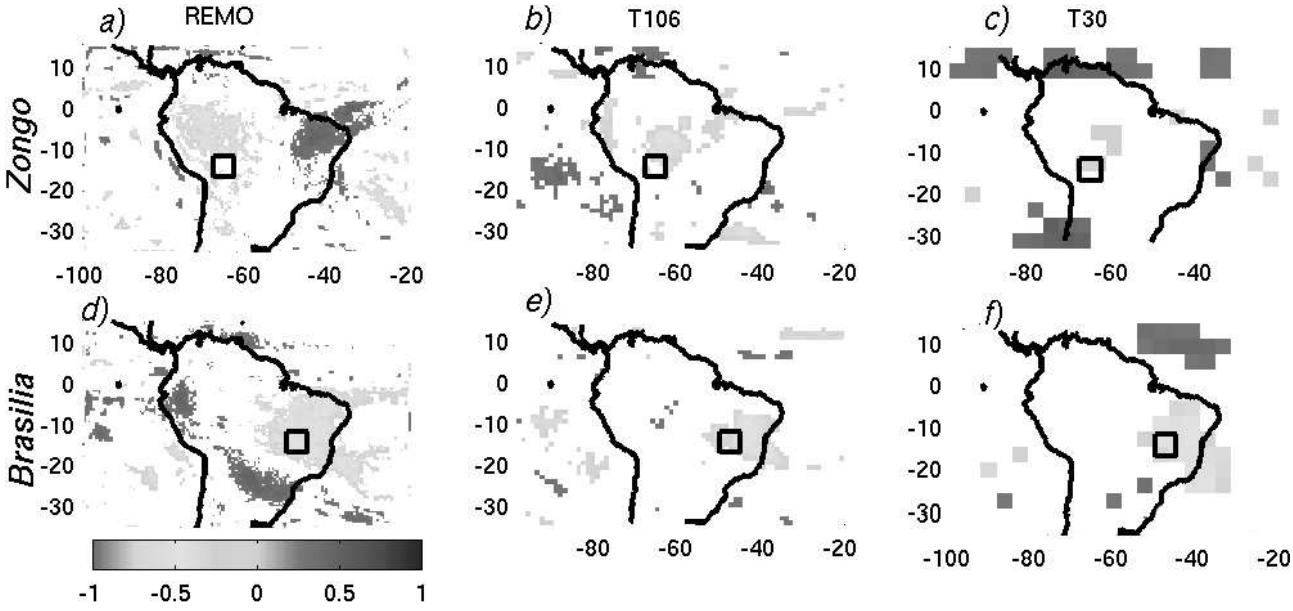

Figure 4.14: Correlation between δ^{18}O anomalies averaged over a $5 \times 5^{\circ}$ box and domain-wide precipitation. In the upper row, average δ^{18}O is computed at the Zongo box, centred [64.5°W; 4.5°S]. In the lower row, average δ^{18}O is computed over the Brasilia box [47.5°W; 14.5°S].

regression slope $\partial\delta^{18}\mathrm{O}/\partial P = -9.17‰ \cdot m^{-1}$ as the regression in the Eulerian referential, but with much higher regression coefficients ($r^2 > 50\%$) during the rainy season. The evolution along the dry season trajectory confirms that evapotranspiration rather than precipitation controls the δ^{18}O.

The present study has focused on the mean (climatological) distribution of δ^{18}O, where the higher resolution improves the simulation of local processes. Hence, variability of δ^{18}O on steep relief is better resolved in REMO, while it remained mostly inaccessible to ECHAM.

The benefits of higher resolution is obvious when looking at other local phenomena, such as the low-level jets (LLJ) along the east flank of the central Andes. As shown on Figure 4.14, correlation of monthly anomalies (from the climatological mean) between the δ^{18}O at the foothills of the Andes and the domain-wide reveals a dipole-shape in REMO. This feature remains largely absent in the coarser ECHAM$_{iso}$ simulations. The dipole structure is related to the variability of the south American monsoon system (SAMS). A detailed investigation of the latter is given in a separate study [Sturm et al., 2005b].

In conclusion, the present study not only validates the REMO$_{iso}$ regional circulation model over South America, but also underlines the benefit of increased resolution for the interpretation of the stable isotopic signal. REMO$_{iso}$ is an appropriate tool to contribute to the interpretation of present isotopic archives (ice-cores, speleothems, isotopic dendrochronology). Further nesting of REMO$_{iso}$ in paleo-simulations by ECHAM$_{iso}$ could assess the regional significance of isotopic archives.

Acknowledgements

The authors would like to thank Martin Werner (Max-Planck-Institute for Biogeochemistry, Jena) for providing the ECHAM$_{iso}$ T106 simulation. Furthermore, the valuable comments by Françoise Vimeux (Institut de Recherche pour le Développement) and Gerhard Krinner (Laboratoire de Glaciologie et Géophysique de l'Environnement) contributed significantly to quality of the manuscript.

All numerical integrations of REMO$_{iso}$ and ECHAM$_{iso}$ were performed on the German Climate Computing Centre (DKRZ, Hamburg). The present work was partly funded by the French science foundation (ACI-Cryosphere and Cli-

mate Change).

Bibliography

E. Aldrian. *Simulations of Indonesian Rainfall with a Hierarchy of Climate Models*. Mpi report 92, Max Planck Institut für Meteorologie, July 2003. 70

R. S. Bradley, M. Vuille, D. Hardy, and L. G. Thompson. Low latitude ice cores record Pacific sea surface temperatures. *Geophysical Research Letters*, 30:23–1, February 2003. 64

V. Brahmananda Rao, I. F. A. Cavalcanti, and K. Hada. Annual variation of rainfall over Brazil and water vapor characteristics over South America. *Journal of Geophysical Research*, 101(10):26539–26552, 1996. 75, 86

S. C. Chou, A. M. B. Nunes, and I. F. A. Cavalcanti. Extended range forecasts over South America using the regional eta model. *Journal of Geophysical Research*, 105(8):10147–10160, 2000. 69, 70

J.H. Christensen, B. Machenhauer, R.G. Jones, C. Schär, P.M. Ruti, M. Castro, and G. Visconti. Validation of present-day regional climate simulations over Europe: LAM simulations with observed boundary conditions. *Climate Dynamics*, 13(7):489 – 506, Aug 1997. 72

M.H. Costa and J.A. Foley. A comparison of datasets for the Amazon basin. *Geophysical Research Letters*, 25(2):155 – 158, 1998. 69

A. Dall'Olio. A composicão isotopica das precipitacãos do Brasil: Modelos isotermicos e a influencia da evapotranspiracão na Basina Amazonica. Master's thesis, University of São Paulo, 1976. 85, 87

W. Dansgaard. Stable isotopes in precipitation. *Tellus*, XVI:436 – 468, 1964. 75

R.M. Doherty, M. Hulme, and C.G. Jones. A Gridded Reconstruction of Land and Ocean Precipitation for the Extended Tropics from 1974 to 1994. *International Journal of Climatology*, 19:119 – 142, 1999. 66, 67

European Center for Medium-Range Weather Forcast ECMWF and B. Raoult. The ECMWF public data server. *ECMWF Newsletter*, 99:18 – 19, July 2003. "http://data.ecmwf.int/data/d/era40_mnth/". 67, 70, 71

P. Ginot, M. Schwikowski, U. Schotterer, W. Stichler, H. W. Gäggeler, B. Francou, R. Gallaire, and B. Pouyaud. Potential for climate variability reconstruction from Andean glaciochemical records. *Annals of Glaciology, vol.35, pp.443-450*, 35:443–450, 2002. 64

R. Gonfiantini, M.A. Roche, J.C. Olivry, J.C. Fontes, and G.M. Zuppi. The altitude effect on the isotopic composition of tropical rains. *Chemical Geology*, 181:147 – 167, Oct 2001. 82

S. Hastenrath. Annual cycle of upper air circulation and convective activity over the tropical Americas. *Journal of Geophysical Research*, 102(11):4267–4274, 1997. 72

A. Henderson-Sellers, K. McGuffie, and H. Zhang. Stable Isotopes as Validation Tools for Global Climate Model Predictions of the Impact of Amazonian Deforestation. *Journal of Climate*, 15:2664–2677, September 2002. 85

G. Hoffmann. Taking the Pulse of the Tropical Water Cycle. *Science*, 301:776 – 777, Aug 2003. 64, 75

G. Hoffmann, E. Ramirez, J.D. Taupin, B. Francou, P. Ribstein, R. Delmas, H. Dürr, R. Gallaire, J. Simões, U. Schotterer, M. Stievenard, and M. Werner. Coherent isotope history of Andean ice cores over the last century. *Geophysical Research Letters*, 30:28–1, February 2003. 64, 75

G. Hoffmann, M. Werner, and M. Heimann. Water isotope module of the ECHAM atmospheric general circulation model: A study on timescales from days to several years. *Journal of Geophysical Research*, 103(14):16 871 – 16 896, 1998. 65, 66

G.J. Huffman. Estimates of root-mean-square random error contained in finite sets of estimated precipitation. *Journal of Applied Meteorology*, 36:1191 – 1201, 1997. 65

G.J. Huffman and D.T. Bolvin. GPCP version 2 combined precipitation data set, April 2004. "http://climate.geog.udel.edu/ climate/html_pages/ download.html". xi, 65, 66, 69

M. Hulme, T. J. Osborn, and T. C. Johns. Precipitation sensitivity to global warming: Comparison of observations with HadCM2 simulations. *Geophysical Research Letters*, 25:3379–3382, September 1998. 65, 66

International Atomic Energy Agency IAEA and World Meteorological Organisation WMO. The Global Network of Isotopes in Precipitation (GNIP) database. *"http://isohis.iaea.org"*, 2001. 66, 67

L. Kornblüh, U. Schulzweida, A. Hellbach, E. Kirk, and M. Ponater. *Afterburner: A postprocessing program for ECHAM data and ECMWF analysis data, v4.14*. Max-Planck-Institut für Meteorologie, MPG-Hamburg, Dec 2003. "http://www.mpimet.mpg.de/ afterburner/after.c". 70

J. D. Lenters and K. H. Cook. Simulation and Diagnosis of the Regional Summertime Precipitation Climatology of South America. *Journal of Climate*, 8:2988–3005, December 1995. 69, 72

J. D. Lenters and K. H. Cook. On the Origin of the Bolivian High and Related Circulation Features of the South American Climate. *Journal of Atmospheric Sciences*, 54:656–678, March 1997. 72

J. D. Lenters and K.H. Cook. Summertime Precipitation Variability in South America: Role of the Large-scale Circulation. *Monthly Weather Review*, 127(3):409 – 443, 1999. 69

L. Merlivat and J. Jouzel. Global climatic interpretation of the deuterium-oxygen 18 relationship for precipitation. *Journal of Geophysical Research*, 84:5029 – 5033, 1979. 65

F. Mesinger. Improvements in Quantitative Precipitation Forecasts with the Eta Regional Model at the National Centers for Environmental Prediction: The 48-km Upgrade. *Bulletin of the American Meteorological Society*, 77(11):2637–2650, November 1996. 70

M. New, M. Hulme, and P. Jones. Representing Twentieth-Century Space-Time Climate Variability. Part II: Development of 1901-96 Monthly Grids of Terrestrial Surface Climate. *Journal of Climate*, 13:2217–2238, July 2000. 65

E. Ramirez, G. Hoffmann, J. D. Taupin, B. Francou, P. Ribstein, N. Caillon, F. A. Ferron, A. Landais, J. R. Petit, B. Pouyaud, U. Schotterer, J. C. Simoes, and M. Stievenard. A new Andean deep ice core from Nevado Illimani (6350 m), Bolivia. *Earth and Planetary Science Letters*, 212:337–350, July 2003. 64

N.A. Rayner, D.E. Parker, E.B. Horton, C.K. Folland, and R.B Hackett. Version 2.2 of the Global Sea-Ice and Sea Surface Temperature Data Set, 1903- 1994. Climate Research Technical Note 74, Hadley Centre, 1994. http://www.metoffice.com/research/ hadleycentre/obsdata/GISST.html. 65

M.A. Roche, R. Gonfiantini, J.C. Fontes, N. Abasto, and L. Noriega. The isotopic composition of precipitation on the Andes and Amazon of Bolivia. In International Atomic Energy Agency, editor, *International Symposium on Isotopes in Hydrology, Vienna, 10-14 May 1999*, volume IAEA-SM-361/3, pages 1 – 10. International Atomic Energy Agency, May 1999. 82

M. Rojas and A. Seth. Simulation and Sensitivity in a Nested Modeling System for South America. Part II: GCM Boundary Forcing. *Journal of Climate*, 16:2454–2471, August 2003. 69, 70, 72

K. Rozanski, L. Araguás-Araguás, and R. Gonfiantini. Isotopic patterns in modern global precipitation. *AGU Monograph*, 78:1–37, 1993. 82

E. Salati, A. Dall'Olio, E. Matsui, and J.R. Gat. Recycling of water in the Amazon basin: an isotopic study. *Water Resource Research*, 15:1250–1257, 1979. 85, 87

A. Seth and M. Rojas. Simulation and Sensitivity in a Nested Modeling System for South America. Part I: Reanalyses Boundary Forcing. *Journal of Climate*, 16:2437–2453, August 2003. 70

U. Siegenthaler and H. Oeschger. Correlation of ^{18}O in precipitation with temperature and altitude. *Nature*, 285:314, 1980. 82

K. Sturm, G. Hoffmann, B. Langmann, and W. Stichler. Simulation of $\delta^{18}O$ in precipitation by the regional circulation model $REMO_{iso}$. *Hydrological Processes – in press*, 2005a. 65

K. Sturm, F. Vimeux, and G. Krinner. The South American Monsoon recorded in Stable Water Isotopes. *Journal of Geophysical Research – submitted*, 2005b. 75, 89

L. G. Thompson, E. Mosley-Thompson, and K. A. Henderson. Ice-core palaeoclimate records in tropical South America since the Last Glacial Maximum. *Journal of Quaternary Science*, 15:377–394, May 2000. 64

C. Vera. Introduction to the SALLJ conference and SALLJEX field campaign. In *VAMOS/CLIVAR/WCRP Conference on South-American low-level jets*, Santa Cruz de la Sierra, Bolivia, Feb 2002. http://www.salljex.at.fcen.uba.ar/sallj/. 75

A. D. Vernekar, B. P. Kirtman, and M. J. Fennessy. Low-Level Jets and Their Effects on the South American Summer Climate as Simulated by the NCEP Eta Model. *Journal of Climate*, 16:297–311, January 2003. 69, 70

F. Vimeux, R. Gallaire, S. Bony, G. Hoffmann, and J.C. Chiang. What are the controls on δD in precipitation in the Zongo Valley (Bolivia) ? Implications for the Illimani ice core interpretation. *Earth and Planetary Science Letters*, -. submitted. 64, 84, 86

J.C. Vogel, J.C. Lerman, and W.G. Mook. Natural isotopes in surface and groundwater from Argentina. *Hydrological Science Bulletin*, XX:203 – 221, 1975. 82

H. von Storch, H. Langenberg, and F. Feser. A Spectral Nudging Technique for Dynamical Downscaling Purposes. *Monthly Weather Review*, 128:3664–3673, 2000. 70

M. Vuille, R. S. Bradley, R. Healy, M. Werner, D. R. Hardy, L. G. Thompson, and F. Keimig. Modeling $\delta^{18}O$ in precipitation over the tropical Americas: 2. Simulation of the stable isotope signal in Andean ice cores. *Journal of Geophysical Research*, 108(6):2–1, March 2003a. 64

M. Vuille, R. S. Bradley, M. Werner, R. Healy, and F. Keimig. Modeling $\delta^{18}O$ in precipitation over the tropical Americas: 1. Interannual variability and climatic controls. *Journal of Geophysical Research*, 108(6):1–1, March 2003b. 64, 75, 79, 85

M. Werner, U. Mikolajewicz, M. Heimann, and G. Hoffmann. Borehole versus isotope temperatures on Greenland : seasonality does matter. *Geophysical Research Letters*, 27:723 – 726, 2000. 65

P.W. White. *Technical and Computational Procedures (CY23R4)*. ECMWF - Meteo France, ifs documentation, part vi edition, 2002. 70

C. J. Willmott and S. M. Robeson. Climatologically Aided Interpolation (CAI) of Terrestrial Air Temperature. *International Journal of Climatology*, 15:221 – 229, 1995. 65, 68

C.J. Willmott and K. Matsuura. Terrestrial Air Temperature and Precipitation: Monthly and Annual Time Series (1950 - 1999), July 2001. "http://climate.geog.udel.edu/ climate/html_pages/ download.html". xi, 65, 66, 69

P. Xie and P.A. Arkin. Global Precipitation: A 17-year monthly analysis based on gauge observations, satellite estimates, and numerical model outputs. *Bulletin of the American Meteorological Society*, 78:2539 – 2558, 1997. 65

P. Xie and P.A. Arkin. CPC Merged Analysis of Precipitation (CMAP), 2002. "http://www.cgd.ucar.edu/cas/catalog/surface/precip/ arkin.html". xi, 65, 66, 69

Chapter 5

The South American Monsoon recorded in Stable Water Isotopes: a modelling study †

Résumé

La partie précédente a permis établir la validité de REMO$_{iso}$ dans le contexte climatique de l'Amérique du Sud. Le cycle saisonnier moyen des paramètres météorologiques et isotopiques, tel que simulé par REMO$_{iso}$, est confirmé par plusieurs sources d'observation. De plus, REMO$_{iso}$ apporte une vision plus détaillée, tout en restant cohérente, du climat sud-américain par rapport aux simulations plus grossières du modèle de circulation général ECHAM$_{iso}$. Il est donc justifié de rechercher les processus qui contrôlent le signal isotopique sur la base des résultats de REMO$_{iso}$.

L'étude suivante s'inscrit dans la vaste perspective de comprendre la signification du signal isotopique en Amérique du Sud. Il s'agit de pouvoir interpréter le signal isotopique archivé dans les carottes de glace en terme de variations climatiques. Historiquement, l'interprétation du signal isotopique dans les carottes tropicales s'est calquée sur le cas polaire : l'appauvrissement en isotopes lourds témoigne d'un refroidissement atmosphérique. Ainsi, les variations de δ^{18}O ont d'abord été assimilées à une manifestation directe des anomalies de températures de surface dans l'océan Pacifique, l'oscillation australe de l'Enfant (El Niño Southern Oscillation). Pourtant, cette interprétation se heurte à deux observations qui la réfutent. Les précipitations sur les sommets orientaux des Andes proviennent principalement de l'Atlantique ; il n'y a donc aucune interactions directes avec le Pacifique tropical, où se manifeste l'ENSO. D'autre part, des études de terrain prouvent que la température locale n'a pas d'influence déterminante sur la composition isotopique des précipitations ; un réchauffement atmosphérique lié à ENSO ne saurait donc expliquer les variations de δ^{18}O observées.

L'objectif de cette étude est d'utiliser la fine résolution de REMO$_{iso}$, et les avantages qui en découlent en relief accidenté, pour analyser les mécanismes physiques qui contrôlent le signal isotopique en Amérique du Sud. Nous nous attachons ci-après à la variabilité intra-saisonnière plutôt qu'à l'état moyen de l'atmosphère, et singulièrement celle des isotopes de l'eau dans les précipitations. La simulation décrite ici présente deux particularités. Premièrement, REMO$_{iso}$ offre une simulation du cycle isotopique à une résolution 2 à 5 fois plus fines que les études précédentes avec des modèles de circulation généraux. Deuxièmement, nous nous affranchissons du forçage océanique sur le système atmosphérique. A la différence des études méso-échelles menées jusqu'à présent, les températures de surface de l'océan sont climatologiques, i.e. elles représentent une cycle annuel standard qui ne varie pas d'année en année. Ainsi nous pouvons observer la variabilité intra-saisonnière inhérente à l'atmosphère. Nous utilisation la technique des fonctions orthogonales empiriques (empirical orthogonal functions – EOF) pour mettre en évidence le mode dominant de variabilité dans des données spatialisées quinde-quotidiennes (moyennées 5 jours). L'ensemble de ces processus inter-dépendants

† K. Sturm, F. Vimeux and G. Krinner, *submitted to Journal of Geophysical Research.*

est regroupé sous l'appellation mousson sud-américaine (South American monsoon system – SAMS). Dans ce contexte, nous insistons particulièrement sur l'identification des phénomènes physiques qui déterminent le signal isotopique. Les variations de pression atmosphériques à basse (dépression du Chaco) et haute altitude (anti-cyclone de Bolivie) interagissent avec la barrière topographique des Andes pour donner naissance à un fréquent vent de basse altitude (low-level jet – LLJ) longeant son flanc est. Ainsi la circulation atmosphérique régionale modifie la position d'une zone de convergence sub-tropicale (South Atlantic convergence zone – SACZ), qui est responsable du dipôle observé dans les précipitations entre le Paranà et le Nordeste. Le signal isotopique enregistre, au pied des Andes, mieux que les précipitations seules la variabilité du SAMS. La mise en évidence des processus méso-échelle liés au SAMS conduit donc à une remise en question de l'interprétation du signal isotopique dans les carottes andines. Ainsi, nous suggérons que δ^{18}O soit interprété prioritairement comme un proxy des précipitations cumulées au long de leur trajectoire. A l'échelle inter-annuelle, le phénomène ENSO perturbe la circulation régionale au-dessus de l'Amérique du Sud. Ce sont donc ces variations de la circulation qui sont enregistrées dans le δ^{18}O glaciaire, plus qu'une conséquence directe du changement de température.

Ces premiers résultats de REMO$_{iso}$ en mode climatologique appellent naturellement ‘a être poursuivis. Une simulation pluri-annuelle de REMO$_{iso}$ est programmée, qui assimilera les conditions de surface océanique réelles et la circulation synoptique observée. Le forçage océanique et atmosphérique par ENSO excite-t-il ce mode de résonance libre de l'atmosphère, ou bien le signal isotopique traduit-il alors une réponse différente du système atmosphérique sous contrainte ?

Zusammenfassung

Die Gültigkeit von REMO$_{iso}$ unter südamerikanischen Klimabedingungen wurde in dem vorherigen Kapitel bestätigt. Der von REMO simulierte säzonale Zyklus meteorologischen und isotopischen Parametern wurde von verschiedenen Beobachtungsmitteln bekräftigt. REMO$_{iso}$ bietet ein detailliertes Bild, jedoch in Übereinstimmung mit gröberen Simulierungen des Generalzirkulationsmodell ECHAM. Es ist daher gerechtfertigt, anhand der REMO$_{iso}$ Ergebnissen die Prozesse zu untersuchen, die das isotopische Signal kontrollieren.

Ziel der folgenden Studie ist, Elemente zur Interpretation des Wasserisotopensignal in Südamerika las Klimaindikator zu erarbeiten. Ursprünglich wurden Andinische Eisbohrkerne ähnlich zu den polaren gedeutet: Abreicherung von schwereren Wasserisotopen weist auf eine atmosphärische Abkühlung hin. Temperaturanomalien über dem Pazifischem Ozean, im Zusammenhang mit der El Niño Southern Oscillation (ENSO), galten zuerst als direkte Ursache für δ^{18}O Schwankungen. Zwei Argumente widersprechen jedoch diese Analyse. Niederschlag über östlichen Andengipfeln stammen hauptsächlich aus dem Atlantischen Ozean; es gibt also keine direkte Wechselwirkung mit dem tropischen Pazifik, Hauptsitz der ENSO. Darüber hinaus belegen Feldmessungen, daß Lokaltemperatur die Isotopenzusammensetzung von Niederschlag kaum beeinflussen. Einer von ENSO verursachte Erwärmung der unteren Atmosphäre kann also δ^{18}O Schwankungen nicht erklären.

In dieser Studie wird REMO$_{iso}$s höhere Auflösung, und dessen Vorteile in Hochgebirgsrelief, dazu angewandt, um physikalischen Isotopenfraktionierungsprozesse zu erforschen. Hier wird mehr auf der intra-säzonales Variabilität als den mittleren Atmosphärezustand geachtet, und vor allem dessen Einfluss auf Wasserisotopen. Die hier beschriebene Simulation unterscheidet in zwei grundlegenden Merkmale. Erstens, REMO$_{iso}$ bietet eine Wasserisotopenkreislaufsimulation mit einer 2- bis 5-mal feineren Auflösung als bisherigen Generalzirkulationsmodellen. Zweitens wurde jeglicher ozeanischer Antrieb der atmosphärischen Variabilität außer Kraft gesetzt, indem klimatologischen Meeresoberflächentemperaturfeldern benutzt wurden. Damit kommt zum Vorschein die inhärente intra-säzonale Variabilität der ungezwungenen Atmosphäre. Zu diesem Anlass werden empirische orthogonal Funktionen (empirical orthogonal functions – EOF) auf 5-täglichen Rastermodellausgabe angesetzt. Die zusammenhängenden meteorologischen Prozessen werden

umfassend als Südamerikanischer Monsun (South American monsoon system – SAMS) bezeichnet. Dieser erfasst Druckschwankungen in der unteren (Chaco Depression) und höheren (Bolivianischer Antizyklon) Tropospäre, die aufgrund des Topographiehindernis einen starken Windstrom entlang der Andinischen Ostflanke verursachen (low-level jet – LLJ). Die dadurch entstehende Konvergenzzone (South Atlantic convergence zone – SACZ) zeichnet sich mit einer abweichenden Position aus, die an dem Dipolmuster des Niederschlags über Paraná und Nordeste zu erkennen ist. Das Isotopensignal in den Andinischen Vorberge erfasst deutlicher als reine Niederschlagsmessungen die SAMS-Variabilität. Dieser neue mezzo-skalige Nachweis weist darauf hin, daß $\delta^{18}O$ in Andinischen Eisbohrkerne hauptsächlich als Proxy für kumulierter Niederschlag entlang seiner Trajektorie interpretiert werden soll. Der Einklang von inter-anualen $\delta^{18}O$- mit ENSO-Variabilität bedeutet nicht, daß Temperaturschwankungen das Isotopensignal beeinflussen, sondern daß von ENSO angetriebenen Zirkulationsänderungen in den Eisbohrkernen gespeichert wird.

Diese vorläufigen Ergebnisse unter klimatologischen Bedingungen rufen natürlich eine Fortsetzung auf. Geplant ist eine Simulation mit $REMO_{iso}$, die sowohl beobachtete Meeresoberflächentemperaturen als auch assimilierte synoptische Zirkulationsmustern berücksichtigt. Regt der ENSO Antrieb das selbe Resonanzmodus der Atmosphäre an, oder offenbart das Isotopensignal eine veränderte Reaktion der Atmopshäre unter ozeanischem Zwang ?

5.1 Introduction

Recent studies have underlined the sensitivity of the Tropics to global climate fluctuations. Tropical ice-cores hence uncover a unique archive of climate variability. The Andean Cordillera, with summits exceeding 6000 m, concentrates most of the tropical glaciers worldwide. Several ice-cores were recovered from the Andes, with climate archives extending back to 25 000 years [Thompson et al., 1998, 2000, Ramirez et al., 2003]. Stable water isotopes are analysed in the ice-core record, reaching an annual resolution on the last decades. The isotopic signal is here expressed as the depletion of the heavy isotope $H_2^{18}O$ from the Vienna standard mean ocean water (V-SMOW), expressed as $\delta^{18}\mathrm{O} = (R_{sample}/R_{SMOW} - 1) \cdot 1000$. R is the molar ratio $[H_2^{18}O]/[H_2^{16}O]$, and the reference $R_{SMOW} = 2.0052e-3$.

The interpretation of climatic controls on isotopic composition is still controversial. On one hand, Bradley et al. [2003] and Thompson et al. [2000] interpret the isotopic signal in tropical ice cores as a proxy for Pacific temperature, similarly to polar ice cores. On the other hand, Hoffmann [2003], Hoffmann et al. [2003], Henderson et al. [1999] report that the isotopic signal in ice cores primarily record changes in precipitation and circulation patterns over the Amazon and the equatorial Atlantic, where the moisture originates. Pierrehumbert [1999] investigated possible controls on δ^{18}O using Rayleigh-type distillation models, but it failed to represent the varying trajectories of air masses precipitating over the Andes. Vuille et al. [2003b,a] conducted a comprehensive study of climate controls on δ^{18}O within isotope enabled GISS-II and ECHAM4 general circulation models. The authors conclude that the El Niño southern oscillation (ENSO) and associated sea surface temperature (SST) anomalies coincide best with inter-annual variability of δ^{18}O over South America, in particular in tropical ice cores.

However, recent observational and modelling studies underlined physical mechanisms that control circulation and precipitation at intra-seasonal time scales. These meteorological mechanisms can be integrated in a comprehensive view: the South American monsoon system (SAMS) [Grimm et al., 2004, Nogues-Paegle et al., 2003]. It reaches its mature stage during summer, and accounts for up to 80% of annual rainfall in tropical and sub-tropical areas. Likewise the east Asian monsoon, typical monsoon features develop across South America, as depicted in Zhou and Lau [1998]. Low-level cross equatorial flow advects moist, warm air that is deviated polewards to the east. Sub-tropical low-level highs over the ocean contrasts with thermal lows over the continent (Chaco low). At upper-level, an anti-cyclonic circulation develops above the continent (Bolivian high). The interaction of the latter two give rise to an intense convergence zone (south Atlantic convergence zone - SACZ), which explains the heavy summertime precipitation. Particular features of the SAMS, especially north-westerly low-level jets (LLJ) are meso-scale features. To be resolved accurately in atmospheric circulation models, they require a fine horizontal resolution that is only obtained in regional circulation models [Vernekar et al., 2003, Chou et al., 2000, Rocha and Ambrizzi, 2004, Rojas and Seth, 2003, Seth and Rojas, 2003, Seth et al., 2004].

So, evidence from meso-scale modelling over South America challenges the interpretation of coarser global circulation models. To which extend does the meso-scale SAMS influence the δ^{18}O signal over tropical and sub-tropical South America ? This issue was investigated using the regional circulation model REMO$_{iso}$, fitted with stable water isotope diagnostics. To identify the singular modes of atmospheric variability, we cancel any oceanic forcing by applying climatological SST as boundary conditions to REMO$_{iso}$. This primarily cancels simulated inter-annual variability related to ENSO, but also to any Atlantic SST anomalies. Sturm et al. [2005a] compared REMO$_{iso}$ to coarser ECHAM4 GCM simulations, as well as gridded precipitation and station δ^{18}O observations. REMO$_{iso}$ proved to reproduce accurately the mean annual cycle of precipitation, circulation and δ^{18}O over South America. Here we focus on intra-seasonal variability simulated by REMO$_{iso}$ during austral summer (December to February), based on pentad (5 day) averages of meteorological and isotopic parameters. In the following section, we first introduce the regional circulation model REMO$_{iso}$ and its stable water isotope module. Secondly, we present the principles and benefits of empirical orthogonal functions (EOF) analysis for revealing intra-seasonal variability. The third section describes the dominant mode of intra-seasonal variability, marked by a bi-modal shape over Paraná and Nordeste. The fourth section underlines how this bi-modal pattern is distinctly recorded in the isotopic signal. In the fifth section, we discuss previous results in order to assess the meteorological processes controlling the δ^{18}O signal in South America. Finally, we extend the comprehension of pure atmospheric variability modes, revealed from the present simulation, to the interpretation of inter-annual, ENSO driven variability of

the δ^{18}O signal over South America.

5.2 Model and methods

The present article seeks to investigate austral summer climate in South America as simulated by the regional circulation model REMO$_{iso}$. The intra-seasonal variability of precipitation is related to isotopic and meteorological parameters by the means of empirical orthogonal functions (EOF).

5.2.1 REMO Experiment with climatological SST

The regional circulation model REMO was originally developed for weather prognosis by the German Weather Service (DWD - Deutscher Wetterdienst [Majewski, 1991]). It was later adapted to climate purposes at the Max-Planck-Institute for Meteorology [Jacob et al., 2001] by incorporating the physics scheme of the ECHAM general circulation model [Roekner et al., 1996]. Similarly, a stable water isotope module developed for ECHAM [Hoffmann et al., 1998, Werner and Heimann, 2002] was adapted to REMO. A detailed description of REMO and its stable water isotope module can be found in Sturm et al. [2005b]. Major technical characteristics of REMO are presented thereafter.

REMO runs on rotated Arakawa C grid with 0.5°, i.e. $\sim 55km$ horizontal resolution and 19 vertical hybrid σ-pressure levels. The study domain spans the tropical South American continent and surrounding oceans, from 100°W to 20°W in longitude and 35°S to 15°S in latitude. The physics scheme [Roekner et al., 1996] has following characteristics. The soil module computes heat transfers at 5 levels, but only total soil moisture is computed (bucket-type). Further prognostic reservoirs include precipitation interception by the canopy and a snow layer. Turbulent surface fluxes are parameterised following the Monin-Obukhov similarity theory, with a higher order closure scheme for the transfer coefficients of momentum, heat, moisture, cloud water within and above planetary boundary layer. The convection scheme use a mass-flux conversion scheme [Tiedtke, 1989], refined by Nordeng [1994], with standard parameters. Stratiform clouds result from a budget equation, accounting for phase changes, coalescence of cloud droplets and gravity settling of ice-crystals.

Fractionation processes of stable water isotopes are computed in REMO identically to ECHAM [Hoffmann et al., 1998]. The isotopic module computes equilibrium and kinetic fractionation for HDO and $H_2^{18}O$ at each model time step. Equilibrium fractionation is temperature dependent [Majoube, 1971] and applies to phase changes in the cloud. Evaporation over the ocean follows Merlivat and Jouzel [1979], taking into account kinetic fractionation effects depending on wind-speed. Both isotopic vapour and precipitable water are prognostic. The cloud micro-physics computes fractionation processes between solid, liquid and gaseous phases of water, including the different diffusion constants in ice at low temperatures for HDO and $H_2^{18}O$ [Jouzel and Merlivat, 1984]. To account for sub-cloud evaporation of rain drops, their isotopic composition is set in partial equilibrium (including kinetic effects [Jouzel and Merlivat, 1984]) with the surrounding moisture. Convective precipitation, with generally larger and faster falling drops, is re-equilibrated to 45% versus 95% for stratiform precipitation. The bucket-type soil hydrology scheme does not account for surface and sub-surface drainage, groundwater formation, etc. Hence, this low-complexity parameterisation cannot make a distinction between evaporation from bare soils and transpiration by the vegetation. Vapour fluxes from the surface are assumed to be dominantly transpiration by vegetation, and thus soil moisture is released un-fractionated into the atmosphere [Bariac et al., 1994b,a].

The present simulation by REMO$_{iso}$ was validated against GNIP observations [IAEA and WMO, 2001] and ECHAM simulations in Sturm et al. [2005a]. REMO was integrated over a period of 5 years, after one year spin-up. Lateral boundary conditions for winds, moisture, liquid water content and their isotopic counterparts were provided by an ECHAM$_{iso}$ simulation at a 6 hour time-step. Sea-surface temperatures (SST) for both ECHAM and REMO are prescribed from the GlSST climatology [Rayner et al., 1994]. Mean monthly SST are linearly interpolated to provide 6 hour forcing to REMO. For any subsequent year, the models use the GISST climatology as a perpetual year. In conclusion, the boundary conditions are such that inter-annual variability, driven by SST, is removed. The simulation can be regarded as an ensemble run, focussing on the intra-seasonal variability of the atmosphere.

5.2.2 Empirical Orthogonal Functions: why and how ?

Climate parameters vary both in space and time. In order to isolate the major modes of variability in the system, we applied a common reduction technique: the empirical orthogonal functions. The method, similar to the principal component analysis (PCA), makes use of the matrix eigenvalue decomposition.
A 4-D climate signal can be decomposed on a basis of independent eigenvectors describing the spatial pattern of variability (the empirical orthogonal functions or 'EOFs'), with their associated 'weight' as a function of time (expansion coefficients 'EC', or loadings). The climate signal can be reconstructed as the sum of the matrix products of spatial patterns (EOF) and their associated strength in time (EC). Usually, the truncation of the reconstruction to the first EOFs captures most of the signal's variance. Hence, we can isolate a particular mode in the climate system by looking at the matching EOF/EC pairs for different climate parameters.

Parameters listed thereafter are analysed for austral summer months (DJF) on a 5 day (pentad) resolution. For computational reasons, we restrict the reduction to the 15 first EOF. The eigenvalue spectrum tends asymptotically towards zero, so the order of reduction (n=15) is sufficient.

- Precipitation. 21% of the variance was captured in the first EOF, 60% in the first 5 EOFs.
- Depletion of the heavy isotope $H_2^{18}O$ defined as $\delta^{18}\mathrm{O} = (R_{sample}/R_{SMOW} - 1) \cdot 1000$. 27% (65%) of the variance is captured in the first (first to fifth) EOF.
- Vertically integrated horizontal moisture transport $\mathbf{H} = \int_0^{\inf} Q \cdot \mathbf{u} \partial z$. In this case, we applied the complex (or Hilbert) EOF method [Venegas, 2001] on $H^* = H_u + \imath \cdot H_v$, to account for the common variability of zonal and meridional advection. 29% (70%) of the variance is captured in the first (first to fifth) EOF.
- Count of low-level jets (LLJ), defined as the number of events on a 6 hour time step where northward wind at 850 hPa exceeds 8 m/s and the difference to 750 hPa wind exceeds 2 m/s [Rocha and Ambrizzi, 2004]. 24% (75%) of the variance is captured in the first (first to fifth) EOF.
- Wind divergence at 200 hPa, calculated as the mean over a pentad of 6-hourly wind divergence. Convection strongly influence ipper-level divergence. Due to its highly local character, the EOFs are fuzzy and the eigenvalue spectrum does not decrease as quickly as the other parameters. Only 10.5% of the variance is related to the first EOF, and a sum of 7 EOF is needed to capture at least 50% of its variance.
- Mean sea-level pressure (SLP). The 2 leading EOFs explain 33% and 26% of the variance. Yet, the spatial pattern of the first EOF matches in first order the orography. We suggest the first EOF to be an artefact due to the SLP computation technique: it mainly captures air temperature changes around high relief. The second EOF i snot biased by altitude and is thus thought to represent the dominant mode of climatic variability.
- Geopotential Φ at 200 hPa. To bypass complications related to the steep orography, the computation of geopotential is based on SLP. Hence its first 'shadow' EOF is equally biased, which explains 28.6% of the variance. The second EOF, physically relevant, explains 20% of the variance.

For all but one parameters (wind divergence), the dominant mode of climate variability explains at least 20% of the variance, with eigenvalue spectra then rapidly decreasing. As seen on figure 5.2, the loadings of the first EOF are all correlated with the bimodal pattern of precipitation described below. For $\delta^{18}\mathrm{O}$ and H_v, the heterogeneous correlation map further shows that precipitation on the Eastern flank of the Andes and Northern Amazon is in phase with the Paraná region, but opposite to the Nordeste/sub-tropical Atlantic.
In the following section, we discuss both the similarities in spatial patterns (EOF) and temporal evolution (EC) of this dominant mode, which is shared by all climate parameters listed above. The naming convention there after define EOF_X^n (EC_X^n) and the n_{th} empirical orthogonal function (expansion coefficients) for parameter X.

Following Dommenget and Latif [2002], Björnsson and Venegas [1997], we adopted several representations for EOF results. Firstly, we illustrate the dominant bi-modal variability in the climate parameters above by presenting their first

EOF in Figure 5.1. Secondly, we investigate whether the illustrated bi-modal variability is concurrent for the different parameters. Table 5.1 shows the cross-correlation coefficients between EC associated with their first EOF. Thirdly, we search for regions where precipitation shares the dominant variability underlined for each climate parameter. Figure 5.2 shows heterogeneous correlation maps between the EC for selected climate parameters and grid-cell precipitation. Finally, we wonder whether station records in key regions are able to identify the bi-modal variability illustrated by the EOF analysis. Figure 5.10 shows the correlation between station precipitation and δ^{18}O record with domain-wide precipitation.

5.3 The Paraná - Nordeste dipole

In agreement with previous studies [Herdies et al., 2002, Carvalho et al., 2002], precipitation over the South American continent simulated by REMO displays a dipolar pattern, with one extremum over north-east Brazil at [40°W; 10°S] (hereafter referred to as Nordeste) and an opposite extremum over the south Brazil and Paraguay at [55°W; 25°S] (hereafter referred to as Paraná). Alternation from one extremum to the other is mainly related to the location of the South Atlantic Convergence Zone (SACZ). The interaction between synoptic and regional circulation during austral summer (DJF), determining the distribution and variability of precipitation, is referred to as the South American Monsoon System (SAMS) [Zhou and Lau, 1998, Nogues-Paegle et al., 2003, Grimm et al., 2004].

In the present section, we first underline the dipolar pattern of precipitation as simulated with REMO. Secondly, we investigate mechanisms in upper and lower level atmospheric motion related to this precipitation regime. Finally, we analyse the isotopic signature of precipitation as an integrative proxy for precipitation and regional circulation patterns.

5.3.1 Oceanic versus continental SACZ

Figure 5.1a shows the first EOF of pentad austral summer (DJF) precipitation over South America. Its main characteristics is bi-modal pattern. Negative values cover the Atlantic off Brazil's East coast between [25°S; 5°S], intruding in the Brazilian highlands to [50°W; 15°S]. This region is referred to as Nordeste hereafter, although its extension is wider than the geographical delimitation of the Nordeste region. Negative loadings (i.e. expansion coefficients) of the first precipitation EOF correspond to a predominantly oceanic SACZ.

Positive counterparts are found mainly in Southern Brazil and Paraguay, hereafter referred to as Paraná region. This feature extends weakly over the South Atlantic, with a corresponding extremum at [40°W; 30°S]. Hence, high precipitation on the Paraná region are associated with positive loadings of the first EOF precipitation. On the other hand, positive values over the Atlantic are found north of the Nordeste, corresponding to the climatological location of the inter-tropical convergence zone (ITCZ). Precipitation over the central Amazon [60°W; 5°S] and the Eastern flank to the Central Andes [70°W; 5°S] are in phase with the Atlantic ITCZ and the Paraná region. This precipitation regime occurs under a predominantly continental location of the SACZ.

Based on the first EOF of precipitation, we define the *oceanic SACZ composite* pentads during which loadings are lower than the 25% percentile of the EOF1 expansion coefficients. The 25% percentile is equal to -0.76 standard deviation of the EOF1 expansion coefficients. Similarly, the *continental SACZ composite* merges all pentads above the 75% percentile (+0.56 standard deviation). Carvalho et al. [2002, 2004] likewise associates precipitation regimes in sub-tropical America with the position of the SACZ: high precipitation over Paraná (Brazil east coast) occurs during dominantly continental (oceanic) location of the SACZ. Thereafter, we refer to extrema of the bi-modal variability as continental (oceanic) SACZ composite, based on this 75% (25%) percentile definition.

Table 5.1 shows the correlation coefficients between the loadings (or expansion coefficients) associated to the first EOF for parameters listed in the previous section: precipitation *Prec*, $H_2^{18}O$ depletion δ^{18}O, zonal and meridional vapour advection (H_u and H_v), low-level jet count *LLJ*, wind divergence at 200 hPa (*Div*), mean sea-level pressure (*SLP*) and geopotential at 200 hPa (Φ). The EOF1 loadings for precipitation correlate well with all other parameters, excepted for H_u.

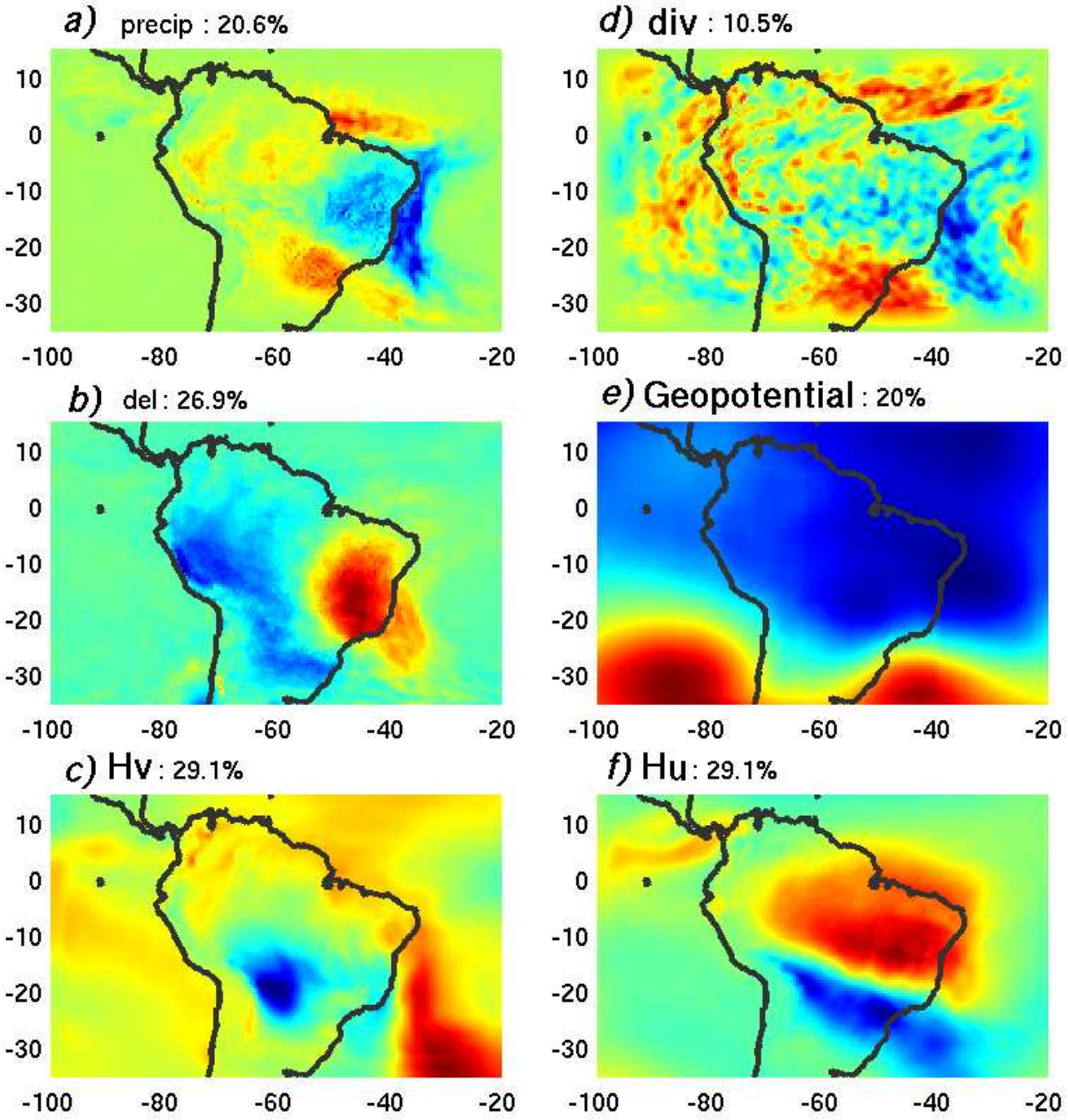

Figure 5.1: Empirical orthogonal functions (EOFs), computed on pentad series for 4 austral summers (DJF), i.e. 72 values. The first EOF is plotted for a) precipitation, b) $\delta^{18}O_p$, c) meridional vapour transport ($H_v = \overline{Q \cdot \vec{v}} \cdot \vec{j}$, positive when flowing northwards), d) wind divergence at 200 hPa, e) geopotential at 200 hPa, f) zonal vapour transport ($H_u = \overline{Q \cdot \vec{u}} \cdot \vec{i}$). All EOF are normalised to arbitrary units, with red (blue) indicating positive (negative) EOF values.

EC	Prec	$\delta^{18}O$	H_u	H_v	LLJ	Div	SLP	Φ
Prec	1	0.64	0.32	0.75	0.43	0.79	0.4	0.33
$\delta^{18}O_p$	0.64	1	$\star$	0.76	0.68	0.66	0.53	0.3
H_u	0.32	$\star$	1	$\star$	0.25	0.35	$\star$	0.26
H_v	0.75	0.76	$\star$	1	0.63	0.69	0.57	0.22
LLJ	0.43	0.68	0.25	0.63	1	0.53	0.76	0.26
Div	0.79	0.66	0.35	0.69	0.53	1	0.44	0.4
SLP	0.4	0.53	$\star$	0.57	0.76	0.44	1	0.45
Φ	0.33	0.3	0.26	0.22	0.26	0.4	0.45	1
σ^2	39%	41%	33%	27%	38%	41%	35%	22%

Table 5.1: Correlation coefficients σ between the expansion coefficients (EC) associated with the first EOF for precipitation (Prec), isotopic composition of precipitation ($\delta^{18}O$), zonal (H_u) and meridional (H_v) vapour transport, low-level jet count (LLJ), wind divergence at 200 hPa (Div), mean sea-level pressure (SLP) and Geopotential at 200 hPa (Φ). The mean common variance of one field with all the other is indicated in the last row (σ^2).

The bi-modal pattern in precipitation between the Nordeste and the Paraná is reported in several studies, based both on observations and simulations. However, authors use different criteria to define extreme phases of the dipole depending on the research focus. In the following paragraph, we briefly review climate parameters associated to extreme precipitation over the Paraná-Nordeste dipole.

Grimm et al. [2004] likewise use the first precipitation EOF to define intra-seasonal modes, although being limited to land precipitation. Their analysis result in a similar opposition between the Paraná and Nordeste. REMO further agrees with Grimm et al. [2004] in the seesaw shape of the second EOF (not shown). North-easterly propagating Rossby waves favour convection over band extending from [30°W; 30 °S] to [60 °W; 5 °S], which corresponds to the climatological location of the SACZ. Simultaneously, convection is suppressed over the tip of Nordeste [35 °W; 5 °S] and the Rio Grande do Sul province in Southern Brazil [50 °W; 30 °S]. Based on EOF analysis of 5-day geopotential at 200 hPa in the NASA-DAO analyses, Lenters and Cook [1999] identify a similar dipole between the Paraná and Nordeste precipitation. Correlation of EC^1_Φ with the NASA-DAO precipitation is positive over the Paraná and negative over Nordeste. A similar heterogeneous correlation map between EC^1_Φ and global precipitation index (GPI) data base further extends the negative correlation in Nordeste over the tropical Atlantic off the Brazil east coast. These observations are in agreement with similar correlation maps by REMO (Figure 5.1e). Doyle and Barros [2002] investigate the interannual variability of summer precipitation over sub-tropical America, based on monthly NCEP reanalyses. Monthly precipitation displays a similar dipole between the Paraná and southern-eastern Brazil, which is found to be correlated to SST in western sub-tropical south Atlantic (WSSA). The continental (oceanic) composites by REMO correspond to the cold (warm) composites described in Doyle and Barros [2002].

5.3.2 Upper level atmospheric motion

Wind divergence at 200 hPa is the parameter in Table 5.1 that correlates best with precipitation, with an squared correlation coefficient $r^2 = 62\%$. Positive wind divergence at upper levels corresponds to wind convergence at lower levels and ascending motion at mid-level. It is associated with enhanced convection, hence increased precipitation. This explains the similar EOF shape for precipitation (Figure 5.1a) and upper-level divergence (Figure 5.1d). Although negative divergence EOF extends equally over land and sea, more precipitation is produced over its continental portion. REMO assumes that maritime air masses contain less cloud condensation nuclei (CCN) than over the continent, which explains the differential condensation efficiency. Heterogeneous correlation of EC^1_{div} with domain wide precipitation represents an alternate way to demonstrate the concordance between both parameters. Figure 5.2d shows positive correlations over eastern Brazil and neighbouring Atlantic. The centre of the negative pole lies over the Paraná and extends towards the sub-tropical Atlantic. Finally, the EOF contains a clear latitudinal alternation of convergence/divergence zones over the Atlantic. In case of

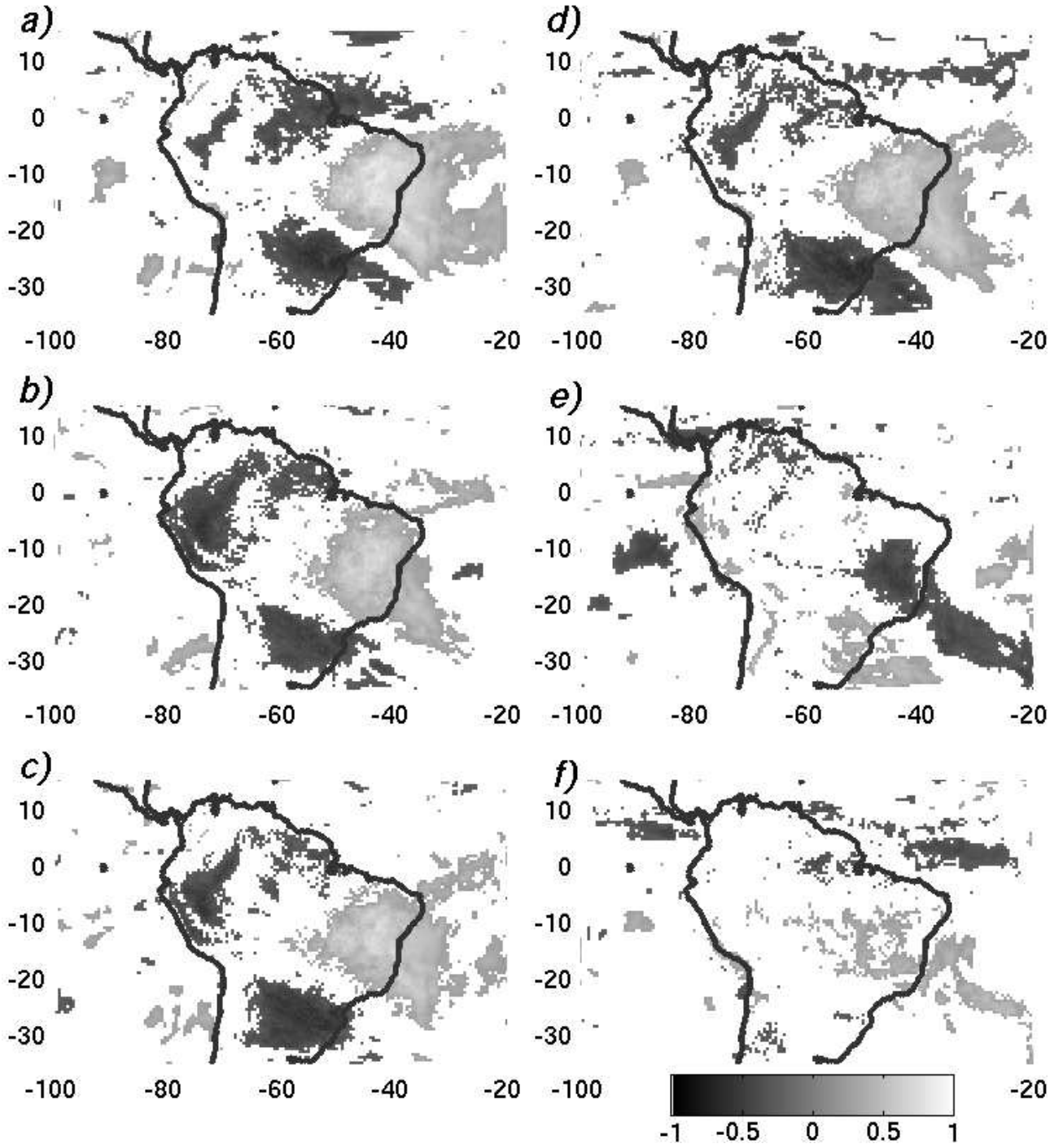

Figure 5.2: Correlation of precipitation over the whole study domain with the expansion coefficients associated to the first EOF for following parameters: a) precipitation, b) $\delta^{18}O_p$, c) meridional moisture transport, d) wind divergence at 200 hPa, e) geopotential at 200 hPa, f) zonal moisture transport.

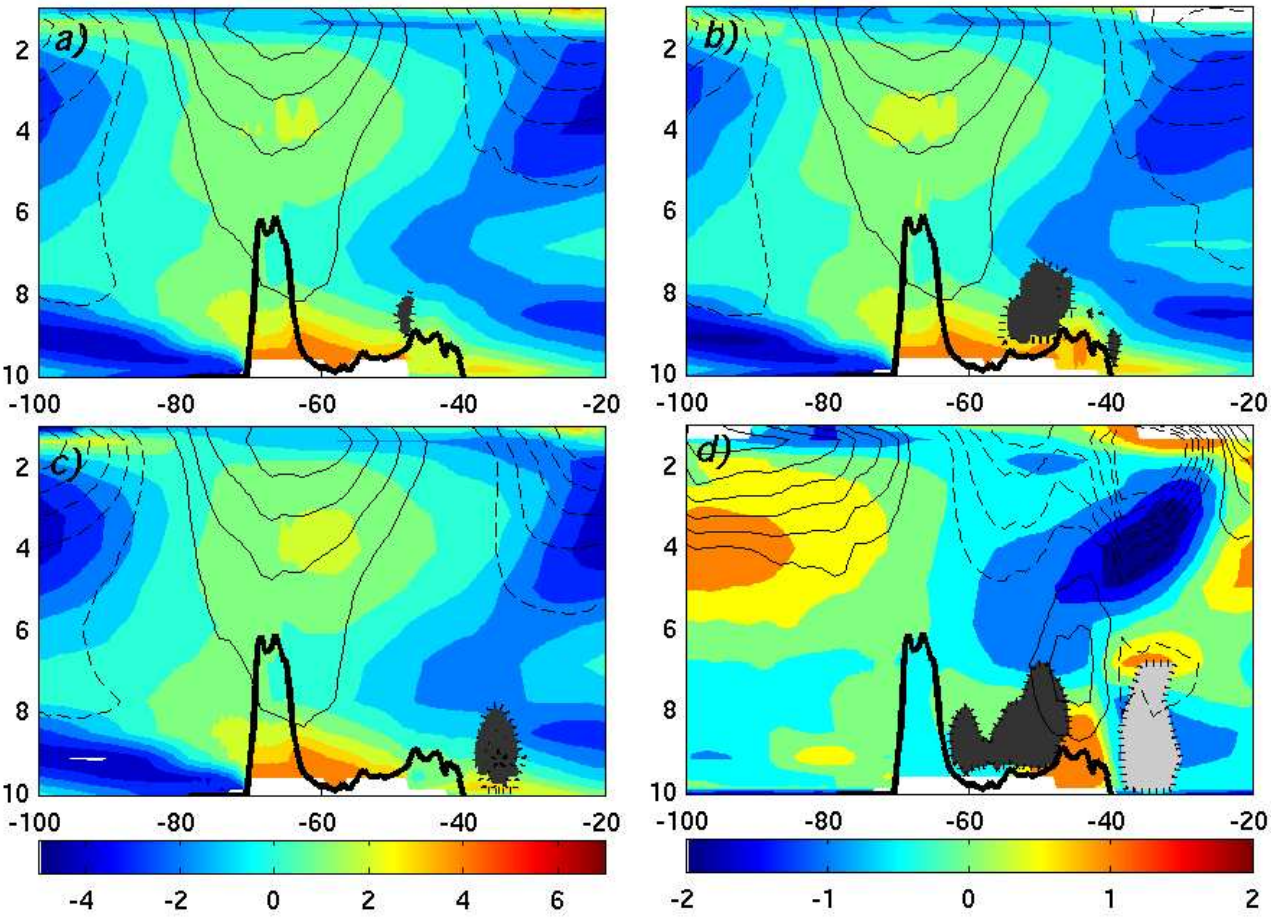

Figure 5.3: Vertical cross section along the 20°S parallel. Altitude is given in pressure levels (1e4 Pa). The thick black line represents the topography. Following situations are depicted: a) DJF climatology, b) continental SACZ (expansion coefficients associated to the first precipitation EOF above the 75% percentile), c) oceanic SACZ (expansion coefficients associated to the first precipitation EOF below the 25% percentile), d) difference between continental and oceanic SACZ. Coloured shading marks the standing temperature eddy (difference from zonal mean, 1 K intervals for a-c, 0.5 K for d), continuous (dashed) lines represent positive (negative) standing geopotential eddies (20m intervals for a-c, 5m for d). The dark (light) grey shaded areas represent southward (northward) meridional winds above 6 m/s (a-c), or anomalies in northerlies larger than 1 m/s.

a north-eastward shift of the SACZ, weak convergence takes place at 5°North over the tropical Atlantic and at [55°W; 22°S] over the Paraná. Upper-level convergence indicates subsidence, which inhibits convection (cf. Figure 5.5). The latter reinforces the contrast between the oceanic/continental SACZ precipitation composite (cf. also Figure 5.6).
These results are in good agreement with a similar study conducted with the CCM3 GCM [Barreiro et al., 2002], both for precipitation and 200 hPa wind divergence EOFs. Opposite to the NCEP re-analyses, both REMO and CCM3 display a dipole across the climatological location of the SACZ, with one pole over the continent at [50°W; 25°S] and the oceanic counterpart at [35°W; 20°S]. Since upper-level divergence is associated to mid-level ascending motion, EOF^1_{div} is consistent with a dipole in vertical wind velocity [Herdies et al., 2002].

Geopotential height at 200 hPa indicates the synoptic forcing of the SAMS. It is not as tightly linked to precipitation as wind divergence, with a squared correlation coefficient $r^2 = 11\%$. The dominant mode, displayed in Figure 5.1f, is consistent with the leading EOF from the NASA/DAO analyses Lenters and Cook [1999]. The strengthening of the Nordeste trough is associated with enhanced precipitation over the Paraná region.
The vertical structure of the atmosphere under continental/oceanic SACZ conditions is shown in Figure 5.3. In the continental SACZ composite, latent heat release by convection over central Amazon shifts the warm core anomaly to the

West by $\sim 5°$. As a consequence, the Bolivian high follows the same shift, but its strength is not significantly altered. On the other hand, the oceanic composite, with high convection off Brazil's East coast, moves the Bolivian high $\sim 3°$ East of its climatological location. In neither case the Bolivian high undergoes a clear latitudinal shift.

5.3.3 Low level atmospheric motion

Precipitation appears to be closely controlled by low-level circulation. Meridional vapour advection is the most determinant. The squared correlation coefficient between loadings of precipitation and meridional vapour transport H_v is the second highest $r^2 = 56\%$, whereas the correlation is poor for zonal vapour transport H_u. We first analyse the meridional advection in terms of extreme events: the low-level jets (LLJ). Adopting the definition by Rocha and Ambrizzi [2004],LLJ were counted as the frequency of 6 hour events during which a) northerly 850 hPa winds exceeding 8 m/s, and b) vertical wind shear between 850 hPa and 700 hPa exceeding 2 m/s. The first EOF (not shown) displays 3 extrema for LLJ. Associated with the oceanic SACZ composite, LLJ are most frequent on the eastern flank of the Northern [70 °W; 3 °S] and Central Andes [75 °W; 10 °S]. They converge later on with weaker LLJ on the western flank of the Brazilian highlands [45 °W; 15 °S]. The only extrema associated with the continental SACZ composite is located above Santa Cruz [63 °W; 20 °S].

Brahmananda Rao et al. [1996] report that specific humidity is higher at lower than upper atmosphere levels, but it does not vary significantly horizontally in tropical regions. Hence the vertically integrated moisture flux $\vec{H}$ is close to low-level wind circulation. The meridional moisture transport H_v achieves the second best squared correlation coefficient with precipitation $r^2 = 56\%$. Its first EOF is marked by an enhanced northerly flow above Santa Cruz [60 °W; 20 °S] associated with high precipitation over the Paraná region. This is related to the frequency of LLJ events at this point. On the opposite, high precipitation over the Nordeste is associated with increased northerly flow off the East coast of Brazil. Pattern of meridional moisture advection is consistent with the location of LLJ depicted in Figure 5.3.

This results are in good agreement with previous modelling studies. Gan et al. [2004] reports a similar opposition between LLJ paths in the oceanic/continental SACZ composites in the NCEP re-analyses. High precipitation in Western Central Brazil are associated with LLJ hedging an enhanced Chaco low, hence diverted from the Eastern flank of the Central Andes directly to the western flank of the Brazilian highlands. High precipitation over the Paraná is associated with a vanishing Chaco low, which enables LLJ to develop over Santa Cruz. Dominant LLJ at the western flank of the Brazilian highlands instead of the eastern flank of the Andes is common between REMO and the RegCM2 RCM [Rocha and Ambrizzi, 2004]. Vernekar et al. [2003] on the other hand reports a prevalence of Andean LLJ at 18°S. For further information, the reader is conferred to publications related to the SALLJEX experiment [Vera, 2002].

A synthetic view of atmospheric dynamic associated with the continental SACZ composite is given in Figure 5.4. Figure 5.5 depicts the equivalent for the oceanic SACZ composite and differences between the two extreme cases are highlighted in Figure 5.6.

In the continental SACZ composite (Figure 5.4), a strengthened Chaco low drives a enhanced cyclonic flow at 20°S. This implies a higher frequency of LLJ events, especially over Santa Cruz [60 °W; 20 °S]. This northerly flow advects air from the Amazon basin with negative 'moist static stability' [Lenters and Cook, 1999], which favours convection over the Paraná region. Hence increased precipitation are related to the continental location of the SACZ. This composite is associated with strong convergence over central Amazon and the ITCZ, and enhanced subsidence off the Brazil's East coast.

The situation is reversed in the oceanic SACZ composite (Figure 5.4). The Chaco low is weakened and shifted westwards to [55 °W; 20 °S]. The reduced cyclonic flow directs both the Andean and Brazilian highland LLJ to East Brazil, provoking increased convection off Brazil's East coast. On the other hand, subsidence to the North and South of the convergence zone blocks convection over the Equator and the Paraná region. The weakening of the Nordeste trough at 200 hPa enables the merging of the ITCZ and the SACZ.

The oceanic/continental composites by REMO, and related atmospheric dynamics match both the description and

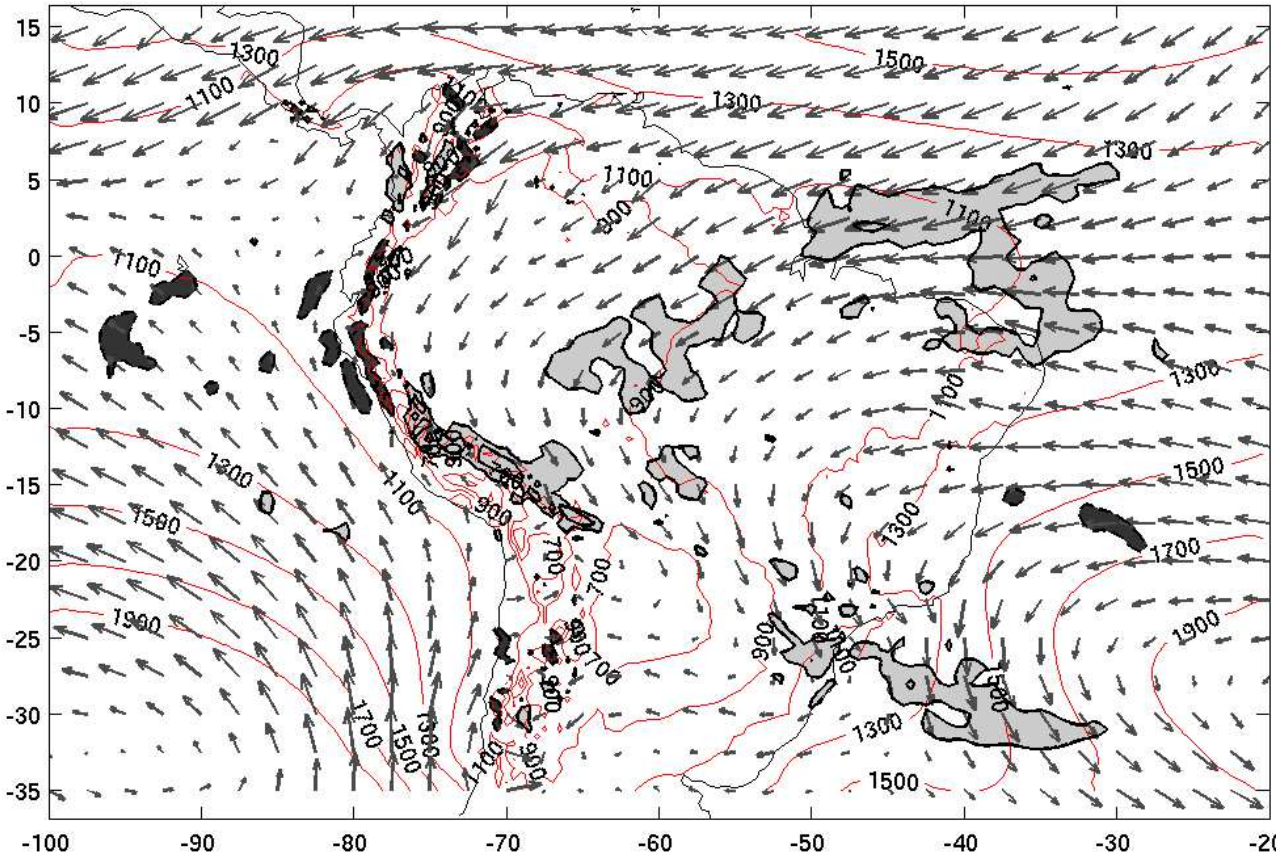

Figure 5.4: Austral summer (DJF) meteorological parameters under continental SACZ conditions. Mean sea-level pressure are displayed in fine contours, in hPa (with a 1e5 Pa subtracted from the mean). The light (dark) grey shaded areas represent wind divergence at 200 hPa above the 75% (below the 25%) percentile. Arrows represent the mean horizontal vapour advection $\vec{H}$.

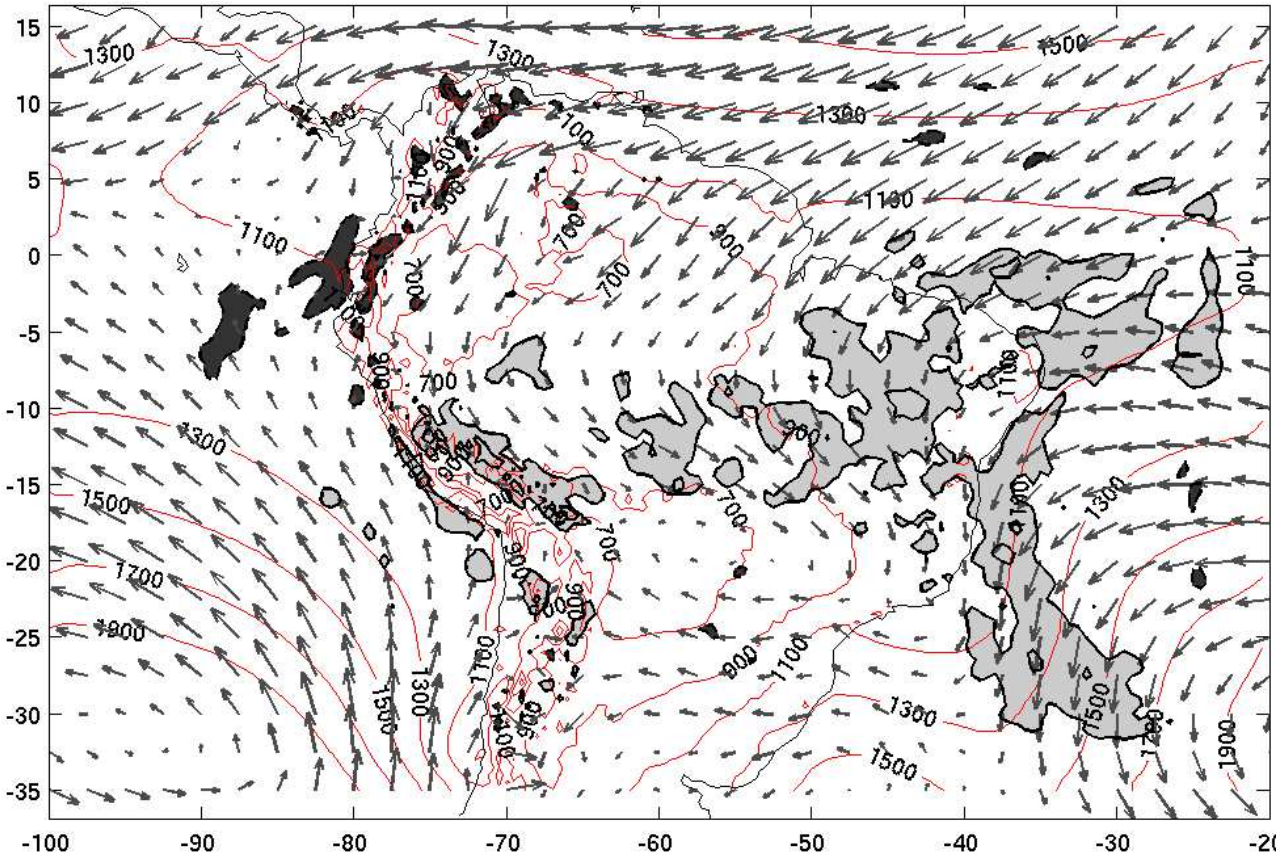

Figure 5.5: As in figure 5.4, but under oceanic SACZ conditions.

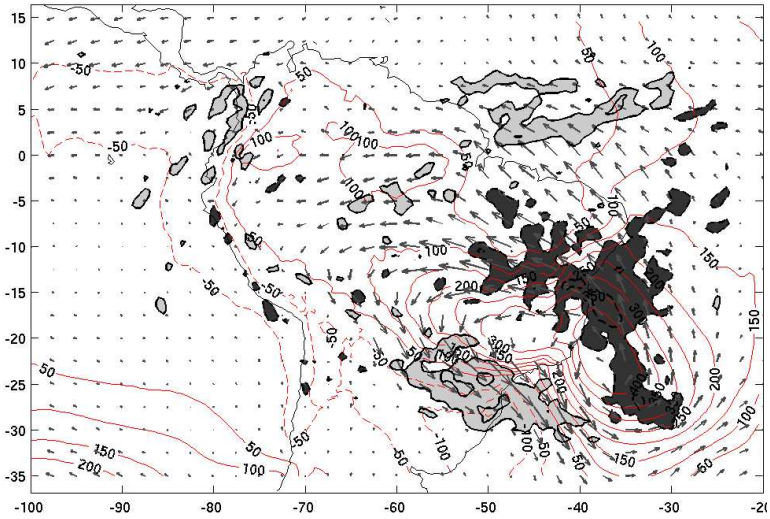

Figure 5.6: Difference between continental and oceanic SACZ conditions, i.e. the subtraction of figure 5.5 from figure 5.4.

interpretation of the SACZ configurations, as discussed in Carvalho et al. [2002, 2004]. The difference between circulation patterns in the continental and oceanic composites (Figure 5.6) summarizes the low-level mechanisms responsible for the dipolar shape of precipitation. In the continental SACZ composite, the South Atlantic high is strengthened and shifted to the North. Likewise, the Chaco low is strengthened. As a consequence, moist Amazonian flow is increased to the Paraná region, and decreased to over east Brazil and the neighbouring Atlantic. This favours convergence over the Paraná, thus increasing precipitation, but causes subsidence over east Brazil. In this situation, the Atlantic ITCZ lies around the Equator. In the opposite, oceanic SACZ composite, the situation is reversed. As a consequent, the ITCZ and the SACZ tend to merge off the east coast of Brazil.

5.4 Stable water isotopes: an integrated proxy of the SAMS

The previous section underlines the atmospheric circulation patterns responsible for the Paraná-Nordeste dipole in precipitation. These mechanisms are accurately reproduced by REMO. Given this validation of intra-seasonal variability in REMO, we can investigate further the imbedded stable water isotope diagnostics: what does δ^{18}O signature in precipitation reveal from the regional circulation patterns ?

The present study is innovative by its use of stable water isotopes to characterize the source and path of moisture from its isotopic signature. The saturation vapour pressure at constant temperature is slightly lower for heavier water isotopes (HDO and $H_2^{18}O$) than for standard water ($H_2^{16}O$). Hence under thermodynamical conditions, the heavier isotopes preferably migrate to the liquid phase. As a consequence, liquid water is enriched and remaining vapour depleted as compared to the original reservoir. The depletion in $H_2^{18}O$ is expressed in reference to the Vienna standard mean ocean water (V-SMOW), by following equation:

$$\delta^{18}\mathrm{O} = \left(\frac{[H_2^{18}O]/[H_2O]_{sample}}{[H_2^{18}O]/[H_2O]_{SMOW}} - 1 \right) \cdot 1000 \; [‰] \tag{5.1}$$

The definition of δD is analogous to equation 5.1, replacing $H_2^{18}O$ with HDO. The equilibrium fractionation is temperature-dependent: the depletion (in absolute values) increases if temperature decreases [Majoube, 1971]. The validity of the δ^{18}O simulation by REMO was assessed with regard to GNIP [IAEA and WMO, 2001] observations and ECHAM simulations in Sturm et al. [2005a]. In this section, we concentrate on sub-seasonal variability of δ^{18}O over South America, which has not been documented so far. Climatological patterns of precipitation and δ^{18}O are compared to GNIP observations, along with the up-streamlines for horizontal vapour transport from selected GNIP stations (not shown). The mean wind directional constancy, calculated on the base of 6 hour wind speeds, is defined in equation 5.2.

$$D_c = \frac{||\overline{\vec{H}}||}{||\vec{H}||} = \frac{\sqrt{\overline{H_u}^2 + \overline{H_v}^2}}{\overline{\sqrt{H_u^2 + H_v^2}}} \tag{5.2}$$

In case of steady winds, $D_c = 1$, whereas it decreases towards 0 if its direction is very variable. The wind constancy is higher than 0.8 over most of the tropical South American continent. This is consistent with the negligible moisture advection by transient eddies in tropical South America [Brahmananda Rao et al., 1996]. Hence, we can make the assumption that up-streamlines represent roughly the mean back-trajectories of air masses that precipitate over the GNIP stations. The sharp boarder of $D_c > 0.8$, approximately a line from the Beni [65 °W; 15 °S] to Rio de Janeiro [44 °W; 23 °S], marks the intrusion of polar fronts in sub-tropical South America up to 15 °S [Garreaud, 1999, 2000].

5.4.1 δ^{18}O and moisture trajectory

The climatological δ^{18}O pattern by REMO is discussed in Sturm et al. [2005a]. In observations as is REMO simulations, mean δ^{18}O varies with altitude and continentality. It results from the balance of two opposing effects: the amount effect (cloud vapour is depleted proportionally to the cumulated rain-out along the trajectory) and recycling effect (non-

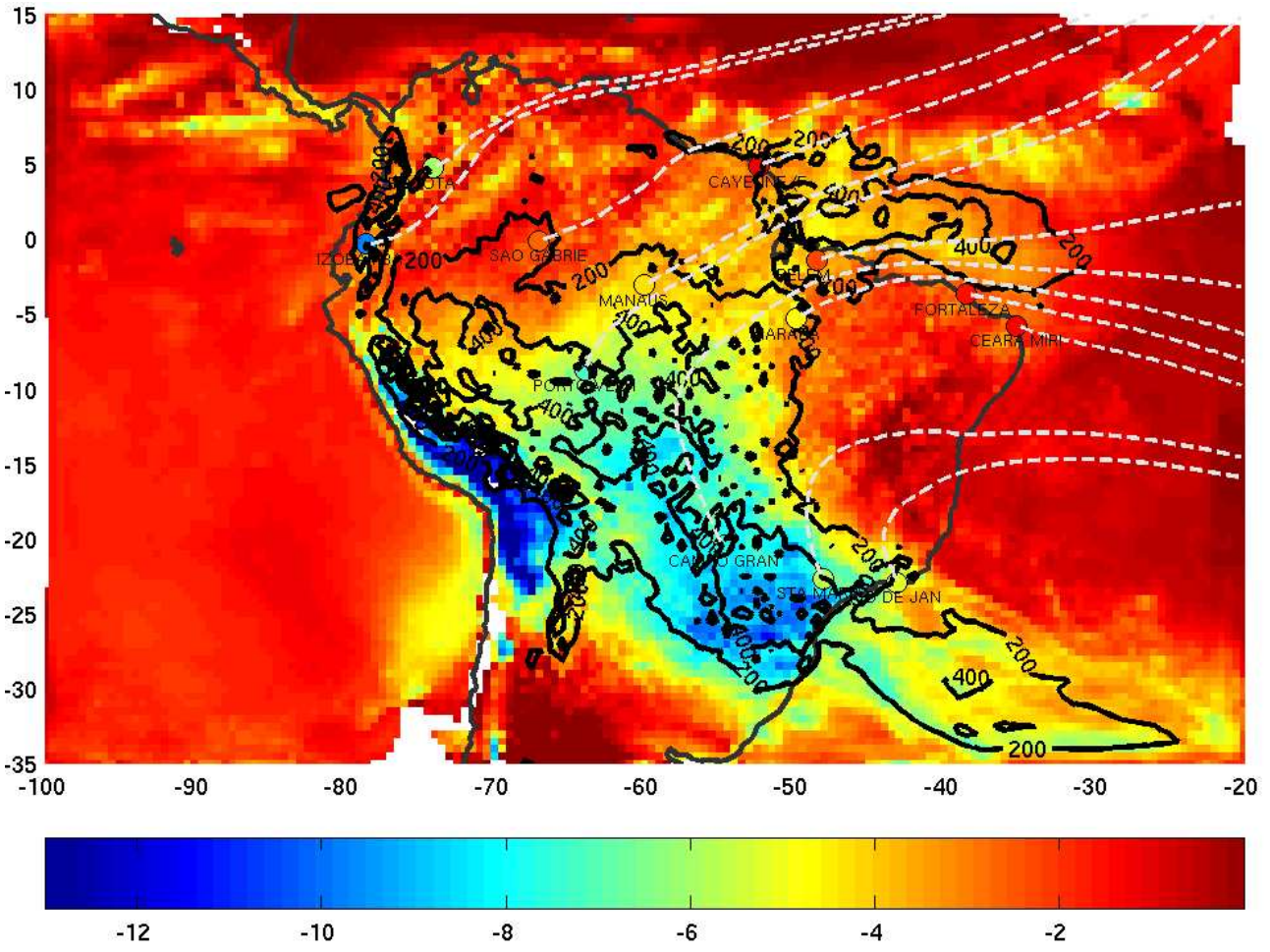

Figure 5.7: Continental SACZ composite for $\delta^{18}O$ (shaded, in $‰$). Contours represent total precipitation (with 200 mm/month increment). Coloured dots represent $\delta^{18}O$ at GNIP stations, with their names displayed below. The dotted lines represent streamlines of mean horizontal vapour advection ($\mathbf{H} = \overline{Q \cdot \mathbf{u}}$).

fractionating transpiration by the vegetation releases comparably enriched vapour in the atmosphere). Along its trajectory, the cloud reservoir undergoes a gradual depletion over the continent (increasing land inwards rainout), especially upon reaching a topographic barrier (increasing precipitation). In both cases, the cumulated rain-fall along the trajectory is responsible for the gradual depletion of the cloud water, hence a lowering of $\delta^{18}O$ in precipitation. The variation of $\delta^{18}O$ over the ocean is much less than over land, since precipitation occurs close to the evaporation point, and is immediately compensated by relatively enriched vapour from the ocean. In REMO, the ocean's $\delta^{18}O$ is constant at $+0.5‰$. In case of colder SST or stronger surface winds, evaporated vapour is more depleted.

The continental (Figure 5.7) and oceanic SACZ composite (Figure 5.8) of $\delta^{18}O$ obey to the same balance between amount and recycling effects. In both cases, the $\delta^{18}O$ pattern follows the precipitation iso-lines, illustrating the amount effect. In the absence of rain, reduced relative humidity leads to increased evaporation, which increases the $\delta^{18}O$ of near-surface moisture, which is imprinted via partial re-equilibration to the precipitation $\delta^{18}O$. Superimposed on these local effects, the continental rainout augments the depletion along the air parcel trajectory.

Under a continental SACZ (Figure 5.7), the strengthened Nordeste trough advects moisture from the sub-tropical Atlantic. The core of depleted precipitation coincides with maximum rainfall in a Northwest/Southeast band ([65 °W; 10 °S] to [50 °W; 25 °S]). Upon reaching the Iguaçu catchment in the Southern Brazilian highlands, precipitation reaches its most depleted values (-10 $‰$). Due to the weak rainout and strong evapo-transpiration, precipitation is hardly depleted over the Nordeste (> -2 $‰$).

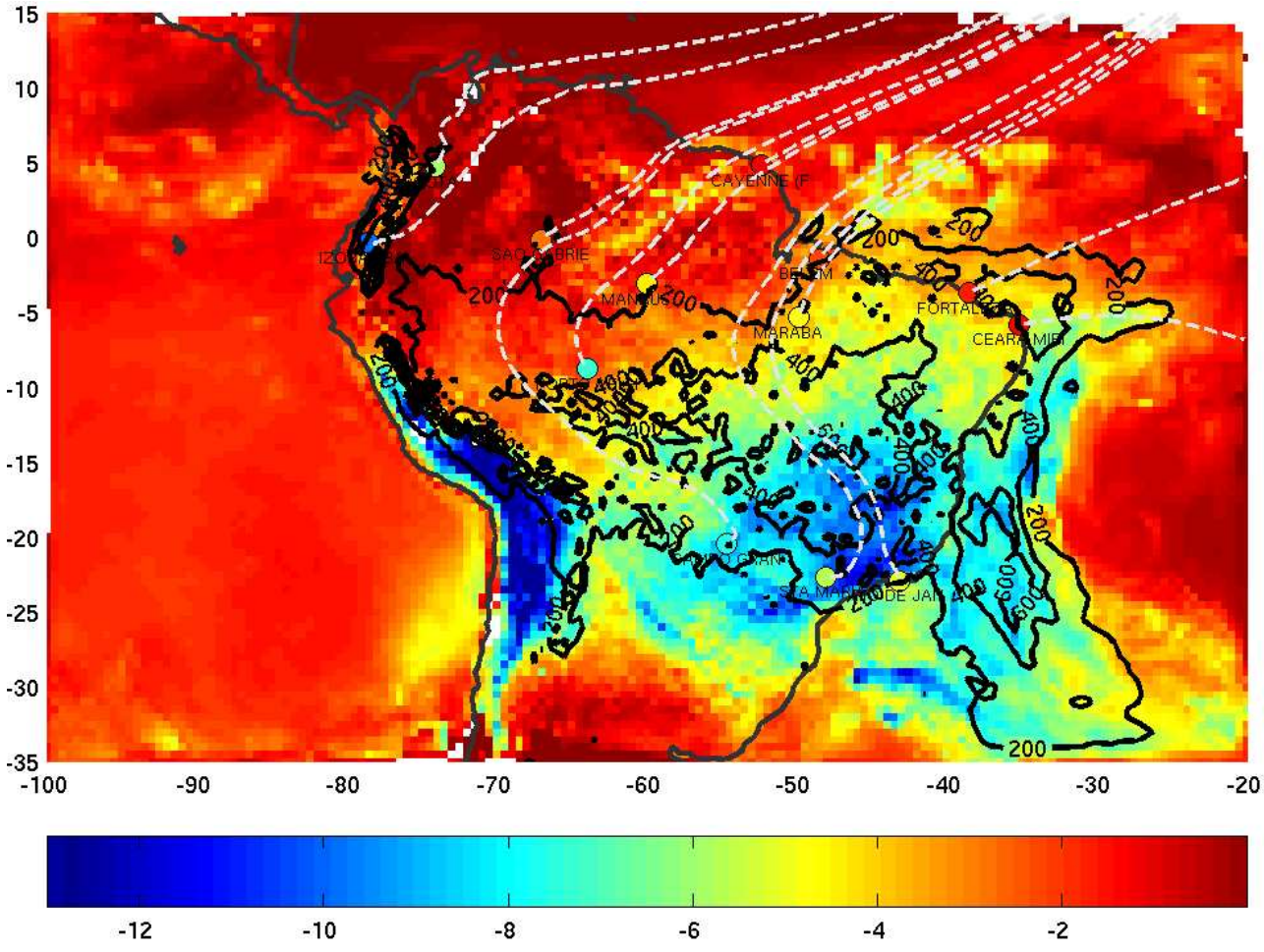

Figure 5.8: As in figure 5.7, but under oceanic SACZ conditions.

Under oceanic SACZ conditions (Figure 5.8), moistures originates in the Northern tropical Atlantic and is advected across the Amazon to the Central Brazilian highlands. Most depleted precipitation spans Eastern Brazil, from [55 °W; 25 °S] to [40 °W; 5 °S], reaching minimum values of -13 ‰ West of Rio de Janeiro. Two factors contribute to the enhanced maximum depletion for the oceanic SACZ. Fist, precipitation are more intense than in the continental SACZ case, reaching local maxima of 600 mm/month. Second, SST are lower in the Northern Atlantic (boreal winter) than in the sub-tropical Atlantic (austral summer). Hence the initial vapour δ^{18}O is lower in the oceanic than in the continental SACZ case. Although precipitation is low over the Paraná region, its δ^{18}O is fairly depleted (-8 ‰), because of the intense upstream rain-out.

The previous paragraph highlights the integrative character of precipitation δ^{18}O. The latter is confirmed by the pattern of δ^{18}O EOF, shown in Figure 5.1b. Because of the amount effect, positive δ^{18}O EOF values dominate Eastern Brazil, in correspondence with the negative EOF values for precipitation. On the other hand, the negative EOF values for a band from the central Andes to the Paraná, instead of the individual positive extrema of the precipitation EOF. Table 5.1 shows that EC^1_δ expansion coefficients correlate remarkably well with that of all climate parameters, apart from the zonal vapour transport $H_u{}^*$. The two best matches are between δ^{18}O and meridional vapour transport H_v ($r^2 = 58\%$), and between δ^{18}O and low-level jet count ($r^2 = 46\%$). This finding reinforces previous conclusions about the SAMS mechanism: low level jets advect warm and moist air from the Amazon, running along the Eastern flank of the Andes, and triggers heavy convection over the continental SACZ. δ^{18}O records better than precipitation this physical relationship, because it keeps a 'memory' of cumulated precipitation along its trajectory. The squared correlation coefficient with EC_{LLJ} marks a clear improvement between δ^{18}O ($r^2 = 0.46$) and precipitation ($r^2 = 0.19$). This indicates that δ^{18}O is a better proxy than precipitation, at pentad resolution, for extreme precipitation events caused by LLJs. The physical explanation for the latter is that extreme precipitation events and corresponding low δ^{18}O are recorded in the weighted mean pentad isotopic signal, whereas no distinction is made between extreme and median events in the pentad precipitation record. LLJ and associated extreme precipitation show a pronounced daily cycle, with night time maxima [Vernekar et al., 2003, Carvalho et al., 2002]. Based on the same argument, extreme precipitation linked with LLJ are better recorded in the δ^{18}O than precipitation signal for any average exceeding that characteristic frequency. In fact, Sturm et al. [2005a] has shown that SAMS characteristics are recorded in the monthly δ^{18}O anomalies, although not being noticeable in monthly precipitation anomalies.

Due to the strong anti-correlation between the first modes for δ^{18}O and precipitation, the EOF^1_δ pattern (Figure 5.1b) is positive over the Nordeste and negative over the Paraná. This opposition likewise appears in the correlation map of EC^1_δ with precipitation (Figure 5.2b) and the difference between the oceanic and continental SACZ composite (Figure 5.9). Both the EOF pattern and the heterogeneous correlation maps highlight the crescent-shaped connection between δ^{18}O in the Paraná, the Central Andes and Northern Amazonian regions. It is worthwhile noticing that the connection between the Northern Amazon, the central Andes and the Paraná region is stronger in the δ^{18}O and H_v correlations (Figure 5.2b-c) than in the homogeneous precipitation correlation map (Figure 5.2a). This supports previous conclusions: the integrative character of δ^{18}O makes it a good proxy for strong convection related to LLJ.
The difference between the oceanic and continental SACZ composite (Figure 5.9) primarily illustrates the amount effect: highly positive δ^{18}O values are found over the Nordeste, coherent with the observed precipitation deficit in the continental SACZ case. The crescent-shaped negative counterpart is less obvious, because δ^{18}O in the Paraná, downstream of the mean precipitation zone, are depleted even in the oceanic SACZ composite.

5.4.2 Regional relevance of station measurements

EOF analysis is a convenient method for analysing physical processes responsible for spatial and temporal variability in climatic signals. The previous sub-section has shown that δ^{18}O in particular is a good proxy of the SAMS variability, as simulated by $REMO_{iso}$. Unfortunately, no gridded data sets are available for δ^{18}O observations. Aim of this section is

*The expansion coefficients for H_u and H_v derive from the complex (or Hilbert) empirical orthogonal function algorithm . By construction, they are chosen to be independant, and thus uncorrelated.

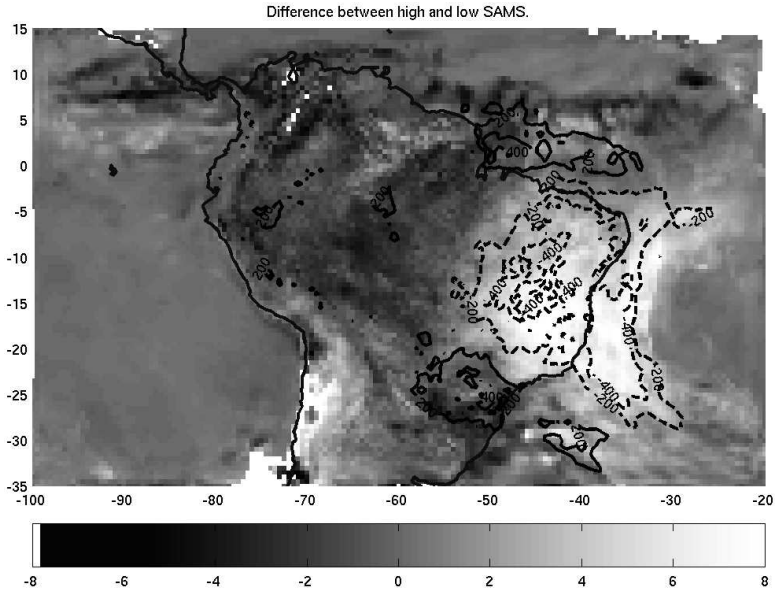

Figure 5.9: Difference between continental and oceanic SACZ conditions, i.e. the subtraction of figure 5.8 from figure 5.7.

to demonstrate that SAMS variability can be identified based on station records, and produces results coherent with the EOF method. Hence, we can establish a link between the present modelling study and isotopic monitoring of a rain-gauge network over Bolivia [Vimeux et al., -].

Six locations were selected for their representativeness of the SAMS variability. In each a $5 \times 5^\circ$ box, we compute the mean precipitation and weighted δ^{18}O; these time-series are hereafter referred to as 'station records', analogously to rain gauge and δ^{18}O observations. These 'virtual' stations are centred at following locations:

- The box including *Belém* is centred at [51.5°W;3.5°S], and marks the meeting point of Amazonian convergence and the ITCZ in the continental SACZ composite.

- The *Equatorian (or Central) Andes* station is centred at [73.5°W;4.5°S]. It lies on the eastern foothill of the Cordillera, at the origin of the Sourthen LLJ.

- The *Nordeste* station is centred at [42.5°W;9.5°S], at the Northern extension of the precipitation maximum in the oceanic SACZ composite.

- The *Paraná (or continental SACZ)* station is centred at [52.5°W;28.5°W]. It marks the precipitation maximum in the continental SACZ composite.

- The *oceanic SACZ*, centred at [42.5°W;31.5°S], marks the extension over the Atlantic of convection over the Paraná in the continental SACZ composite.

- The *Zongo* station is centred at [65.5°W;14.5°S], at the foothills of the Altiplano. Extensive isotopic observations at daily and monthly time-scale have been conducted along this valley, as reported in Vimeux et al. [-].

The location of the $5 \times 5^\circ$ station boxes in shown in Figure 5.10.

Table 5.2 shows the cross-correlation coefficients between mean precipitation and δ^{18}O for all six stations, including EC^1_{Prec} and EC^1_δ. We first examine how station records individually correlate with SAMS variability, represented by EC^1_{Prec} and EC^1_δ. Then we investigate the cross-correlations between station records, to identify SAMS variability mechanisms without the help of EOFs.

	Stations	Andes	Nordeste	Paraná	Zongo	Belém	sub. Atl.	Prec	δ^{18}O
		Precipitation						EC#1	
Precipitation	**Andes**	1	-0.39	0.3	⋆	⋆	⋆	0.34	-0.62
	Andes^{-1}	0.38	-0.44	0.29	⋆	⋆	⋆	0.33	-0.49
	Nordeste	-0.39	1	-0.5	⋆	-0.27	-0.28	-0.88	0.7
	Paraná	0.3	-0.5	1	⋆	⋆	0.39	0.57	-0.55
	Zongo	⋆	⋆	⋆	1	⋆	⋆	⋆	⋆
	Zongo^{-1}	⋆	⋆	⋆	⋆	⋆	-0.32	⋆	⋆
	Belém	⋆	-0.27	⋆	⋆	1	⋆	0.33	⋆
	sub. Atl.	⋆	-0.28	0.39	⋆	⋆	1	0.35	-0.32
		δ^{18}O						EC#1	
δ^{18}O	**Andes**	1	-0.35	⋆	0.63	⋆	⋆	-0.33	0.59
	Andes^{-1}	0.5	-0.43	0.22	0.3	⋆	⋆	-0.39	0.57
	Nordeste	-0.35	1	-0.36	-0.42	0.2	⋆	0.55	-0.76
	Paraná	⋆	-0.36	1	⋆	⋆	⋆	-0.54	0.4
	Zongo	0.63	-0.42	⋆	1	-0.21	⋆	-0.21	0.62
	Zongo^{-1}	0.5	-0.4	⋆	0.45	⋆	⋆	-0.36	0.61
	Belém	⋆	0.2	⋆	-0.21	1	⋆	-0.38	⋆
	sub. Atl.	⋆	⋆	⋆	⋆	⋆	1	⋆	⋆

Table 5.2: Correlation coefficients between mean δ^{18}O and precipitation over selected locations. Each location is represented by a $5 \times 5^{\circ}$ box. The Equatorian Andes box is centred at [73.5°W;4.5°S], Nordeste at [42.5°W;9.5°S], Paraná at [52.5°W;28.5°S], Zongo at [65.5°W;14.5°S], Belém at [51.5°W;3.5°S] and subtropical Atlantic at [42.5°W;31.5°S]. The Equatorian Andes^{-1} and Zongo^{-1}, located to the west of the study domain, were correlated with a -1 pentad lag. Remarkable correlations, discussed in the text are displayed in grey cells. Correlations that fail the Student-t significance test at 90% level are replaced by ⋆.

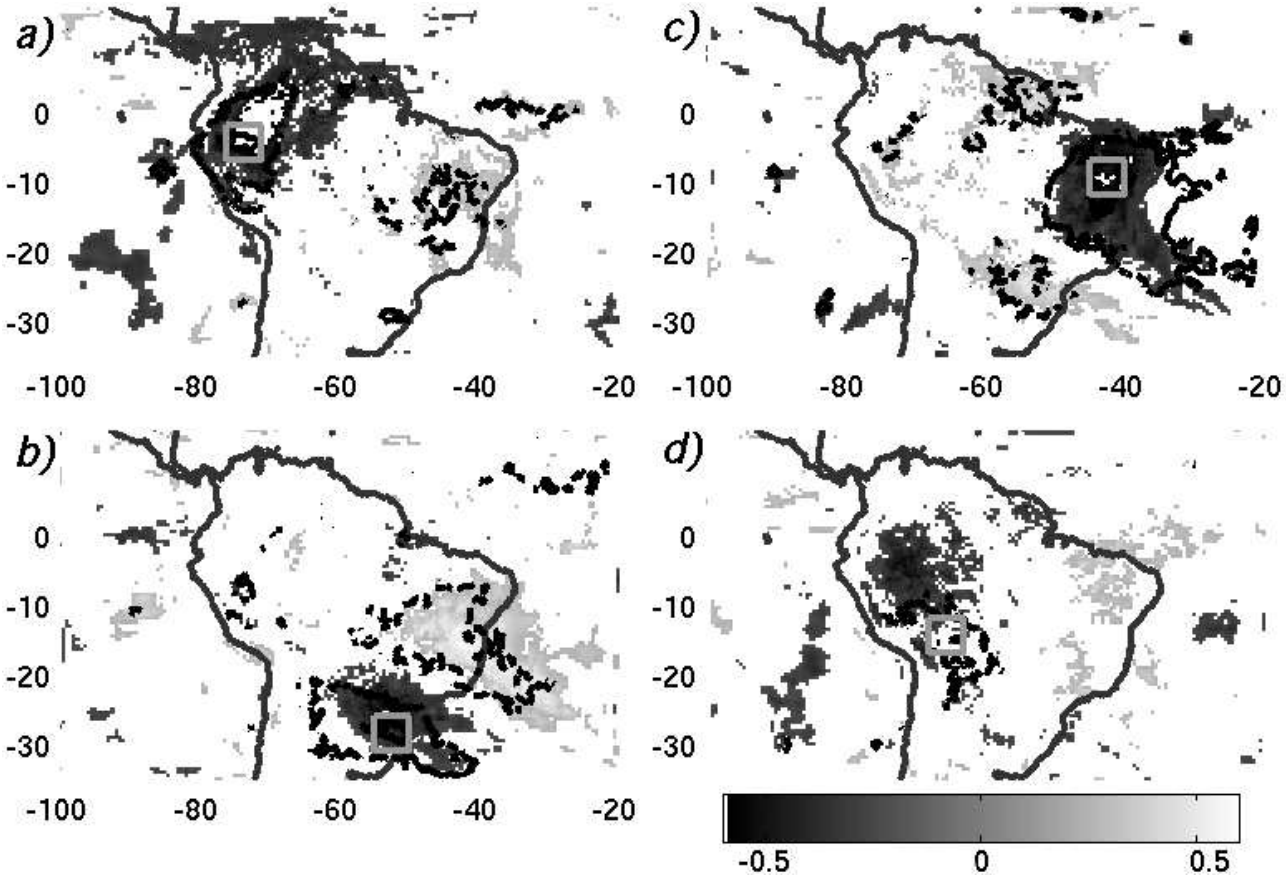

Figure 5.10: Correlation of station data with domain-wide precipitation. The shaded values indicate correlation of $\delta^{18}O$ in the grey box with precipitation. The plain (dashed) black lines indicate correlations of mean precipitation in the box greater than 0.35 (lower than -0.35). Only correlations significant at a 95% level are plotted. The box represent a) the Equatorian Andes, averaged over [76°W; 71°W], [7°S; 2°S], b) Paraná, averaged over [55°W; 50°W], [31°S; 26°S], c) the Nordeste [45°W; 40°W], [12°S; 7°S], d) Zongo valley at the foothills of the Altiplano [68°W; 63°W], subtropical Atlantic [17°S; 12°S].

Precipitation from the Paraná and Nordeste stations primarily illustrate the bi-modal pattern of the SAMS variability. Similar to the EOF^1_{Prec} pattern (Figure 5.1a), the correlation coefficient with EC^1_{Prec} is strongly negative for Nordeste (-0.88) and positive for Paraná (0.57). Accordingly, precipitation at the two stations are strongly anti-correlated ($r = -0.5$). Significant positive correlations with EC^1_{Prec} are also found all along the crescent-shaped continental SACZ maximum: Belém (0.33), central Andes (0.34) and subtropical Antlantic (0.35). Accordingly, precipitation over the central Andes are weakly anti-correlated with Nordeste precipitation ($r \sim 0.3$). Precipitation over the sub-tropical South Atlantic is not as strongly controlled by the SAMS variability as precipitation over Paraná. Carvalho et al. [2004] also reports that continental SACZ anomalies in the NCEP reanalyses have no influence on the climatological location of the SACZ, in the western southern sub-tropical Atlantic (WSSA). The difference between land and sea precipitation could further be enhanced by their different parameterisation of convection in the ECHAM physics.

Station δ^{18}O is a better proxy for the SAMS variability than precipitation, because it underlines the associated circulation patterns. As for precipitation, δ^{18}O in Nordeste is strongly anti-correlated with EC^1_δ ($r = -0.76$). In agreement with the EOF^1_δ pattern (5.1b), the source region of LLJ (central Andes: $r = 0.59$, Zongo:$r = 0.62$) is better correlated with EC^1_δ than its exit region (Paraná: $r = 0.4$).

Table 5.2 further underlines the role of LLJ on the δ^{18}O station signals. δ^{18}O in the central Andes and Zongo stations are closely related ($r = 0.63$), which contrasts with the uncorrelated precipitation at the two sites. Back-trajectory computations show that the average travel time for an air parcel from the Atlantic the Zongo valley ranges from 6 [Sturm et al., 2005a] to 10 days [Vimeux et al., -] during the wet season. The same duration is needed for an air-parcel to travel from the central Andes to the Paraná. Accordingly, -1 pentad lagged correlations are shown in Table 5.2 for the two eastern stations: central Andes and Zongo. Figures 5.7 and 5.8 demonstrate that both stations lie upstream of the Nordeste-Paraná dipole. The δ^{18}O correlation coefficients increase (in absolute values) when accounting for the delay between upstream (central Andes, Zongo) and downstream (Nordeste, Paraná) stations. Lagged central Andes δ^{18}O reveals a stronger anti-correlation with Nordeste δ^{18}O ($r = -0.43$), and significant positive correlation arises with Paraná δ^{18}O ($r = 0.22$). Similarly, lagged Zongo δ^{18}O matches better the variability of EC^1_{Prec}, focussed on the downstream Nordeste-Paraná dipole.

Following Dommenget and Latif [2002], the δ^{18}O/precipitation station records were correlated with domain-wide precipitation. We retain four stations that record maximum SAMS variability, materialised by $5 \times 5^\circ$ grey boxes in Figure 5.10: Nordeste, Paraná and central Andes and Zongo. Precipitation at the first three stations are representative of a wider zone, which is marked by contiguous positive correlation (continuous contours). In the case of Paraná and Nordeste, station precipitation is clearly anticorrelated with other regions (dashed contours). Precipitation over the Paraná, typical for the continental SACZ composite, is in opposite phase to precipitation over eastern Brazil, with an extremum at [45 °W; 20 °S]. Only a limited positive connection exists between the Paraná station and precipitation over the central Andes, at [73 °W; 7 °S]. Typical for the oceanic SACZ composite, precipitation over the Nordeste is anti-correlated with two distinct regions, the Amazon delta (at [55 °W; 3 °N]) and the Paraná (with an extremum at [55 °W; 25 °S]). Correlation of central Andes precipitation gives weak negative values over the Nordeste [45 °W; 10 °S]. On the other hand, hardly any positive connection to the Paraná region is noticeable.

Shaded areas on Figure 5.10 represent correlation of station δ^{18}O with domain-wide precipitation. Station δ^{18}O correlation reflects primarily the same relationships as precipitation, with opposite signs because of the amount effect. However, station δ^{18}O tend to have a wider extension of significant remote correlations, whereas correlation with precipitation reaches its highest scores locally, around the station. It is most obvious at the central Andes station (Figure 5.10a), where δ^{18}O is not significantly correlated with precipitation in its immediate vicinity, but shows strong correlations with regions further upstream (North of Belém). Similarly, Nordeste δ^{18}O record less extended correlation domain than precipitation over eastern Brazil, but it has a wider remote coverage. Hence, δ^{18}O in Nordeste clearly reveals the crescent-shaped phase opposition between northern Amazon, the central Andes and the Paraná region.

Table 5.2 underlines the regional representativeness of the Zongo station, which is further stressed in Figure 5.10d. Zongo precipitation has only a very local significance: no correlation is marked apart from a close downstream region to the southeast. However, Zongo δ^{18}O is clearly anti-correlated with precipitation upstream, in the central Andes region up to Belém. It further features an anti-correlation with the Nordeste. A weak connection with the Paraná region is also

noticeable, which is enhanced by taking into account the a -1 pentad time-lag.

In conclusion, correlations between $\delta^{18}O$ station records and domain-wide precipitation bring into light the SAMS variability revealed by EOF analysis. The precipitation regime over Nordeste is in phase opposition primarily with the Paraná region. $\delta^{18}O$ further reveals the connection of Paraná precipitation with upstream regions, stretching from Zongo and the central Andes up to Northern Amazonian in a crescent shape around eastern Brazil. The superposition of $\delta^{18}O$ correlation maps for the central Andes, Zongo and Paraná stations (Figures 5.10 a-d) is an approximation of the $\delta^{18}O$ EOF pattern (Figure 5.1b); the reconstruction is not complete, because the time sampling (5 days) is in the same order of magnitude as the travelling time of vapour across the selected sites. Correlation between upstream and downstream stations can be improved by taking into account the air parcel travel time, which is in the same order of magnitude as the data sampling frequency (5 days).

5.5 Discussion

The previous sections underline the SAMS variability in precipitation and atmospheric circulation, which are both integrated in the isotopic signal. Our objective now is to verify whether the SAMS mechanisms, as suggested in previous publications, are consistent with new evidence from the stable water isotopes. The present simulation covers 5 years in climatological conditions. It is thus well suited for analysing intra-seasonal variability. We suggest as an hypothesis that physical modes of intra-seasonal variability are relevant on inter-annual time scale. Based on previous results with longer time-series, we assess under which conditions this assumption is valid.

Firstly, we discuss the validity of the South American summer climate as simulated by REMO. This is a pre-requisite for the analysis of the isotopic signal. Secondly, the $\delta^{18}O$ variability confirms the dominant role of LLJ on the SAMS. Hence, a good representation of orography is needed to reproduce the features of the South American monsoon. Thirdly, the particularity of the present simulation is the use of climatological, non-interactive SST prescription, which allows significant variability in the location and intensity of the SAMS is observed. We discuss the possible feedback between the atmosphere and the ocean surface in controlling the SACZ. Finally, we discuss the competing influence of the SAMS and the El Niño Southern Oscillation (ENSO) on the isotopic signal in South America.

5.5.1 Synoptic forcing of the SAMS

Interpretation of the isotopic signal is only valid if the South American climate is reasonably well reproduced by REMO. REMO has proved to accurately reproduce the mean summer climate [Sturm et al., 2005a], albeit excessive precipitation amounts. Thereafter, we discuss how REMO accounts for intra-seasonal variability in comparison to both modelling and observational studies.

Lenters and Cook [1999] suggests three major mechanisms explaining above normal precipitation over the Altiplano at a pentad resolution. The leading one involves extra-tropical cyclone activity. Low-level cyclonic activity, denoted 'Chaco lows', form or intensify on the lee of the Southern central Andes (between 20°and 40°S). The decreased wind directional constancy simulated by REMO on the east flank of the Andes reflects the penetration of extra-tropical cold fronts up to 15°S. Following Lenters and Cook [1999], 'strong pressure gradients to the north-east of the extra-tropical cyclones lead to warm, moist, low-level flow from the north-east and an intense, active SACZ, which is displaced westward of its climatological position'. Such events are associated with increased precipitation over the central Andes and the Paraná, and reduced precipitation over east Brazil. The third mechanism, which produces similar precipitation anomalies, involves a westward enhancement of South Atlantic High and SACZ. Both situations appear to be merged in the continental SACZ composite simulated by REMO. In Figure 5.4, strong SLP gradients north of the Chaco low are combined with enhanced south Atlantic high to increase the north-westerly flow of Amazonian moisture to the Paraná region. The SACZ is shifted westward and penetrates onto the continent. This situation is associated with a maximal precipitation north-west/south-east band, stretching from the central Andes to the Paraná. In this situation, the Atlantic ITCZ is clearly distinct from the SACZ, leading to a precipitation maximum over the Amazon delta.

The composite for maximum January precipitation over West-Central Brazil reported by Gan et al. [2004] exhibit the same circulation patterns as REMO oceanic SACZ composites. The Chaco low is enhanced and shifted to the North by 5°, together with a weakening of the South Atlantic high. Anomalous cyclonic circulation diverts the Amazonian air flow to the west instead of the south-west, where it converges with northerly Atlantic flow. Moist, unstable air convergence cause an intensification of the SACZ, which is shifted northwards. Similar strengthening and northward shift of the SACZ is reported by Carvalho et al. [2002], Barreiro et al. [2002]. It results in increased precipitation over Central-West Brazil, extending down to São Paolo.
REMO reproduces correctly the SACZ variability, and associated precipitation and circulation anomalies. A discrepancy is yet observed in the location of the ITCZ: it is shifted 10°S of its location in the continental SACZ composite, reaching between 5°-10°S. This discrepancy is partly inherited from its host model ECHAM [Sturm et al., 2005a]. Other RCM/GCM studies experience the same difficulties in a correct localization of the Atlantic ITCZ [Rojas and Seth, 2003, Barreiro et al., 2002]. As a consequence of this mismatch, the ITCZ and the SACZ tend to merge of the eastern coast of Brazil, producing unrealistic precipitation >200 mm/month over the arid Nordeste.

5.5.2 Role of the low-level jets (LLJ)

Vernekar et al. [2003] describes the simulation of South American summer climate at daily to inter-annual time-scales with the NCEP Eta RCM. In particular, the association of LLJ events and high precipitation is clearly documented. The variability of LLJ shows a peak at diurnal peak, with night time precipitation maxima at the exit of the LLJ east of the Andes. Furthermore, a periodicity of 20 days is reported. Nogues-Paegle et al. [2003] links this variability to the Pacific-South American teleconnection pattern (PSA). Barros et al. [2003] defines the case where the LLJ penetrates southward of 25 °as Chaco Jet Events. Citing Nicolini et al. [2002], composites of CJE 'account for an important fraction of seasonal precipitation in northeastern Argentina, northern Urugay, eastern Paraguay and southern Brazil (...) reaching maximum of 55% in summer'. The role of LLJ is further documented in Nogues-Paegle et al. [2003], Grimm et al. [2004], Carvalho et al. [2002].
Due to the pentad averaging in the present study, the diurnal variability of LLJ and associated precipitation cannot be documented directly. Nevertheless, weighted mean δ^{18}O gives more prominence to extreme events, which tend to be more depleted. The higher correlations of δ^{18}O than precipitation with both meridional vapour transport H_v and and LLJ count reflects this dependency. An FFT analysis on the expansion component associated with the first EOF of H_v reveal two minor peaks at 13 and 14 day periods, with larger peaks at 24 and 51 day period. Hence REMO seems to capture correctly the $\sim$ 20 day cyclicity of LLJ. According to Paegle et al. [2000], Carvalho et al. [2004], the $\sim$ 50 day periodicity could represent the modulation of SACZ activity by the Madden-Julian Oscillation (MJO) over the tropical Pacific.

5.5.3 South Atlantic SST feedback on the SACZ

Doyle and Barros [2002] present an extensive study Atlantic SST anomalies and related circulation patterns over Subtropical South America. Monthly SST in the western sub-tropical South Atlantic (WSSA) is found to be correlated with the position and intensity of the SACZ, hence with precipitation patterns over sub-tropical South America. The region of highest correlation is located between [20°S; 30°S] in latitude and [30°W; 50°W] in longitude. Based on canonical correlation analysis of monthly NCEP reanalyses, warm (W) and cold (C) SST composites are build. Barreiro et al. [2002] identify similar correlations between precipitation EOF loadings and South Atlantic SST indices in ensemble runs by the CCM3 GCM. Yet, both articles introduce some limitations about the observed correlations. SST forcing explains a significant part of the SACZ variability over the Atlantic, but has little influence on the variability of continental precipitation. The C (W) composite corresponds to the oceanic (continental) SACZ composite simulated by REMO. There is an apparent contradiction is the composite resemblance, since the SAMS variability in REMO takes place with stationary SST.
The contradiction can be resolved by considering the SACZ variability as being primarily of atmospheric origin, with positive feedback from the surface ocean. Singular value decomposition show that sea-level pressure lead SST changes by 1-2 months [Venegas et al., 1997], indicating an atmosphere-to-ocean forcing. The SACZ location in its continental

composite tend to decrease the SST over the WSSA. The enhanced cloudiness reduces the radiative heating of surface ocean, and increased surface winds mix the ocean boundary layer. The negative SST anomalies in turn enhances the temperature contrast between land and ocean, strengthening a giant land-sea breeze that intensifies the oceanic SACZ. Furthermore, the Brazilian Current flowing along the east Brazil coast advects negative SST anomalies to the South. Similar to Lenters and Cook [1999]'s second mechanism, the cold-core subtropical low is strengthened, thus enhances moist westward flow into the oceanic SACZ and helps maintaining a strong SACZ activity on seasonal time-scales.

In conclusion, the short integration (5 years) of REMO using climatological SSTs exclusively reflects the atmospheric variability of the SACZ. The variability is highest over land, where feedbacks by energy and moisture exchanges with the surface conforts the stochastic behaviour of the SAMS. Nevertheless, the fact that the variability patterns agree well with observations and coupled model studies supports the assumption of an atmosphere-to-ocean forcing between the SACZ and South Atlantic SST. The lack of a coupled ocean model in REMO merely limits the positive feedback from SST on the SACZ, which could affect the persistence of the simulated SACZ. In this given case, the physical modes of intra-seasonal variability can be transposed to the inter-annual time-scale.

5.5.4 ENSO modulation of the SAMS

The modulation of SACZ by extreme phases of the El Niño Southern Oscillation (ENSO) is demonstrated at inter-annual time-scales. It is beyond the scope of the present article to discuss the different connection patterns, which have been addressed in several studies [Grimm, 2003, Lau and Zhou, 2003, Nogues-Paegle et al., 2003]. Here, we focus here on the analysis of the δ^{18}O signal: is it possible to distinguish the internal (SAMS) from the remote (ENSO) modes in the recorded isotopic signal ? The discussion is based on a mechanical analogy. The present experiment exhibits the pure atmospheric variability modes during austral summer in South America, equivalent to the own resonance frequency of a mechanical spring system. Can oceanic forcing by SST anomalies excite this dominant atmospheric mode, just as external oscillation can bring a spring in resonance ? It further raises the question to which extent the intra-seasonal modes can be extended to the inter-annual time-scale.

Vuille and Werner [-] investigate the SAMS and its isotopic signature, in GNIP observations and a 20-year ECHAM$_{iso}$ T106 ($\sim$ 125 km resolution) simulation at a monthly resolution. The authors define the monsoon activity as vertical wind shear derived from zonal wind anomalies at the 850 and 250 hPa level, averaged over the region [7.5°N - 2.5°N] in latitude and [45°W; 20°W] in longitude. Albeit the different definition of high/low SAMS, the relationship between SAMS and δ^{18}O signature in the present study is in overall agreement with Vuille and Werner [-]'s results. The GNIP data set indicates significant negative correlations between δ^{18}O and monsoon index, except along the East coast of Brazil where weak positive correlations arise. Unlike REMO, ECHAM4 does not capture this behaviour over the Nordeste region. We argue that the improvement of topography representation, especially for the Brazilian highlands, explain the difference. In the continental SACZ composite, increased South Atlantic high channels the Amazonian flow between the Andean ridge and the Brazilian highlands, causing increased convergence over the Paraná. In the oceanic SACZ composite, the stronger Chaco low diverts the Amazonian flow westwards, causing increased precipitation over eastern Brazil. In ECHAM, the moist Amazonian air is advected undifferentiatedly to the climatological location of the SACZ. Hence, the SACZ variability in the coarser ECHAM GCM mainly reflects changes in intensity rather than in location. For the same reason, ECHAM is believed not represent accurately LLJ and their crucial role on precipitation anomalies in sub-tropical South America. Accordingly, the dipole pattern identified in ECHAM is not as sharp as in REMO, featuring a loose opposition between tropical and sub-tropical precipitation (cf. Sturm et al. [2005a]).

As previous authors, Vuille and Werner [-] report the high correlation between the monsoon and ENSO 3.4 indices. Yet, the SAMS response to ENSO forcing is still a matter of debate. Carvalho et al. [2002] associates strong El Niño with intense oceanic SACZ composite (which is in good agreement with the oceanic SACZ composite simulated by REMO). The same pattern is observed by Grimm [2003] for strong El Niño January. Yet, December and February display precipitation anomalies which do not match either SACZ composite described earlier. Negative anomalies over the Amazon basin and positive over east Brazil are in common with the oceanic SACZ composite, but positive anomalies

over the Paraná contradicts it.
Gridded precipitation from the Xie and Arkin data set [Xie and Arkin, 1997] show a similar zonal behaviour: during El Niño events, tropical (sub-tropical) South America tend to be dryer (wetter) than normal. This contradicts the crescent-shaped precipitation deficit in the REMO oceanic SACZ composite. Lau and Zhou [2003] offers a unified view of the modulation of the SACZ by the ENSO. During El Niño events, warm anomalies over the eastern Pacific trigger excessive convection over the northern Peru and Ecuador. Latent heat release develops an anomalous east-west overturning motion (eastward shift of the Walker circulation), whose descending branch is located over northern Brazil, therefore suppresses convection over most of the Amazon basin. Rossby wave response to tropical heat source causes the South Atlantic (Pacific) high to intensify (weaken). The latter increases the LLJ, which produces increased precipitation over the Paraná.

Considering the variety of suggested responses, it is difficult to extend our comprehension of the SACZ intra-seasonal variability in climatological conditions to the ENSO forced mode. If El Niño events were associated to intense oceanic SACZ composites, they should be marked by above-normal $\delta^{18}O$ in the central Andes and the Paraná region. Due to the connection between $\delta^{18}O$ in the latter regions and Zongo, this would imply a positive inter-annual anomaly in the $\delta^{18}O$ signal of Bolivian ice-cores (Illimani). If warm ENSO events affect the SAMS as suggested by Lau and Zhou [2003], reduced precipitation upstream of Zongo would also imply positive $\delta^{18}O$ anomalies in tropical ice-core records. This is in agreement the Andean Isotope Index (mean $\delta^{18}O$ for the Huascarán, Quelccaya, Illimani and Sajama ice-cores [Hoffmann, 2003]).

Vuille and Werner [-] a priori regard ENSO as the major control on the $\delta^{18}O$ distribution over tropical and sub-tropical South America. In a first step, a linear regression between ENSO and $\delta^{18}O$ signal is performed. Correlation values that exceed a 95% Student-t significance test define the extension of ENSO control on $\delta^{18}O$. Thus $\delta^{18}O$ over the Amazon basin down to Paraguay and northern Argentina are identified as being primarily governed by ENSO. The residual variability (i.e. after subtraction of the common variance of $\delta^{18}O$ and ENSO) is correlated with the monsoon index, with the same 95% significance threshold. Hence, the $\delta^{18}O$ pattern over the Paraná and east Brazil is analysed as primarily governed by the SAMS. The latter confirms Barreiro et al. [2002]'s conclusion that precipitation in the ([15°S; 50 °S] and [60°W; 10°W]) sector shows no correlation with Pacific SSTs.
The present study brings physical evidence that questions the interpretation by Vuille and Werner [-]. ENSO 3.4 and monsoon index are strongly correlated, so they cannot be used as independent vectors against which to perform a bi-linear regression of $\delta^{18}O$. Furthermore, two observations oppose a direct control of Pacific SST on tropical South American $\delta^{18}O$. Local temperature is proved to have hardly any impact on the $\delta^{18}O$ distribution in tropical South America [Vimeux et al., -]. Precipitation on the eastern Andean flank predominantly originates from the Atlantic, after crossing the Amazon basin. In addition to previous evidence by Hoffmann [2003], Henderson et al. [1999], the present study underlines the importance of meso-scale LLJ in linking Amazonian moisture to Zongo precipitation. $\delta^{18}O$, as an integrative proxy for precipitation along its trajectory, recalls the latter connection. Rayleigh distillation processes then prescribe the $\delta^{18}O$ in air masses ascending along the Zongo valleys [Vimeux et al., -, Sturm et al., 2005a, Gonfiantini et al., 2001]. Hence meso-scale evidence reinforces that the isotopic signal in Andean ice cores primarily records changes in circulation patterns. Accumulation on east Andes summits occurs mainly during summer. It is thus to a large extent related to SAMS mechanisms.

In conclusion, the intra-seasonal mechanisms controlling the $\delta^{18}O$ distribution confirm the connection between the Amazon and the Eastern Andes $\delta^{18}O$. ENSO remotely modulates the circulation patterns (including the SAMS) over South America, at inter-annual time-scales. The latter explains the significant correlations found between ENSO 3.4 and $\delta^{18}O$ over most parts of the tropical and sub-tropical South American continent. This interpretation is coherent with the analysis of outgoing long-wave radiation (OLR) EOF over South America [Kousky and Kayano, 1994]. The authors asserts that OLR and upper-level circulation result of a combination of ENSO (zonal) and SAMS (dipole) variability modes. This suggestion further accommodates both statistical evidence of shared variance between ENSO and ice core $\delta^{18}O$ signal [Bradley et al., 2003], and physical evidence from amount effect and flow path in South America [Hoffmann et al., 2000, Vimeux et al., -].

5.6 Summary and conclusion

The present study investigates the intra-seasonal variability of austral summer South American climate based on a 5 year integration of the regional circulation model $REMO_{iso}$ with climatological SST. We chose a 5-day (pentad) sampling interval and perform an EOF analysis on different climate parameters: precipitation, 200 hPa wind divergence, 200 hPa geopotential height, mean sea-level pressure, vertically integrated moisture transport and meridional low-level jet counts. Particularity of the present study is to investigate the stable water isotope signal in precipitation and relate it to the oscillating precipitation and circulation regimes.

Intra-seasonal variability during austral summer is marked by a bimodal shape, with contrasting poles over the Paraná [55°W; 25°S] and the Nordeste [40°W; 10°S]. The EOF pattern of pentad precipitation (Figure 5.1a) primarily underlines this dipole. It further reveals weaker connections between high precipitation over the Paraná and the central Andes/Northern Amazon, forming a crescent-shaped counterpart to low precipitation over Eastern Brazil (Nordeste). Subtropical rainfall variability is stronger over land than over the Atlantic. This dipole structure is widely documented in both observation and modelling studies [Herdies et al., 2002, Grimm et al., 2004, Lenters and Cook, 1999, Doyle and Barros, 2002, Carvalho et al., 2002, 2004, Barreiro et al., 2002, Lau and Zhou, 2003, Barros et al., 2003, Gan et al., 2004, Nogues-Paegle et al., 2003].

The simulated precipitation variability is physically related to oscillations in the atmospheric circulation patterns. In the case of a predominantly continental location of the South Atlantic convergence zone (SACZ) (Figure 5.4), both the Chaco low and South Atlantic high are strengthened. The cyclonic flow in turn is enhanced, which increases meridional advection of moist Amazonian air to the Paraná by means of more frequent low-level jets (LLJ) on the east flank of the central Andes. In the opposite case (oceanic SACZ composite - Figure 5.5), Amazonian moisture is advected zonally towards east Brazil. This leads to a north-eastern shift of the SACZ, which tends to merge with the inter-tropical convergence zone (ITCZ) around 5°S.
The interaction between the SACZ location, changes of regional circulation patterns and resulting precipitation variability is referred to as the South American monsoon system (SAMS).

This variability in precipitation amounts and air-parcel trajectory is recorded in the stable water isotope signal. The amount effect accounts for anti-correlation between $\delta^{18}O$ and precipitation. Furthermore, $\delta^{18}O$ integrates the cumulated rain-fall along the trajectory. Hence $\delta^{18}O$ is a better proxy for the SAMS than precipitation alone, since its 'memory effect' gives prominence to the crucial role of LLJ on the dipole pattern.

At last, we discuss possible controls on the inter-annual variability of $\delta^{18}O$ on the basis of mechanisms described above. Given the assumption that SAMS variability stimulates similar physical modes at intra-seasonal and inter-annual time scales, the present study reinforces the connection of $\delta^{18}O$ along their trajectories. This would imply that the isotopic signal in the Zongo valley (recorded in the Illimani ice-core) is primarily controlled by precipitation and circulation patterns over the Amazon.
However, inter-annual climate variability over South America is proved to depend primarily on the El Niño southern oscillation (ENSO). ENSO has wide ranging consequences in that it modifies the location of up- and downdrafts in the Hadley-Walker circulation. Hence the physical mode of SAMS variability underlined in the present (climatological) simulation can differ from the inter-annual, ENSO governed variability. The assumption above is thus proved to be only partially valid. In summary, we suggest that the isotopic signal from Illimani ice-core is physically controlled by precipitation and circulation patterns over the Amazon basin. ENSO exerts a strong influence on the synoptical circulation patterns over South America, which is indirectly recorded in the ice-core $\delta^{18}O$ signal.

In conclusion, the present study introduces a high resolution simulation of the stable water isotopes in precipitation over South America. It underlines the benefits of improved topography in representing meso-scale features, as the low-level jets, and their influence on $\delta^{18}O$ variability at intra-seasonal time scale. Nevertheless, longer integrations of $REMO_{iso}$ with observed sea-surface temperatures are needed to determine the mechanisms on inter-annual variability (such as related to ENSO).

Acknowledgements

The authors would like to thank Georg Hoffmann (Laboratoire des Sciences du Climat et de l'Environnement) for his valuable comments. Simulations were performed at the German High Performance Computing Centre for Climate- and Earth System Research (DKRZ, Hamburg). The present study was supported by French Science Foundation grant ACI 'Changement climatique et cryopshère'.

Bibliography

T. Bariac, J. Gonzalez-Dunia, N. Katerji, O. Béthenod, J.M. Bertolini, and D. Mariotti. Spatial variation of the isotopic composition of water (^{18}O, ^{2}H) in organs of aerophytic plants: 2. Assessment under field conditions. *Chemical Geology*, 115(3-4):317 – 333, Aug 1994a. 99

T. Bariac, J. Gonzalez-Dunia, F. Tardieu, T. Tessier, and D. Mariotti. Spatial variation of the isotopic composition of water (^{18}O, ^{2}H) in organs of aerophytic plants: 1. Assessment under laboratory conditions. *Chemical Geology*, 115(3-4):307 – 315, Aug 1994b. 99

M. Barreiro, P. Chang, and R. Saravanan. Variability of the South Atlantic Convergence Zone Simulated by an Atmospheric General Circulation Model. *Journal of Climate*, 15:745–763, April 2002. 105, 118, 120, 121

V. Barros, M. Doyle, M. González, I. Camilloni, R. Bejarán, and R.C. Caffera. Climate Variability over Subtropical South America and the South American Monsoon: a Review. *Meteorologica*, 27(1-2):33 – 57, 2003. 118, 121

H. Björnsson and S.A. Venegas. A manual for EOF and SVD Analyses of Climate Data. Technical report, Center for Climate and Global Change Research, McGill University, 1997. http://www.dcess.ku.dk/ silvia/eofsvd/eofsvd.html. 100

R. S. Bradley, M. Vuille, D. Hardy, and L. G. Thompson. Low latitude ice cores record Pacific sea surface temperatures. *Geophysical Research Letters*, 30:23–1, February 2003. 98, 120

V. Brahmananda Rao, I. F. A. Cavalcanti, and K. Hada. Annual variation of rainfall over Brazil and water vapor characteristics over South America. *Journal of Geophysical Research*, 101(10):26539–26552, 1996. 106, 109

L. M. V. Carvalho, C. Jones, and B. Liebmann. Extreme Precipitation Events in Southeastern South America and Large-Scale Convective Patterns in the South Atlantic Convergence Zone. *Journal of Climate*, 15:2377–2394, September 2002. 101, 109, 112, 118, 119, 121

L. M. V. Carvalho, C. Jones, and B. Liebmann. The South Atlantic Convergence Zone: Intensity, Form, Persistence, and Relationships with Intraseasonal to Interannual Activity and Extreme Rainfall. *Journal of Climate*, 17:88–108, January 2004. 101, 109, 116, 118, 121

S. C. Chou, A. M. B. Nunes, and I. F. A. Cavalcanti. Extended range forecasts over South America using the regional eta model. *Journal of Geophysical Research*, 105(8):10147–10160, 2000. 98

D. Dommenget and M. Latif. A Cautionary Note on the Interpretation of EOFs. *Journal of Climate*, 15:216–225, January 2002. 100, 116

M. E. Doyle and V. R. Barros. Midsummer Low-Level Circulation and Precipitation in Subtropical South America and Related Sea Surface Temperature Anomalies in the South Atlantic. *Journal of Climate*, 15:3394–3410, December 2002. 103, 118, 121

M.A. Gan, V.E. Kousky, and C.F. Ropelewski. The South American Monsoon Circulation and its Relationship to Rainfall over West-Central Brazil. *Journal of Climate*, pages 47 – 66, 2004. 106, 118, 121

R.D. Garreaud. Cold air incursions over subtropical and tropical South America. A numerical case study. *Monthly Weather Review*, 127:2823 – 2853, 1999. 109

R.D. Garreaud. Cold air incursions over Subtropical South America: Mean structure and dynamics. *Monthly Weather Review*, 128:2544 – 2559, 2000. 109

R. Gonfiantini, M.A. Roche, J.C. Olivry, J.C. Fontes, and G.M. Zuppi. The altitude effect on the isotopic composition of tropical rains. *Chemical Geology*, 181:147 – 167, Oct 2001. 120

A. M. Grimm. The El Niño Impact on the Summer Monsoon in Brazil: Regional Processes versus Remote Influences. *Journal of Climate*, 16:263–280, January 2003. 119

A.M. Grimm, C.S. Vera, and C.R. Mechoso. The South American Monsoon System. In C.P. Chang, editor, *Third International Workshop on Monsoons (IWM-III)*, pages 23 – 41, Hangzhou, China, Nov 2004. World Meteorological Organisation. http://www.nps.edu/Academics/gseas/IWM-III/Index.html. 98, 101, 103, 118, 121

K. A. Henderson, L. G. Thompson, and P.-N. Lin. Recording of El Niño in ice core $\delta^{18}O$ records from Nevado Huascarán, Peru. *Journal of Geophysical Research*, 104(13):31053–31066, 1999. 98, 120

D. L. Herdies, A. da Silva, M. A. F. Silva Dias, and R. Nieto Ferreira. Moisture budget of the bimodal pattern of the summer circulation over South America. *Journal of Geophysical Research (Atmospheres)*, 107(20):42–+, September 2002. 101, 105, 121

G. Hoffmann. Taking the Pulse of the Tropical Water Cycle. *Science*, 301:776 – 777, Aug 2003. 98, 120

G. Hoffmann, J. Jouzel, and V. Masson. Stable water isotopes in atmospheric general circulation models. *Hydrological Processes*, 14:1385 – 1406, 2000. 120

G. Hoffmann, E. Ramirez, J.D. Taupin, B. Francou, P. Ribstein, R. Delmas, H. Dürr, R. Gallaire, J. Simões, U. Schotterer, M. Stievenard, and M. Werner. Coherent isotope history of Andean ice cores over the last century. *Geophysical Research Letters*, 30:28–1, February 2003. 98

G. Hoffmann, M. Werner, and M. Heimann. Water isotope module of the ECHAM atmospheric general circulation model: A study on timescales from days to several years. *Journal of Geophysical Research*, 103(14):16 871 – 16 896, 1998. 99

International Atomic Energy Agency IAEA and World Meteorological Organisation WMO. The Global Network of Isotopes in Precipitation (GNIP) database. *"http://isohis.iaea.org"*, 2001. 99, 109

D. Jacob, U. Andrae, G. Elgered, C. Fortelius, L.P. Graham, S.D. Jackson, U. Karstens, C. Koepken, R. Lindau, R. Podzun, B. Rockel, F. Rubel, H.B. Sass, R.N.D. Smith, B.J.J.M. Van den Hurk, and X. Yang. Comprehensive Model Intercomparison Study Investigating the Water Budget during the BALTEX-PIDCAP Period. *Meteorology and Atmospheric Physics*, 77:19 – 43, 2001. 99

J. Jouzel and L. Merlivat. Deuterium and oxygen 18 in precipitation: modeling of the isotopic effects during snow formation. *Journal of Geophysical Research*, 89:11 749 – 11 757, 1984. 99

V. E. Kousky and M. T. Kayano. Principal Modes of Outgoing Longwave Radiation and 250-mb Circulation for the South American Sector. *Journal of Climate*, 7:1131–1138, July 1994. 120

K.M. Lau and J. Zhou. Anomalies of the South American summer monsoon associated with the 1997-99 El Niño-southern oscillation. *International Journal of Climatology*, 23:529 – 539, 2003. 119, 120, 121

J. D. Lenters and K.H. Cook. Summertime Precipitation Variability in South America: Role of the Large-scale Circulation. *Monthly Weather Review*, 127(3):409 – 443, 1999. 103, 105, 106, 117, 119, 121

D. Majewski. The Europa-Modell of the Deutscher Wetterdienst. *ECMWF Seminar on numerical methods in atmospheric models*, 2:147 – 191, 1991. 99

M. Majoube. Fractionnement en oxygène 18 et en deutérium entre l'eau et sa vapeur. *Journal of Chemical Physics*, 10: 1423 – 1436, 1971. 99, 109

L. Merlivat and J. Jouzel. Global climatic interpretation of the deuterium-oxygen 18 relationship for precipitation. *Journal of Geophysical Research*, 84:5029 – 5033, 1979. 99

M. Nicolini, P. Salio, J. J. Katzfey, J. L. McGregor, and A. C. Saulo. January and July regional climate simulation over South America. *Journal of Geophysical Research*, 22:12–+, November 2002. 118

J. Nogues-Paegle, C.R. Mechoso, R. Fu, E.H. Berbery, W.C. Chao, T.C. Chen, K. Cook, A.F. Diaz, D. Enfield, R. Ferreira, A.M. Grimm, V. Kousky, B. Liebmann, J. Marengo, K. Mo, J.D. Neelin, J. Paegle, A.W. Robertson, A. Seth, C.S. Vera, and J. Zhou. Progress in Pan American CLIVAR Research: Understanding the South American Monsoon. *Meteorologica*, 27(1 - 2):1 – 30, 2003. 98, 101, 118, 119, 121

T.E. Nordeng. Extended versions of the convective parametrization scheme at ECMWF and their impact on the mean and transient activity of the model in the tropics. *ECMWF Research Department, Technical Memorandum No. 206*, 1994. 99

J.N. Paegle, L. A. Byerle, and K. C. Mo. Intraseasonal Modulation of South American Summer Precipitation. *Monthly Weather Review*, 128(3):837 – 850, 2000. 118

R. T. Pierrehumbert. Huascaran $\delta^{18}O$ as an indicator of tropical climate during the Last Glacial Maximum. *Geophysical Research Letters*, 26:1345–1348, May 1999. 98

E. Ramirez, G. Hoffmann, J. D. Taupin, B. Francou, P. Ribstein, N. Caillon, F. A. Ferron, A. Landais, J. R. Petit, B. Pouyaud, U. Schotterer, J. C. Simoes, and M. Stievenard. A new Andean deep ice core from Nevado Illimani (6350 m), Bolivia. *Earth and Planetary Science Letters*, 212:337–350, July 2003. 98

N.A. Rayner, D.E. Parker, E.B. Horton, C.K. Folland, and R.B Hackett. Version 2.2 of the Global Sea-Ice and Sea Surface Temperature Data Set, 1903- 1994. Climate Research Technical Note 74, Hadley Centre, 1994. http://www.metoffice.com/research/ hadleycentre/obsdata/GISST.html. 99

R.P. Rocha and T. Ambrizzi. Regional Climate Model2 simulations of the Low Level Jet East of the Andes. In *CLIVAR Science Conference, Baltimore*, Jun 2004. http://www.clivar2004.org/electronic%20posters/ monsoon_table.html. 98, 100, 106

E. Roekner, E.K. Arpe, L. Bengtsson, M. Christoph, M. Claussen, L. Dümenil, M. Esch, M. Giorgetta, U. Schlese, and U. Schulzweida. The atmospheric circulation model ECHAM-4: model description and simulation of the present day climate. *Max-Planck-Institute für Meteorologie Report*, 218, 1996. 99

M. Rojas and A. Seth. Simulation and Sensitivity in a Nested Modeling System for South America. Part II: GCM Boundary Forcing. *Journal of Climate*, 16:2454–2471, August 2003. 98, 118

A. Seth and M. Rojas. Simulation and Sensitivity in a Nested Modeling System for South America. Part I: Reanalyses Boundary Forcing. *Journal of Climate*, 16:2437–2453, August 2003. 98

A. Seth, M. Rojas, B. Liebmann, and J.-H. Qian. Daily rainfall analysis for South America from a regional climate model and station observations. *Geophysical Research Letters*, 31:7213 – 7216, April 2004. 98

K. Sturm, G. Hoffmann, and B. Langmann. Climatology of stable water isotopes in South America: comparing general to regional circulation models. *Journal of Climate – submitted*, 2005a. 98, 99, 109, 112, 116, 117, 118, 119, 120

K. Sturm, G. Hoffmann, B. Langmann, and W. Stichler. Simulation of $\delta^{18}O$ in precipitation by the regional circulation model $REMO_{iso}$. *Hydrological Processes – in press*, 2005b. 99

L. G. Thompson, M. E. Davis, E. Mosley-Thompson, T. A. Sowers, K. A. Henderson, V. S. Zagorodnov, P.-N. Lin, V. N. Mikhalenko, R. K. Campen, J. F. Bolzan, J. Cole-Dai, and B. Francou. A 25,000-Year Tropical Climate History from Bolivian Ice Cores. *Science*, 282:1858–+, December 1998. 98

L. G. Thompson, E. Mosley-Thompson, and K. A. Henderson. Ice-core palaeoclimate records in tropical South America since the Last Glacial Maximum. *Journal of Quaternary Science*, 15:377–394, May 2000. 98

M. Tiedtke. A comprehensive mass flux scheme for cumulus parametrizations in large-scale models. *Monthly Weather Review*, 117:1779 – 1800, 1989. 99

S. A. Venegas, L. A. Mysak, and D. N. Straub. Atmosphere-Ocean Coupled Variability in the South Atlantic. *Journal of Climate*, 10:2904–2920, November 1997. 118

S.A. Venegas. Statistical Methods for Signal Detection in Climate. Technical report, Danish Center for Earth System Science, 2001. http://www.dcess.ku.dk/ silvia/. 100

C. Vera. Introduction to the SALLJ conference and SALLJEX field campaign. In *VAMOS/CLIVAR/WCRP Conference on South-American low-level jets*, Santa Cruz de la Sierra, Bolivia, Feb 2002. http://www.salljex.at.fcen.uba.ar/sallj/. 106

A. D. Vernekar, B. P. Kirtman, and M. J. Fennessy. Low-Level Jets and Their Effects on the South American Summer Climate as Simulated by the NCEP Eta Model. *Journal of Climate*, 16:297–311, January 2003. 98, 106, 112, 118

F. Vimeux, R. Gallaire, S. Bony, G. Hoffmann, and J.C. Chiang. What are the controls on δD in precipitation in the Zongo Valley (Bolivia) ? Implications for the Illimani ice core interpretation. *Earth and Planetary Science Letters*, -. submitted. 113, 116, 120

M. Vuille, R. S. Bradley, R. Healy, M. Werner, D. R. Hardy, L. G. Thompson, and F. Keimig. Modeling $\delta^{18}O$ in precipitation over the tropical Americas: 2. Simulation of the stable isotope signal in Andean ice cores. *Journal of Geophysical Research*, 108(6):2–1, March 2003a. 98

M. Vuille, R. S. Bradley, M. Werner, R. Healy, and F. Keimig. Modeling $\delta^{18}O$ in precipitation over the tropical Americas: 1. Interannual variability and climatic controls. *Journal of Geophysical Research*, 108(6):1–1, March 2003b. 98

M. Vuille and M. Werner. Stable Isotopes in Precipitation Recording South American Summer Monsoon and ENSO Variability - Observations and Model Results. *Climate Dynamics*, page submitted, -. 119, 120

M. Werner and M. Heimann. Modeling interannual variability of water isotopes in Greenland and Antarctica. *Journal of Geophysical Research (Atmospheres)*, 107(1):1–+, January 2002. 99

P. Xie and P.A. Arkin. Global Precipitation: A 17-year monthly analysis based on gauge observations, satellite estimates, and numerical model outputs. *Bulletin of the American Meteorological Society*, 78:2539 – 2558, 1997. 120

J. Zhou and K.-M. Lau. Does a Monsoon Climate Exist over South America?. *Journal of Climate*, 11:1020–1040, May 1998. 98, 101

Chapter 6

Conclusion and perspectives: current and future applications of REMO$_{iso}$

Résumé

Ce chapitre résume les résultats obtenus au cours de la thèse, tels qu'ils on été présentés dans les chapitres précedents. Il s'agit de la mise en perspective du travail de thèse dans la problématique du changement climatique ; la description du modèle de circulation régionale REMO$_{iso}$ et de son module traitant des isotopes de l'eau ; la validation initiale de REMO$_{iso}$ sur l'Europe ; l'étude des variations saisonnières des précipitations, de la circulation atmosphérique régional et du signal isotopique en Amérique du Sud ; de l'enregistrement par les isotopes stables de l'eau de la mousson sud-américaine.

Ensuite, nous dégageons certaines perspectives de ce travail de thèse. Cela concerne la poursuite des simulations avec modèle en l'état avec de nouvelles conditions aux limites (forçage spectral), autant que l'extension à de nouvelles régions géographiques (p.ex. Canada, Tibet, Antarctique et Groenland). Les développements du modèle sont envisagés pour répondre à des applications nouvelles, comme la modification des spécifications de surface pour une simulation paléo-climatique (dernier maximum glaciaire), ou une paramétrisation améliorée des processus isotopiques à l'interface entre le sol, la végétation et l'atmosphère.

Zusammenfassung

In diesem Kapitel werden Ergebnisse dieser Arbeit, die in den vorherigen Kapiteln beschrieben wurden, zusammengefaßt. Diese betreffen die Stellung dieser Doktorarbeit aus der allgemeine Perspektive des Klimawandels; die Beschreibung des Regionalzirkulationsmodells REMO$_{iso}$ und dessen Moduls für stabile Wasserisotope; die Validation von REMO$_{iso}$ über Europa; die Studie des Jahresganges von Niederschlag, regionaler atmosphärischer Zirkulation und Wasserisotopensignal über Südamerika; und den Einfluß des südamerikanischen Sommermonsun auf das Wasserisotopensignal.

Anschießend werden Perspektiven für diese Arbeit vorgeschlagen. Im jetzigen Zustand des Modells können Simulationen mit neuen Randbedingungen (Spektralnudging) ausgeführt werden, und REMO$_{iso}$ kann über weiteren geographischen Gebieten angewandt werden (z.B. Kanada, Tibet, Grönland und Antarktis). Zukünftige Weiterentwicklungen von REMO$_{iso}$ werden angedeutet. Diese entsprechen neuen Anwendungen, wie zum Beispiel angemessene Bodenspezifikationen für Paleoläufe (letztes Eiszeit-Maximum) oder eine verbesserten Berücksichtigung der isotopischen Prozessen an der Schnittstelle zwischen Boden, Vegetation und Atmosphäre.

6.1 Summary of studies with REMO$_{iso}$

The present document summarises the research activities conducted during a PhD in joint French-German supervision, between the Université Joseph Fourier-Grenoble I and the Universität Hamburg. The main task of the PhD project was to implement embedded stable water isotope (SWI) diagnostics in the regional circulation model REMO$_{iso}$. For that purpose, the isotopic module developed for the global circulation model ECHAM$_{iso}$ [Hoffmann et al., 1998] was adapted to REMO, taking advantage of their similar physical parameterisation. Upon completing this task, REMO$_{iso}$ became the first operational stable water isotope enabled regional circulation model.

Chapter 1 on page 1 gives a broad introduction to the climate change topic. Basics of stable water isotope physics are recalled, in which the role of SWI as climate proxy is emphasised. The singular relevance of tropical ice-cores recovered from Andean summits is underlined, as they records climate variations in the highly sensitive inter-tropical belt. Finally, the state-of-the-art modelling studies concerning the interpretation of SWI in South America are briefly reviewed.

A detailed description of REMO$_{iso}$ follows in chapter 2, on page 15. Technical characteristics of the horizontal and vertical discretisation are described, along with the program flowchart. The physical parameterisation of sub-grid hydrological processes are then presented, together with the inherent isotopic fractionation processes. Finally, the pre-processing procedure of surface and lateral boundary conditions is explained.

6.1.1 Validation over Europe

REMO has been extensively operated over Europe [Jacob and Podzun, 1997, Jacob et al., 2001, Hagemann et al., 2002]. Furthermore, Europe displays the densest spatial coverage of SWI monitoring stations worldwide [IAEA and WMO, 2001]. Hence the initial validation of REMO$_{iso}$ was performed over the standard European domain (cf. Table 2.1). The results as presented in chapter 3, on page 29.

Two formulations for the SWI lateral boundary conditions were tested. In a first set-up, REMO$_{iso}$ is driven by analyses from the European Centre for Midterm Weather Forecasts (ECMWF, Norris, 1997), with a temperature-dependent prescription SWI composition. This set-up implies an overall underestimation of the δ^{18}O signal by -4.5$^{\circ}/_{\circ\circ}$. On the other hand, nesting REMO$_{iso}$ into a ECHAM$_{iso}$ simulation removes the systematic bias. The classical isotope effects, reported by Dansgaard [1964], are correctly reproduced in the REMO$_{iso}$ simulation. A preliminary evaluation of daily precipitation δ^{18}O simulated by REMO$_{iso}$ is conducted against daily observations at Arkona, Nordeney and Hohenpeissenberg [Stichler, personal communication]. Nudging techniques applied to ECHAM and REMO [von Storch et al., 2000] improve greatly the agreement of daily simulated temperature, precipitation amounts and vapour δ^{18}O, as compared to daily station measurements at Saclay [Jouzel, personal communication].

6.1.2 South America isotope climatology

REMO$_{iso}$ was ported over South America and integrated over a 5 year period under climatological sea-surface temperature conditions. Results are presented in chapter 4, on page 61.

Our main interest focuses on the mean annual cycle of precipitation, regional circulation patterns and δ^{18}O signal in precipitation. Despite an overestimation of rainfall by 30%, REMO reproduces accurately the observed precipitation patterns. In comparison to coarser simulations by ECHAM$_{iso}$, REMO$_{iso}$ offers a better resolution of the meso-scale processes affecting the δ^{18}O signal in connection to abrupt orography. The simulated altitude effect and the anomalously low continental gradient across the Amazon basin is investigated in both REMO$_{iso}$ and ECHAM$_{iso}$ output. Furthermore, we adopt a Lagrangian referential to describe the joint evolution of precipitation and δ^{18}O along its trajectory. This approach is consistent with the interpretation of δ^{18}O as an integrative proxy for precipitation and regional circulation.

6.1.3 South American monsoon system recorded in stable water isotopes

Unexpectedly, the 5-year climatological simulation by REMO$_{iso}$ revealed a distinctive mode of intraseasonal variability. It is characterised by a dipole in austral summer (DJF) precipitation: if above normal precipitation occurs over Nordeste, Paraná receives below normal precipitation.

By the means of empirical orthogonal functions (EOF), we investigated the dominant variability mode simulated by REMO$_{iso}$. From a meteorological perspective, this dominant intra-seasonal variability mode corresponds to the South American summer monsoon system (SAMS). Among all climate parameters, δ^{18}O is the most appropriate to convey a comprehensive view of the SAMS: δ^{18}O records the combined variability of regional atmospheric circulation, low-level jet occurrence and precipitation.

The latter evidence underlines the strong impact of the SAMS on the δ^{18}O across South America, and particularly in the tropical Andes. We hence address some consequences for the interpretation of Andean isotopic ice-core records.

6.2 Further applications of REMO$_{iso}$

Continuous developments and bug-tracking has made the REMO$_{iso}$ code fully operational by now. Hence REMO$_{iso}$ is suitable in its current set-up for a wide range of still unexplored simulations.

6.2.1 Nudged simulation over South America

The most recent development implemented in REMO$_{iso}$ concerns spectral nudging of the simulated high altitude winds [von Storch et al., 2000]. According to this technique, the upper atmosphere winds a relaxed towards the large wave numbers of the synoptic circulation from its host model. As a consequence, the large-scale features (e.g. location of upper atmospheric highs and lows) are accommodated by the regional circulation model, leaving its (isotopic) hydrological unaltered. A preliminary application, outlined in the last section of chapter 3 of the technique underlined the related improvements for model/data comparison over a given period.

The first results obtained from climatological simulations over South America (chapters 4-5) summon a pursuance with observed sea-surface temperatures and assimilated meteorological conditions. From the latter, a significant breakthrough is expected concerning the impact of the El Niño Southern Oscillation (ENSO) phenomenon on the isotopic water cycle voer South America. This simulation will further test the sensitivity of the convection scheme over South America, fitted with optimal tropical parameters [Aldrian, 2003].

6.2.2 Collaborative projects: Canada, Tibet, polar regions

In response to various solicitations, REMO$_{iso}$ was applied in other geographical zones. Appendix B presents preliminary results from a simulation over Canada. Further applications of REMO$_{iso}$ over that area is required for evaluation against the impressive SWI data-set elaborated by the Environmental Isotope Laboratory at the University of Waterloo (Canada).

The high resolution by REMO$_{iso}$ is particularly profitable is steep orography. Accordingly, REMO$_{iso}$ was included in a German science project led by Martin Werner (Max Planck Institute for Biogeochemistry), which focuses on SWI measurements and simulation over the Tibetan Plateau. This project benefits from an extensive validation of REMO climate simulations by Xuefeng (Steven) Cui at the Max Planck Institute for Meteorology. This project contributes to the general effort of understanding the climatic variability of the Asian mosoon, as e.g. recorded in Himalayan ice-cores [Thompson et al., 2000].

Finally, great interest has been expressed among the French ice-core community (in particular V. Masson-Delmotte, F. Vimeux and G. Hoffmann at the Laboratoire des Sciences du Climat and G. Krinner, H. Galée and C. Genthon at the Laboratoire de Glaciologie et Géophysique de l'Environnement) to apply REMO$_{iso}$ over polar regions. In its current set-up, REMO$_{iso}$ adopts a horizontal resolution of 0.5°, twice the resolution of the zoomable grid of the LMDz GCM

(Laboratoire de Meteorologie Dynamique). The representation of local meteorological effects that affect the ice-core drilling site could further be improved by nesting REMO$_{iso}$ into itself, reaching a resolution of 1/6°($\sim$ 18 km).

6.3 Suggested development of REMO's stable water isotope module

Analyses of completed REMO$_{iso}$ simulations reveal several deficiencies in the parameterisation of fractionation processes. Following suggestions aim at mitigating the dominant observed biases. These improvements are not domain-dependent, hence all the application domains listed in the previous section could benefit from them.

6.3.1 Adaptation of boundary conditions for paleo-simulations

REMO$_{iso}$ uncovers a tremendous potential for supporting the interpretation of isotopic ice-core archives. In fact, coarse global circulation models fail to represent accurately the topography around the drilling site and thus neglects local meteorological processes that affect the ice-core archive.

Simulations of the global SWI cycle under paleo-conditions (notably the last glacial maximum, 21 ka BP) have been performed with the ECHAM$_{iso}$ GCM. REMO$_{iso}$ offers the prospective of regional paleo-simulations. For that purpose, the pre-processing procedure (cf. chapter 1) requires an adaptation to account for modified ice-age surface specifications. The treatment of e.g. ice-sheet extent and related sea-level lowering, sensitivity to vegetation/soil type, CLIMAP prescription for sea-surface temperatures has been suggested by the paleo-climate modelling intercomparison project (PMIP).

Langmann and Heil [2004] reports the implementation of a passive aerosol transport module in REMO. Ice-core analysis relies on a multi-proxy approach: along with the isotopic signal, the dust content reveals to origin and seasonality of precipitation [Ginot et al., 2002]. Hence joint paleo-simulations of the SWI cycle and dust transport by the REMO model suite would enhance their potential for the interpretation of low and mid latitude ice-cores.

6.3.2 Soil hydrology improvements for isotopic catchment studies

At present, the SWI diagnostics are imbedded in the REMO 5.0 version, which is characterised by a rough parameterisation of soil processes. Later REMO versions (currently v5.1) incorporate an improved representation of fractional sea-ice distribution, snow-melt and runoff collection scheme [Semmler, 2002, Semmler and Jacob, 2004, Kotlarski and Hagemann, 2003]. Ongoing projects include several improvements of the soil module in REMO, e.g. interactive vegetation parameterisation [Rechid, personnal communication], dynamical glacier scheme [Kotlarski, personal communication].

As demonstrated in chapter 4, the surface processes impose a significant feedback on the atmospheric SWI cycle. Hence upgrading the SWI diagnostics from REMO v5.0 to v5.1 or later would improve the representation of both the hydrological cycle and its isotopic component. As a consequence, catchment-wide SWI balance studies could be performed with REMO$_{iso}$, e.g. as a validation tool for human-induced climate change in the Amazon basin [Henderson-Sellers et al., 2002].

6.3.3 Coupling to an improved SVAT model : MECBETH

REMO$_{iso}$ provides the forcing fields the SWI enabled land-surface scheme (LSS) intercomparison experiment IPILPS (cf. Appendix C, Henderson-Sellers et al., 1996, Henderson-Sellers and McGuffie, 2003). It takes part in the inter-comparison as bucket-type on-line LSS. MECBETH [Cuntz, personal communication] is another participating model, with a detailed treatment of soil-vegetation-atmosphere-transfer (SVAT) parameterisation [Cuntz et al., 2003b,a]. Its particularity is to include fractionation processes of the carbon isotopes along with oxygen isotopes. Hence both transpiration and photosynthesis processes are traced with this module. MECBETH was implemented in the ECHAM$_{iso}$ GCM, which permits the identification of the Earth's Dole effect [Hoffmann et al., 2004].

Taking profit of the similarity between the ECHAM and REMO physical schemes, it was suggested to implement MECBETH in REMO$_{iso}$ as well. A further, long-term step would be to introduce Carbon isotope tracers in REMO, based

on the CO_2 transport module readily available in REMO [Chevillard et al., 2002]. Consequently, REMO$^2_{iso}$ would feature both the ^{13}C, ^{18}O and ^{2}H tracers in the water and carbon cycle.

Bibliography

E. Aldrian. *Simulations of Indonesian Rainfall with a Hierarchy of Climate Models*. Mpi report 92, Max Planck Institut für Meteorologie, July 2003. 129

A. Chevillard, U. Karstens, P. Ciais, Sebastien Lafont, and M. Heimann. Simulation of atmospheric CO_2 over Europe and western Siberia using the regional scale model REMO. *Tellus B*, 54(5):872–894, Nov 2002. 131

M. Cuntz, P. Ciais, G. Hoffmann, C. E. Allison, R. J. Francey, W. Knorr, P. P. Tans, J. W. C. White, and I. Levin. A comprehensive global three-dimensional model of $\delta^{18}O$ in atmospheric CO_2: 2. Mapping the atmospheric signal. *Journal of Geophysical Research (Atmospheres)*, 108(17):2–1, September 2003a. 130

M. Cuntz, P. Ciais, G. Hoffmann, and W. Knorr. A comprehensive global three-dimensional model of $\delta^{18}O$ in atmospheric CO_2: 1. Validation of surface processes. *Journal of Geophysical Research (Atmospheres)*, 108(17):1–1, September 2003b. 130

W. Dansgaard. Stable isotopes in precipitation. *Tellus*, XVI:436 – 468, 1964. 128

P. Ginot, M. Schwikowski, U. Schotterer, W. Stichler, H. W. Gäggeler, B. Francou, R. Gallaire, and B. Pouyaud. Potential for climate variability reconstruction from Andean glaciochemical records. *Annals of Glaciology, vol.35, pp.443-450*, 35:443–450, 2002. 130

S. Hagemann, B. Machenhauer, O.B. Christensen, M. Déqué, D. Jacob, R. Jones, and P.L. Vidale. Intercomparison of water and energy budgets simulated by regional climate models applied over Europe. Technical Report 338, Max-Planck-Institute for Meteorology, 2002. 128

A. Henderson-Sellers and K. McGuffie. Incorporating and Evaluating Stable Water Isotopes into Land-surface Parameterisation Schemes. In *AGU Fall Meeting Abstracts*, December 2003. 130

A. Henderson-Sellers, K. McGuffie, and A. J. Pitman. The Project for Intercomparison of Land-surface Parametrization Schemes (PILPS): 1992 to 1995. *Climate Dynamics*, 12:849–859, 1996. 130

A. Henderson-Sellers, K. McGuffie, and H. Zhang. Stable Isotopes as Validation Tools for Global Climate Model Predictions of the Impact of Amazonian Deforestation. *Journal of Climate*, 15:2664–2677, September 2002. 130

G. Hoffmann, M. Cuntz, C. Weber, P. Ciais, P. Friedlingstein, M. Heimann, J. Jouzel, J. Kaduk, E. Maier-Reimer, U. Seibt, and K. Six. A model of the Earth's Dole effect. *Global Biogeochemical Cycles*, 18:1008–+, January 2004. 130

G. Hoffmann, M. Werner, and M. Heimann. Water isotope module of the ECHAM atmospheric general circulation model: A study on timescales from days to several years. *Journal of Geophysical Research*, 103(14):16 871 – 16 896, 1998. 128

International Atomic Energy Agency IAEA and World Meteorological Organisation WMO. The Global Network of Isotopes in Precipitation (GNIP) database. *"http://isohis.iaea.org"*, 2001. 128

D. Jacob, U. Andrae, G. Elgered, C. Fortelius, L.P. Graham, S.D. Jackson, U. Karstens, C. Koepken, R. Lindau, R. Podzun, B. Rockel, F. Rubel, H.B. Sass, R.N.D. Smith, B.J.J.M. Van den Hurk, and X. Yang. Comprehensive Model Intercomparison Study Investigating the Water Budget during the BALTEX-PIDCAP Period. *Meteorology and Atmospheric Physics*, 77:19 – 43, 2001. 128

D. Jacob and R. Podzun. Sensituvity studies with the regional climate model REMO. *Meteorology and Atmospheric Physics*, 63:119 – 129, 1997. 128

S. Kotlarski and S. Hagemann. Shaping of the global Hydrological Discharge model to a high resolution regional climate model domain. In *EGS - AGU - EUG Joint Assembly, Abstracts from the meeting held in Nice, France, 6 - 11 April 2003*, pages 7323–+, April 2003. 130

B. Langmann and A. Heil. Release and dispersion of vegetation and peat fire emissions in the atmosphere over Indonesia 1997/1998. *Atmospheric Chemistry and Physics*, 4:2145 – 2160, 2004. 130

B. Norris. Change of the operational forecasting system. *ECMWF Newsletter*, 74, 1997. 128

T. Semmler. *Der Wasser- und Energiehaushalt der arktischen Atmosphäre*. PhD thesis, Max-Planck-Institut für Meteorologie, Apr 2002. 130

T. Semmler and D. Jacob. Modeling extreme precipitation events-a climate change simulation for Europe. *Global and Planetary Change*, 44:119–127, December 2004. 130

L. G. Thompson, T. Yao, E. Mosley-Thompson, M. E. Davis, K. A. Henderson, and P.-N. Lin. A High-Resolution Millennial Record of the South Asian Monsoon from Himalayan Ice Cores. *Science*, 289:1916–1920, September 2000. 129

H. von Storch, H. Langenberg, and F. Feser. A Spectral Nudging Technique for Dynamical Downscaling Purposes. *Monthly Weather Review*, 128:3664–3673, 2000. 128, 129

Appendix A

Computation of mean sea-level pressure

Computing the mean sea-level pressure in atmospheric models

Introduction

Most current atmospheric circulation models have adopted either σ or η vertical coordinates, which are linear functions (with offset in the upper layers for η levels) of the surface pressure P_s. Yet P_s is highly dependent on the orography, thus on the horizontal resolution of the model. Hence, P_s is not well suited for identifying synoptic scale variations of pressure, and to compare simulations at different horizontal resolutions.

Meteorologists usually refer to the mean sea-level pressure (MSLP). MSLP is an idealized parameter: it is the pressure that would be measured at the geoide in the absence of continental elevation. Over the ocean, it is equal to the measured surface pressure; over continent, one needs to specify which atmosphere structure we assume *below* the orographical surface.

Differences in pressure with altitude can be computed * using the hypsometric equation A.3. Hydrostatic equation:

$$\partial P = -\rho g \partial z \tag{A.1}$$

Equation of state for perfect gases:

$$PV = nR_d T_v$$

$$P\alpha = R_d T_v$$

$$\rho = \frac{P}{R_d T_v} \tag{A.2}$$

Combining A.1 and A.2, we obtain:

$$\frac{\partial P}{P} = -\frac{g}{R_d T_v}\partial z$$

$$\frac{P_1}{P_2} = \exp\left(-\int_{z_1}^{z_2} \frac{g}{R_d T_v}\partial z\right) \tag{A.3}$$

The gravity g is generally considered constant with altitude, but a vertical profile of virtual temperature T_v needs to be specified, in order to perform the integration of equation A.3 between the surface (z_s) and the geoide altitude (z_0).

The Sheull method

The standard method, also referred to as Sheull method, is applied e.g. by the European Centre for Medium-Range Weather Forecast (ECMWF †). The atmosphere is considered as dry, ($T_v = T$), and the vertical profile of T is taken linear.

$$T(z) = T_s + \Gamma \cdot (z - z_s) \tag{A.4}$$

Hence A.3 becomes:

$$\ln\left(\frac{P_0}{P_s}\right) = \int_{z_0}^{z_s} \frac{g \cdot \partial z}{R_d(T_s + \Gamma z)}$$

*temperature: $T\,[K]$
pressure: $P\,[Pa]$
gravity acceleration $g = 9.80665\,m\,s^{-2}$
gaz constant for dry air: $R_d = 287.04\,m^2\,s^{-2}\,K^{-1}$
gaz constant for water vapour: $R_v = 178.64\,m^2\,s^{-2}\,K^{-1}$
virtual temperature: $T_v = T\,\frac{1+R_v/R_d \cdot e}{1+e} \approx T\,(1+\varepsilon e)\,[K]$
vapour mixing ratio: $e\,[kg^{-1}/kg^{-1}]$
ratio of dry air and water vapour constants: $\varepsilon = 0.608$

†The method is described in White [2002]. The same algorithm is used by the 'afterburner' package, used to process ECHAM data [Kornblüh et al., 2003].

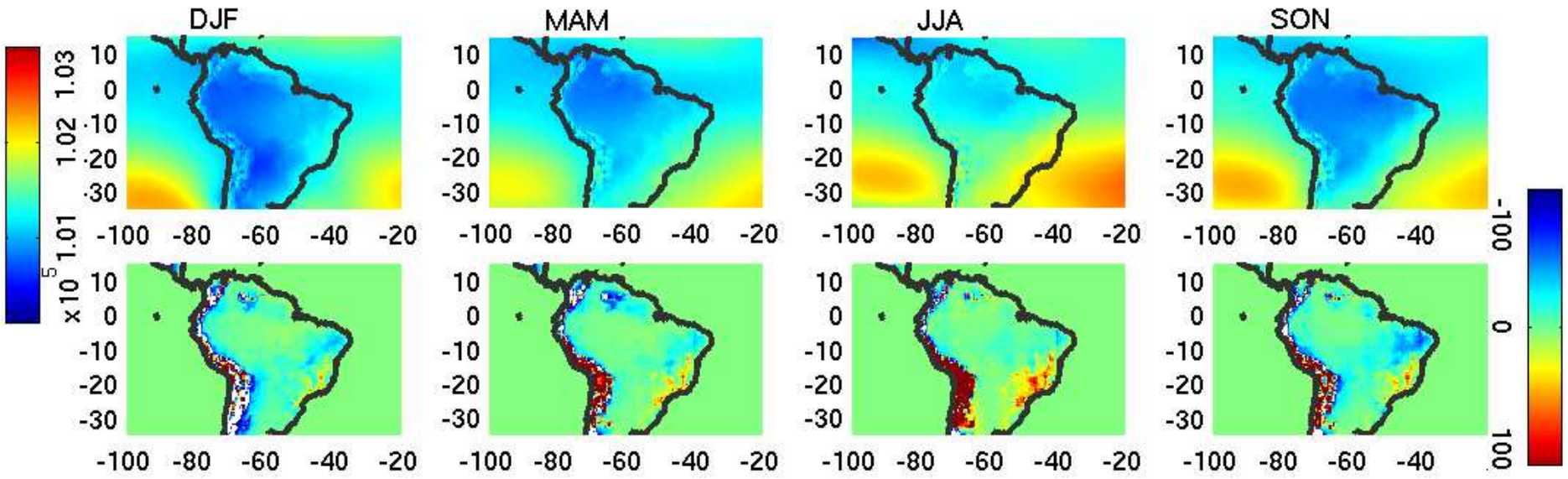

Figure A.1: Upper row: Mean sea-level pressure from REMO, according to the refined Mesinger method. Lower row: Difference between the classical and refined Mesinger method. Columns represent the year seasons: austral summer (DJF), autumn (MAM), winter (JJA) and spring (SON).

A variable change can make it easier. $x = \frac{\Gamma\Phi}{gT_s} = \frac{\Gamma z}{T_s}$

$$\ln\left(\frac{P_0}{P_s}\right) = \frac{g}{R_d T_s}\int_{z_0}^{z_s} \frac{\partial z}{1+\frac{\Gamma z}{T_s}}$$

$$\ln\left(\frac{P_0}{P_s}\right) = \frac{g}{R_d \Gamma}\int_{x_0}^{x_s} \frac{\partial x}{1+x} \tag{A.5}$$

Applying the Taylor development in the vicinity of 0, at the second order:

$$\frac{1}{1+x} \sim 1+x+x^2$$

$$\int_{x_0}^{x_s} \frac{\partial x}{1+x} \sim \left[x - \frac{x^2}{2} + \frac{x^3}{3}\right]_{x_0}^{x_s}$$

$$\int_{x_0}^{x_s} \frac{\partial x}{1+x} \sim x_s - \frac{x_s^2}{2} + \frac{x_s^3}{3} \tag{A.6}$$

Combining A.5 and A.6, we find the final formula:

$$\ln\left(\frac{P_0}{P_s}\right) \sim \frac{g}{R_d \Gamma}\left(x_s - \frac{x_s^2}{2} + \frac{x_s^3}{3}\right)$$

$$P_0 \sim P_s \cdot \exp\left(\frac{g z_s}{R_d T_s}\left(1 - \frac{x_s}{2} + \frac{x_s^2}{3}\right)\right) \tag{A.7}$$

The lapse rate Γ is chosen by default equal to the standard tropospheric lapse rate $\Gamma^{st} = -6.5 K \cdot km^{-1}$. In case of low pressures over high and warm surfaces, or high pressures over cold surfaces, the lapse rate is modified according to empirical relations [White, 2002].

The Mesinger method

Instead of prescribing the tropospheric lapse rate, it is possible to infer it from environmental condition. This is the idea of the Mesinger method, where virtual temperature below the surface is interpolated horizontally from the nearest atmospheric fields. This method, also known as membrane SLP deduction scheme, is commonly used for regional circulation models, as described in Chuang and Manikin [2001]. Temperature below the surface is computed by horizontally relaxing virtual temperatures on pressure levels:

$$\nabla^2 T_v = 0 \tag{A.8}$$

The vertically averaged virtual temperature is then used to compute the MSLP, according to equation A.3. In other terms, equation A.3 is averaged as:

$$\frac{P_0}{P_s} = \exp\left(\frac{g}{R_d \overline{T_v}}\Delta z\right) \tag{A.9}$$

where

$$\overline{T_v} = \Delta z \cdot \left(\int_0^z \frac{\partial z}{T(z)}\right)^{-1} \tag{A.10}$$

Assuming that the vertical profile of virtual temperature is linear, equation A.10 can be explicited as :

$$\overline{T_v} = \Delta z \cdot \left(\int_0^{z_s} \frac{\partial z}{T_0 + \Gamma \Delta z}\right)^{-1}$$

$$\overline{T_v} = \frac{z \cdot \Gamma}{\ln(|1 + \Gamma z_s / T_0|)}$$

Z	200	400	600	800	1000	1200	1400	1600
T_s	24.4	24.97	23.91	22.36	21	19.53	18.18	18.45
Γ_S	3.701	-5.292	-7.756	-6.791	-7.36	-6.716	1.326	-5.697
Z	1800	2000	2200	2400	2600	2800	3000	3200
T_s	17.31	15.95	15.29	14.24	13.05	12.65	9.668	10.2
Γ_S	-6.784	-3.332	-5.217	-5.973	-2	-14.91	2.633	-8.653
Z	3400	3600	3800	4000	4200	4400	4600	4800
T_s	8.464	7.63	5.779	5.368	4.481	3.16	1.369	-1.366
Γ_S	-4.174	-9.253	-2.055	-4.434	-6.607	-8.952	-13.67	-

Table A.1: Mean annual lapse rate Γ_s extrapolated under the surface, from near-surface values. Altitude Z is given in [m], Temperature T_s in [^{o}C] and Γ_s in $[K \cdot km^{-1}]$.

Applying the Taylor development of second order:

$$\frac{x}{\ln(1+x)} \sim 1 + \frac{x}{2} - \frac{x^2}{12}$$

therefore, assuming (A.4), equation A.10 is equivalent to :

$$\overline{T_v} \sim T_0 + \frac{\Delta z \cdot \Gamma}{2} - \frac{(\Delta z \cdot \Gamma)^2}{12 \cdot T_0} \tag{A.11}$$

$$\overline{T_v} \sim \frac{T_s + T_0}{2} - \frac{(T_s - T_0)^2}{12 \cdot T_0}$$

Approximating at the first order, $\overline{T_v}$ is equivalent to the arithmetic mean virtual temperature.

We now consider the lapse rate Γ no longer as constant through the troposphere, but constant in each layer. The vertical profile of temperature is then peace-wise linear. Hence equation A.11 becomes:

$$\overline{T_v} \sim T_0 + \frac{\Delta z \cdot \sum_{i=1}^{n} \Gamma_i}{2} - \frac{\Delta z^2 \cdot \sum_{i=1}^{n} \Gamma_i^2}{12 \cdot T_0} \tag{A.12}$$

Refi nement of the Mesinger method

The critical point in SLP reconstruction is the specification of the temperature profile below the surface. Chuang and Manikin [2001] suggest to interpolate horizontally the adjacent virtual temperature. This method is well suited for high, narrow mountains. In case of wide mountains, adjacent temperatures are no longer representative of the local state of the atmpshpere extended below the surface. Hence a refinement of Mesinger method is suggested here. The interpolation of temperature below the surface is conducted along all three directions of space.

$$\overline{T_v} = T_v|_{\perp x} + T_v|_{\perp y} + T_v|_{\perp z} \tag{A.13}$$

where $\perp$ means 'perpendicular to' one direction of the orthogonal referential (x,y,z).
Furthermore, the reconstruction only took into account virtual temperatures from σ-level to upwards ($\sim 100m$ above the surface) not be biased by radiative heating from the surface. The results are shown on Tables A.1 and A.2.

A case study over South America

We can assess the maximal error from the quadratic term in a given case study, e.g. over South America. The altitude reaches up to 5000m, with surface temperatures around 300K. Assuming the standard lapse rate, the quadratic error in

P_a	10078	994	965.8	919.6	855.8	777.3	688.5	594
Z	65.88	232.4	555.0	1059	1754	2639	3708	4949
T_a	16.11	15.66	14.20	11.70	7.908	2.930	-3.223	-10.9
Γ_a	-7.275	-6.221	-5.759	-5.614	-5.65	-5.781	-6.203	-6.701
$T^\star$	16.09	17.39	13.89	9.44	6.24	2.22	-3.38	-10.74
$\Gamma^\star$	11.234	-14.25	-10.8	-5.399	-5.108	-5.719	-6.333	-6.782
P_a	499.4	408.6	325.3	252.2	191	141.2	102.7	73.44
Z	6343	7876	9513	11234	13058	14996	17021	19174
T_a	-20.28	-31.26	-43.53	-55.12	-60.82	-61.05	-61.4	-61.64
Γ_a	-7.179	-7.496	-6.733	-3.124	-0.1324	-0.1906	-0.1035	0.9169
$T^\star$	-19.79	-30.59	-43.95	-55.79	-61.49	-61.23	-60.88	-60.83
$\Gamma^\star$	-7.2572	-8.2553	-6.9296	-3.1938	0.1387	0.1733	0.0253	0.8767

Table A.2: Mean annual lapse rate Γ_a in the atmosphere. Level pressure P_a is given in [hPa], altitude Z in [m], Temperature T_s in [^{o}C] and Γ_a in $\left[K \cdot km^{-1}\right]$. The methods present in this paper is presented with an asterisk *.

A.11 would be at most 0.3 K. The approximation error is about a third of the models accuracy for surface temperature ($\sim 1K$). Given the hypothesis in equation A.4, it is thus reasonable to neglect quadratic terms.

According to experimental evidence [Folkins, 2002], Γ varies between -0.5 and -6.5 $K \cdot km^{-1}$ below 6000 m. To test the validity of the method, we compare the lapse rate *below the surface*, to the actual lapse rate in the atmosphere. Γ_s represents the lapse rate from the interpolation of atmospheric near surface values (first two η levels). Γ_a represents the tropospheric lapse rate in the atmosphere over the continent. $\Gamma^\star$ represent the atmospheric lapse rate extrapolated below the surface according to the refined Mesinger method. All three are indicated in annual means, in table A.1 and table A.2 respectively.

Simulated vertical temperature and lapse rate profiles, given in tables A.1 and A.2, are plotted in figure A.2. Γ_a is comprised between -7 and -6 $K \cdot km^{-1}$, with a mean value of 6.1 $K \cdot km^{-1}$. Hence the linear assumption from equation A.4 is correct.

The mean lapse rate from the interpolation is -5.6 $K \cdot km^{-1}$. Large scatter is mainly due to the few grid cells with altitudes above 2000m. Inferring the tropospheric profile of temperature from near-surface values underestimates the mean lapse rate at lower altitudes, and introduces a positive bias of nearly 10 K. This is consistent with an observed mean difference of 1 K between the soil and the 2-m temperatures, in the ERA40 [ECMWF and Raoult, 2003] data set over the same domain. Taking a mean altitude of 200 m in equation A.9, this positive bias in mean temperatures results in a generalised underestimation of MSLP by 2 hPa.

The refined Mesinger method produces a temperature profile nearly identical to that of the free atmosphere. Since the first 2 σ-levels are ignored, the refined Mesinger method overcomes the 10K bias due to surface heating. Its lapse-rate profile is very similar to that of the free atmosphere at upper levels and joins up with the classical Mesinger method at lower levels.

In conclusion, the Mesinger method proves to be valid both from the theoretical and applied point of view. The interpolation introduces a positive bias in the sub-surface temperatures, but it accounts for seasonal and geographical variations in a more consistent way than the Sheull method. This inconvenient can be bypassed by the 'refined Mesinger method': virtual temperatures *below the surface* are inferred from all surrounding (instead of horizontal only) free atmospheric conditions. As shown in Figure A.1, strong relief does not introduce a significant bias in the SLP field, which retains its synoptical coherence. The improvements by the refined Mesinger method are most obvious at very high altitudes (Andean Cordillera), as well as lower elevations (Brazilian highlands).

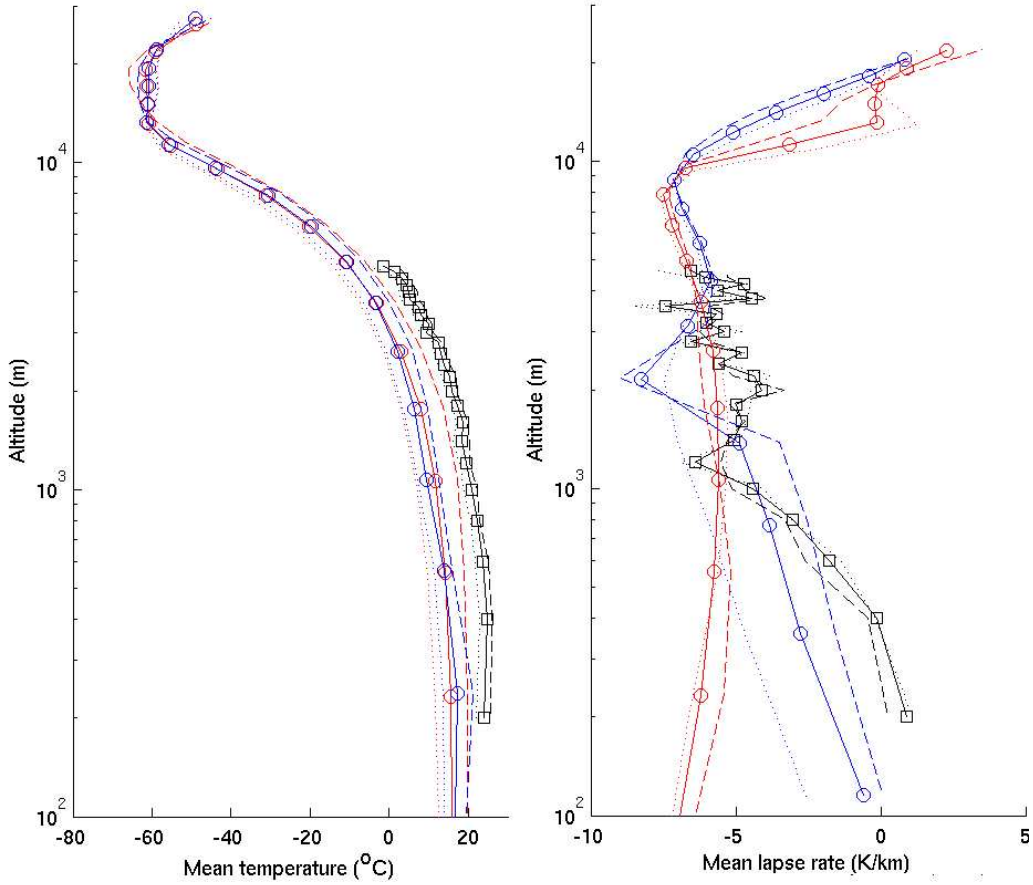

Figure A.2: Mean annual temperature profile and lapse rate in the atmosphere. Both variables are spatially averaged over land in the study domain [100^{o}W; 20^{o}W],[35^{o}S; 15^{o}N]. The red continuous line stands for the atmosphere, the black continuous line stands for interpolated values below the surface; dashed lines represent the mean for austral summer (DJF), the dotted lines austral winter (JJA). The method presented in this paper produces the temperature and lapse rate profiles marked in blue.

Bibliography

H.Y. Chuang and G. Manikin. The NCEP Meso Eta Model Post Processor: A Documentation. Technical Report 438, National Centers for Environmental Prediction, Apr 2001. http://www.emc.ncep.noaa.gov/mmb/papers/chuang/1/OF438.html. 138, 139

European Center for Medium-Range Weather Forcast ECMWF and B. Raoult. The ECMWF public data server. *ECMWF Newsletter*, 99:18 – 19, July 2003. "http://data.ecmwf.int/data/d/era40_mnth/". 140

I. Folkins. Origin of Lapse Rate Changes in the Upper Tropical Troposphere. *Journal of Atmospheric Sciences*, 59: 992–1005, March 2002. 140

L. Kornblüh, U. Schulzweida, A. Hellbach, E. Kirk, and M. Ponater. *Afterburner: A postprocessing program for ECHAM data and ECMWF analysis data, v4.14*. Max-Planck-Institut für Meteorologie, MPG-Hamburg, Dec 2003. "http://www.mpimet.mpg.de/ afterburner/after.c". 136

P.W. White. *Technical and Computational Procedures (CY23R4)*. ECMWF - Meteo France, ifs documentation, part vi edition, 2002. 136, 138

Appendix B

Preliminary results of REMO$_{iso}$ over Canada †

† J. Birks and K. Sturm, *unpublished, preliminary results, April 2005*

Presentation of CNIP

In the present chapter, we introduce the Canadian network for isotopes in precipitation (CNIP), a long-standing participant in the IAEA/WMO Global Network for Isotopes in Precipitation (GNIP [IAEA and WMO, 2001]) program. CNIP is operated by the Environmental Isotope Laboratory at the University of Waterloo, in cooperation with Meteorological Service of Canada, as reported in Birks et al. [2004], Edwards et al. [2002], Moorman et al. [1996]. A preliminary simulation of REMO$_{iso}$ was conducted over Canada and Greenland, to assess the model's ability in Artic climate and provide further evidence for the interpretation of CNIP observations.

Citing Birks et al. [2004], 'CNIP (Phase I) currently comprises 17 stations collecting monthly-composite samples, providing for the first time reasonably well- distributed spatial coverage for the entire country (see Figure B.1 and B.4). This interim configuration is planned to exist for several years, permitting sufficient ongoing analysis of accumulating data to discern fundamental linkages between the isotopic composition of precipitation and synoptic climatology and to aid in designing and optimising a more permanent future network.

An important feature of CNIP is its function as an observational research network, producing data that are readily accessible and of immediate value. It also provides a framework compatible with GNIP, within which other finer-resolution networks and sampling campaigns can be nested to address particular regional and local questions. Present examples include extensive isotopic observations of precipitation, atmospheric moisture, and surface waters in the Mackenzie River Basin, as part of hydrologic studies within the Global Energy and Water Cycle Experiment (GEWEX-MAGS), as well as daily precipitation sampling at three sites in eastern Canada. Location of present or past CNIP stations is given in Table B.1.

In the present document, we evaluate preliminary results by the simulated isotopic composition of precipitation over Canada by the regional circulation model REMO$_{iso}$, in comparison to observations from the CNIP network. REMO$_{iso}$ was integrated over a 15 month period. The first three months, considered as model spin-up, are not considered in the following analysis. REMO$_{iso}$ was operated with climatological boundary conditions. In particular, sea-surface temperatures (SST) are taken fro, the GlSST climatology [Rayner et al., 1994]. The simulation settings and physical parameterisation are identical to those reported in Sturm et al. [2005, -].

The depletion in $H_2^{18}O$ is expressed in reference to the Vienna standard mean ocean water (V-SMOW), by following equation B.1.

$$\delta^{18}\mathrm{O} = \left(\frac{[H_2^{18}O]/[H_2O]_{sample}}{[H_2^{18}O]/[H_2O]_{SMOW}} - 1 \right) \cdot 1000 \; [‰] \tag{B.1}$$

We also consider preliminary results of a second order isotopic signal, i.e. the deuterium excess. It is defined as $d = \delta\mathrm{D} - 8 \times \delta^{18}\mathrm{O}$ [Dansgaard, 1964], where δD expresses the depletion of HDO. Both δ^{18}O and d are expressed in ‰.

Mean annual δ^{18}O distribution

Figure B.1 shows an interpolation of annual weighted δ^{18}O means from the CNIP stations. The corresponding map by REMO$_{iso}$ is shown on Figure B.2. First, REMO$_{iso}$ and observations have in common a clear latitude gradient: δ^{18}O decreases from -5‰ at 40°N to -20‰ at 75°N. Yet REMO$_{iso}$ over-estimates δ^{18}O by 5‰, with a maximal discrepancy at 70°N in transect B-B' (Figure B.8a).

Secondly, δ^{18}O on Figure B.2 shows a clear dependance on altitude. In particular, the Rocky Mountains across Britisch Columbia stand out with a -10‰ anomaly from the zonal mean. Minor mountain ranges such as the Brooks range (in Alaska) or the Baffin land (Nort-West territories) also mark the altitude effect. Altitude and temperature effect are combined Greenland. A minimum δ^{18}O of -34‰ is found at [71.24°N; -34.51°W], close to Greenland Summit.

In conclusion, these preliminary results confirm that REMO$_{iso}$ accurately captures the dominant isotopic effects controlling δ^{18}O in precipitation. The temperature effect [Dansgaard, 1964] dominates, imprinting a strong latitudinal gradient to the δ^{18}O distribution. Next comes the altitude effect, being most noticeable over the Rocky Mountains. This explains

STATION	PROVINCE	LATITUDE	LONGITUDE	ELEVATION	Period
Alert	Nunavut	82.20°N	62.30°W	62 m	1989 - 2003
Atikokan	Ontario	48.75°N	91.62°W	393 m	1976 - 1980
Bay D'Espoir	Newfoundland	47.98°N	55.82°W	190 m	1999 - 2002
Bonner Lake	Ontario	49.38°N	82.12°W	245 m	1999 - 2002
Cambridge Bay	Nunavut	69.06°N	105.07°W	23 m	1989 - 1999
Chapais	Quebec	49.82°N	74.97°W	382 m	1999 - 2002
Churchill	Manitoba	58.45°N	94.00°W	28 m	1989 - 1998
Edmonton	Alberta	53.57°N	113.52°W	671 m	1963 - 1965
Egbert	Ontario	44.23°N	79.77°W	224 m	1998 - 2002
Esther	Alberta	51.67°N	110.20°W	707 m	1999 - 2002
Eureka	Nunavut	80.00°N	85.56°W	10 m	1989 - 2001
Experimental Lakes Area	Ontario	49.67°N	93.72°W	369 m	1999 - 2002
Fort Smith	Northwest Territories	60.02°N	111.97°W	203 m	1962 - 1965
Gimli	Manitoba	50.62°N	96.98°W	223 m	1975 - 1981
Goose Bay	Newfoundland	53.32°N	60.42°W	46 m	1961 - 1969 1997 - 2003
Hall Beach	Nunavut	68.47°N	81.15°W	8 m	1990 - 1994
Harcourt	New Brunswick	46.50°N	65.27°W	40 m	1999 - 2002
Inuvik	Northwest Territories	68.18°N	133.29°W	59 m	1986- 1989
Mayo	Yukon Territory	63.62°N	134.13°W	504 m	1986- 1989
Mould Bay	Northwest Territories	76.14°N	119.20°W	15 m	1989 - 1995
Ottawa	Ontario	45.32°N	75.67°W	114 m	1973 - 2003
Pond Inlet	Nunavut	72.40°N	78.00°W	55 m	1990- 1991
Resolute Bay	Nunavut	74.72°N	94.98°W	67 m	1989 - 2002
Saskatoon	Saskatchewan	52.10°N	106.43°W	504 m	1990- 2002
Saturna Island	British Columbia	48.78°N	123.13°W	178 m	1999 - 2002
Simcoe	Ontario	42.85°N	80.27°W	240 m	1975 - 1983
Snare Rapids	Northwest Territories	63.52°N	116.00°W	241 m	1997 - 2003
Ste. Agathe	Quebec	46.05°N	74.28°W	395 m	1976 - 1983
The Pas	Manitoba	53.97°N	101.10°W	272 m	1976 - 1983
Truro	Nova Scotia	45.37°N	63.27°W	40 m	1976 - 1983
Victoria	British Columbia	48.65°N	123.43°W	20 m	1976 - 1983
Whitehorse	Yukon Territory	60.72°N	135.07°W	702 m	1961 - 1965 1986 - 1989
Wynyard	Saskatchewan	51.77°N	104.20°W	561 m	1975 - 1983
Yellowknife	Northwest Territories	62.28°N	114.27°W	205 m	1989 - 1997

Table B.1: Station locations in the CNIP network

the shape of the east-west $\delta^{18}O$ transect shown on Figure B.7a.

Figure B.3 shows the discripancies between $\delta^{18}O$ simulated by REMO$_{iso}$ and CNIP observations. Although being qualitatively correct, REMO$_{iso}$ underestimates quantatively the isotopic gradients. We suggest that the overestimation of $\delta^{18}O$ at high altitudes/latitudes is primarily related to the initial conditions. Soil moisture and snow layer in REMO are initialised at $\delta^{18}O = 0‰$, and the 3-month spin-up is too short to reach an equilibrium with atmospheric processes. Previous studies over Europe demonstrated that the soil reservoirs need up to 3 years to equilibrate with the atmosphere. Hence longer simulations are required to assess REMO$_{iso}$ performances over the Canadian domain.

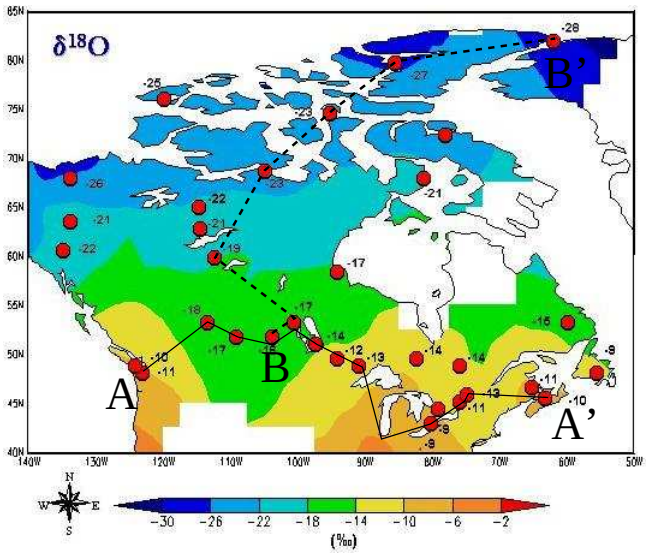

Figure B.1: Mean annual $\delta^{18}O$ in the CNIP data set, monitored by the Environmental Isotope Laboratory (University of Waterloo) in collaboration with the the Meteorological Service of Canada. Stations selected for the east-west (south-north) gradient are linked by a continuous (dashed) line, from point A to A' (B to B').

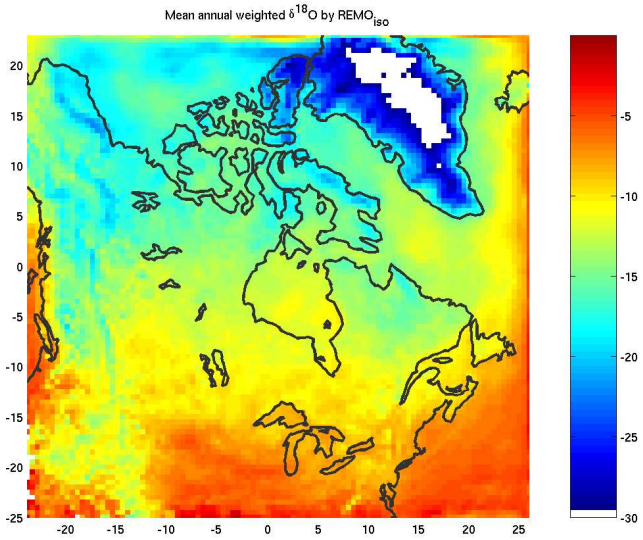

Figure B.2: Mean annual $\delta^{18}O$ as simulated by $REMO_{iso}$. Due to the rotated coordinated grid, the map is displayed in an azimuthal equal-area projection. The colour-scale is identical to Figure B.1.

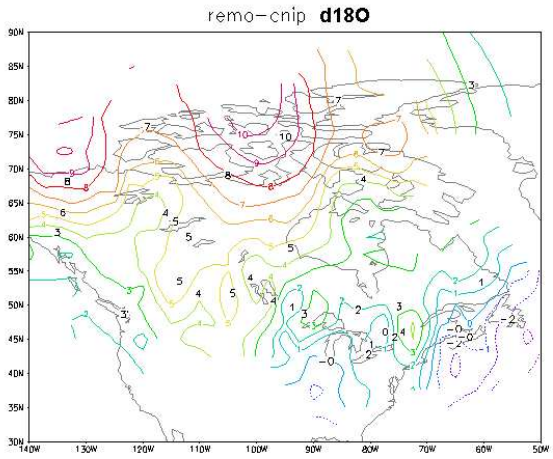

Figure B.3: Difference in mean annual $\delta^{18}O$ between $REMO_{iso}$ and CNIP data set. Values taken at the location of the CNIP stations are subtracted to each other, and the resulting field is interpolated to underline the spatial patterns of REMO discripancies.

Preliminary results for D excess

Simulation of D excess is still a widely controversial issue in the isotope GCM community. Nevertheless, REMO$_{iso}$ performs astonishingly well in reproducing the mean *d* gradients across Canada. In particular, the east to west decrease is in good agreement between modelled and observed *d* (Figure B.9a).

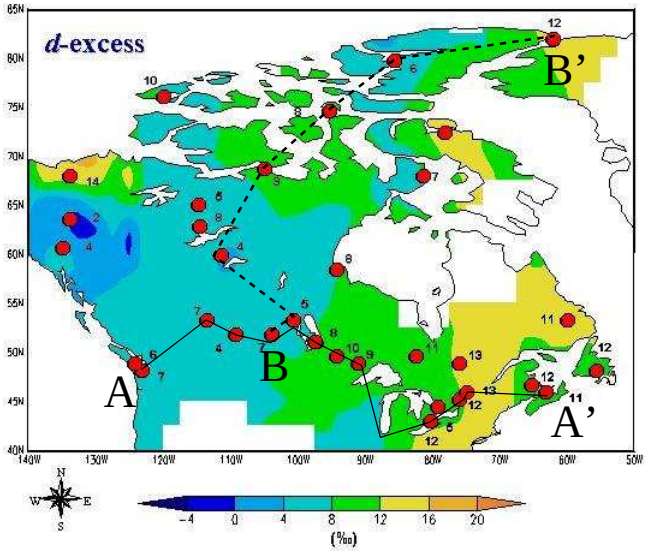

Figure B.4: Mean annual D-excess in the CNIP data set, monitored by the Environmental Isotope Laboratory (University of Waterloo) in collaboration with the the Meteorological Service of Canada. Stations selected for the east-west (south-north) gradient are linked by a continuous (dashed) line, from point A to A' (B to B').

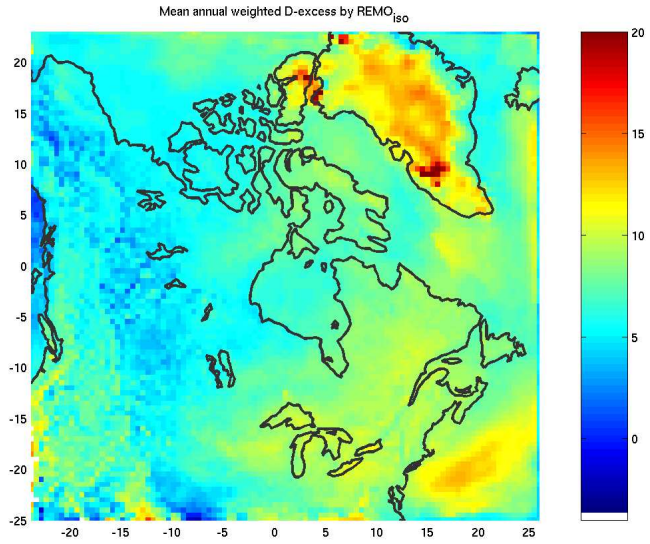

Figure B.5: Mean annual D excess as simulated by REMO$_{iso}$. Due to the rotated coordinated grid, the map is displayed in an azimuthal equal-area projection. The colour-scale is identical to Figure B.1.

The mean annual *d* is very similar between CNIP observations (Figure B.4) and REMO$_{iso}$ (Figure B.5). This good agreement would indicate that kinetical effects are well represented in the model physics. These preliminary results further support experimental evidence by Jouzel and Merlivat [1984], concerning the differential isotope diffusion through the oversaturated zone around the forming ice-crystals in clouds below -20°C.

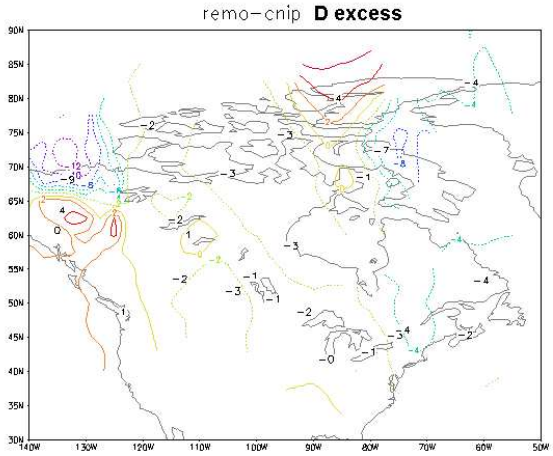

Figure B.6: Difference in mean annual D excess between REMO$_{iso}$ and CNIP data set. Values taken at the location of the CNIP stations are subtracted to each other, and the resulting field is interpolated to underline the spatial patterns of REMO discripancies.

Figure B.6 shows that d is slightly underestimated in REMO$_{iso}$, but no systematic bias is noticeable. This is encouraging for further investigation of the simulated d excess over Canada. It is beyond the scope of the present evaluation to suggest a comprehensive interpretation of d variations over Canada.

Seasonal evolution of $\delta^{18}O$ and d

The preliminary results from a one-year integration should be regarded with caution. First, the integration is too short for the soil moisture to balance with atmospheric processes. This influences the isotopic composition of precipitation both through moisture recycling (manly transpiration by the vegetation) and partial re-equilibration of rain drops with sub-cloud under-saturated atmosphere. Second, inherent atmospheric variability causes significant variance in mean monthly $\delta^{18}O$ even under climatological conditions.

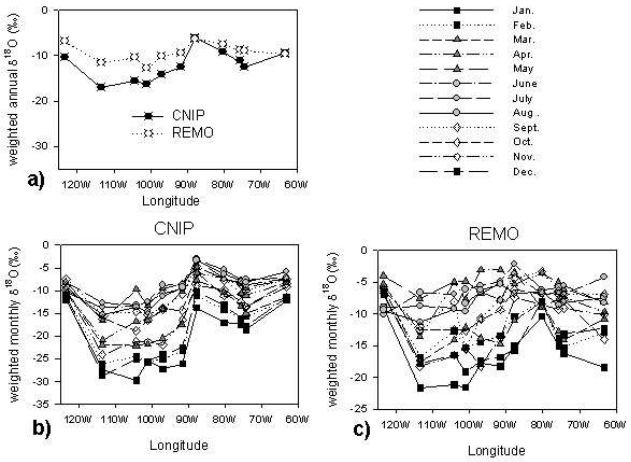

Figure B.7: East-west transect of $\delta^{18}O$ across Canada, from point A to A' as indicated on Figure B.1. In sub-figure a), the continuous line with filled circles represents CNIP mean annual measurements, whereas the dashed line with empty circles stand for $REMO_{iso}$. The weighted monthly means for the CNIP measurements (b) and $REMO_{iso}$ simulations are plotted respectively in sub-figure (b) and (c).

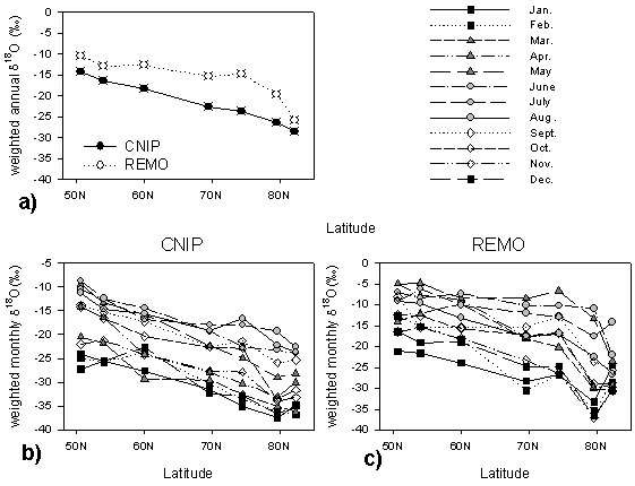

Figure B.8: South-north transect of $\delta^{18}O$ across Canada, from point B to B' as indicated on Figure B.1. Legends are identical to Figure B.7.

Nevertheless, variations of monthly $\delta^{18}O$ and d transect are mostly coherent between $REMO_{iso}$ and CNIP observations (Figures B.7, B.8, B.9, B.10 b-c). The seasonal temperature effect causes $\delta^{18}O$ in winter to be more depleted than in summer. Furthermore, the south-north gradient of $\delta^{18}O$ is stronger in winter than in summer.

In conclusion, preliminary results of regional isotopic modelling over Canada are promising. The spatial variability of $\delta^{18}O$ and d, well documented thanks to the large coverage of the CNIP observations, is correctly captured by $REMO_{iso}$.

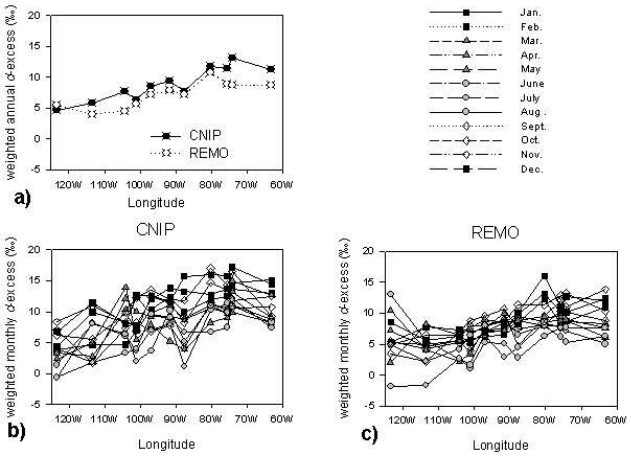

Figure B.9: East-west transect of *d* across Canada, from point A to A' as indicated on Figure B.4. Legends are identical to Figure B.9.

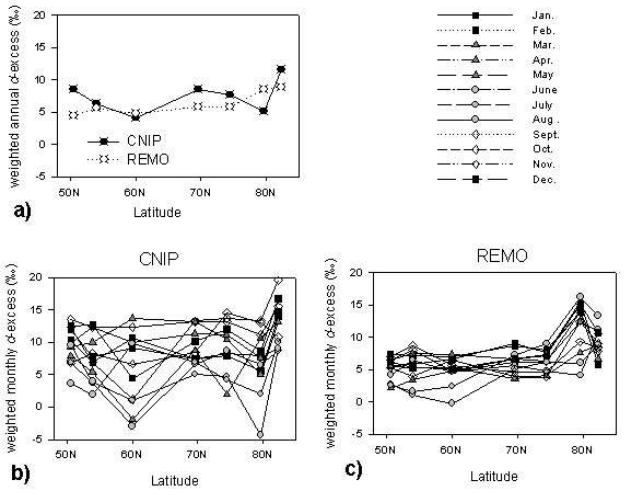

Figure B.10: South-north transect of $\delta^{18}O$ across Canada, from point B to B' as indicated on Figure B.4. Legends are identical to Figure B.7.

Nevertheless, the present one-year integration period is too short to give definite answers. The present simulation needs to be continued with climatological conditions, to achieve isotopic balance between the soil and atmospheric reservoirs. This could further acquaint with the inherent monthly variability of the isotopic signal. Finally, inter-annual variability in the CNIP data-set can be investigated with help of $REMO_{iso}$. For that purpose, $REMO_{iso}$ needs to be driven by observed instead of climatologic SST. A better representation of the actual circulation patterns can be achieved by nudging REMO with re-analyses, i.e. forcing upper-level winds in REMO towards observed fields.

Bibliography

S.J. Birks, T.W.D. Edwards, J.J. Gibson, R.J. Drimmie, and F.A. Michel. Canadian Network for Isotopes in Precipitation - CNIP. Technical report, Environmental Isotope Laboratory, University of Waterloo, 2004. 144

W. Dansgaard. Stable isotopes in precipitation. *Tellus*, XVI:436 – 468, 1964. 144

T.W.D. Edwards, S.J. Birks, and J.J. Gibson. Isotope tracers in global water and climate studies of the past and present. In *International Conference on the Study of Environmental Change Using Isotope Techniques*, volume 66. International Atomic Energy Agency, Vienna, 2002. 144

International Atomic Energy Agency IAEA and World Meteorological Organisation WMO. The Global Network of Isotopes in Precipitation (GNIP) database. *"http://isohis.iaea.org"*, 2001. 144

J. Jouzel and L. Merlivat. Deuterium and oxygen 18 in precipitation: modeling of the isotopic effects during snow formation. *Journal of Geophysical Research*, 89:11 749 – 11 757, 1984. 148

B.J. Moorman, F.A. Michel, and R.J. Drimmie. Isotopic variability in arctic precipitation as a climatic indicator. *Geoscience Canada*, 23:189 – 194, 1996. 144

N.A. Rayner, D.E. Parker, E.B. Horton, C.K. Folland, and R.B Hackett. Version 2.2 of the Global Sea-Ice and Sea Surface Temperature Data Set, 1903- 1994. Climate Research Technical Note 74, Hadley Centre, 1994. http://www.metoffice.com/research/ hadleycentre/obsdata/GISST.html. 144

K. Sturm, G. Hoffmann, and B. Langmann. Climatology of stable water isotopes in South America: comparing general to regional circulation models. *Journal of Climate*, page submitted, -. 144

K. Sturm, G. Hoffmann, B. Langmann, and W. Stichler. Simulation of $\delta^{18}O$ in precipitation by the regional circulation model $REMO_{iso}$. *Hydrological Processes*, page accepted, 2005. 144

Appendix C

Isotopes in Project for Intercomparison of Land-surface Parameterisation Schemes (IPILPS): REMO provides the forcing fields[†]

[†]K. Sturm, M. Fischer, K. McGuffie, A. Henderson-Sellers, *REMO$_{iso}$ manual for the IPILPS workshop, April 18-22, 2005, Sydney, Australia*

Abstract

The present document introduces IPILPS (Isotopes in Project for Intercomparison of Land-surface Parameterisation Schemes). The scientific reasons for choosing $REMO_{iso}$ to provide forcing fields for IPILPS are illustrated in the present document. Preliminary results are displayed, which were discussed and applied to several isotope enabled land-surface schemes during the inaugural IPILPS workshop that took place at ANSTO, Sydney, from April 18^{th} to 22^{nd}, 2005.

Introduction to isotope hydrology

Considering the vital issue of water resource management in a changing climate, the need for a better comprehension of the continental water cycle is clearly established. Hence the international panel on climate change [IPCC, 2001] focuses on global, and recently on regional circulation models to simulate it. Yet the water cycle complexity makes it difficult to constrain every processes at work, thus large uncertainties remain concerning the sensitivity of the water cycle to specific steps. As a consequence, model projections still lack reasonable confidence in the effects of the global warming on the regional water cycle that will affect the population.

Historical background

Since the beginning of the Cold War and inherent atmospheric nuclear bombing tests, several national atomic institutes are monitoring isotopes in precipitation. Later these data sets proved to be highly relevant for environmental research. The international atomic energy agency (IAEA) centralised the national database in the global network of isotopes in precipitation (GNIP) [IAEA and WMO, 2001]. A climatic interpretation of the isotopic signal was proposed by Dansgaard [1964]: the depletion in heavier stable isotopes (18O, 2H aka deuterium D) in a precipitation sample is related to the temperature at which phase changes occurred, as well as the air parcel's rainout and recycling rate. The comprehension of the present isotopic signal in precipitation was extended e.g. to paleo-climatic records, which enabled the global temperature reconstruction up to $\sim$740 ky BP from polar ice cores [EPICA, 2004]. While the isotopic signal is quite well understood in polar environment, much remains to be done in order to interpret it at low latitudes, and exploit all information from isotopic paleo-records (e.g. tropical ice-cores, speleothemes, $\delta^{18}O$ in tree rings).

The stable water isotopes (SWI) hence represent far more than a tracer of atmospheric circulation : they truly represent a integrated climate proxy for the water cycle, both on a global and regional spatial scale, from event to interglacial time frames.

The IPILPS program

Isotopic fractionation processes are nevertheless complex, which complicates the deconvolution of the isotopic signal into climatic features. Especially, the partial re-equilibration of rain drops with surrounding vapour in non-polar sites introduces a strong local feedback in punctual precipitation samplings. It is hence essential to further investigate surface atmosphere exchanges, considering the isotopic signature of vapour fluxes, in order to discriminate between local influence and regional/global features, or the ratio between recycled and advected vapour. A distributed approach at basin level is required to analyse the integrated isotopic signal monitored in the global network for isotopes in rivers (GNIR, headed by the IAEA environmental section).

The isotopic project for the intercomparison of land-surface parameterisation schemes (IPILPS), approved by the GEWEX-GLASS panel, addresses specifically these issues [Henderson-Sellers and McGuffie, 2003]. Its aim is to conduct offline intercomparison of land-surface schemes (LSS) incorporating SWI information to better constrain the parameterisation of surface atmosphere energy and vapour fluxes in regional/global circulation models. IPILPS constitutes a new experiment in follow-up of the PILPS framework [Henderson-Sellers et al., 1996]. Three typical climatic environments

were selected : humid tropical forest, arid grassland and mid-latitude, temperate regimes. The corresponding site studies will be performed respectively in the Amazon (Manaus), Southern Australia (Tumbarumba) and Germany (Neuherberg).

Regional modelling of the stable isotope cycle

As commonly proceeded in modelling approach, simulations will evolve from local offline case studies, to reach eventually inline embedded LSS in a coupled regional/global circulation model (RCM/GCM).

REMO$_{iso}$ provides the best suited boundary conditions for LSS

Following this scope, the first step of IPILPS will be to validate the LSS to be compared against experimental data from selected sites. Hence the offline simulations need appropriate boundary conditions, i.e. input from a host model representing the atmospheric processes as close as possible to the actual meteorological conditions. Furthermore, both climatic and isotopic variables should be coherent.

Due to their finer resolution, RCM take better into account local features such as topography, surface type, etc. than GCM. The major task of my PhD was to integrate a isotope module to the REMO RCM (REgionales MOdel, developed by the Max-Planck-Institute for Meteorology, Hamburg). Currently, REMO$_{iso}$ is the only functional RCM with SWI module worldwide, hence it is a crucial component of IPILPS.

REMO uses the same physical schemes as the ECHAM-4, which provides its lateral boundary conditions [Roekner et al., 1996]. It runs on a Arakawa C grid with 0.5° resolution (∼54 km), hence a factor-two improvement as compared with the highest resolution for ECHAM (T106 ∼ 125 km). REMO can further be nested in itself, reaching a 1/6° resolution (∼18 km). The SWI module computes the H218O and HD16O cycles identically to the standard H216O hydrological cycle. Fractionation processes are represented at all steps of the hydrological cycle: kinetic fractionation during open-sea evaporation, thermodynamical equilibration between vapour, liquid and ice phases according to convective and large-scale cloud microphysics, re-evaporation and kinetic equilibration of falling rain droplets and vertical diffusion through the planetary boundary layer (PBL) [Hoffmann and Heimann, 1993, Hoffmann et al., 1998, Werner, 2000].

REMO$_{iso}$ was applied and validated in several climatic environments. One study domain covers the European continent, including temperate, Mediterranean and subpolar climates. My current interest focuses on the South American continent, including the Amazon as well as arid grassland regions such as Brazil's Nordeste. The model / data comparisons were successful both for total simulated precipitation amounts and their isotopic signature. The model parameterisation proved to be elaborated enough to well represent secondary effects as the deuterium excess. For the requirements of IPILPS, REMO$_{iso}$ was integrated over Australia. As shown on Figure C.1, REMO$_{iso}$ reproduces reasonably well the monthly precipitation amounts and δ^{18}O. The discrepancies are largest at very dry stations (e.g. Alice Springs). Furthermore, the model has some difficulties to cope with double minima shape of δ^{18}O in tropical context (Darwin, Brisbane).

Even though the surface features are better represented in REMO$_{iso}$, running in a climatological mode does not permit to reproduce a specific synoptical meteorological situation. Hence, large discrepancies may occur between model output and measured climatic (precipitation, temperature, wind speed, etc.) and isotopic variables. It is unclear whether the LSS results could be validated against experimental data with such a set-up. Reanalyses, which assimilate all available meteorological observations, provide the best estimation of the actual state of the atmosphere, but no corresponding isotopic information is available. In order to bridge over this problem, Georg Hoffmann, Max Kelley and M. Wener have developed a nudged version of ECHAM$_{iso}$: leaving the (isotopic) water cycle untouched, the model dynamics is forced to match the reanalyses while conserving the water budget. Hence the simulated precipitation events correspond better to sampled precipitation. This nudging technique applied to a SWI GCM is a unique feature, from which REMO$_{iso}$ greatly benefits in the form of accurate lateral boundary conditions. Furthermore, the spectral nudging technique has been applied to REMO$_{iso}$ [von Storch et al., 2000].

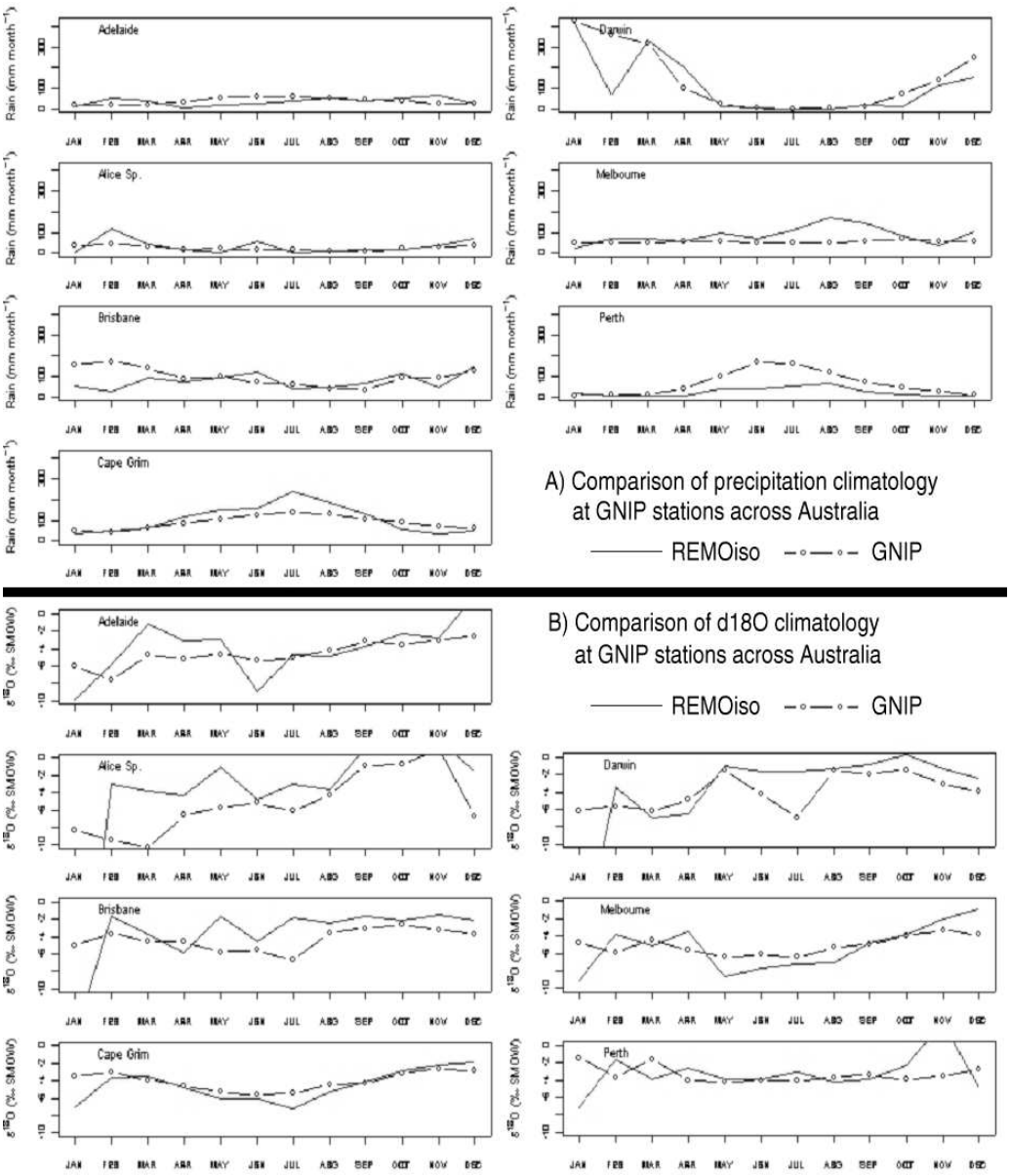

Figure C.1: Comparison of monthly precipitation amounts (A –upper panel) and $\delta^{18}O$ (B – lower panel) between $REMO_{iso}$ and GNIP stations. The GNIP station across Australia are located in Adelaide, Alice Springs, Brisbane, Cape Grim, Darwin, Melbourne and Perth, covering a wide spectrum of climate regimes.

Preliminary results of LSSi$_{iso}$ forcing fields by REMO$_{iso}$

In compliance with the needs of IPILPS, a new routine was built in REMO$_{iso}$ to write out selected parameters at the model time-step (5'). These parameters comprise all quantities relevant to the energy, water and SWI surface balance at IPILPS study sites. Figure C.2 shows a 1-year forcing data-set for Tumbarumba. Of particular interest for the present experiment is the daily cycle, which displays significant seasonal variability. It is shown on Figure C.3. Furthermore, REMO$_{iso}$ features a non-negligible interannual variability of the diurnal cycle.

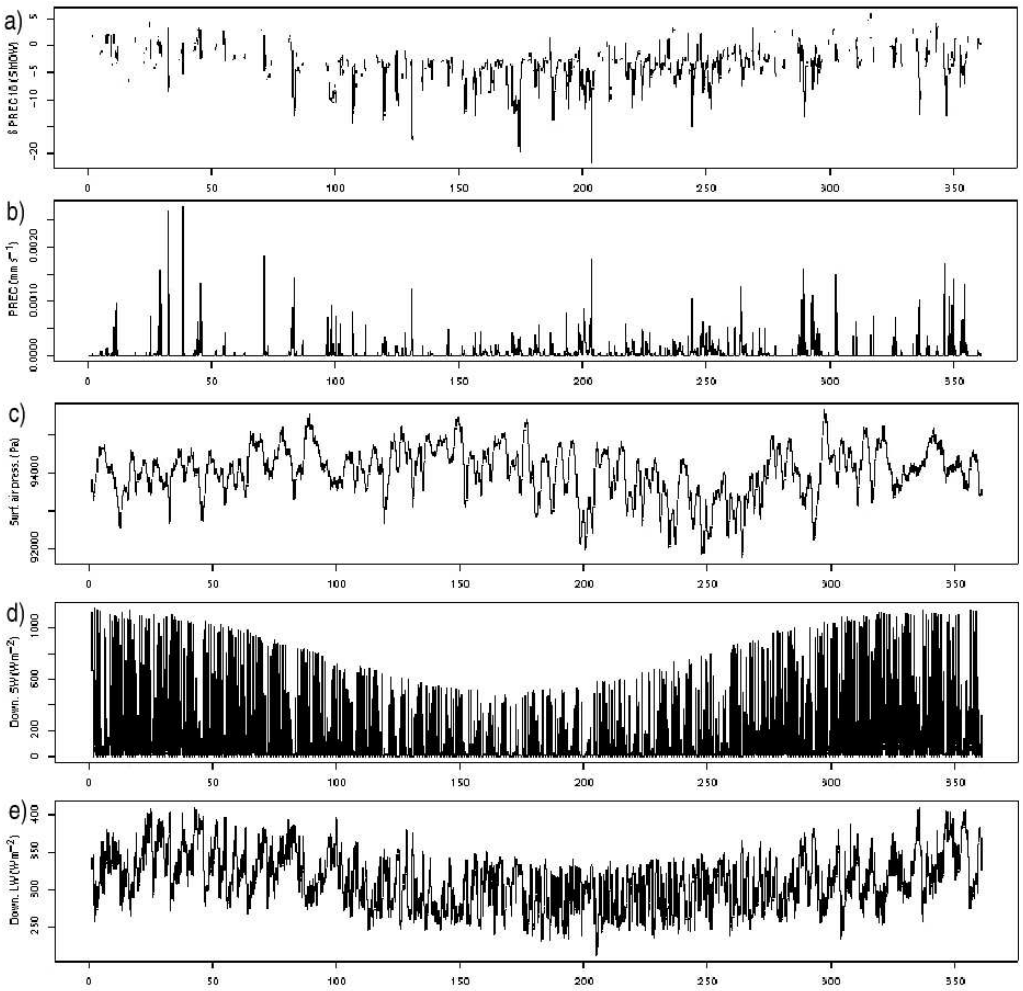

Figure C.2: One year LSS$_{iso}$ forcing data set by REMO$_{iso}$ at Tumbarumba, Australia, for selected quantities of the energy, water and SWI surface balance. (a) δ^{18}O in precipitation, (b) precipitation amount, (c) atmospheric surface pressure, (d) downward shortwave radiation, (e) downward longwave radiation.

Further unknowns in the (isotopic) water cycle simulations

In the previous section, the benefits of using REMO$_{iso}$ as host model for LSS intercomparison were demonstrated. But the benefits would actually be shared, since IPILPS addresses a crucial part of the (isotopic) water cycle that is poorly parameterised in current physical schemes. As long as GCM were run at coarse resolutions, many surface-atmosphere fluxes could arguably be dismissed as negligible (?) sub-grid processes. This is no longer true at the typical resolution of RCM, neither will it be for future resolution of GCM (cf. the Japanese Earth Simulator project, with a global coverage at a 0.5° resolution). Many RCM/GCM, among which REMO$_{iso}$ and ECHAM$_{iso}$, use a very rough representation of the soil reservoir (bucket-type soil models). The vegetation cover is fixed a priori, and its effects on the recycling rate

largely uncertain. The SWI proxy is a unique tool to better discriminate between transpiration and evaporation, as soon as the vegetation feedback is well understood and represented ! Furthermore, the more detailed topography implies that (sub-)surface runoff shall be accounted for in RCM, which bucket models do not permit. Hence IPILPS is un urgent prerequisite to further development in climate models.

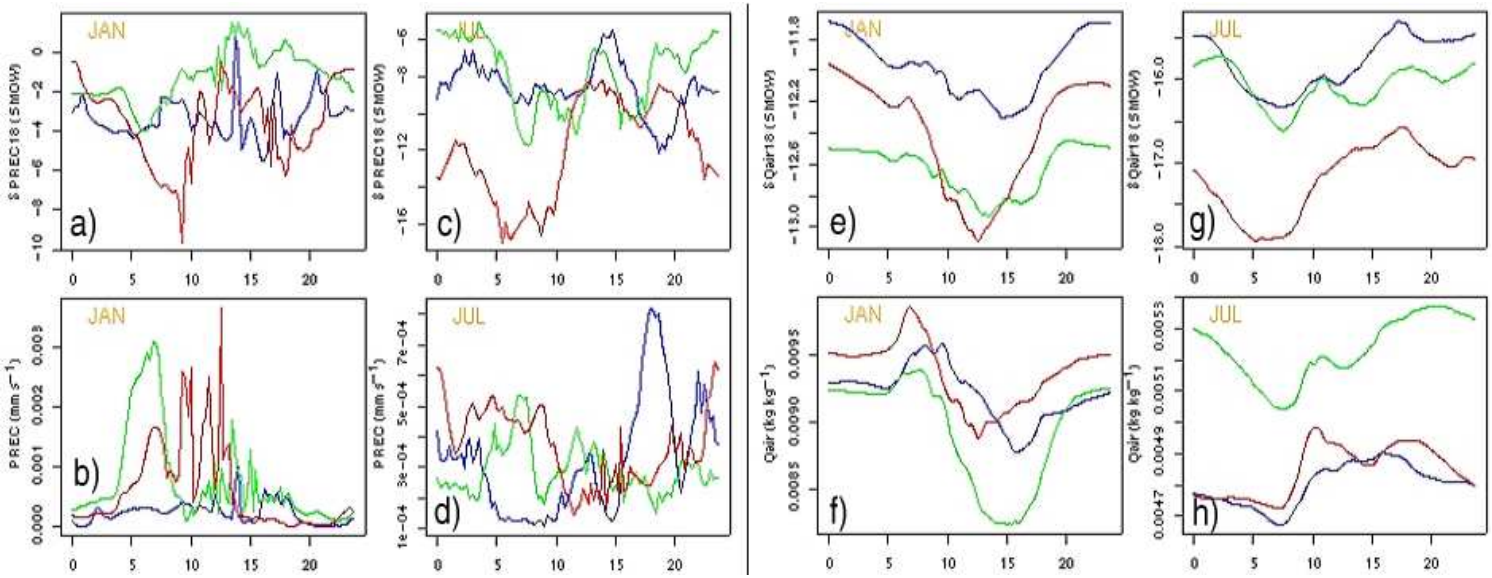

Figure C.3: Interannual variability of the diurnal cycle at Tumbarumba in summer (January – a,b,e,f) and winter (July – c,d,g,h). The left panel (a-d) represents precipitation, the right panel (e-h) surface humidity. The upper row (a,c,e,g) represent the $\delta^{18}O$ signature and the lower row (b,d,f,h) absolute values.

Bibliography

W. Dansgaard. Stable isotopes in precipitation. *Tellus*, XVI:436 – 468, 1964. 154

EPICA. Eight glacial cycles from an Antarctic ice core. *Nature*, 429:623 – 238, 2004. EPICA team: L. Augustin, C. Barbante, P.R.F. Barnes, J.M. Barnola, M. Bigler, E. Castellano, O. Cattani, J. Chappellaz, D. Dahl-Jensen, B. Delmonte, G. Dreyfus, G. Durand, S. Falourd, H. Fischer, J. Flückiger, M.E. Hansson, P. Huybrechts, G. Jugie, S.J. Johnsen, J. Jouzel, P. Kaufmann, J. Kipfstuhl, F. Lambert, VY. Lipenkov, G.C. Littot, A. Longinelli, R. Lorrain, V. Maggi, V. Masson-Delmotte, H. Miller, R. Mulvaney, J. Oerlemans, H. Oerter, G. Orombelli, F. Parrenin, DA. Peel, J.R. Petit, D. Raynaud, C. Ritz, U. Ruth , J. Schwander, U. Siegenthaler, R. Souchez , B. Stauffer, J.P. Steffensen, B. Stenni , T.F. Stocker, I.E. Tabacco, R. Udisti, R.S.W. van de Wal, M. van den Broeke, J. Weiss , F. Wilhelms, J.G. Winther, E.W. Wolff, M. Zucchelli. 154

A. Henderson-Sellers and K. McGuffie. Incorporating and Evaluating Stable Water Isotopes into Land-surface Parameterisation Schemes. In *AGU Fall Meeting Abstracts*, December 2003. 154

A. Henderson-Sellers, K. McGuffie, and A. J. Pitman. The Project for Intercomparison of Land-surface Parametrization Schemes (PILPS): 1992 to 1995. *Climate Dynamics*, 12:849–859, 1996. 154

G. Hoffmann and M. Heimann. Water tracers in the General Circulation Model ECHAM. Technical Report 110, Max Planck Institut für Meteorologie, 1993. 155

G. Hoffmann, M. Werner, and M. Heimann. Water isotope module of the ECHAM atmospheric general circulation model: A study on timescales from days to several years. *Journal of Geophysical Research*, 103(14):16 871 – 16 896, 1998. 155

International Atomic Energy Agency IAEA and World Meteorological Organisation WMO. The Global Network of Isotopes in Precipitation (GNIP) database. *"http://isohis.iaea.org"*, 2001. 154

Intergovernmental Panel on Climate Change IPCC. Climate Change 2001: The Scientific Basis – Contribution of Working Group I to the Third Assessment Report of IPCC. *UNEP/WMO Publications*, 2001. 154

E. Roekner, E.K. Arpe, L. Bengtsson, M. Christoph, M. Claussen, L. Dümenil, M. Esch, M. Giorgetta, U. Schlese, and U. Schulzweida. The atmospheric circulation model ECHAM-4: model description and simulation of the present day climate. *Max-Planck-Institute für Meteorologie Report*, 218, 1996. 155

H. von Storch, H. Langenberg, and F. Feser. A Spectral Nudging Technique for Dynamical Downscaling Purposes. *Monthly Weather Review*, 128:3664–3673, 2000. 155

M. Werner. *Spatial and Temporal Variability of Water Isotopes in Polar Precipitation*. PhD thesis, Max Planck Institut für Meteorologie, 2000. 155

Abstract

Climate change has recently become a major concerning among scientists and the general public. A better knowledge of past climates helps forecasting the future evolution of climate. Stable water isotopes stand as an outstanding paleo-climate proxy. Physical properties of heavy stable water isotopes ($H_2^{18}O, HDO$) cause fractionation processes related to temperature and degree of distillation. If the isotopic signal is correctly inverted, past climate change can be inferred from isotopic archives.

Andean ice-cores offer a unique records of tropical climate and its variability through time. However, the interpretation of the isotopic signal is difficult because of complex atmospheric dynamic over South America. For this purpose, we developed a module handling the stable water isotope fractionation processes within the regional circulation model REMO and applied it to South America.

The manuscript outlines the major milestones of the present PhD. We first introduce the research topic in the wider scope of climate change; the description of the stable water isotope enabled regional circulation model REMOiso; an initial validation of REMOiso over Europe; an investigation of the seasonal variations of precipitation, atmospheric circulation and isotopic signal over South America; and at last the recording of the south American monsoon system (SAMS) by stable water isotope diagnostics.

$\star \ ^{\star} \ \star$

Dans un contexte de changement climatique, la connaissance des climats passés permet de mieux cerner l'évolution future du climat. Les isotopes stables de l'eau constituent un excellent proxy paléo-climatique. Les propriétés physiques des isotopes lourds de l'eau ($H_2^{18}O, HDO$) induisent des fractionnements isotopiques, qui dépendent de la température et du taux de distillation. Sous réserve d'une inversion bien conditionnée du signal isotopique, on peut reconstruire les variations passées du climat à partir d'archives isotopiques. Les carottes de glace andines constituent un enregistrement unique de la variabilité du climat tropical. En revanche, la complexité de la circulation atmosphérique rend plus ardue l'interprétation de leur signal isotopique.

En conséquence, nous avons développé au cours de cette thèse un module traitant du fractionnement des isotopes stables de l'eau au sein du modèle de circulation régionale REMO pour application au cas de l'Amérique du Sud. Le manuscrit retrace les principales étapes de la thèse. Il s'agit de la mise en perspective du travail de thèse dans la problématique du changement climatique ; la description du modèle de circulation régionale REMO_{iso} et de son module traitant des isotopes de l'eau ; la validation initiale de REMO_{iso} sur l'Europe ; l'étude des variations saisonnières des précipitations, de la circulation atmosphérique régionale et du signal isotopique en Amérique du Sud ; de l'enregistrement par les isotopes stables de l'eau de la mousson sud-américaine.

$\star \ ^{\star} \ \star$

Klimawandel regt steigendes Interesse unter Wissenschaftlern und in der öffentlichen Meinung an. In diesem Zusammenhang kann eine bessere Kenntnis des vergangenen Klimas dazu verhelfen, die zukünftige

Entwicklung des Klimas genauer vorherzusagen. Die stabilen Wasserisotopen machen einen vorbildlichen paleoklimatischen Proxy aus. Die physischen Eigenschaften der schweren Wasserisotopen ($H_2^{18}O, HDO$) bewirken isotopische Fraktionierungen, die von der Temperatur und dem Ausregnensgrad abhängen. Wenn das isotopische Signal richtig invertiert wird, können klimatischen Schwankungen aus isotopischen Archiven nachgebildet werden. Die Andinischen Eisbohrkerne liefern eine einmalige Aufzeichnung der klimatischen Variabilität in den Tropen. Wegen der komplexen atmosphärischen Zirkulation kann deren Isotopensignal aber nicht direkt gedeutet werden.

Von daher haben wir im Laufe dieser Doktorarbeit einen Modul entwickelt, der den Kreislauf der stabilen Wasserisotope im regionalen Zirkulationsmodell REMO nachbildet. Im Manuskript werden die wesentlichen Etappen der Doktorarbeit beschrieben. Die wissenschaftliche Fragestellung der Doktorarbeit wird in der Perspektive der Klimawandelforschung eingeleitet; die technische Beschreibung des regionalen Zirkulationsmodell REMO und dessen Wasserisotopenmodul folgt; die ursprüngliche Validation von REMO$_{iso}$ über Europa wird dargestellt; die säzonalen Variationen des Niederschlags, der atmosphärischen Zirkulation und des isotopischen Signals über Südamerika werden untersucht; zuletzt wird die Aufzeichnung des südamerikanischen Monsuns in dem isotopischen Signals hervorgehoben.

$\star \ ^{\star} \ \star$